Modelling the transport and pattern formation of gyrotactic microswimmer suspensions

Lloyd Sun-lloyd Fung

Submitted in part fulfilment of the requirements for the degree of
Doctor of Philosophy

Department of Aeronautics
Imperial College London

Aug 2021

Abstract

Gyrotaxis describes the tendency of bottom-heavy motile micro-organisms to swim sideways under the balancing of gravitational and viscous torque. A suspension of gyrotactic microswimmers will self-focus into a plume in a pipe with a shearing downflow. This work utilises the dilute assumption and model microswimmers, such as the gyrotactic Chlamydomonas and Dunaliella, as hydrodynamically contributing (but not interacting) particles in a flowing suspension that are also subjected to rotational noise. In this framework, the suspension is governed by the Smoluchowski equation and the Navier-Stokes equation.

We then further reduce the Smoluchowski equation into a transport equation for the swimmers using the Fokker-Planck model and the generalised Taylor dispersion (GTD) model. Both models are used to calculate the formation of the gyrotactic plume and the subsequent blip instability via a stability analysis. The Fokker-Planck model is found to be not as accurate as the GTD model. The calculation of the gyrotactic plume also results in the discovery of a series of imperfect transcritical bifurcations in the uniform solution and a singular solution when the Richardson number approaches a certain threshold. The transcritical bifurcations are likely linked to the formation of bioconvective patterns, whereas the singular solution is found to be an extension of Kessler (1986).

Despite encouraging results from the GTD model, it cannot be applied in a general flow field or capture shear trapping in inhomogeneous shear flows. Therefore, a new model using a novel transformation and local approximation of the Smoluchowski equation is proposed. The resulting new transport model performs better than the GTD model due to its ability to capture shear trapping. It also exposes many new drifts and dispersions arising from the interaction between the orientational and spatial dynamics. Nevertheless, this new framework can be further improved by including the semi-dilute effect and better modelling at the wall.

Copyright Declaration

Statement of Originality

I, Lloyd Fung, confirm that the work presented in this thesis is my own. Where information has been derived from other sources, I confirm that this has been indicated in the thesis.

Lloyd Fung, September 7, 2021

Contents

List of Figures

List of Tables

List of publications

1. L. Fung, Y. Hwang. Linear instability of tilted parallel shear flow in a strongly stratified and viscous medium. *JMST Advances*, 2, 37-51, 2020.

2. L. Fung, R. Bearon and Y. Hwang. Bifurcation and stability of downflowing gyrotactic micro-organism suspensions in a vertical pipe. *J. Fluid. Mech.*, 902, A26, 2020.

3. L. Fung and Y. Hwang. A sequence of transcritical bifurcations in a suspension of gyrotactic microswimmers in vertical pipe. *J. Fluid. Mech.*, 902, R2, 2020.

Publication 1 is not appearing in this thesis. Publications 2 and 3 are editted into chapters 2 and 3 respectively. Another publication based on chapter 4 is currently underway.

Acknowledgements

I would like to express my deepest gratitude to my sole supervisor, Dr Yongyun Hwang, who has led me into this field and has been a great mentor in both my research and my career. I would also like to thank Professor Rachel Bearon for hosting me during my short visit to Liverpool and for the wonderful chat, through which we had several breakthroughs.

Special thanks go to Professor Tim Pedley for the short but insightful discussion we had at Cambridge.

This work was supported by the President's PhD Scholarships of Imperial College London.

Chapter 1

Introduction

1.1 Motivation

Many aqueous microorganisms, such as bacteria, algae and certain types of phytoplankton, have developed motility, that is, their ability to propel themselves in a fluid environment by various 'swimming' mechanism. From a fluid dynamics perspective, these motile (swimming) microorganisms are self-propelling, orientable particles suspended in a fluid environment. In this work, they shall be referred to as 'microswimmers', or 'swimmers' for short. Each microswimmer is subjected to forces from their surroundings, such as the viscous force from fluid flow and gravity, while they swim towards a certain direction. By regulating their swimming mechanism or using their own geometry, many of them are also capable of steering themselves, sometimes against the environmental trend, towards a direction that can increase their chances of survival. Therefore, collectively, their transport in a fluid medium is not trivial but strongly dependent on their swimming direction and the fluid flow. This strong coupling between their overall transport and the fluid flow prompts an interesting fluid dynamics problem.

Accurate modelling of the transport of microswimmers in a suspension in response to the environment is of fundamental importance for many biological, ecological and engineering applications. In evolutionary biology, motile microorganisms develop taxis, which is their tendency to swim towards or away from environmental cues such as gravity, light intensity and chemical gradient, to seek food and energy or to evade predators. Quantifying the mechanism of these taxes help us understand the evolutionary pressure behind the development of motility. For example, many phytoplanktons in the ocean are not motile, as the development of motility without taxes only add to the consumption of energy

without much benefit. However, some microalgae, especially those heavier than water, developed taxes by using their geometry. They are bottom-heavy, such that they can orient themselves to swim upward (towards the water surface) to maximise the sunlight one can receive for photosynthesis. Their tendency to swim upward is known as gravitaxis. However, the side effect of being bottom-heavy is that their upswimming can be disrupted in a shear flow, as the viscous torque from the ambient flow balances out the restoring gravitational torque acting on the bottom-heavy microswimmer, resulting in a sideway swimmer transport on average. This tendency to swim sideways under shear is known as gyrotaxis (Kessler, 1985*b*). There seems to be a delicate balance between the development of motility and taxes and the energy investment needed for swimming. A quantitative study of gyrotaxis and the resulting collective transport might help us fully understand this interesting trade-off.

The collective transport of microswimmers as a result of gravitaxis and gyrotaxis also has ramifications in ecology. For example, gyrotaxis in the motile species among phytoplankton might be responsible for the formation of ecological hotspots in the ocean (Durham *et al.*, 2009). When a strong shear in the ocean disrupts their upward motility, gyrotactic species are trapped at a certain depth, triggering the formation of a thin phytoplankton layer. This thin layer is often found in coastal waters where the shearing is strong but the turbulent intensity is low (Durham & Stocker, 2012). Durham *et al.* (2013) have also shown that the gyrotactic motility in some phytoplanktons encourages their aggregation into microscale patches in turbulent water, which might play a role in their sexual reproduction.

In a more controlled environment, the interaction between the orientation-dependent transport of microswimmers and the fluid they are suspended in can also lead to interesting patterns. For example, it has long been observed that patterns of convective rolls can spontaneously appear in a shallow suspension of gravitactic microswimmers if the swimmers are also slightly denser than the fluid. The phenomenon is known as bioconvection because the pattern resembles that of a Rayleigh-Bérnard convection. Based on this analogy, it was suggested that the overturning instability is the main mechanism driving the pattern formation (Childress *et al.*, 1975), in which gravitactic swimmers would accumulate at the top surface of the fluid, aggregate due to the instability, and sink back down as a plume due to their negative buoyancy. However, it was later shown that a gyrotactic instability could also accumulate swimmers into a downflowing plume without an upper boundary (Pedley *et al.*, 1988). In a vertical downflowing pipe, the same gyrotactic mechanism can focus the microswimmers into a plume-like structure. This phenomenon, dubbed as gyrotactic focusing, was first shown by Kessler (1985*b*) to demonstrate the mechanism of gyrotaxis. It has been proposed that the above phenomena can also be used in the production of biofuel to reduce the energy cost of mixing or harvesting bottom-heavy algal species (Croze *et al.*, 2013; Bees & Croze, 2014).

All of the above are the results of the collective behaviour of swimmers in a suspension in which the emergent behaviour arises from the individuals' orientational responses to their environment. While an individual swimmer can be modelled in a Stokesian environment given its small size (1-10 μm for bacteria and 10-100 μm for algae), the emergent behaviour and the macroscopic flow of a suspension of swimmers often occur at a macroscopic scale orders of magnitude larger than the individuals. For example, the bioconvective pattern has a typical length scale of millimetres to centimetres (see Bees, 2020, fig. 1), whereas the turbulence in the ocean has a dissipative scale of millimetres (see Durham *et al.*, 2013, p.4). The difference in lengthscale poses a significant challenge to the modelling of their collective behaviour and pattern formation. Therefore, many model the suspension under some form of coarse-graining instead of modelling the discrete individuals at a large scale. However, creating an accurate and widely applicable coarse-grained model for microswimmers remains a major challenge (Bees, 2020).

This work aims to find ways to overcome the challenge by using and evaluating existing coarse-graining models while developing better ones that can be used to model phenomena such as gyrotactic focusing and bioconvection. We hope that by further developing and evaluating models for the transport of microswimmers in an experimentally realisable set-up, one can eventually use them in more a complex context, such as the engineering of biofuel production and the study of ecology and carbon cycle in the ocean.

1.2 Flow around individual swimmers

1.2.1 Stokes flow

As mentioned, microorganisms such as bacteria and algae have diameters no larger than 100 μm. Their swimming speed can range between tens to hundreds μm per second (Pedley & Kessler, 1992; Bees, 2020). As a result, the Reynolds number of individual microswimmers in water are typically no larger than 10^{-2} (Pedley & Kessler, 1992), and the flow around a microswimmer can be treated as a Stokes flow, where the flow field $\mathbf{u}^*$ and pressure q^* around the microswimmer are governed by the Stokes equation

$$-\mu^* \nabla^{2*}_{\mathbf{x}} \mathbf{u}^*(\mathbf{x}^*) + \boldsymbol{\nabla}^*_{\mathbf{x}} q^*(\mathbf{x}^*) = \mathbf{f}^*, \qquad \boldsymbol{\nabla}^*_{\mathbf{x}} \cdot \mathbf{u}^*(\mathbf{x}^*) = 0. \tag{1.1}$$

Here μ^* is the dynamic viscosity of the fluid and $\mathbf{f}^*$ the disturbance force per unit volume. In this thesis, * denotes dimensional variables. One can then non-dimensionalise the Stokes equation by a

characteristic length a^* and characteristic speed U^* to get

$$-\nabla^2_{\mathbf{x}}\mathbf{u}(\mathbf{x}) + \boldsymbol{\nabla}_{\mathbf{x}} q(\mathbf{x}) = \mathbf{f}, \qquad \text{and} \qquad \boldsymbol{\nabla}_{\mathbf{x}} \cdot \mathbf{u}(\mathbf{x}) = 0, \tag{1.2}$$

where the non-dimensionalised pressure $q = q^* a^*/(\mu^* U^*)$ and disturbance force $\mathbf{f} = \mathbf{f}^* a^{2*}/(\mu^* U^*)$ have been further normalised by μ^* . Typically, the swimmer's length (radius or equivalent) and swimming speed are taken as a^* and U^* for the disturbance flow around a single swimmer.

It is well known that in a Stokesian environment, the flow is linear and time-independent. These properties of the Stokes flow leads to the celebrated Scallop Theorem (Purcell, 1977), which stated that the reciprocal motion (i.e. time-symmetric motion that is invariant under time-reversal) of a swimmer could not achieve a net displacement over a long time in an environment with a vanishing Reynolds number. Instead, locomotion can be only achieved by a non-reciprocal motion. In many bacteria, motility is achieved by a 'corkscrew' swimming mechanism, the continuous rotation of their helical tail. For algae, locomotion is typically achieved by the non-reciprocal 'breast stroke' beat of its flagella. The detailed mechanism of cell motility can be accurately modelled with the Stokes equation. It has been an intensely studied subject in the recent decade, spurred by many numerical methods (e.g. Cortez, 2001; Smith, 2009; Schoeller *et al.*, 2021) for Stokes flows and the recent advancement in experimental techniques such as light microscopy (see review by Lauga & Powers, 2009). However, this work is not as concerned about the detailed mechanics of individuals' swimming as their collective dynamics. Therefore, we shall refer readers to the recent publication by Lauga (2020) for more details on the subject of cell motility.

1.2.2 Multipole representation

Instead of modelling the detailed geometry and swimming mechanism of an individual swimmer, this work uses a multipole representation to approximately describe the influence of a microswimmer in the Stokes flow. To derive the multipole representation, we first write down the impulse response $\mathbf{u}^\delta(\mathbf{x})$ to the Stokes equation

$$\mathbf{u}^\delta(\mathbf{x}) = \left(\frac{\boldsymbol{I}}{r} + \frac{\mathbf{x}\mathbf{x}}{r^3}\right) \cdot \frac{\mathbf{F}^\delta}{8\pi} = \mathcal{G} \cdot \frac{\mathbf{F}^\delta}{8\pi}. \tag{1.3}$$

It is the solution to the problem

$$-\nabla^2_{\mathbf{x}}\mathbf{u}^\delta(\mathbf{x}) + \boldsymbol{\nabla}_{\mathbf{x}} q^\delta(\mathbf{x}) = \mathbf{F}^\delta \delta(\mathbf{x}), \qquad \boldsymbol{\nabla}_{\mathbf{x}} \cdot \mathbf{u}^\delta(\mathbf{x}) = 0, \tag{1.4}$$

where $\mathbf{F}^\delta$ is the unit vector representing the viscosity-normalised impulse (and its direction), $\delta(\mathbf{x})$ the Dirac-delta at the origin and $r = |\mathbf{x}|$ the distance from the origin. Here,

$$\mathcal{G} = \frac{\boldsymbol{I}}{r} + \frac{\mathbf{xx}}{r^3}$$

is the Oseen-Burger tensor, Green's function of the Stokes equation. The solution $\mathbf{u}^\delta$ also represents the flow around a point force $\mathbf{F}^\delta$ (normalised by viscosity) applied on the fluid at the origin.

Because of linearity, a passive particle or swimmer of arbitrary shape and swimming mechanism can be represented as the summation of point forces, surface tractions and surface velocity. Therefore, the flow around the particle/swimmer can be represented as the summation of the free-stream flow $\mathbf{u}^\infty$ and the disturbance flow $\mathbf{u}^d$ created by either a set of forces, surface tractions, surface velocities or a combination of the above.

In this work, we are only concerned with the flow field far from the particle or swimmer at the origin. Therefore, a Taylor expansion of $\mathcal{G}(\mathbf{x}-\mathbf{x}_\alpha)$ about $\mathbf{x}_0 = \mathbf{x}_\alpha = 0$ would provide a far-field representation of the flow, resulting in

$$u_i^d(\mathbf{x}) = -\frac{F_j}{8\pi}\mathcal{G}_{ij} + \frac{M_{jk}}{8\pi}\frac{\partial \mathcal{G}_{ij}}{\partial x_k} + H.O.T., \tag{1.5}$$

where $\mathbf{F}$ is the overall drag and $\boldsymbol{M}$ the overall first moment of traction on the swimmer or particle. The above expansion only shows the zeroth- and first-order terms. The higher-order terms at order n would decay as $1/r^{n+1}$. Therefore, regardless of the swimming mechanism or shape, the influence seen faraway would be well approximated by the first few singularities in this multipole expansion.

The tensor $\boldsymbol{M}$ can be split into its symmetric and antisymmetric parts $\boldsymbol{M} = \boldsymbol{S} + \boldsymbol{L}$. Together with the overall drag, $\mathbf{F}$, $\boldsymbol{S}$ and $\boldsymbol{L}$ provide a low-order representation of the swimmer or particle, which can be measured experimentally (e.g. Drescher *et al.*, 2011) or modelled according to the swimmer's geometry (e.g. Pedley & Kessler, 1990). The singularities $\mathbf{F}$, $\boldsymbol{S}$ and $\boldsymbol{L}$ are also referred to as the Stokeslet, stresslet and rotlet, respectively, as they each represents a point force, a force dipole with vanishing dipole length and a point torque in the flow. Fig. 1.1 shows the streamline of the three-dimensional Stokesian flow field generated by a Stokeslet, a stresslet and a rotlet on the cross-sectional plane at which the Stokeslet, stresslet rotlet are applied. The vector fields are equivalent to the two-dimensional flow fields.

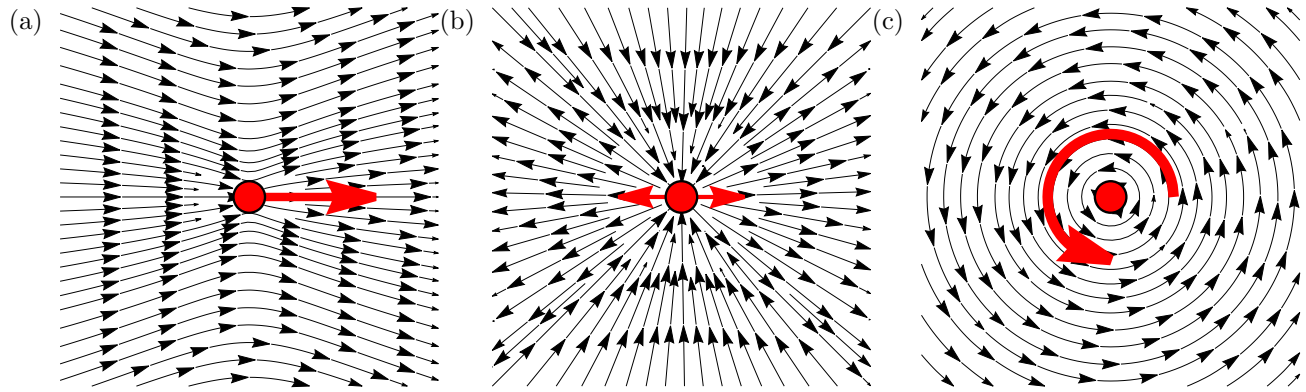

Figure 1.1: The streamline driven by (a) a Stokeslet (point force, $\mathbf{F}$), (b) a stresslet (force dipole, $\boldsymbol{S}$) and (c) a rotlet (point torque, $\boldsymbol{L}$) in a two-dimensional flow. The streamlines also represent the cross-section vector field of a three-dimensional flow on the plane where the point Stokeslet/stresslet/rotlet is acting.

1.2.3 Approximating swimmers as pushers or pullers

We have shown that the far-field velocity induced by a suspended particle or swimmer in a Stokesian environment can be well approximated by the first few expansion of the Green's function of the Stokes equation, i.e. the Stokeslet, stresslet and rotlet. If a swimmer is force-free ($\mathbf{F} = 0$) and torque-free ($\boldsymbol{L} = 0$), then the leading order effect comes from the stresslet. Furthermore, if the swimmer is also axisymmetric about and moving along the swimming direction $\mathbf{p}$, then the tensor $\boldsymbol{S}$ must be in the form of $\boldsymbol{S} = \sigma_0(\mathbf{pp} - \boldsymbol{I}/3)$ (see Kim & Karrila, 1991, §3.3.4), where the scalar σ_0 can be empirically measured as a property of the swimmer.

The sign of σ_0 is of important physical significance as it determines if an isotropic suspension of swimmers would be subjected to hydrodynamic instability (Saintillan & Shelley, 2008a). Swimmers with $\sigma_0 > 0$ are called pullers. The straining flow around a puller comes towards the cell body parallel to the swimming direction and is pushed away from the body perpendicular to the swimming direction (fig. 1.2b). This is known as contractile swimming. Swimmers with $\sigma_0 < 0$ are called pushers. The straining flow comes towards the cell body perpendicular to the swimming direction and is pushed away from the body parallel to the swimming direction (fig. 1.2a). This is known as extensile swimming. Saintillan & Shelley (2008a,b) have shown that a homogeneous and isotropic pusher suspension ($\sigma_0 < 0$) is prone to an instability due to the hydrodynamic stresses from the pushers, while a puller suspension is stable. Therefore, accounting for the hydrodynamic stresses from swimmers is particularly important in a pusher suspension.

Drescher *et al.* (2010a, 2011) and Guasto *et al.* (2010) used particle image velocimetry to measure the flow field around a swimming bacterium *Escherichia coli* and an alga *Chlamydomonas reinhardtii*.

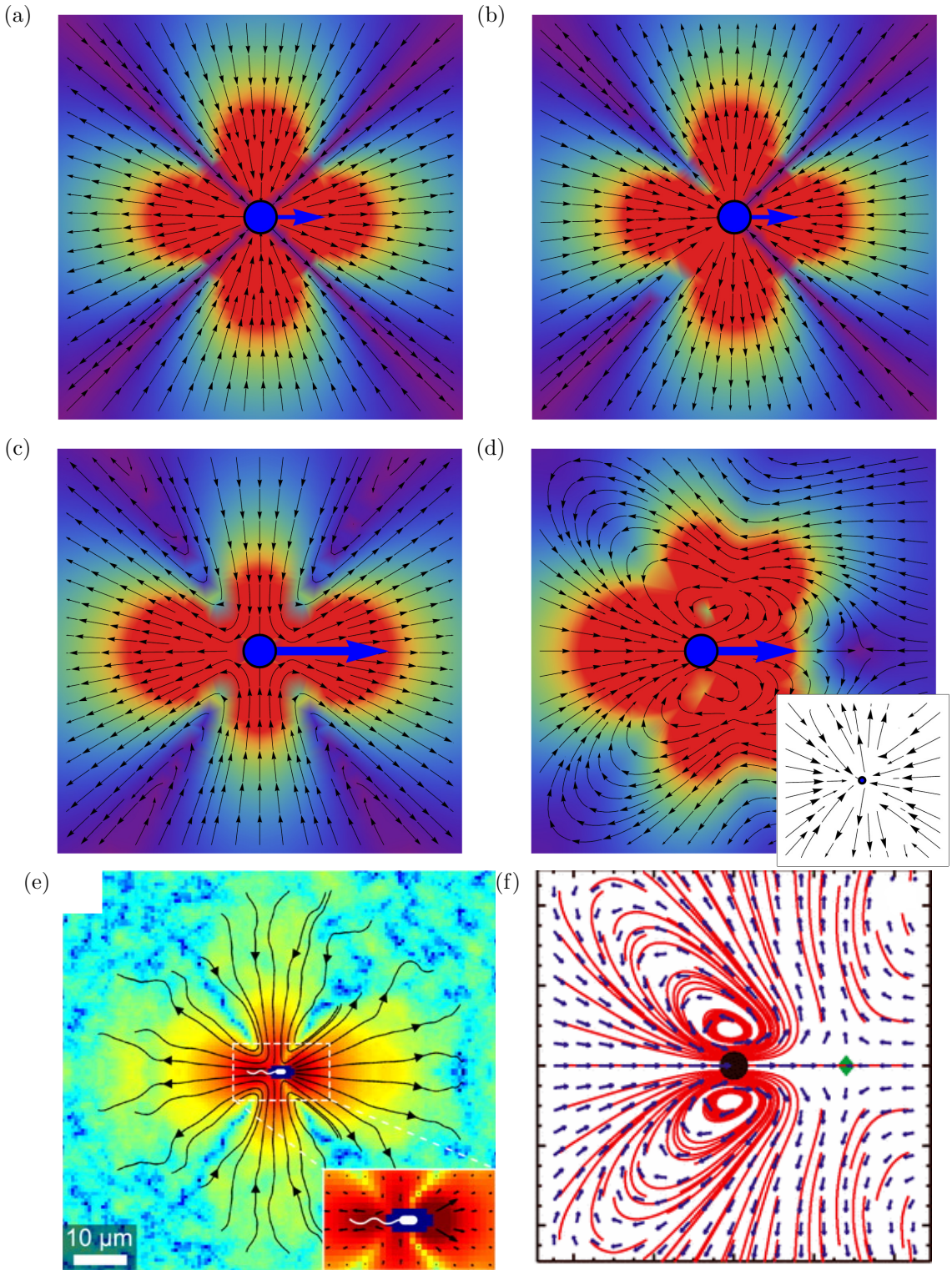

Figure 1.2: The streamline around (a) a pusher ($\sigma_0 < 0$), (b) a puller ($\sigma_0 > 0$), (c) an idealised *E. coli* (c.f. Drescher *et al.* 2011) and (d) an idealised representation of the time- and azimuthally-averaged flow around *C. reinhardtii* (c.f. Drescher *et al.* 2010*a*; Guasto *et al.* 2010). The colour of the contour shows the magnitude of the velocity of the flow in log scale. In (d), the inset shows the far-field idealised flow around *C. reinhardtii*. For comparison, (e, f) show the experimental measurements of the flow field around (e) an *E. coli* (adapted from Drescher *et al.* 2011, DOI: 10.1073/pnas.1019079108. Copyright (2011) by the National Academy of Sciences.) and (f) a *C. reinhardtii* (adapted with permission from Guasto *et al.* 2010, DOI: 10.1103/PhysRevLett.105.168102. Copyright (2010) by the American Physical Society.).

Their measurements showed that the far-field flow around *E. coli* could indeed be well approximated by an idealised force dipole with a finite dipole length (figs. 1.2c,e), closely resembling that of an idealised pusher. However, the flow near the cell body also showed a significant departure from the idealised low-order approximation, which is expected as higher-order singularities are likely playing a more significant role locally near the cell body (see Drescher *et al.*, 2011, fig. 1). The measurement around *C. reinhardtii* painted a more complex picture (Guasto *et al.*, 2010; Drescher *et al.*, 2010*a*). Because of the unsteady 'breast-stroke' beating of the two flagella, the flow field near the algae cell is inherently unsteady. Guasto *et al.* (2010) took a time-resolved measurment of the unsteady flow around a beating cell, while both Guasto *et al.* (2010) and Drescher *et al.* (2010*a*) presented the beat-cycle averaged velocity field. Despite the unsteadiness, the time-averaged flow remains dominated by the stresslet, especially in the far-field, as suggested by the theory. The near-field time- and azimuthally-averaged flow can be more faithfully represented by three off-centred point forces (stokeslets), in which the two acting outside the cell body represents the beating flagella pulling the cell towards the swimming direction, and the other one represents the drag force acting on the cell body in the opposite direction (compare fig. 1.2d with fig. 1.2f). However, at around seven swimmer radius away from the centre, the flow topology began resembling that of an idealised puller (see inset of 1.2d). In summary, the low-order approximation works well in the far-field for both swimmers, but a higher-order expansion might be needed to describe the near-field flow.

This thesis will only consider microswimmers as their idealised low-order representation, i.e. the summation of Stokeslets, stresslets and rotlets. As long as the occurrences of two swimmers encountering at a close distance are low, the detailed flow field near the cell body would not strongly affect the dynamics of the suspension macroscopically. In other words, we assume that the near-field hydrodynamic interactions are rare and negligible. This assumption implicitly implies that the suspension has a characteristic lengthscale much larger than the swimmer and is dilute enough such that the average distance between swimmers is much larger than the size of swimmers. In the following section, we shall further discuss the concentration regime at which this presumption is valid.

1.3 Suspension Regime

As mentioned, it is important to be aware of the different regimes a suspension can have and how different theories are more suitable for each regime. The division of concentration regime presented in this section is based on the volume fraction ϕ. It dictates the significance of the interactions

between swimmers, which may include the far-field and near-field hydrodynamic interactions and the direct contact between swimmers if the volume fraction ϕ is high enough. The hydrodynamic disturbance velocity at a distance R^* caused by a net force on a swimmer of effective radius a^* is of order $\mathcal{O}(a^*/R^*)$. Therefore, the importance of these interactions scales with the volume fraction $(\phi^*)^{-1/3} \sim a^*/R^*$. In the following subsections, we shall present the regimes at an increasing order of the volume fractions.

1.3.1 Dilute solution

In this regime, the concentration is low enough such that the average distance between swimmers R^* is much larger than the swimmer size a^*, i.e. $\phi \to 0$. Therefore, one can approximate the Stokesian flow field by linearly superposing the hydrodynamic contribution of the low-order representation of each swimmer. The superposition allows the development of a continuum model for the suspension of swimmers later in the thesis. However, this superposition is, strictly speaking, not mathematically legal, as the solution flow field about each swimmer does not account for the presence of other swimmers, i.e. the superposed solutions do not share the same boundaries. If ϕ is not tending to zero, the superposition may lead to unwanted artefacts such as the divergence paradox (see §1.4 and Hinch (2010)). However, if the solution is dilute enough, the presence of other swimmers far away would not have a strong effect on the swimmer in consideration, and the approximation by superposition is justified.

This work assumes the swimmer suspension in consideration is diulte enough for the dilute approximation, i.e. $\phi \to 0$. However, in reality, the suspensions have a finite but small volume fraction. We will discuss the threshold at which the dilute approximation is valid shortly.

1.3.2 Semi-Dilute solution

We define semi-dilute as the regime where the naive superposition can no longer capture interactions between swimmer. At the dilute end of this regime, hydrodynamic interactions are still dominated by the far-field, but modelling for the discrete swimmers is needed to capture the interactions accurately. One of the commonly used methods to capture such interaction is the method of reflection. "The method of reflection is based on the idea that the ambient field about each particle consists of the original ambient field plus the disturbance field produced by other particles. The method is iterative, since a correction of the ambient field about a given particle generates a new disturbance solution for

that particle, which in turn modified the ambient field about another particle" (cited from Kim & Karrila, 1991, chapter 8). The accuracy of each pairwise hydrodynamic interaction can be improved by a factor of order $\mathcal{O}(a^*/R^* \sim \phi^{1/3})$ per iteration of reflection. Therefore, considering more reflections improve the accuracy of the hydrodynamic forcing on swimmers in a suspension of finite but small volume fraction.

However, at the more concentrated end of this regime, the approximation provided by the method of reflection would no longer be enough due to the poor representation of the flow field near the cell body by the low-order multipole representation. Typical approaches to model suspension in this regime, such as Stokesian Dynamics (Brady & Bossis, 1988), utilise lubrication theory to account for the near-field interaction. Other computational methods, such as regularised Stokeslet (Cortez, 2001), boundary element method (e.g. Smith, 2009) or force-coupling method (e.g. Schoeller *et al.*, 2021), involve simulation of the detailed geometry and swimming motion of the swimmer. It should be noted that, for biological swimmers, the near-field is much more complex than the multipole representation and often involves the spatiotemporal dynamics of the swimmer's swimming mechanism (c.f. §1.2.3). While the detailed modelling of these complex behaviour deviates from the reductionist approach this work is seeking, we note that some swimming mechanisms can create novel interactions, such as the synchronised beating of sperm flagella (e.g. Schoeller & Keaveny, 2018), that cannot be captured otherwise. Seeking a macroscopic model that can capture these interactions remains a major challenge that sits outside the current scope.

The volume fraction threshold at which solution becomes semi-dilute is not clear cut, but it is clear from the method of reflection that the significance of the far-field hydrodynamic interactions between swimmers scale with the volume fraction. For example, Batchelor (1972) made an $\mathcal{O}(\phi)$ correction to the sedimentation speed of a suspension of sedimenting particles due to the effect of hydrodynamic interaction and showed that the average sedimentation speed slows down by $-6.55\phi\mathbf{u}_s$ compared to the standalone sedimentation speed $\mathbf{u}_s$.

Earlier experiments by Kessler *et al.* (1992) have shown that the interactions between gyrotactic swimmers may not be neglected at an average volume fraction of $\phi = 0.25\%$. However, the density fluctuation in their experiments may also imply that the local volume fraction where the interaction becomes significant is higher than the averaged value. For all intents and purposes of this thesis, we shall use $\phi = 2.5\%$ as an arbitrary local threshold to indicate any local breakdown of the dilute assumption since this value corresponds to the lowest volume fraction Ishikawa & Pedley (2007*a*,*b*) have considered in their work on the semi-dilute suspension. However, one should note that hydrodynamic interactions may have already become significant at a lower volume fraction than the arbitrary threshold.

1.3.3 Concentrated / Liquid crystalline solution

At the concentrated side of the spectrum of volume fractions, the direct interactions between swimmers become important. This is the regime where concentrated collective behaviour, such as bacterial turbulence (Dombrowski *et al.*, 2004; Koch & Subramanian, 2011) and the spontaneous flow in a confined suspension (Wioland *et al.*, 2013), occurs. These phenomena are driven by both the nematic alignment of swimmers (Simha & Ramaswamy, 2002) and the long-ranged hydrodynamic interactions (Saintillan & Shelley, 2008*a*,*b*).

It is not easy to model the collective behaviour in this regime using a discrete simulation, as one should resolve both the complex near-field flow and the nematic alignment of multiple bodies simultaneously. Crude approximations of the hydrodynamic forces, such as slender body theory (e.g. Saintillan & Shelley, 2007) and Jeffery orbit (e.g. Lushi *et al.*, 2014), can be used in conjunction with models for the nematic alignment between swimmers to capture the dynamic of individual swimmers. However, these individual-based models would not be as accurate as the Stokesian based simulations used in the semi-dilute suspension, as they assumed a locally linear flow field and ignored higher-order hydrodynamic interactions.

Alternatively, many phenomenological continuum models have been proposed. Some use the fact that some bacteria are long and thin, which invites the use of liquid crystal theory (e.g. Simha & Ramaswamy, 2002; Marchetti *et al.*, 2013) to model the neumatic order of swimmers. Others (e.g. Wensink *et al.*, 2012; Dunkel *et al.*, 2013; Linkmann *et al.*, 2019) directly seek a continuum equation phenomenologically using the Toner-Tu theory (Toner & Tu, 1998), i.e. writing a phenomenological equation that accounts for the most relevant physical effects and satisfies all the necessary symmetry. This thesis notes the value of these more phenomenologically-driven approaches, which might be more relevant when the nematic alignment is important, and modelling from the first principle is difficult. Some of these approaches, such as the Toner-Tu theory, might also be applicable to derive a macroscopic description for the suspension this thesis set out to study. However, whenever possible, a bottom-up approach is preferred because it gives more physical insight at every level of approximation or abstraction.

1.3.4 Flow regime

Besides the volume fraction of suspension, the Reynolds number of the flow is also an important parameter. Often in an active suspension, novel collective behaviour emerges at the micro- to meso-scale such that a Stokesian environment can be assumed. However, for bioconvection and many other

potential applications and examples listed in §1.1, the macroscopic flow can become inertial even if the microscopic flow around the swimmer is Stokesian. Such is the characteristic that distinguishes bioconvection and gyrotaxis-related phenomena from other phenomena in the field of active matter. Consequently, many of the aforementioned Stokesian-based theories or numerical tools alone are not adequate to fully model the collective behaviour in a nonlinear flow environment.

1.4 Modelling a dilute suspension

One of the objective of this thesis is to seek a continuum model for a dilute suspension of microswimmers that is suitable for phenomena such as bioconvection and gyrotactic focusing. To relate the microscopic mechanics governed by the Stokesian dynamics introduced in the previous subsection to the macroscopic properties we seek, we will use statistics to describe a suspension with a large number of microswimmers. In other words, we will model the conservation of the probability density function $\Psi(\mathbf{x}, \mathbf{p}, t)$ of finding a swimmer at position $\mathbf{x}$ with orientation $\mathbf{p}$ at time t, where $\mathbf{p}$ also defines the swimming direction. However, to use this approach, we must first write down the governing equations for the trajectories of swimmers. In following the subsections, we shall list the ingredients that govern the orientational and spatial trajectories for a single microswimmer.

It should be noted that, although the trajectories of swimmers are derived microscopically in a Stokes flow, the utilisation of statistics at the macroscopic level under the dilute assumption and the clear separation between the microscopic and macroscopic scales allow the model to be used in a wide range of scenario. In particular, the continuum model presented in this section was developed with the aspiration that it can be applied to high Reynolds number flow in the future. However, high Reynolds number flows remain outside the scope of this thesis.

1.4.1 Jeffrey's Equation

Derived directly from the Stokes equation (1.2), Jeffrey's orbit (Jeffery, 1922; Bretherton, 1962)

$$\dot{\mathbf{p}}^* = \frac{1}{2}\boldsymbol{\Omega}^* \wedge \mathbf{p} + \alpha_0 \mathbf{p} \cdot \boldsymbol{E}^* \cdot (\boldsymbol{I} - \mathbf{pp}) \tag{1.6}$$

governs the orientational trajectory of a general body of revolution in a linear flow field with vorticity $\boldsymbol{\Omega}^* = \boldsymbol{\nabla}^*_{\mathbf{x}} \wedge \mathbf{u}^*$ and rate-of-strain tensor $\boldsymbol{E}^* = (\boldsymbol{\nabla}^*_{\mathbf{x}}\mathbf{u}^* + \boldsymbol{\nabla}^*_{\mathbf{x}}\mathbf{u}^{*T})/2$. Were the body a spheroid, the

Bretherton constant $\alpha_0 = (\kappa^2 - 1)/(\kappa + 1)$ can be calculated from the aspect ratio κ and represents how slender the particle/swimmer is. Jeffrey's orbit is also widely used as an approximation model for the orientational dynamics of microswimmers as they are often idealised as bodies of revolution about their swimming directions (see Pedley & Kessler, 1992; Saintillan & Shelley, 2015). This work will take the same approximation, i.e. assuming swimmers as general bodies of revolution subjected to a locally linear flow field. As the flow features of our target application are orders of magnitude larger than the swimmer, the assumption of a locally linear flow field is a valid approximation (see §1.1).

1.4.2 Effective torque from taxes

Taxes in biological microswimmers modify the swimmers' orientation according to the environment. In the Jeffrey's orbit framework, the effective torque from a taxis can be included in $\dot{\mathbf{p}}^*$. Pedley & Kessler (1990) have first written down the formula accounting for the gravitational restoring torque when a bottom-heavy swimmer is perturbed from its upright position. The modified trajectory of the swimmers' orientation is

$$\dot{\mathbf{p}}^* = \frac{1}{2B^*}\left[\hat{\mathbf{k}} - (\hat{\mathbf{k}}\cdot\mathbf{p})\mathbf{p}\right] + \left(\frac{\boldsymbol{\Omega}^*(\mathbf{x})}{2}\wedge\mathbf{p} + \alpha_0\mathbf{p}\cdot\boldsymbol{E}^*\cdot(\boldsymbol{I}-\mathbf{pp})\right), \tag{1.7}$$

where $\hat{\mathbf{k}}$ is the unit vector pointing upwards (against gravity) and B^* the gyrotactic time scale. The factor $1/(2B^*)$ represents the strength of gyrotaxis, where B^* is defined as

$$B^* = \frac{\mu^*\alpha_\perp}{2h^*\rho_s^* g^*}. \tag{1.8}$$

Here μ^* is the fluid viscosity, $\alpha_\perp$ the dimensionless resistance coefficient for rotation about an axis perpendicular to $\mathbf{p}$, h^* the offset (along $\mathbf{p}$) between the swimmer's centre-of-mass and centre-of-buoyancy, ρ_s^* the swimmer's density, and g^* the gravitational acceleration. In the absence of rotational noise, one can demonstrate the gyrotaxis of bottom-heavy swimmers by considering the equilibrium orientation, i.e. by solving $\dot{\mathbf{p}}^* = 0$ in (1.7). For example, in a quiescent flow, the swimmer's equilibrium orientation would be the upright position ($\mathbf{p} = \hat{\mathbf{k}}$). This results in negative gravitaxis. However, if a small shear is imposed, the swimmer would be perturbed slightly sideways from its upright position. With the swimmers' motility, the perturbed orientation to one side results in gyrotaxis. If one defines θ as the angle between $\mathbf{p}$ and $\hat{\mathbf{k}}$ and assumes the direction of vorticity $\boldsymbol{\Omega}^*$ from the shearing is perpendicular to $\hat{\mathbf{k}}$, the orientation $\mathbf{p}$ for a spherical ($\alpha_0 = 0$) bottom-heavy swimmer is

given by

$$\sin\theta = B^*\omega^*, \qquad \cos\theta > 0, \tag{1.9}$$

where $\omega^* = |\mathbf{\Omega}^*|$. This model, first formulated by the series of work by Pedley and Kessler (see Pedley & Kessler, 1992), is further evident experimentally by Durham *et al.* (2009). Here, θ would only have a solution if $B^*\omega^* \leqslant 1$, which represents the range of shear relative to the gravitational torque ($\sim 1/B^*$) before the vorticity too strong for the gravitational torque to balance. At $B^*\omega^* > 1$, the swimmer would follow the strong shear and tumble without a static equilibrium.

Besides gyrotaxis, the framework can also be used to model some other taxes such as phototaxis (e.g. Williams & Bees, 2011; Drescher *et al.*, 2010*b*) or chemotaxis of phoretic artificial swimmers (e.g. Tătulea-Codrean & Lauga, 2018). The framework is applicable as long as the taxes can be represented by an effective torque on the swimmer. However, not all taxes can be represented by an effective torque in the modified Jeffrey's orbit. For example, many bacteria perform chemotaxis by decreasing the tumbling frequency of their run-and-tumble motion in a nutrient-rich environment (Berg, 1993). The $\dot{\mathbf{p}}^*$ framework is not suitable for the stochastically driven run-and-tumble chemotaxis. Instead, it has to be modelled by the stochastic run-and-tumble term. More discussion on the run-and-tumble motion will follow shortly.

1.4.3 Swimming and sedimentation

As a result of the linearity of Stokes flow, the spatial trajectory of a swimmer can be written as

$$\dot{\mathbf{x}}^* = \mathbf{u}^* + V_c^*\mathbf{p} + \mathbf{u}_s^*, \tag{1.10}$$

the superposition of passive advection by the flow $\mathbf{u}^*$, active swimming $V_c^*\mathbf{p}$ in direction $\mathbf{p}$ and 'slip' velocity $\mathbf{u}_s^*$, which is the velocity relative to the local flow due to an external force. In the context of biological microswimmers, $\mathbf{u}_s^*$ usually represents the sedimentation velocity of a swimmer. We note that the swimming speed V_c^* and the sedimentation velocity $\mathbf{u}_s^*$ are not constant in some swimmers. For example, some bacteria lower their swimming speed in nutrient-rich environments via chemokinesis to increase their nutrient uptake (Son *et al.*, 2016). The sedimentation speed of a slender body can also vary with the orientation (Clifton *et al.*, 2018). In this work, the swimming speed V_c^* is assumed to be constant in this work and the sedimentation velocity $\mathbf{u}_s^*$ is assumed relatively negligible compared to V_c^* or $\mathbf{u}^*$ for simplicity (see Pedley, 2010*a*). However, in the rare occasion where there is no vertical ambient flow, $\mathbf{u}_s^*$ might become significant (Maretvadakethope *et al.*, 2019).

1.4.4 Stochasticity in the trajectory

Most microswimmers are between 1-100 μm in diameters, which are too large to be subjected to a significant thermal translational diffusion (Pedley & Kessler, 1992; Saintillan, 2018; Bees, 2020). However, fluctuations from their swimming mechanism, such as flagellar beating, may subject the swimmers to rotational noise. Here we assume the rotation noise as Gaussian such that later we can characterise it as a rotational diffusion with a rotational diffusivity d_r^*. The coupling between rotational diffusivity and swimming results in a correlated random walk, which behaves like an effective spatial diffusion in a quiescent fluid. Using the generalised Taylor dispersion theory (Brenner, 1980; Frankel & Brenner, 1991), one can demonstrate that the effective spatial diffusivity scales with $(V_c^*)^2/6d_r^*$. However, applying this theory in a general flow field would be a subject for discussion later in the thesis. A more thorough introduction to the theory will follow in §1.5.2.

Conventionally, the spreading of biological microswimmers is only characterised by the coupling between rotational diffusion and swimming, while translational diffusion is disregarded. However, if the fluctuations from the swimming mechanism can subject the swimmer to rotational diffusion, there is no reason the randomness would not partly manifest as translational diffusion too. There is little evidence suggesting that the translational diffusion from fluctuations is negligible, despite the conventional treatment of microswimmers. Separating translational diffusion from the random walk due to rotational diffusion is experimentally difficult, so there are no measurements on such translational diffusivity. Nevertheless, this work shall consider the possibility of a non-negligible translational diffusivity D_T^* later in chapter 4.

Besides translational and rotational diffusion, biological microswimmers also exhibit other stochastic behaviour. Most notable, bacteria such as *E. coli* randomly alternate between swimming in a nearly straight line and fast random reorientation (Alt, 1980), caused by the unbundling and re-bundling of their flagella (Berg, 2004). By adjusting the tumbling frequency according to the local chemical concentration in this rum-and-tumble motion, bacteria perform chemotaxis in such a stochastic way that it cannot be captured by a deterministic torque.

Given the stochastic nature of the motion of microswimmers, their trajectories are governed by a Langevin equation. In the next subsection, we shall summarise all of the above ingredients for the motion of bottom-heavy microswimmers and write down a conservation equation.

1.4.5 Formulating the governing equations

Smoluchowski Equation

The configuration of a dilute suspension of microswimmers subjected to translational D_T^* and rotational d_r^* noise at time t^* can be described by the probability density/distribution function $\Psi^*(\mathbf{x}^*, \mathbf{p}^*, t)$ of finding a swimmer with the centre-of-mass position $\mathbf{x}^*$ and orientation $\mathbf{p}$, governed by the Fokker-Planck equation,

$$\frac{\partial \Psi^*}{\partial t^*} + \boldsymbol{\nabla}_{\mathbf{x}}^* \cdot [\dot{\mathbf{x}}^* \Psi^* - D_T^* \boldsymbol{\nabla}_{\mathbf{x}}^* \Psi^*] + \boldsymbol{\nabla}_{\mathbf{p}} \cdot [\dot{\mathbf{p}}^* \Psi^* - d_r^* \boldsymbol{\nabla}_{\mathbf{p}} \Psi^*] = 0. \tag{1.11}$$

derived from the Langevin equations governing the swimmers' rotational and spatial trajectories. Here, $\boldsymbol{\nabla}_{\mathbf{p}} = (\boldsymbol{I} - \mathbf{pp})(\partial/\partial \mathbf{p})$ denotes the gradient operator on the unit sphere. An extra term

$$-\frac{1}{\tau_r}\left[\Psi^* - \int_{S_{\mathbf{p}}} K(\mathbf{p}|\mathbf{p}')\Psi^*(\mathbf{x}^*, \mathbf{p}', t^*) d\mathbf{p}'\right] \tag{1.12}$$

can be added to the right-hand side to account for the run-and-tumble dynamics of some chemotactic bacteria, where the kernel $K(\mathbf{p}|\mathbf{p}')$ is the probability associated with an orientation jump (tumbling) from $\mathbf{p}'$ to $\mathbf{p}$, given the pre-tumble orientation was $\mathbf{p}'$. However, since the algal species do not usually perform such manoeuvres, we shall omit this term in this thesis. Equation (1.11) is the Fokker-Planck equation for the probability density function of a swimmer's spatial and orientational position. When a Fokker-Planck equation is applied to the position of a Brownian particle, it is also sometimes referred to as the Smoluchowski equation (Smoluchowski, 1906). To avoid confusion with the Fokker-Planck model to be introduced later, eq. (1.11) shall be referred to as the Smoluchowski equation in the rest of this work. Here, Ψ^* is normalised by

$$\int_{S_{\mathbf{p}}} \Psi^*(\mathbf{x}^*, \mathbf{p}, t^*) d\mathbf{p} = n^*(\mathbf{x}^*, t^*), \tag{1.13}$$

where $n^*(\mathbf{x}, t)$ is the dimensional number density of swimmers and $S_{\mathbf{p}}$ the unit sphere of orientations. Because of how this work normalises Ψ^*, it has the same dimension as n^*, which is the inverse of volume. Here we also define the local orientational probability density function (p.d.f.) $f(\mathbf{x}^*, \mathbf{p}, t^*)$ as $\Psi^*(\mathbf{x}^*, \mathbf{p}, t^*)$ further normalised by the local number density $n^*(\mathbf{x}^*, t^*)$, i.e.

$$f(\mathbf{x}^*, \mathbf{p}, t^*) = \Psi^*(\mathbf{x}^*, \mathbf{p}, t^*)/n^*(\mathbf{x}^*, t^*). \tag{1.14}$$

Here, $f(\mathbf{x}^*, \mathbf{p}, t^*)$ is subjected to the normalisation condition

$$\int_{S_\mathbf{p}} f(\mathbf{x}^*, \mathbf{p}, t^*) d\mathbf{p} = 1. \tag{1.15}$$

Note that $f(\mathbf{x}^*, \mathbf{p}, t^*)$ is both a function of $\mathbf{p}$ and $\mathbf{x}^*$. For bottom-heavy microswimmers the spatial trajectory $\dot{\mathbf{x}}^*$ and orientational trajectory $\dot{\mathbf{p}}^*$ are governed by eqs. (1.7) and (1.10) respectively.

Equation of flow and the bulk stress tensor

Equations (1.7) and (1.10) require the knowledge of the flow field, which accounts for both the ambient flow and the disturbance flow from each swimmer. In the context of the Smoluchowski equation, the flow field should have been a random variable because the disturbance flow depends on the random configuration of the swimmers. However, in a dilute system with many swimmers, the mean-field $\mathbf{u}^*(\mathbf{x}^*, t^*)$ of the flow can be used instead based on a coarse-graining approximation (Saintillan & Shelley, 2008*a*,*b*). In the approximation, the hydrodynamic contributions of the swimmers are rewritten as the bulk stresses and forces, which would then be added to the mean-field flow equation for $\mathbf{u}^*(\mathbf{x}^*, t^*)$. For a dilute suspension ($\phi \to 0$), the superposition let us use the ensemble average of the stresses and forces from the multipole representation of swimmers as the bulk stress and force. This coarse-graining approach, sometimes referred to as the *Doi-Saintillan-Shelley* model, was used by Saintillan & Shelley (2008*a*,*b*) to demonstrate the long-range hydrodynamic instability of pusher suspension in the Stokes regime. However, similar approaches had already been widely adopted for passive suspensions prior to the applications in active suspensions (see Doi & Edwards, 1988).

In this work, swimmers are further idealised as self-propelling particles that are axisymmetric along the swimming direction. Hence, the hydrodynamic contribution from the swimming motion of each individual can be written as $\boldsymbol{S}^* = \sigma_0^*(\mathbf{pp} - \boldsymbol{I}/3)$, given by the idealised pusher/puller assumption (see §1.2.3). The bulk stress, taken from the ensemble average of the stresslets, is

$$\boldsymbol{\Sigma}^{p*}(\mathbf{x}^*, t^*) = \frac{1}{V^*} \int_{V^*} \int_{S_\mathbf{p}} \Psi^*(\mathbf{x}_0^*, \mathbf{p}, t^*) \sigma_0^*(\mathbf{pp} - \boldsymbol{I}/3) \delta(\mathbf{x}^* - \mathbf{x}_0^*) d\mathbf{p} d\mathbf{x}_0^* = \sigma_0^* n^* \left(\langle \mathbf{pp} \rangle - \boldsymbol{I}/3 \right). \tag{1.16}$$

Here the bracket $\langle \cdot \rangle$ represents the ensemble average, and V^* the volume of the $\mathbf{x}^*$-space. Meanwhile, the ensemble average of the negative buoyancy forces on the swimmers gives the bulk buoyancy force

$$\frac{1}{V^*} \int_{V^*} \int_{S_\mathbf{p}} \Psi^*(\mathbf{x}_0^*, \mathbf{p}, t^*) (-\upsilon^* g^* \Delta\rho^* \hat{\mathbf{k}}) \delta(\mathbf{x}^* - \mathbf{x}_0^*) d\mathbf{p} d\mathbf{x}_0^* = -n^* \upsilon^* g^* \Delta\rho^* \hat{\mathbf{k}}, \tag{1.17}$$

where v^* is the volume of each swimmer, g^* the gravitational acceleration, $\Delta\rho^*$ the density of swimmer minus that of the fluid and $\hat{\mathbf{k}}$ the upward unit vector. We note that the stress system calculated by Batchelor (1970) for passive orientable particles would also contribute hydrodynamic stresses to the flow due to the excluded volume of the particles. The stress system also includes the rotlet contribution when a particle experiences external torque, such as the gravitational restoring torque. Random rotation, as given by d_r^*, would also contribute extra stresses (Hinch & Leal, 1972*a*,*b*). However, a calculation by Pedley & Kessler (1990) on *C. augustae* (née *C. nivalis*, Bees 2020) has shown that the stresslet contribution from the swimmers' active swimming dominates the hydrodynamic contribution. Therefore, this work shall neglect the hydrodynamic contributions from the excluded volume, the external torque and the rotational noise on swimmers.

To calculate $\mathbf{u}^*(\mathbf{x}^*, t)$, one can add the bulk stress and buoyancy force to the equation governing the flow. As mentioned in §1.3.4, this thesis is aspired to develop a model suitable for cases where the macroscopic might be in the inertial regime. For example, the flow in phenomena such as bioconvection and gyrotactic trapping in the ocean is highly nonlinear. Therefore, here we shall keep the inertial terms in the Navier-Stokes equation instead of the Stokes equation adopted by most work on microswimmer suspension. The equation governing $\mathbf{u}^*$ are

$$\frac{\partial \mathbf{u}^*}{\partial t^*} + (\mathbf{u}^* \cdot \boldsymbol{\nabla}_{\mathbf{x}}^*)\mathbf{u}^* = -\frac{1}{\rho^*}\boldsymbol{\nabla}_{\mathbf{x}}^* q^* + \nu^* \nabla_x^{2*}\mathbf{u}^* + \frac{1}{\rho^*}\boldsymbol{\nabla}_{\mathbf{x}}^* \cdot \boldsymbol{\Sigma}^{p*} - n^* v^* g'^* \hat{\mathbf{k}}, \tag{1.18}$$

and the continuity condition

$$\boldsymbol{\nabla}_{\mathbf{x}}^* \cdot \mathbf{u}^* = 0, \tag{1.19}$$

where $g'^* = \Delta\rho^*/\rho^* g^*$ is the reduced gravity. Note that n^* and Σ^{p*} depend on Ψ^*.

In summary, the Smoluchowski equation (1.11), the Navier-Stokes equations (1.18), and the continuity condition (1.19) form the system of equations governing the dilute microswimmer suspension. Since $\dot{\mathbf{x}}^*$ and $\dot{\mathbf{p}}^*$ in (1.11) depend on $\mathbf{u}^*$ while $\boldsymbol{\Sigma}^{p*}$ and n^* in (1.19) depend on Ψ^*, the set of equations are coupled and shall be solved simultaneously.

Nonetheless, by using the ensemble average as the bulk stress tensor and the bulk buoyancy force, we are also effectively taking a linear superposition of the Stokeslets and stresslets without considering the hydrodynamic interactions between them (see §1.3.1). It is easy to show that, in the absence of an external flow, the disturbance flow field calculated from the naive superposition of Stokeslets scales with $V_c^*\phi^*(L^*/a^*)^2$, which will diverge with increasing domain size L^* (see Guazzelli & Hinch, 2011; Hinch, 2010). The divergence is not physical but an artefact of the naive superposition. This so-called

divergence paradox was resolved by Batchelor (1972) using a technique known as hydrodynamic renormalisation. Calculations by Batchelor (1972) and later work such as Hinch (1977) are $\mathcal{O}(\phi)$ to $\mathcal{O}(\phi^2)$ corrections to the sedimentation speed of negatively buoyant particles. Based on the dilute assumption ($\phi \to 0$) and the fact that sedimentation speed is relatively small relative to the strong ambient flow and swimming speed, the divergence and its correction are likely negligible in the grand scheme. Moreover, previous work such as the *Doi-Saintillan-Shelley* model from Saintillan & Shelley (2008*a*,*b*), seminal work on bacterial suspension (Subramanian & Koch, 2009), as well as some of the foundational work on bioconvection (Pedley & Kessler, 1990, 1992), were all built upon the dilute assumption without considering the divergence paradox. Yet, their theories were still successful in demonstrating some key physics and phenomena of microswimmer suspension. Therefore, this work has chosen to build upon the same dilute assumption and will not consider the paradox's effect. Nevertheless, readers should be aware when extending this work to a non-dilute suspension.

1.5 Modelling the transport of microswimmers in a suspension

The combination of the Smoluchowski equation and the Navier-Stokes equation described in the previous section is a suitable model for a dilute suspension of microswimmers, with the added benefit of being able to model nonlinear phenomena in contrast to the other Stokesian models. Despite its descriptive merit, direct numerical simulations of the equations were rarely performed due to the challenge in computational cost. In a three-dimensional simulation, the Smoluchowski equation is resolved in both translational space $\mathbf{x}$ (3 dimensions) and orientational space $\mathbf{p}$ (2 dimensions), as well as in time t (1 dimension). When combining the 6-dimensions equation with the high resolution required for the nonlinear Navier-Stokes equation, our calculation suggests that a full numerical simulation is barely achievable with a high-performance computer cluster. Saintillan & Shelley (2008*a*,*b*) reduced it to a two-dimensional problem to illustrate the hydrodynamic instability. Others, such as Jiang & Chen (2019, 2020), utilised a parallel assumption from the specific example to reduce the number of dimensions resolved. However, to fully capture phenomena such as bioconvection, a three-dimensional simulation remains necessary.

Such a challenge can be overcome by directly simulating individual swimmers using the Langevin equations instead (e.g. Durham *et al.*, 2013; Lushi *et al.*, 2014). With a larger number of swimmers, the simulation may provide some phenomenological observation, but the cost of discrete methods do

not scale well with the number of swimmers and the results are hard to analyse theoretically due to their noisy output.

Instead, this work seeks a macroscopic transport model for the swimmer density n^* in place of the Smoluchowski equation. The macroscopic model should capture how the local flow and the environment affect the transport of swimmers by pre-computing an approximated orientational distribution. In other words, we seek a way to decouple the orientational space operations from the Smoluchowski equation such that we can pre-compute the orientation-dependent transport properties. In this work, we shall introduce two existing models for the transport of microswimmers, both of which overcame the challenge of the Smoluchowski equation by taking a semi-heuristic approach to the transport of swimmers. In both models, the quasi-steady orientational distribution is solved separately under a certain flow field, and the effective transport coefficients are estimated using a phenomenological model. Both models assume the transport equation takes the form of an advection-diffusion equation

$$\frac{\partial n^*}{\partial t^*} + \boldsymbol{\nabla}^* \cdot [(\mathbf{u}^* + \mathbf{V}_m^*) n^*] = \boldsymbol{\nabla}^* \cdot [(\boldsymbol{D}_m^* + D_T^* \boldsymbol{I}) \cdot \boldsymbol{\nabla}^* n^*] \,, \tag{1.20}$$

where $\mathbf{V}_m^*$ is the advection from the swimmer's motility (and sedimentation) and $\boldsymbol{D}_m^*$ the effective diffusivity from the combined effect of the swimmer's stochasticity and motility. The detailed definition of $\mathbf{V}_m^*$ and $\boldsymbol{D}_m^*$ will be introduced below with the subscript m.

1.5.1 The Fokker-Planck Model (Model F)

The Fokker-Planck model was first introduced by Pedley & Kessler (1990) when they tried to model the bioconvective pattern exhibited by a gyrotactic suspension. For simplicity, hereafter, we shall refer to the Fokker-Planck model as model F. The model was developed based on the postulation that the particle's orientation dynamics have reached a/an (quasi-) equilibrium. In other words, they have postulated that the orientational p.d.f. $f(\mathbf{x}^*, \mathbf{p}, t^*) \approx g(\mathbf{p}; \mathbf{x}^*, t^*)$, where $g(\mathbf{p}; \mathbf{x}^*, t^*)$ satisfies

$$\boldsymbol{\nabla}_\mathbf{p} \cdot [\dot{\mathbf{p}}^*(\mathbf{x}^*, t^*) g(\mathbf{p}; \mathbf{x}^*, t^*)] = d_r^* \boldsymbol{\nabla}_p^2 g(\mathbf{p}; \mathbf{x}^*, t^*), \tag{1.21a}$$

subject to

$$\int_{S_p} g(\mathbf{p}; \mathbf{x}^*, t^*) d^2\mathbf{p} = 1, \tag{1.21b}$$

and $\dot{\mathbf{p}}^*$ is given by eq. (1.7). It should be stressed that the above equations were directly postulated in the original publication where model F first appeared (Pedley & Kessler, 1990). Moreover,

the equations only consider the orientational dynamics. In contrast, the Smoluchowski equation (1.11) couples the spatial and orientational dynamics together as a governing for a single p.d.f. in both orientational and spatial positions. Later in §4.5, we shall demonstrate to what limit this approximation can be justified asymptotically from the Smoluchowski equation.

Because $\dot{\mathbf{p}}^*$ depends on the local flow field, which might vary with $\mathbf{x}^*$ and t^*, the solution $g(\mathbf{p};\mathbf{x}^*,t^*)$, which should be solved in $\mathbf{p}$-space, would also depend on $\mathbf{x}^*$ and t^* as parameters. Given the orientational p.d.f. approximation, the advection due to swimmers' motility naturally arises as the ensemble average

$$V_c^*\langle\mathbf{p}\rangle(\mathbf{x}^*,t^*) \equiv V_c^* \int_{S_p} \mathbf{p}g(\mathbf{p};\mathbf{x}^*,t^*)\ d^2\mathbf{p}. \tag{1.22}$$

Therefore, in the Fokker-Planck model, the advection of swimmers by their motility is given as

$$\mathbf{V}_F^* = V_c^*\langle\mathbf{p}\rangle, \tag{1.23}$$

where the subscript F in place of m denotes model F. The original theory did not consider sedimentation of swimmers because it is relatively small compared to the motility. Although Pedley (2010*b*) has later superposed a constant sedimentation $-V_s^*\hat{\mathbf{k}}$ to $\mathbf{V}_F^*$, sedimentation is neglected in this thesis as it is relatively insignificant to the vertical ambient flow to be introduced later (see §1.4.3).

As for the diffusivity, Pedley & Kessler (1990) took inspiration from the fluctuation-dissipation theory and postulated an effective diffusivity, given by the covariance matrix multiplied by a correlation time, i.e.

$$\boldsymbol{D}_F^* = V_c^{*2}\tau^*(\langle\mathbf{pp}\rangle - \langle\mathbf{p}\rangle\langle\mathbf{p}\rangle), \tag{1.24}$$

in which the correlation time τ^* of swimmers' random walk was empirically measured. It should be stressed that $\boldsymbol{D}_F^*$ is postulated instead of being rigorously derived from the Smoluchowski equation (1.11). Pedley (2010*b*) also admitted that $\boldsymbol{D}_F^*$ is essentially *ad hoc*, as the correlation time scale considers both the natural variability of the swimmer properties in the population and the randomness in the swimming direction. Therefore, the correlation time scale τ^* was often measured directly from experiments (e.g Hill & Häder, 1997; Vladimirov *et al.*, 2000).

1.5.2 Generalise Taylor Dispersion Theory (Model G)

The generalised Taylor dispersion theory was originally developed by Brenner (1980) as an extension of the classical Taylor-Aris dispersion (Taylor, 1953; Aris & Taylor, 1956) and later further extended

by Frankel & Brenner (1989, 1991, 1993) to the transport of passive particles in a suspension. The theory approximated the spatial ($\mathbf{x}$-space) moments of the impulse response solution of (1.11) in a quiescent or homogeneous shear flow. The resulting long time growth rates of the first and second moments were used as the effective drift and diffusivity for the coarse-grained advection-diffusion equation. The theory was later extended to gyrotactic swimmers separately by Hill & Bees (2002) and Manela & Frankel (2003). For simplicity, hereafter, we shall refer to this model from the generalise Taylor dispersion theory as model G.

The long-time and homogeneous shear flow assumptions allowed the swimmers to sample long enough in the orientational space under the same condition, such that the orientational distribution of each swimmer would have reached an equilibrium. Although model G share the same orientational p.d.f. $g(\mathbf{p};\mathbf{x}^*,t^*)$ as model F, which satisfies (1.21), they have different interpretations. Model F relies on a local approximation at each location $\mathbf{x}$ and assumes the orientational p.d.f. has reached a quasi-equilibrium without the interaction with the spatial dynamics (i.e. separating orientational dynamics from the spatial ones in the Smoluchowski equation). Meanwhile, model G was developed assuming that the flow is homogeneous in $\mathbf{x}$ and derived following the Langrangian orientational p.d.f. of each particle.

Despite the difference in the interpretation of g, using the growth rate of the first-order statistical moment of the distribution calculated from the Smoluchowski equation, model G derived the same effective drift $\mathbf{V}_G^* = \mathbf{V}_F^* = V_c^*\langle\mathbf{p}\rangle$. However, model G has derived a different effective diffusivity directly from the Smoluchowski equation using the second-order statistical moment instead of postulating one like in model F. Following a similar procedure as Aris & Taylor (1956)'s method of moments, one can derive the effective diffusivity as given by

$$\boldsymbol{\nabla}_\mathbf{p}\cdot[\dot{\mathbf{p}}^*\mathbf{b}_{GTD}^*] - d_r^*\boldsymbol{\nabla}_p^2\mathbf{b}_{GTD}^* - \mathbf{b}_{GTD}^*\cdot\boldsymbol{G}^* = V_c^*\left(\mathbf{p}-\langle\mathbf{p}\rangle_g\right)g; \quad \int_{S_p}\mathbf{b}_{GTD}^*(\mathbf{p};\mathbf{x}^*,t^*)d^2\mathbf{p} = 0 \quad (1.25a)$$

leading to

$$\boldsymbol{D}_G^* = \int_{S_p}\left[V_c^* d_r^*\mathbf{b}_{GTD}^*\mathbf{p} + \frac{\mathbf{b}_{GTD}^*\mathbf{b}_{GTD}^*\cdot\boldsymbol{G}^*}{g}\right]^{sym} d^2\mathbf{p}, \quad (1.25b)$$

where $\boldsymbol{G}^*(\equiv\boldsymbol{\nabla}_\mathbf{x}^*\mathbf{u}^*)$ is the velocity gradient tensor. Here, $\mathbf{b}_{GTD}^*(\mathbf{p};\mathbf{x}^*,t^*) = \mathbf{B}^*(\mathbf{p};\mathbf{x}^*,t^*)g(\mathbf{p};\mathbf{x}^*,t^*)$, where $\mathbf{B}^*$ is the long-time limit of the difference between the overall average position and the average position of the swimmer with orientation $\mathbf{p}$ (Frankel & Brenner, 1991, 1993; Hill & Bees, 2002).

1.5.3 Preliminary comparison between model F and G and the need for a new model

While the advection of swimmers from model F and G are the same, their effective diffusivities are, in principle, accounting for slightly different physics. The model G diffusivity $\boldsymbol{D}_G$ accounts for only the random walk from the swimmer's random rotation, but that of model F also accounts for other physics such as the natural variability among swimmers.

We can compare the two models by assuming the stochasticity in swimmer's orientation as the only source of randomness in the swimmers. On this assumption, Pedley (2010*b*) later suggested that one can impose $\tau^* \sim 1/d_r^*$. However, model F remains a more heuristic approach than model G because the link between $\boldsymbol{D}_F^*$ and the Smoluchowski equation is missing. In contrast to the postulated model F, model G derived the effective diffusivity $\boldsymbol{D}_G^*$ directly from the solution of the Smoluchowski equation (1.11). The scaling of $\mathbf{b}_{GTD}^* \sim \mathcal{O}(V_c^*/d_r^*)$ and $\boldsymbol{D}_G^* \sim \mathcal{O}(V_c^{2*}/d_r^*)$ naturally emerge, and $\boldsymbol{D}_G^*$ is the result of dispersion in $\mathbf{x}^*$-space due to randomness in $\mathbf{p}$-space and $\mathbf{p}$-dependent motility in $\mathbf{x}^*$.

Because of the more rational derivation and the correct scaling of $\boldsymbol{D}_G^*$ with d_r^*, model G has been demonstrated on multiple occasions, both numerically (Croze *et al.*, 2013) and experimentally (Croze *et al.*, 2017), to be more accurate than model F. In particular, model G shows that the magnitude of the cross-stream component in $\boldsymbol{D}_G^*$ in a shear flow decays to zero as shearing increases towards infinity, while that of $\boldsymbol{D}_F^*$ tends to a finite constant (see Bearon *et al.*, 2012, fig. 1). Bees interpreted the qualitative difference in the following paragraph: "as vorticity increases beyond a threshold, the cells tumble, and in a plane normal to the vorticity vector, their orientations scan all directions, yielding in the F model in the limit of large vorticity $\boldsymbol{D} \propto \mathrm{var}(\mathbf{p})$ with three nonzero eigenvalues. However, the G model explicitly evaluates the spatial moments: As vorticity increases, the tumbling cells swim in tighter trajectories and sample less of the shear flow; components of the diffusion tensor normal to the vorticity decay to zero with increasing vorticity" (Bees, 2020, §4.2). This qualitative difference can result in vastly different gyrotactic plumes, which we will exploit later in the thesis to demonstrate the superiority of model G when comparing the results from both models with experimental observations.

However, the model G has an important limitation when applied to a general flow field, in which various forms of $\boldsymbol{G}^*$ would appear. The formulae (1.25a) and (1.25b) proposed by Frankel & Brenner (1991, 1993) were derived by extending the original GTD theory in a quiescent flow (Frankel & Brenner, 1989) to a homogeneous shear flow. For this purpose, Frankel & Brenner (1991) introduced a transformation that maps the position in a sheared suspension into a stationary one, such that

the original theoretical framework in Frankel & Brenner (1989) can be applied. The transformation resulted in the extra terms $-\mathbf{b}^*_{GTD} \cdot \boldsymbol{G}^*$ and $\mathbf{b}^*_{GTD}\mathbf{b}^*_{GTD} \cdot \boldsymbol{G}^*/g$ in (1.25a) and (1.25b). In principle, the mapping is only valid if $\mathbb{R}(\mathrm{eig}(\boldsymbol{G}^*)) \leqslant 0$, thereby restricting the framework's applicability to the subset of linear flows which are not straining-dominant. Moreover, if $\mathbb{R}(\mathrm{eig}(\boldsymbol{G}^*)) > 0$, the left-hand-side operator on $\mathbf{b}^*_{GTD}$ in (1.25a) might become singular, resulting in a singular $\mathbf{b}^*_{GTD}$ and $\boldsymbol{D}^*_{GTD}$. For example, Bearon *et al.* (2011) demonstrated the singularity in $\boldsymbol{D}^*_{GTD}$ as a function of local velocity gradient $\boldsymbol{G}^*$ in the straining-dominant region of a two-dimensional convective cell. This restriction of model G needs to be overcome if one seeks to couple the transport of swimmers with the flow equation to model any macroscopic phenomena.

1.6 Objective and Overview

This thesis aims to improve the transport model of swimmers by developing better methodologies and evaluating existing ones using known examples of pattern formation. The suspension of gyrotactic motile microorganisms has been selected as the main subject of this thesis. Gyrotaxis was chosen because it is relatively simple to model, yet its consequences are significant in nature. It is also one of the simplest phenomena that invovles both the microscopic and the macroscopic scale. It is particularly challenging to model because while the microscopic flow is Stokesian and linear, the macroscopic flow can become nonlinear. Yet, it is also easily realisable in experiments and can be quantitatively measured and compared with theoretical results (e.g. Croze *et al.*, 2017). Moreover, the phenomena related to gyrotaxis are often found at a large scale with a low volume fraction, which fulfils the dilute assumption. Therefore, it is an ideal phenomenon to study while developing a multiscale model for dilute microswimmer suspensions. Ultimately, we hope that by developing the mathematical tools for analysing and modelling a gyrotactic suspension, we can gain a fundamental understanding of how the motility and taxes of microorganisms interact with the flow field and give rise to complex macroscopic phenomena.

This thesis has of two main objectives. The first is to better understand the behaviour of gyrotactic suspension from the dynamical system perspective. We will study some classical collective behaviour of gyrotactic swimmers, such as the formation of gyrotactic plumes, blips and bioconvection, from the point of view of the suspension's stability and bifurcation. The second is to evaluate existing transport models for the swimmers in the context of the aforementioned phenomena and develop better ones that can be applied in the future in other contexts. These two objectives serve each other,

as a better model gives better predictions of the collective behaviour, while a better understanding of the collective behaviour helps us better evaluate different models. Ultimately, we hope to create a transport model that is transferable to other types of collective behaviour and swimmers.

The thesis is organised as follow. In chapter 2, we will apply model F and G to model gyrotactic focusing and evaluate their merits by comparing their qualitative results with experimental observations. In modelling gyrotactic focusing, we will also show how the solution for the gyrotactic plume may become unstable or even bifurcate with changing parameters. Such a bifurcation and instability can be used in conjunction with the qualitative experimental observation to show that model G can more faithfully capture the dispersion of swimmers than model F. In chapter 3, the bifurcation analysis is further extended to show how the suspension bifurcates from a single plume solution to potentially multiple plumes as one increases the container size or the number of swimmers in the system.

Given that model G will be shown to be more accurate, in chapter 4, we will focus on the shortcomings of model G by evaluating it against the Smoluchowski equation in a parallel flow. While model G can more accurately capture the dispersion of swimmers in a homogeneous shear flow, it cannot capture the shear trapping of non-spherical swimmers in an inhomogeneous shear flow (Rusconi *et al.*, 2014; Bearon & Hazel, 2015). Then, we will present a new model that is more accurate in capturing the net swimmer flux in an inhomogeneous shear flow and can overcome the restriction of model G mentioned in §1.5.2.

After that, in chapter 5, we will discuss how the new model can be applied to the gyrotactic suspension and what implications the new model might bring. We will also briefly discuss the limitation of the dilute assumption, including the semi-dilute and wall effects. Lastly, in chapter 6, we summarise the achievements of this thesis. We will conclude this work with an outlook on the development of continuum models for the microswimmer suspension and the modelling of gyrotactic bioconvection.

Chapter 2

Formation of gyrotactic plumes and blips

2.1 Introduction to gyrotaxis

Gyrotaxis is typically observed a in suspension of motile and bottom-heavy micro-organisms such as *Chlamydomonas*, *Dunaliella*, *Heterosigma* and *Volvox*. Because their centre of gravity is offset from their centre of buoyancy, the gravitational torque from the offset tends to orient the micro-organisms upright. With their flagellum positioned at the opposite side of their centre of buoyancy, they tend to swim upward (against gravity) in the absence of flow, which also makes them gravitactic. However, in the presence of a vortical or shearing flow, they deviate from the upright orientation due to the viscous torque from the vorticity of the flow. The balance between the viscous and gravitational torques creates a sideway net drift, which results in gyrotaxis (see §1.4.2).

Kessler first demonstrated the mechanism and coined the term 'gyrotaxis' in a series of experimental studies carried out in a vertical pipe (Kessler, 1984, 1985*a*,*b*, 1986). In his experiments, a downflowing pipe naturally created a shearing flow due to the higher velocity at the centre and the no-slip condition at the wall. The balance between the viscous torque from the shearing and the gravitational torque on each swimmer created a motility-induced flux towards the centre of the cylindrical pipe, resulting in their accumulation along the centreline of the pipe. The column of the accumulated swimmers, often called a gyrotactic plume, could further accelerate the flow at the centreline due to the negative buoyancy force exerted by the swimmers, thereby further increasing the shear rate and attracting even more swimmers towards itself (Kessler, 1986).

Further to the formation of a gyrotatic plume along the pipe centreline in a downward flow, Kessler observed that, under certain conditions, the plume could subsequently break down into multiple blips.

The blips are localised regions with high density of swimmers. They appear to be uniformly spaced vertically and remain axisymmetric (Kessler, 1986; Denissenko & Lukaschuk, 2007). In the right condition, they can spontaneously appear along the gyrotactic plume, usually at the later stage of the plume formation. In general, the plumes, and consequently the blips, are more pronounced when the background number density is high. Kessler (1986) argued that the blips were the consequence of a singularity in the parallel plume solution. To resolve the singularity, either the axisymmetry or steadiness would break down with the streamwise invariance. However, the solution was built upon a primitive model of swimmer transport, as we shall discuss shortly. Later, Hwang & Pedley (2014*b*) performed a linear stability analysis on the plume structure in a two-dimensional channel flow using model F. In contrast to the previous work, Hwang & Pedley did not report any singularity in the plume. Instead, they found the emergence of a varicose-type instability mode in the plume that shared some structural similarities with the blips. Their theory also seemed to have recovered the spacing between the blips. In this thesis, we will show that both theories are possible explanation to the formation of blips.

Kessler (1986) originally modelled the spatial distribution of swimmers with a simple advection-diffusion equation for the swimmers to understand his experimental observations. In the primitive model, the horizontal drift was proportional to ambient vorticity, while the diffusivity was assumed to be constant and isotropic. Although the model was primitive, it enabled the subsequent finding of an analytic solution to the plume structure when the pressure gradient was zero. The primitive model of Kessler (1986) was later superseded by the Fokker-Planck model (model F, Pedley & Kessler 1990) and the generalized Taylor dispersion theory (model G, Hill & Bees 2002; Manela & Frankel 2003). Since then, there have been a number of studies applying either model to the gyrotactic plume. For example, model F was used in Hwang & Pedley (2014*b*) to study both the plume and the blip formation in a rectangular channel. Model G was used by Bees & Croze (2010) and Bearon *et al.* (2012) to study the dispersion of gyrotactic swimmers in the plume. In particular, Bearon *et al.* (2012) showed that the prediction of the swimmer distribution from model G is significantly different from that of model F. The individual-based simulation by Croze *et al.* (2013) further showed that model G provides a more accurate prediction of the swimmer distribution than model F, especially when the shear (or vorticity) rate of the surrounding flow is high. The experiment by Croze *et al.* (2017) showed a similar result. Recently, Jiang & Chen (2020) have also demonstrated the superiority of model G by comparing the results with the Smoluchowski equation.

In this chapter, we will study the emergence of plumes and blips observed in the original pipe flow experiment of Kessler (1986) using both model F and G. We will update the previous study by

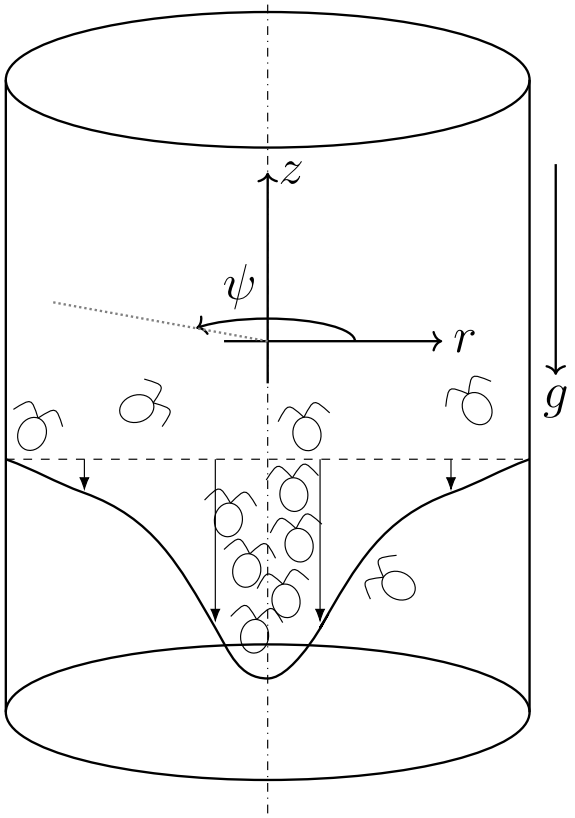

Figure 2.1: Schematic diagram of the flow configuration and the frames of reference. Here the stability analysis is performed on the global frame of reference $\mathbf{x} = (r, \psi, z)$.

Hwang & Pedley (2014*b*), where they analysed the plume in a rectangular channel using model F, to a cylindrical pipe using both model F and G. Despite the encouraging results of Hwang & Pedley (2014*b*) in showing the blips as the result of an instability, no such analysis is available for pipe flows. Hence, it is not possible to make any direct comparison with the previous experiments (Kessler, 1986; Denissenko & Lukaschuk, 2007; Croze *et al.*, 2017). Predicting the occurrence of blips is particularly important for experiments such as Croze *et al.* (2017) because one may want to actively encourage or avoid blips for the study of gyrotactic suspension. Another objective of this chapter is to extensively study the bifurcation and stability of the suspension. Unlike the channel flow studied by Hwang & Pedley (2014*b*), in this set up we shall see the emergence of bistability and the related hysteresis in the bifurcation of the basic state, the possibility of which was previously conjectured by Bees & Croze (2010). Further to this, a particular emphasis of the present study is given to an extensive and comparative assessment of model F and model G for studying bifurcation and stability of the suspension in a downward pipe flow. From this, we shall see that the prediction of model G offers a more realistic description for the experimental observation on the blip instability than that of model F, highlighting the need for an accurate swimmer transport model to describe the pattern-formation in a suspension of gyrotactic micro-organisms.

This chapter is organised as follows. In §2.2, the equations of motion are introduced and formulated

for linear stability analysis with the model F and G. The numerical methods used in this analysis are introduced in §2.3. In §2.4, the bifurcation of the basic state given in the form of a steady axisymmetric and axially uniform plume is presented with a particular emphasis on their bistable nature in some parameter regime. The instability of these basic states is subsequently studied in §2.5. The implication of these findings is discussed in §2.6 from both experimental and theoretical perspectives.

2.2 Problem formulation

We consider a downward fluid flow in a cylindrical vertical pipe, in which a puller-type gyrotactic species of microswimmers are suspended. For simplicity, we will assume the swimmers are spherical ($\alpha_0 = 0$) in chapters 2 and 3. For more rounded algal species like those in the *Chlamydomonas* genus, O'Malley & Bees (2012) showed that the effective eccentricity while they swim is much smaller than that of their inanimate bodies due to the influence of their flagella beating. Therefore, in effect, a spherical approximation of the swimmer might be quite reasonable at the continuum level.

We express the position in space in a cylindrical co-ordinate $\mathbf{x}^* = [r^*, \psi^*, z^*]^T$, where r^* is the radial, ψ^* the azimuthal and z^* the streamwise (or axial) direction pointing upward (against gravity). We define vectors $\hat{\mathbf{i}}$, $\hat{\mathbf{j}}$ and $\hat{\mathbf{k}}$ as the unit vectors in the direction of r, ψ and z respectively. We will also use r, ψ and z as subscripts to express the componets of vectors or tensors in their respective direction (e.g. $\mathbf{p} = [p_r, p_\psi, p_z]^T$). Both of the coordinate systems and the flow geometry are sketched in fig. 2.1.

As mentioned in §1.3.1, this work is built upon the dilute assumption, in which we will neglect any swimmer-swimmer interactions. Following Pedley & Kessler (1990) and Hwang & Pedley (2014*b*), we will further neglect the stresslet term $(1/\rho^*)\boldsymbol{\nabla}^*_{\mathbf{x}} \cdot \boldsymbol{\Sigma}^*_p$ for the majority of the chapter, as it is negligible compared to the negative buoyancy. As discussed in §1.2.3, the stresslet term $\boldsymbol{\Sigma}^*_p$ is not responsible for the generation of any instabilities for the puller-type swimmers considered in this chapter (Saintillan & Shelley, 2007, 2008*a*; Pedley, 2010*b*), so negligance of the term would not significant alter the stability calculation. Later in §2.6.3, we will also briefly discuss the significance of the term.

2.2.1 Non-dimensionalisation and boundary conditions

In this chapter, the governing eqs. (1.18) to (1.21) are non-dimensionalised by the swimmer speed V_c^* and the pipe radius h^*,

$$\mathbf{x} = \frac{\mathbf{x}^*}{h^*}, \quad t = \frac{t^* V_c^*}{h^*}, \quad \mathbf{u} = \frac{\mathbf{u}^*}{V_c^*}, \quad q = \frac{q^*}{\rho^* V_c^{*2}}, \quad n = \frac{n^*}{N^*}, \tag{2.1a-e}$$

where N^* is the background swimmer density (i.e. the swimmer number density when the suspension is uniform). The resulting dimensionless equations are

$$\boldsymbol{\nabla}_{\mathbf{x}} \cdot \mathbf{u} = 0, \tag{2.2a}$$

$$\frac{\partial \mathbf{u}}{\partial t} + (\mathbf{u} \cdot \boldsymbol{\nabla}_{\mathbf{x}})\mathbf{u} = -\boldsymbol{\nabla}_{\mathbf{x}} q + \frac{1}{Re}\nabla_x^2 \mathbf{u} - Ri\ n\ \hat{\mathbf{k}}, \tag{2.2b}$$

$$\frac{\partial n}{\partial t} + \boldsymbol{\nabla}_{\mathbf{x}} \cdot [(\mathbf{u} + \langle \mathbf{p} \rangle) n] = \frac{1}{d_r} \boldsymbol{\nabla}_{\mathbf{x}} \cdot (\boldsymbol{D}_m \cdot \boldsymbol{\nabla}_{\mathbf{x}} n), \tag{2.2c}$$

$$\boldsymbol{\nabla}_{\mathbf{p}} \cdot \left[\beta[\hat{\mathbf{k}} - (\hat{\mathbf{k}} \cdot \mathbf{p})\mathbf{p}] g + \frac{1}{2} \boldsymbol{\Omega} \wedge \mathbf{p} g \right] = \nabla_p^2 g, \tag{2.2d}$$

with boundary conditions

$$\mathbf{u}|_{r=1} = \mathbf{0}, \tag{2.2e}$$

$$\left[(\mathbf{u} + \langle \mathbf{p} \rangle) n - \frac{1}{d_r} \boldsymbol{D}_m \cdot \boldsymbol{\nabla}_{\mathbf{x}} n \right] |_{r=1} \cdot \mathbf{i} = 0, \tag{2.2f}$$

where

$$Ri = \frac{N^* \upsilon^* g'^* h^*}{V_c^{*2}},\ Re = \frac{V_c^* h^*}{\nu^*},\ \beta = \frac{1}{2B^* d_r^*},\ d_r = \frac{d_r^* h^*}{V_c^*},\ \boldsymbol{\Omega} = \frac{\boldsymbol{\Omega}^*}{d_r^*}. \tag{2.2g}$$

Here, Re is the Reynolds number based on the swimming speed, Ri the Richardson number and d_r the dimensionless rotational diffusivity. We note that (2.2d) is further divided by d_r, since the appropriate time scale in the orientation space would be $1/d_r^*$, different from h^*/V_c^* in the physical space. Lastly, the dimensionless translational diffusivities for models F and G are given by

$$\boldsymbol{D}_F = \frac{\boldsymbol{D}_F^* d_r^*}{V_c^{*2}} = \tau(\langle \mathbf{pp} \rangle - \langle \mathbf{p} \rangle \langle \mathbf{p} \rangle) \tag{2.2h}$$

and

$$\boldsymbol{D}_G = \frac{\boldsymbol{D}_G^* d_r^*}{V_c^{*2}} = \int_{S_p} \left[\mathbf{b}_{GTD}(\mathbf{p})\mathbf{p} + \frac{\mathbf{b}_{GTD}(\mathbf{p})\mathbf{b}_{GTD}(\mathbf{p})}{g(\mathbf{p})} \cdot \boldsymbol{G} \right]^{sym} d^2\mathbf{p} \tag{2.2i}$$

respectively, where $\mathbf{b}_{GTD} = \mathbf{b}_{GTD}^* d_r^* / V_c^*$, i.e.

$$\boldsymbol{\nabla}_{\mathbf{p}} \cdot [\dot{\mathbf{p}} \mathbf{b}_{GTD}] - \boldsymbol{\nabla}_p^2 \mathbf{b}_{GTD} - \mathbf{b}_{GTD} \cdot \boldsymbol{G} = (\mathbf{p} - \langle \mathbf{p} \rangle)\, g; \quad \int_{S_p} \mathbf{b}_{GTD} d^2\mathbf{p} = 0, \tag{2.2j}$$

where $\tau = \tau^* d_r^*$ and $\boldsymbol{G} = \boldsymbol{G}^*/d_r^* = \boldsymbol{\nabla}_{\mathbf{x}}\mathbf{u}/d_r$.

2.2.2 Basic state

The basic state of (2.2) is first calculated under the parallel assumption. In other words, we assume the velocity and swimmer distribution are steady, axisymmetric and homogeneous along the axial direction, i.e.

$$\mathbf{u} = \mathbf{u_0} = U(r)\hat{\mathbf{k}}, \qquad n = N(r), \qquad \frac{\partial}{\partial t} = \frac{\partial}{\partial z} = \frac{\partial}{\partial \psi} = 0. \tag{2.3}$$

The basic-state pressure $q_0(r, z)$ is obtained by integrating (2.2b) in the radial direction

$$\frac{\partial q_0}{\partial z} = \frac{2}{Re}\left.\frac{\partial U}{\partial r}\right|_{r=1} - Ri, \tag{2.4a}$$

which is composed of the pressure gradient driving the flow,

$$\frac{\partial q_0^d}{\partial z} = \frac{2}{Re}\left.\frac{\partial U}{\partial r}\right|_{r=1}, \tag{2.4b}$$

and the hydrostatic pressure gradient balancing out the gravitational term (i.e. Ri) in (2.4a).

Substituting (2.3-2.4) into (2.2) yields the following equations for the basic state:

$$-r\frac{\partial q_0^d}{\partial z} + \frac{1}{Re}\frac{\partial}{\partial r}r\frac{\partial U}{\partial r} - rRi(N-1) = 0, \tag{2.5a}$$

$$-\frac{\partial q_0^d}{\partial r} = 0, \tag{2.5b}$$

$$\frac{\partial}{\partial r}(rN\langle p_r\rangle_0) = \frac{1}{d_r}\frac{\partial}{\partial r}(rD_{rr,0}\frac{\partial N}{\partial r}), \tag{2.5c}$$

with the boundary conditions

$$U(1) = 0, \quad \left[\langle p_r\rangle_0 N - \frac{D_{rr,0}}{d_r}\frac{\partial N}{\partial r}\right]\Big|_{r=1} = 0, \tag{2.5d}$$

and the compatibility condition at the centre

$$\left.\frac{\partial U}{\partial r}\right|_{r=0} = 0, \quad \left.\frac{\partial N}{\partial r}\right|_{r=0} = 0. \tag{2.5e}$$

Here, the subscript 0 in $\langle p_r\rangle_0$ and $D_{rr,0}$ indicates the variables are calculated from $U(r)$ of the steady basic state.

Since the total number of the swimmers is preserved over the given control volume, we impose the normalisation condition for the swimmer number density,

$$\int_0^1 N(r) r dr = \frac{1}{2}. \tag{2.6}$$

The flow rate Q given as a parameter, such that

$$-\int_0^1 U(r) r dr = \frac{Q}{2\pi}. \tag{2.7}$$

The negative sign is placed such that when Q is positive, there is a net downflow.

2.2.3 Linear stability analysis

Now, we consider a small perturbation about the basic state

$$\mathbf{u} = \mathbf{u_0} + \epsilon \mathbf{u}' + O(\epsilon^2), \quad q = q_0 + \epsilon q' + O(\epsilon^2), \quad n = N + \epsilon n' + O(\epsilon^2), \tag{2.8}$$

where $\mathbf{u_0} = (0, 0, U(r))$, $\mathbf{u}' = (u_r', u_\psi', u_z')$ and $\epsilon \ll 1$. We also define $\mathbf{\Omega_0} = \boldsymbol{\nabla}_\mathbf{x} \wedge \mathbf{u_0}/d_r$, $\mathbf{\Omega}' = \boldsymbol{\nabla}_\mathbf{x} \wedge \mathbf{u}'/d_r$, $\boldsymbol{G_0} = \boldsymbol{\nabla}_\mathbf{x} \mathbf{u_0}/d_r$ and $\boldsymbol{G'} = \boldsymbol{\nabla}_\mathbf{x} \mathbf{u}'/d_r$ accordingly. Here, we note that the axial velocity perturbation and the swimmer number density over a given control volume V_0 should satisfy

$$\int_{V_0} n' dV = \int_{V_0} u_z' dV = 0, \tag{2.9}$$

as the flow rate Q is fixed and the total number of the swimmers over the entire domain is preserved in time. The linearised equations for the small perturbation are then given as

$$\frac{\partial u_z'}{\partial z} + \frac{1}{r}\frac{\partial (r u_r')}{\partial r} + \frac{1}{r}\frac{\partial u_\psi'}{\partial \psi} = 0, \tag{2.10a}$$

$$\frac{\partial u_z'}{\partial t} + U\frac{\partial u_z'}{\partial z} + u_r'\frac{\partial U}{\partial r} = -\frac{\partial q'}{\partial z} + \frac{1}{Re}\nabla^2 u_z' - Ri\ n', \tag{2.10b}$$

$$\frac{\partial u_r'}{\partial t} + U\frac{\partial u_r'}{\partial z} = -\frac{\partial q'}{\partial r} + \frac{1}{Re}(\nabla^2 u_r' - \frac{u_r'}{r^2} - \frac{2}{r^2}\frac{\partial u_\psi'}{\partial \psi}), \tag{2.10c}$$

$$\frac{\partial u_\psi'}{\partial t} + U\frac{\partial u_\psi'}{\partial z} = -\frac{1}{r}\frac{\partial q'}{\partial \psi} + \frac{1}{Re}(\nabla^2 u_\psi' - \frac{u_\psi'}{r^2} + \frac{2}{r^2}\frac{\partial u_r'}{\partial \psi}), \tag{2.10d}$$

$$
\begin{aligned}
\frac{\partial n'}{\partial t} &+ n'\left(\frac{\langle p_r\rangle_0}{r}+\frac{\partial\langle p_r\rangle_0}{\partial r}\right)+\langle p_r\rangle_0\frac{\partial n'}{\partial r}+U\frac{\partial n'}{\partial z}+\langle p_z\rangle_0\frac{\partial n'}{\partial z}+\frac{\langle p_z\rangle_0}{r}\frac{\partial n'}{\partial\psi}+u_r'\frac{\partial N}{\partial r}\\
&+ \langle p_r\rangle'\frac{\partial N}{\partial r}+N\frac{\partial\langle p_r\rangle'}{\partial r}+N\frac{\langle p_r\rangle'}{r}+N\frac{\partial\langle p_z\rangle'}{\partial z}+\frac{N}{r}\frac{\partial\langle p_\psi\rangle'}{\partial\psi}\\
&= \frac{1}{d_r}\left[\frac{D_{rr}'}{r}\frac{\partial N}{\partial r}+\frac{\partial D_{rr}'}{\partial r}\frac{\partial N}{\partial r}+D_{rr}'\frac{\partial^2 N}{\partial r^2}+\frac{\partial D_{rz}'}{\partial z}\frac{\partial N}{\partial r}+\frac{1}{r}\frac{\partial D_{r\psi}'}{\partial z}\frac{\partial N}{\partial r}\right.\\
&+ \frac{1}{r}\left(D_{rr,0}\frac{\partial n'}{\partial r}+D_{rz,0}\frac{\partial n'}{\partial z}+2D_{r\psi,0}\frac{\partial^2 n'}{\partial r\partial\psi}+\frac{\partial D_{r\psi,0}}{\partial r}\frac{\partial n'}{\partial\psi}+2D_{\psi z,0}\frac{\partial^2 n'}{\partial\psi\partial z}\right)\\
&+ \frac{\partial D_{rr,0}}{\partial r}\frac{\partial n'}{\partial r}+2\frac{\partial D_{rz,0}}{\partial r}\frac{\partial n'}{\partial z}+D_{rz,0}\frac{\partial^2 n'}{\partial r\partial z}\\
&+ \left.D_{rr,0}\frac{\partial^2 n'}{\partial r^2}+D_{zz,0}\frac{\partial^2 n'}{\partial z^2}+\frac{1}{r^2}D_{\psi\psi,0}\frac{\partial^2 n'}{\partial\psi^2}\right],
\end{aligned}
\tag{2.10e}
$$

with the boundary conditions at the wall

$$
u_z'|_{r=1}=u_r'|_{r=1}=u_\psi'|_{r=1}=0, \tag{2.10f}
$$

$$
Nu_r'+N\langle p_r\rangle'+n'\langle p_r\rangle_0=\frac{1}{d_r}\left(D_{rr}'\frac{\partial N}{\partial r}+D_{rr,0}\frac{\partial n'}{\partial r}+D_{rz,0}\frac{\partial n'}{\partial z}+\frac{D_{r\psi,0}}{r}\frac{\partial n'}{\partial\psi}\right). \tag{2.10g}
$$

Here, $\boldsymbol{D}_m'$ and $\langle\mathbf{p}\rangle'$ are computed by linearising (2.2d) and (1.25a) in a similar manner to Hwang & Pedley (2014*a*,*b*). The detailed set of lengthy linearised equations can be found in Appendix A.1.

Finally, the following normal-mode solution is introduced for linear stability analysis:

$$
\begin{aligned}
&\mathbf{u}'(r,\psi,z,t)=\hat{\mathbf{u}}(r)e^{i(\alpha z+m\psi-\omega t)}+c.c,\ q'(r,\psi,z,t)=\hat{q}(r)e^{i(\alpha z+m\psi-\omega t)}+c.c.\\
&n'(r,\psi,z,t)=\hat{n}(r)e^{i(\alpha z+m\psi-\omega t)}+c.c,
\end{aligned}
\tag{2.11}
$$

where α is the axial wavenumber (real), m the wavenumber in the azithumal direction (positive integer) and ω the complex frequency. Substitution of the normal-mode solution into (2.10) yields an eigenvalue problem, as detailed in Appendix A.2.

2.3 Numerical methods

2.3.1 Calculating the orientational distribution

To obtain the basic state from (2.5) and subsequently examine its stability, one must first compute $\langle\mathbf{p}\rangle$ and $\boldsymbol{D}_m$ in (2.2c) as a function of $\boldsymbol{\Omega}$ (models F and G) and $\boldsymbol{G}$ (model G): see §1.5.1 and §1.5.2. To obtain them, one need to solve for $g(\mathbf{p})$ and $\mathbf{b}(\mathbf{p})$ in $\mathbf{p}$-space at each $\boldsymbol{G}$ (which includes $\boldsymbol{\Omega}$). In

this chapter, we represent the $\mathbf{p}$-space by the Eulerian angles $(\lambda, \theta) \in [-\pi, \pi] \times [0, \pi]$, where λ is the longitudinal angle from the r-axis on the $r - \psi$ plane and θ the latitudinal angle from the z-axis. The discretisation is performed using a central finite difference scheme of sixth order in λ and second order in θ. For the compatibility conditions in $\mathbf{p}$-space, a periodic condition is implicitly prescribed in λ and Neumann conditions are explicitly prescribed in θ at $\theta = 0$ and $\theta = \pi$. The discretisation is applied to (1.21) and (1.25a) in `MATLAB` and directly inverted (with the respective normalisation conditions) to obtain $g(\mathbf{p})$ and $\mathbf{b}(\mathbf{p})$ at each $\boldsymbol{G}$, which are then used to compute $\langle \mathbf{p} \rangle$ and $\boldsymbol{D}_m$. The computation is performed with 32×101 points in $\lambda \otimes \theta$. The numerical method is validated with the steady result from the unsteady pseudo-spectral solver for $g(\mathbf{p})$ in Hwang & Pedley (2014*a*,*b*). Since the base flow is a pure shear flow, we only have to compute a library of $\langle \mathbf{p} \rangle$ and $\boldsymbol{D}_m$ for both model F and G when $\boldsymbol{G} = -2S\hat{\mathbf{i}}\hat{\mathbf{k}}$ (and $\boldsymbol{\Omega}/2 = S\hat{\mathbf{j}}$), where $S \equiv -(\partial_r U)/(2d_r)$ is the local shear rate normalised by d_r. Similarly, $\langle \mathbf{p} \rangle'$ and $\boldsymbol{D}'_m$ used in (2.10e) are calculated by applying the same discretisation schemes to the equations in Appendix A.1 as a function of S.

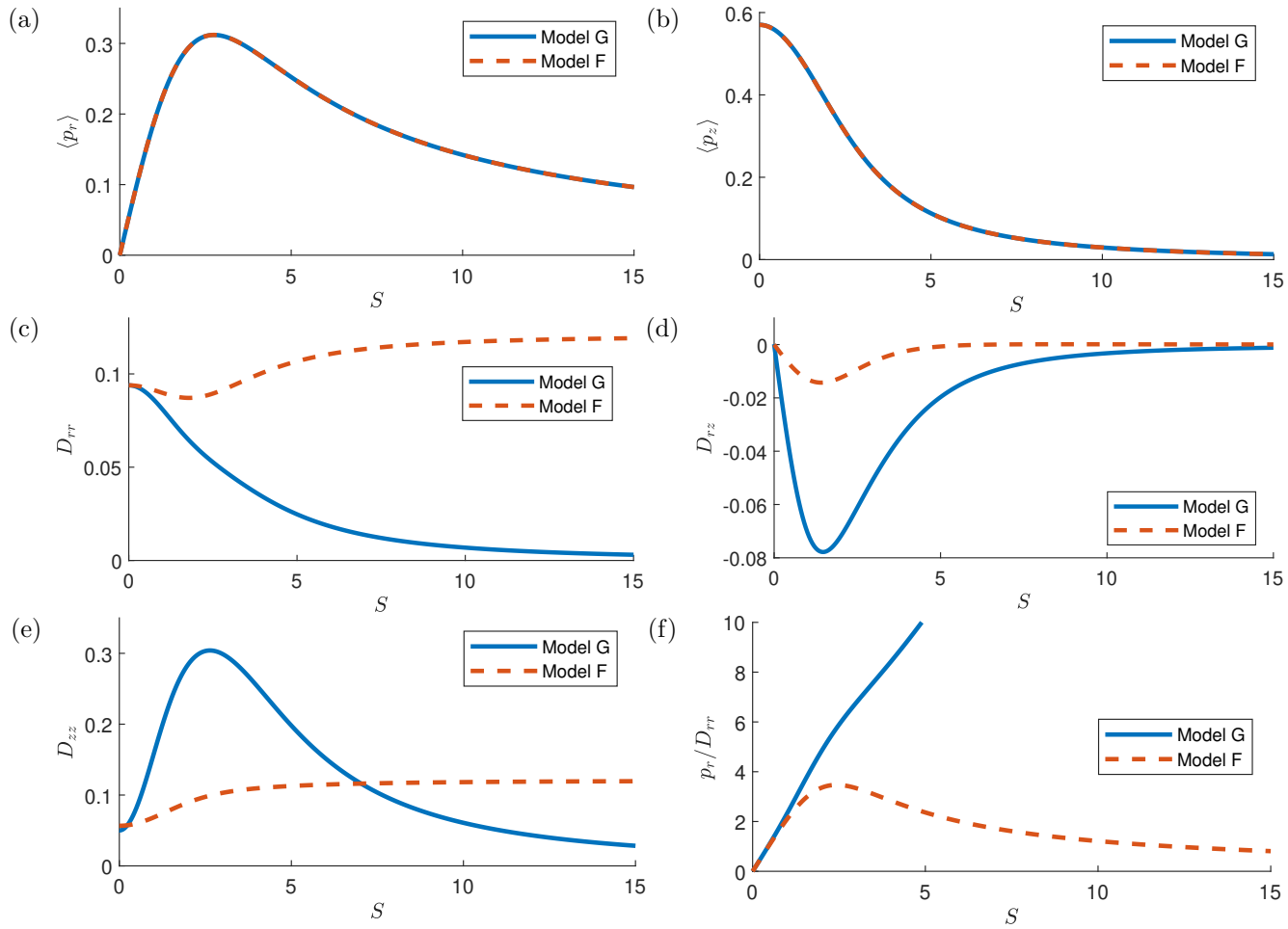

Figure 2.2: Components of $\langle \mathbf{p} \rangle$ and $\boldsymbol{D}_m$ against S from model F (red dashed lines) and model G (blue lines) (c.f. Bearon *et al.* 2012, fig. 1).

Fig. 2.2 shows the resulting $\langle \mathbf{p} \rangle$ and $\boldsymbol{D}_m$ as function of S for *C. augustae* using both model F and G,

which is also the equivalent of fig. 3 of Hwang & Pedley (2014*a*) ($S \mapsto S/2$ in their notation) and fig. 1 of Bearon *et al.* (2012) ($S \mapsto -\sigma$ in their notation).

2.3.2 Solving for the basic state

To compute the basic state, the radial direction is discretised using a Chebyshev collocation method. The collocation points and differential matrices in r are generated using the script provided by Weideman & Reddy (2000). To improve numerical accuracy, (2.5c) is pre-integrated with the no-flux condition (2.5d), while the variable $N(r)$ in (2.5) is transformed into $H(r) = \ln N(r)$. The resulting equations governing the variables $[\partial_z q_0^d; U(r); H(r)]$ are

$$-r\frac{\partial q_0^d}{\partial z} + \frac{1}{Re}\frac{\partial}{\partial r}r\frac{\partial U}{\partial r} - rRi(\exp(H) - 1) = 0, \tag{2.12a}$$

$$\langle p_r \rangle_0 = \frac{1}{d_r} D_{rr,0}\frac{\partial H}{\partial r}, \tag{2.12b}$$

with the boundary condition

$$U(1) = 0, \tag{2.12c}$$

the compatibility conditions at the centre

$$\left.\frac{\partial U}{\partial r}\right|_{r=0} = 0, \quad \left.\frac{\partial N}{\partial r}\right|_{r=0} = 0, \tag{2.12d}$$

and the normalisation conditions

$$\int_0^1 \exp(H(r)) r dr = \frac{1}{2} \tag{2.12e}$$

and

$$-\int_0^1 U(r) r dr = \frac{Q}{2\pi}, \tag{2.12f}$$

in which the comptability conditions (2.12d) are explicitly prescribed at $r = 0$, the no-slip condition (2.12c) at $r = 1$ for $U(r)$, the normalisation condition (2.12e) at $r = 1$ for $H(r)$ and the flow rate (2.12f) at the driving pressure $\partial_z q_0^d$.

A Newton-Ralphson method is implemented in `MATLAB` to solve (2.12) for $[\partial_z q_0^d; U(r); H(r)]$ at each value of Ri and Q. The function used to calculate the residue from the Newton-Ralphson method is also modified and used in conjunction with the ODE solver `ode15s` in `MATLAB` to create an *ad hoc* unsteady solver for the time evolution of the axisymmetric and axially-uniform plume. The two solver give identical steady results when the steady plume is stable to an axially uniform and axisymmetric

Parameter	Description	Reference Value	Units
ρ^*	Fluid density	1	g/cm^3
g^*	Gravitational acceleration	980	cm/s^2
ν^*	Dynamic viscosity	0.00957	cm^2/s
h^*	Radius of pipe	$0.1 \sim 0.4$ (0.19)	cm
N^*	Average swimmer number density	$0 \sim 3.13 \times 10^5$	swimmers/cm^3
$\Delta\rho/\rho$	Relative swimmer number density	0.05	–
v^*	Cell volume	2.1×10^{-9}	cm^3
$g'(= g^*\Delta\rho/\rho)$	Relative gravity	49	cm/s^2
B^*	gyrotactic time scale	3.4	sec
V_c^*	Swimming speed	6.3×10^{-3}	cm/s
τ^*	Correlation time scale	5.35	s
$D_V^*(= V_c^{*2}\tau^*)$	Nominal translation swimmer diffusivity	2.12×10^{-4}	cm^2/s
d_r^*	Rotational diffusivity	0.067	1/s

Table 2.1: Dimensional parameters and their reference values in the present study. Most of the parameters for the swimmer properties are taken from the data for *C. augustae* (Pedley & Kessler, 1990; Bees *et al.*, 1998; Pedley, 2010*b*).

Parameter	Description	Reference Value
Ri	Richardson number	$0 \sim 160$
Q	Dimensionless Flow Rate	$0 \sim 7$
Re	Reynolds number based on V_c^*	$0.066 \sim 0.26$ (0.126)
β	gyrotactic time scale divided by d_r^*	2.2
d_r	Rotational diffusivity normalised by V_c^*/h^*	2.13

Table 2.2: Dimensionless parameters and their values in the present study.

perturbation, but the unsteady solver will diverge from an unstable solution.

2.3.3 Solving for the linear stability

For the linear stability, the radial direction of (A.7) is discretised using the same discretisation method as the one for the basic state. The boundary conditions are applied explicitly. The discretised eigenvalue problem is solved using the function `eig` in `MATLAB`, which support explicit boundary conditions. The computation is performed with $N_r = 175$, showing no difference from the results with $N_r = 100$. The computed eigenvalues for $Ri = 0$ are validated against pipe flow stability data of Schmid & Henningson (1994, 2001) and Meseguer & Trefethen (2003) with excellent agreement.

2.3.4 Parameters

A list of parameters and their values used in the present study are summarised in table 2.1. In the present study we will use $\tau^* = 5.35s$, which is slightly different from $\tau^* = 5s$ used in previous studies (e.g. Hwang & Pedley, 2014*b*). To provide consistent and quantitatively comparable results between the two models, the value for τ^* is chosen such that the two models to share the same radial diffusivity in a stationary suspension. In other words, we follow the approach of Bearon *et al.* (2012), in which τ^* is chosen to match $D_{G,rr}$ with $D_{F,rr}$ in the absence of any flow (i.e. stationary medium). This gives $\tau = 0.36$, consistent with that of Bearon *et al.* (2012).

In this study the radius of the cylindrical pipe is chosen to be around 0.2cm, so that we obtain results comparable with to Hwang & Pedley (2014*b*). The parameters for the swimmer's properties, including swimming speed V_c^*, gyrotactic time scale B^*, relative density $\Delta\rho/\rho$ and rotational diffusivity d_r^*, are taken for *C. augustae* from previous studies (e.g. Pedley & Kessler, 1990; Bees *et al.*, 1998; Pedley, 2010*b*; Hwang & Pedley, 2014*b*), except for the shape of the swimmer, which we assume to be spherical. As in the linear stability analysis of Hwang & Pedley (2014*b*) and the experiment of Croze *et al.* (2017), only the flow rate Q and the background swimmer number density (represented by Ri) are varied in this study. Based on the parameter values given in table 2.1, the dimensionless parameters and their values are given in table 2.2.

2.3.5 Pseudo-arclength continuation

Finally, to study the bifurcation of the basic state, the Newton-Raphson solver is combined with a pseudo-arclength continuation algorithm such that we can seek steady plume solutions in the $Ri - Q$ parameter space exhaustively. In this chapter, the continuation is performed by keeping Q constant while we continue the solution in Ri. In chapter 3, we shall further extend the same continuation methodology to varying Q, Ri or the pressure gradient while keeping one of the parameters constant.

The pseudo-arclength continuation method is briefly described as follow. First, we rewrite the system of equations (2.12) for the basic state (i.e. the steady plume solution) as $F(\mathcal{U}, \Lambda) = 0$, where $\mathcal{U} = [\partial_z q_0^d; U(r); H(r)]$ represents the solution we seek, and $\Lambda = Ri$ the parameter to be varied. For a given initial Λ_0, we can solve for $\mathcal{U}_0$ in $F(\mathcal{U}_0, \Lambda_0) = 0$ using the Newton solver mentioned in §2.3.2. Then, we can find the next solution $\mathcal{U}$ at Λ by using $(\mathcal{U}, \Lambda) = (\mathcal{U}_0, \Lambda_0) + \Delta s(\dot{\mathcal{U}_0}, \dot{\Lambda_0})$ as the initial

guess and solving

$$F(\mathcal{U}, \Lambda) = 0, \tag{2.13a}$$

$$\dot{\mathcal{U}}_0(\mathcal{U} - \mathcal{U}_0) + \dot{\Lambda}_0(\Lambda - \Lambda_0) = 0 \tag{2.13b}$$

iteratively in a Newton solver. Here, Δs is a prescribed step size and $(\dot{\mathcal{U}}_0, \dot{\Lambda}_0)$ the tangent vector to the solution $(\mathcal{U}_0, \Lambda_0)$. In general, the tangent vector $(\dot{\mathcal{U}}, \dot{\Lambda})$ at $(\mathcal{U}, \Lambda)$ can be found by linearly solving

$$\partial F(\mathcal{U}, \Lambda) \cdot (\dot{\mathcal{U}}, \dot{\Lambda}) = 0, \tag{2.14a}$$

$$(\dot{\mathcal{U}}_0, \dot{\Lambda}_0) \cdot (\dot{\mathcal{U}}, \dot{\Lambda}) = 1 \tag{2.14b}$$

after the convergence of each solution set $(\mathcal{U}, \Lambda)$. Here $\partial F(\mathcal{U}, \Lambda)$ is the last Jacobian of $F(\mathcal{U}, \Lambda)$ taken from the Newton iteration for $(\mathcal{U}, \Lambda)$. The initial $(\dot{\mathcal{U}}_0, \dot{\Lambda}_0)$ for the first iteration is $(\dot{\mathcal{U}}_0, \dot{\Lambda}_0) = (\mathbf{0}, 1)$, which also sets the direction of the continuation. The above steps are repeated to generate a series of solutions $\mathcal{U}$ at each $\Lambda = Ri$, which we will use as the basic state for the stability analysis later.

2.4 Basic state

In this section, we shall present the basic-state solutions, i.e. the plumes, found in the $Q - Ri$ space using either model F or G.

2.4.1 Very low flow rate

At a very low flow rate (i.e. $Q \to 0$), models F and G share the same asymptotic value for $\langle \mathbf{p} \rangle$ and the radial diagonal component of $\boldsymbol{D}_m$ (see Bearon *et al.* (2012) and fig. 2.8). Therefore, the two models would give almost identical results when Q is small enough. Hence, here we report the result from model G only.

When $Q = 0$, a stationary uniform suspension (i.e. $U(r) = 0$ and $N(r) = 1$) is a solution to (2.5). However, a further numerical search has also found that there exists another solution at $Q = 0$ featured with non-trivial $U(r)$ and $N(r)$, consistent with Bees & Croze (2010). Bifurcation diagrams of these two solutions with respect to Ri are shown for small positive Q in fig. 2.3, where the centreline number density $N(0)$ and axial velocity $U(0)$ are used to represent the state of the steady solutions. For $Q = 0$, the two solutions meet at $Ri = Ri_c (\simeq 189.9)$, and their stabilities have been checked using

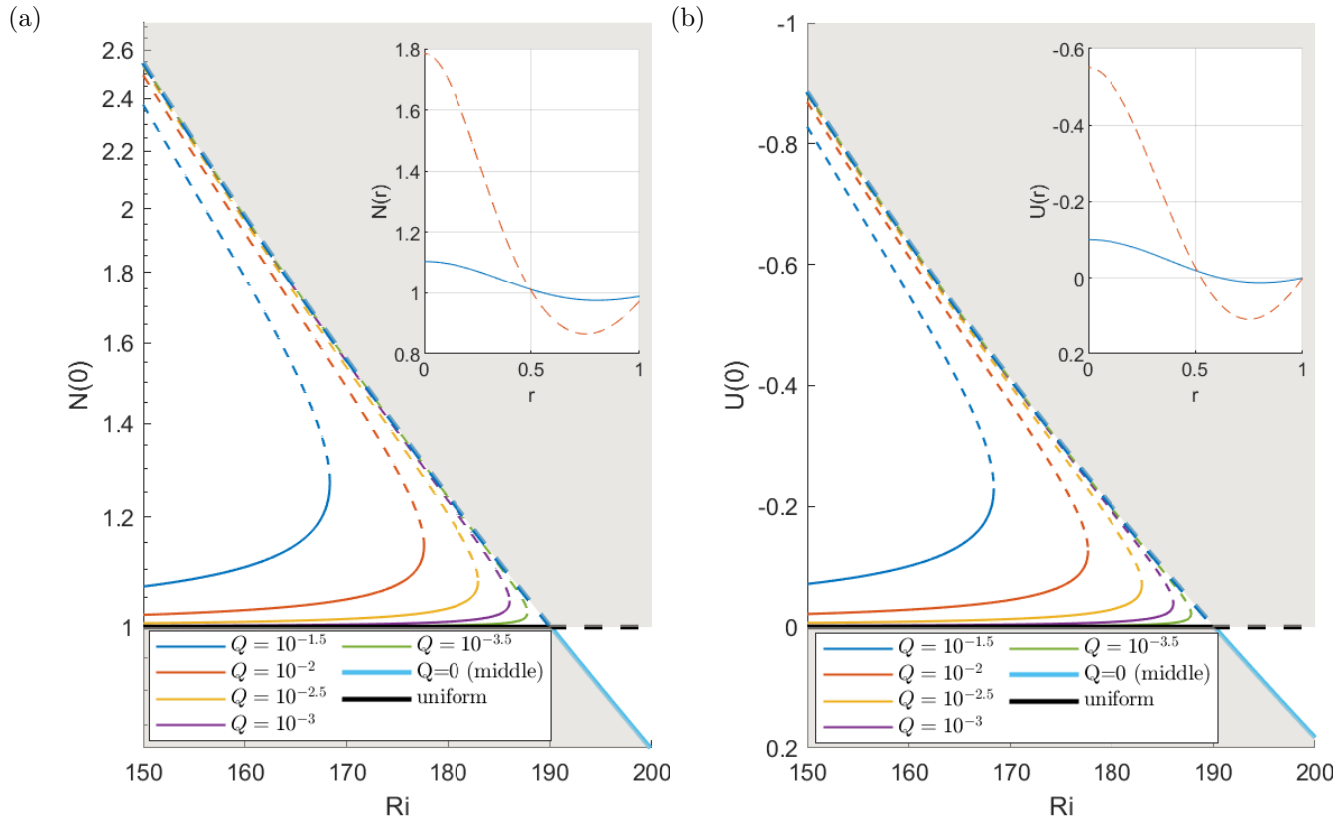

Figure 2.3: Bifurcation of steady solutions with Ri at very low flow rates: (a) the swimmer number density $N(0)$ and (b) the centreline velocity $U(0)$ along the pipe axis. Here, ——, stable; - - - -, unstable. The grey area indicates where $Q < 0$ contours would be. The insets show $N(r)$ and $U(r)$ at $Ri = 160$: blue ——, the lower branch; red - - - -, the middle branch. Note that as $Q \to 0$, the results from models F and G coincides. Also, see fig. 3.2 for the full transcritical bifurcation diagram.

the unsteady solver described in §2.3. The stationary solution ($U(r) = 0$ and $N(r) = 1$) is found to be stable for $Ri < Ri_c$, but becomes unstable for $Ri > Ri_c$. On the other hand, the non-trivial solution, featured with a downflow and a high swimmer number density along the pipe axis, is unstable for $Ri < Ri_c$. This solution gains its stability when $Ri > Ri_c$, and the form of the solution is subsequently changed with an upflow and a lower swimmer number density along the pipe axis. The interchange of the stability of the two solutions at $Ri = Ri_c$ indicates that the stationary suspension in the vertical pipe experiences a transcritical bifurcation with Ri.

When a small downflow ($Q > 0$) is applied, the transcritical bifurcation point given at zero flow rate turns into a saddle-node point. At $Ri > Ri_c$, the axial velocity is upward instead of downward (i.e. $U(0) > 0$), even though the overall net flow is downward ($Q > 0$). If a small upflow ($Q < 0$) is applied instead then the opposite is true, as shown by the grey area in fig. 2.3. The transition from a transcritical to a saddle-node bifurcation is the consequence of an imperfect bifurcation caused by the addition of a small non-zero flow rate. This behaviour of the solutions with two parameters, Ri and

Q, can be understood within the framework of codimension two bifurcation (i.e. bifurcation with two parameters). The overall bifurcation is also closely related to how the system would evolve with the flow direction. The imperfect transcritical bifurcation is also related to the wavelength of gyrotactic bioconvection, which we will discuss further in chapter 3.

2.4.2 Model F

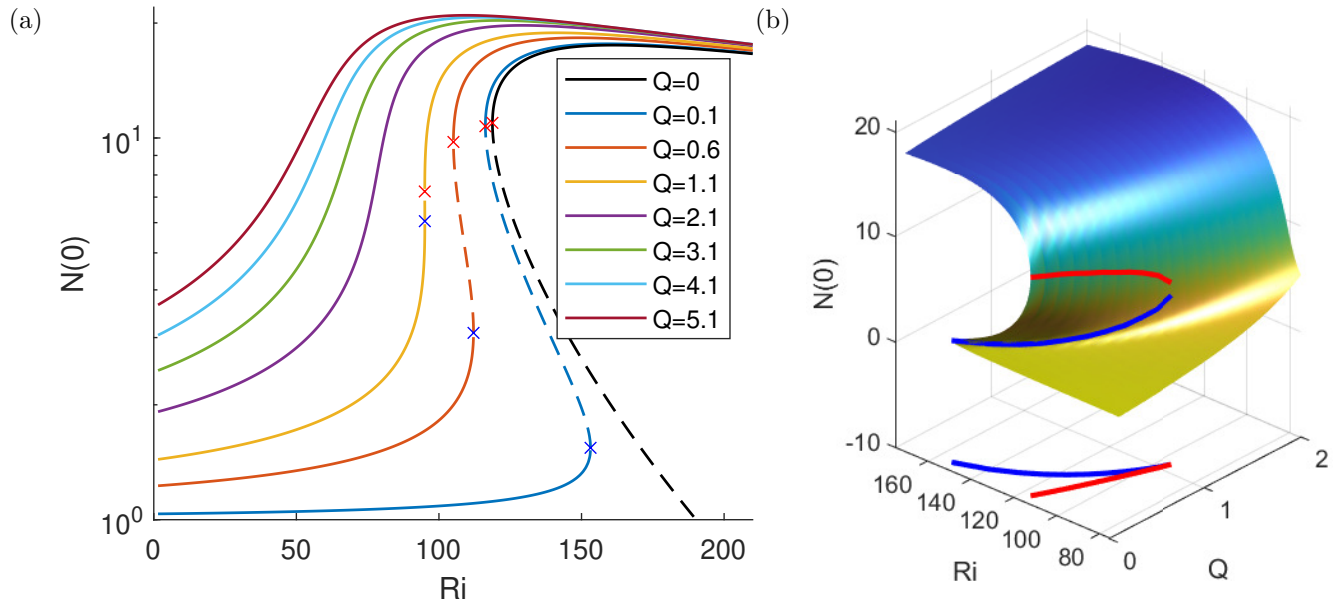

Figure 2.4: Bifurcation of the steady solutions at high flow rates (model F): (a) $N(0)$ with respect to Ri for several flow rates Q; (b) surface plot of $N(0)$ in the $Q - Ri$ space. In (a), ——, stable; - - - -, unstable. The blue cross (x) indicates the first saddle-node point where lower and middle branches meet, while the red cross (x) indicates the second saddle-node point where middle and upper branches meet. In (b), the blue and red curves indicate the trajectories of the two saddle-node points with change in Q, respectively. The graph at the bottom shows the projection of the trajectories onto the $Q - Ri$ plane.

The solution featured with $N(0) > 1$ and $U(0) < 0$ in fig. 2.3 is further continued for much higher flow rates with model F. Fig. 2.4a shows the result from such continuation with model F, in which the number density at the pipe axis $N(0)$ is used to represent the state of the corresponding steady solution. At sufficiently low flow rate ($Q \lesssim 1$), the bifurcation of the solutions featured with two saddle-node points (highlighted by the crosses in fig. 2.4a), indicating the emergence of three solutions at the given flow rate. With the increasing order of $N(0)$, the three types of solutions will be denoted by lower, middle and upper branches, respectively, and they are visualised in fig. 2.5. Here, we note that $N(0)$ was found to uniquely represent each solution per parameter set, and hence was used as a representation for each solution. In general, as the solution is continued from the lower to upper branch, both the velocity and swimmer distribution near the pipe axis ($r = 0$) tend to be sharper.

This is expected because the lower branch state is a homotopy of the uniform suspension obtained with increasing flow rate (i.e. state without gyrotactic instability), while the middle and upper branch states are homotopy of nonlinearly developed plumes from the gyrotatic instability at zero flow rate (i.e. state with nonlinearly saturated gyrotactic instability). Examination of the stability of each solution to axially and radially uniform perturbations (i.e. unsteady calculation of the basic state) reveals that the lower and upper branches are stable, whereas the middle one is unstable, indicating the bistable nature of the basic state featured with hysteresis.

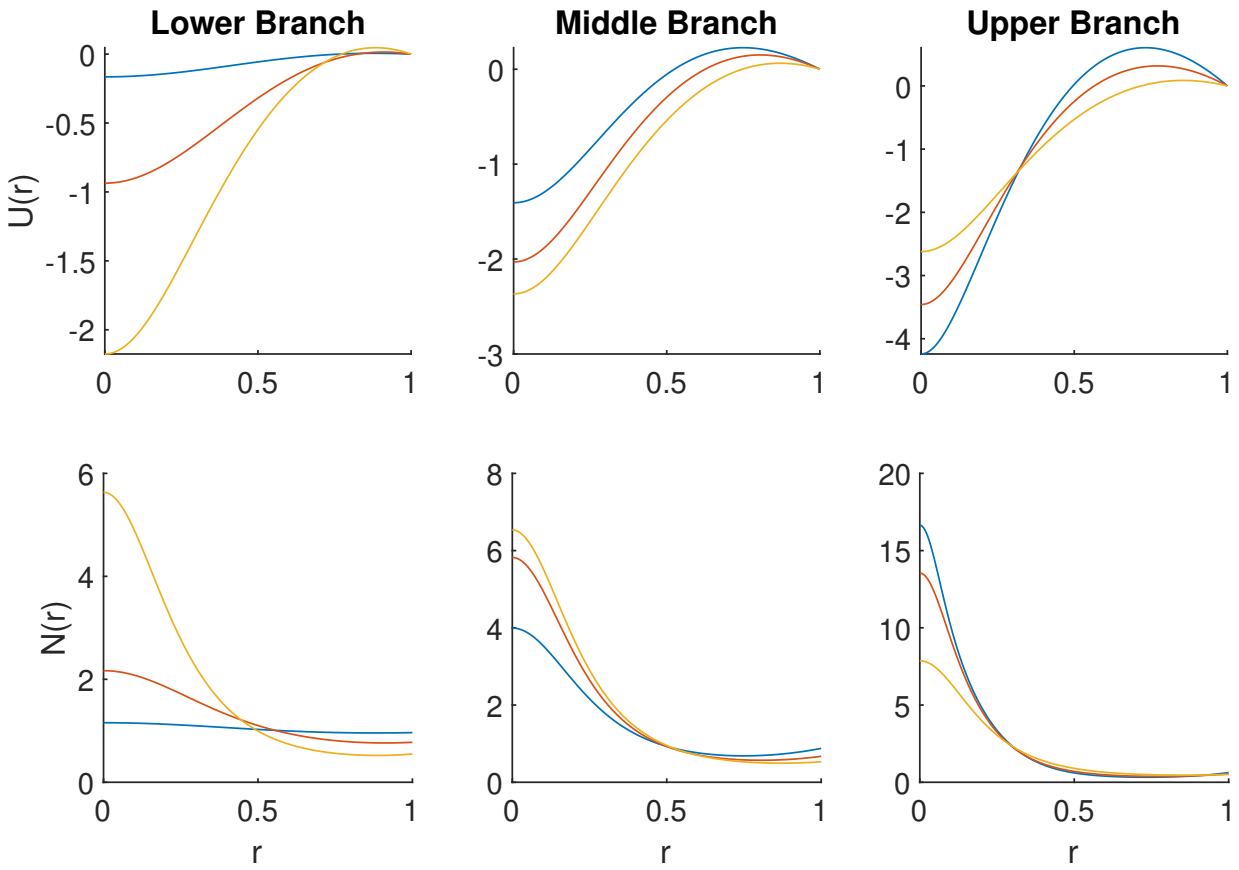

Figure 2.5: Steady plume solutions in different branches (model F): Downward velocity $U(r)$ (top) and swimmer number density $N(r)$ (bottom) profiles at (blue) $Q = 0.1; Ri = 132$, (red) $Q = 0.6; Ri = 108$ and (yellow) $Q = 1.1; Ri = 95.04$ (model F). Here, the left, middle and right columns represent the lower , middle and upper branch solutions, respectively.

As the flow rate Q is further increased, the two saddle-node points become closer. They eventually merge and disappear with the increasing Q. The curves in fig. 2.4b show how the two saddle-node points evolved with Q in the $Q - Ri - N(0)$ space. At the bottom of this figure, the trajectories of the two saddle-node points are projected onto the $Q - Ri$ plane to visualise how the Ri values at these points change with Q. The two saddle-node points in the $Q - Ri$ plane indeed merge as Q increases. Beyond this merging point, the bistable behaviour of the steady solutions disappears, as there exists only a single steady solution. This type of codimension two bifurcation is a cusp bifurcation (see Zeeman, 1976; Thom, 1989).

Lastly, it is worth mentioning that, in model F, the density at the pipe axis $N(0)$ decreases with increasing Ri for sufficiently large Ri (see the upper branch in fig. 2.4a). As discussed in Hwang & Pedley (2014*b*), the decrease of $N(0)$ is the direct consequence of increasing D_{rr} with the increase of background base-flow shear (see fig. 2.8b of this paper and fig. 3b of Hwang & Pedley (2014*b*)), which smooths out the gyrotactic focusing near the pipe axis.

2.4.3 Model G

Now, we compare the steady basic-state solutions obtained from model F to those from model G. Fig. 2.6a shows the bifurcation diagram of the steady solution obtained using model G. When the swimmer number density at the pipe axis is relatively small (i.e. $N(0) < 10^2$), the same kind of cusp bifurcation is seen in this case (compare with fig. 2.4a). Also, the related form of the steady solutions is qualitatively identical to that obtained with model F, as shown in fig. 2.7. However, as the solution is continued further from the middle branches, its behaviour turns out to be very different from that obtained with model F. In particular, for all the flow rates considered, the bifurcation curves do not properly form the upper branches, contrary to model F (compare with fig. 2.4b). Indeed, irrespective of the flow rate Q, the continued solution from the middle branch asymptotically exhibits a singular

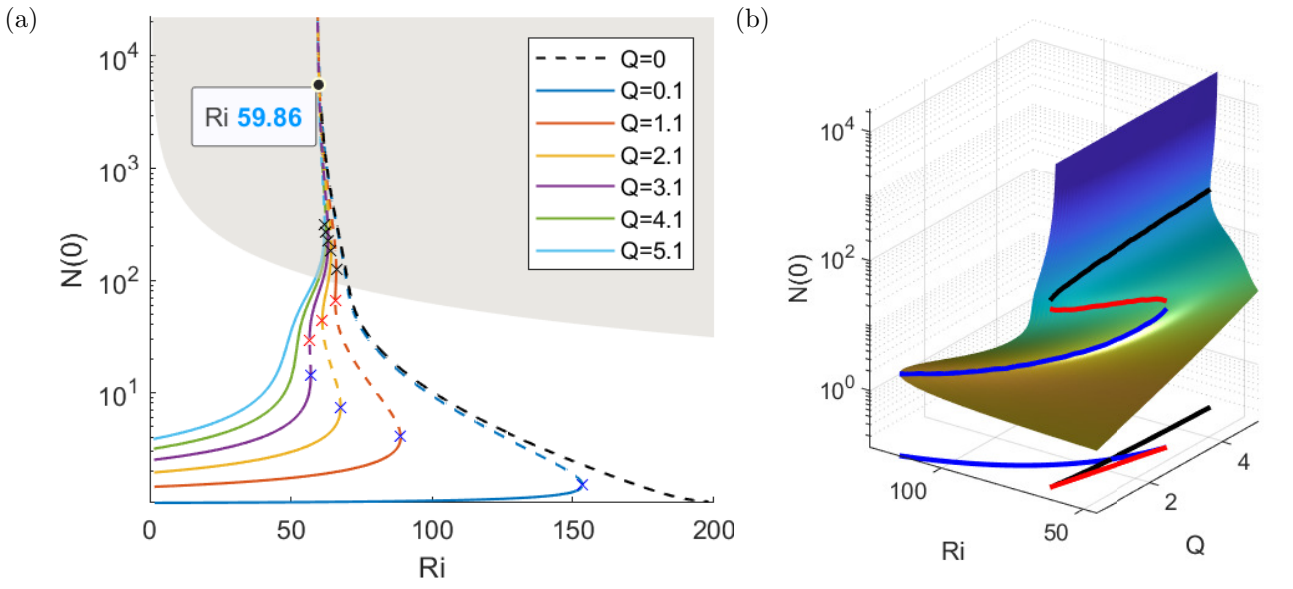

Figure 2.6: Bifurcation of the steady solutions at high flow rates (model G): (*a*) $N(0)$ with respect to Ri for several flow rates Q; (*b*) surface plot of $N(0)$ in the $Q - Ri$ space. In (*a*), ——, stable; - - - -, unstable. Here, the blue, red and black crosses (x) indicate the first, second and third saddle-node points, respectively, as the solution is continued from the lower to the upper branch. The grey area indicates the cases where the volume fraction at the pipe axis is greater than 2.5% (see §1.3.2). Note that all curves asymptotically approach a vertical line that corresponds to $Ri_s \simeq 59.86$. In (*b*) the blue and red curves indicate the trajectories of the two saddle-node points with change in Q, respectively. The graph at the bottom shows the projection of the trajectories onto the $Q - Ri$ plane.

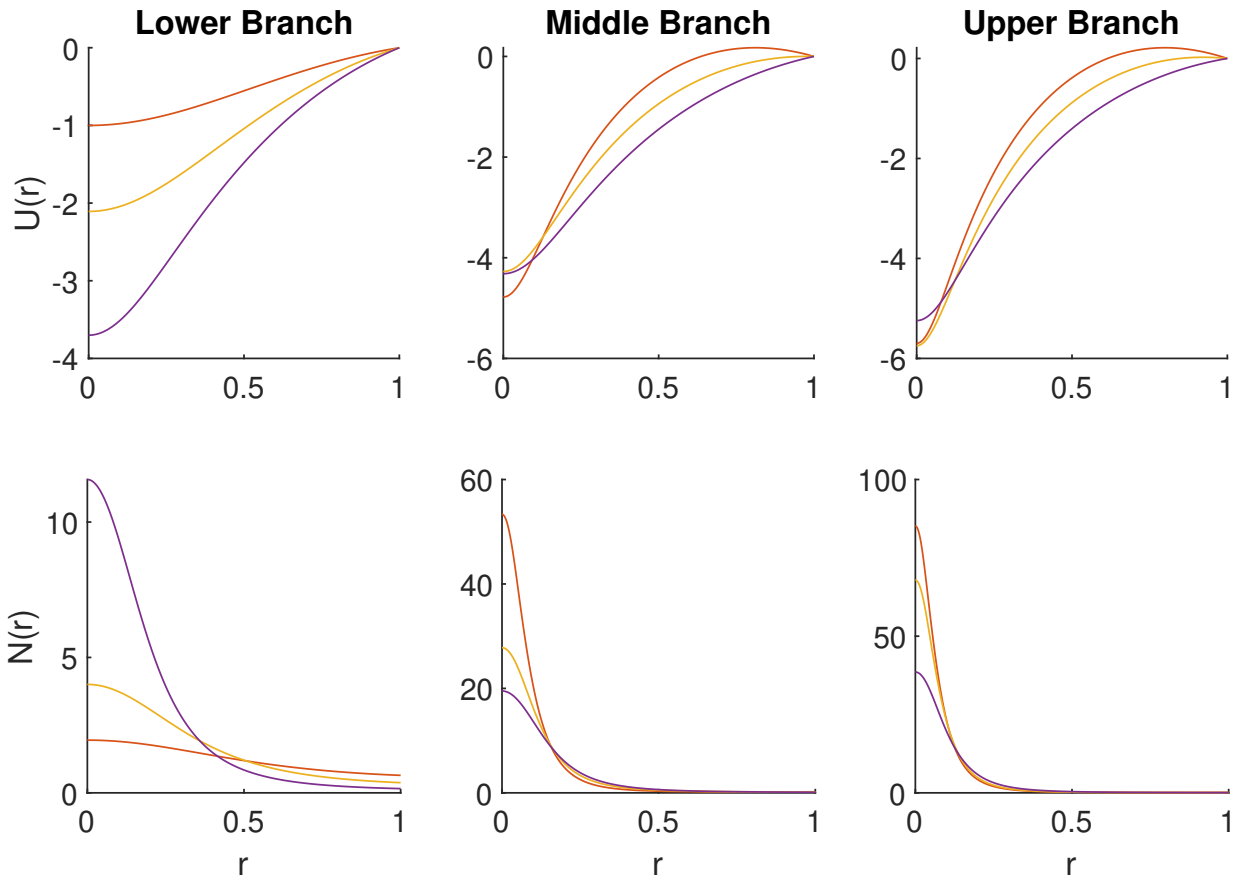

Figure 2.7: Steady plume solutions in different branches (model G): Downward velocity $U(r)$ (top) and swimmer number density $N(r)$ (bottom) profiles of the steady basic states at (red) $Q = 1.1; Ri = 65.9$, (yellow) $Q = 2.1; Ri = 62$ and (purple) $Q = 3.1; Ri = 56.9$ (model G). Here, the left, middle and right columns represent the lower, middle and upper branch solutions, respectively.

behaviour at $Ri = Ri_s (\simeq 59.86)$ in fig. 2.6a), implying $N(0) \to \infty$ with the continuation. This suggests that a steady downflowing upper branch solutions may not necessarily exist for $Ri > Ri_s$.

The origin of the singularity in the steady solution can be further studied from the following explicit form of $N(r)$ obtained with (2.5c) and (2.5d) (Bees & Croze, 2010):

$$N(r) = N(0) \exp\left(d_r \int_0^r \frac{\langle p_r \rangle_0}{D_{rr,0}} dr\right). \tag{2.15}$$

This form of the solution indicates that the singularity would be directly related to the behaviour of $\langle p_r \rangle_0 / D_{rr,0}$ with prescribed background shear $S \equiv -(dU/dr)/(2d_r)$. Note that S is varying with the radial position r (fig. 2.9) because of the coupling via the negative buoyancy. In effect, $S(r)$ can also be interpreted as the local rotary Péclet number. Fig. 2.8a shows the behaviour of $\langle p_r \rangle_0 / D_{rr,0}$ with the background shear S for both model F and model G (see also fig. $1(f)$ in Bearon *et al.* (2012)). For model F, the magnitude of $\langle p_r \rangle_0 / D_{rr,0}$ is bounded ($\max(|\langle p_r \rangle_0 / D_{rr,0}|) = -3.47$) for all the values of S. However, in the case of model G, $\langle p_r \rangle_0 / D_{rr,0}$ monotonically decreases with S and is roughly linearly proportional to S for sufficiently large S (fig. 2.8a). It should be mentioned that this difference in

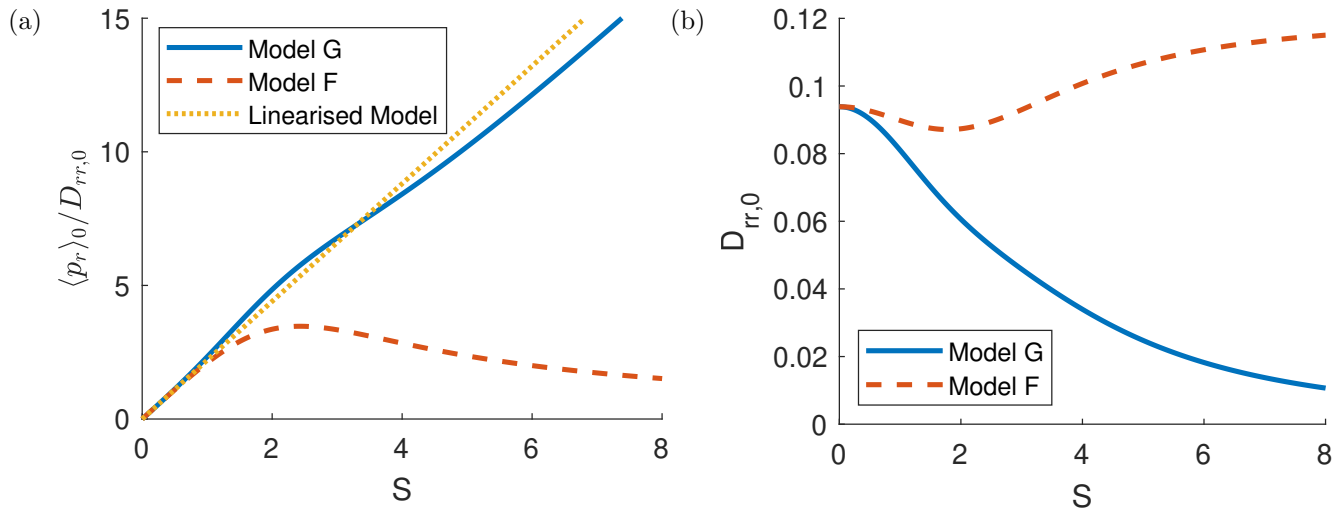

Figure 2.8: Averaged radial swimming velocity and radial diagonal component of diffusivity tensor with the dimensionless shear rate, $S = -(dU/dr)/(2d_r)$ (see also fig. 1 Bearon *et al.*, 2012): (*a*) $\langle p_r\rangle_0/D_{rr,0}$; (*b*) $D_{rr,0}$. Here, - - - -, model F; ——, model G. In (*a*), ·····, linearised model (see 2.16).

$\langle p_r\rangle_0/D_{rr,0}$ between models F and G must originate from the difference in the translational diffusivity, because they share exactly the same $\langle p_r\rangle$ (see also §2.2). This is shown in fig. 2.8b.

Fig. 2.9 visualises the radial profiles of $S(r)$ and $\langle p_r\rangle_0/D_{rr,0}(r)$ for models F and G along the continuation curves at $Q = 2.1$. As the solution is continued from the lower to the upper branch, the absolute values of $S(r)$ monotonically increase for both model F and model G (figs. 2.9a,b). However, $\langle p_r\rangle_0/D_{rr,0}(r)$ do not behave like $S(r)$. In particular, $\langle p_r\rangle_0/D_{rr,0}(r)$ for model F is bounded due to the nature shown in fig. 2.8a. As a result, $\langle p_r\rangle_0/D_{rr,0}(r)$ in fig. 2.9b is bounded, whereas that in fig. 2.9d is not. This suggests that the singularity developed at Ri_s from model G originates from the unboundedness of $\langle p_r\rangle_0/D_{rr,0}(S)$.

If the behaviour of $\langle p_r\rangle_0/D_{rr,0}$ in model G is further simplified, the threshold Ri_s in fig. 2.6b can be predicted analytically. For this purpose, we consider a simplified model for $\langle p_r\rangle_0/D_{rr,0}$: the translational diffusivity is set such that $\langle p_r\rangle_0/D_{rr,0}$ is linearly proportional to the background shear dU/dr. In other words, the simplified model assumes

$$\frac{\langle p_r\rangle_0}{D_{rr,0}} = \eta S = \frac{-\eta}{2d_r}\frac{dU}{dr}, \tag{2.16}$$

where the proportionality constant η is obtained from the slope of $\langle p_r\rangle_0/D_{rr,0}$ at $S = 0$ from either model F or G, i.e. $\eta \equiv \partial(\langle p_r\rangle_0/D_{rr,0})/\partial S|_{S=0}$. Meanwhile, the $\langle p_r\rangle_0$ in the simplified model is kept to be the same as that used in both model F and model G. We shall refer to this model as the 'linearised model'. It is easy to show via an asymptotic analysis that $\eta = \beta$ in both model F and G (see Bearon *et al.*, 2012, appendix B). The two models share the same asymptotics at $S = 0$ (c.f. §2.4.1). We

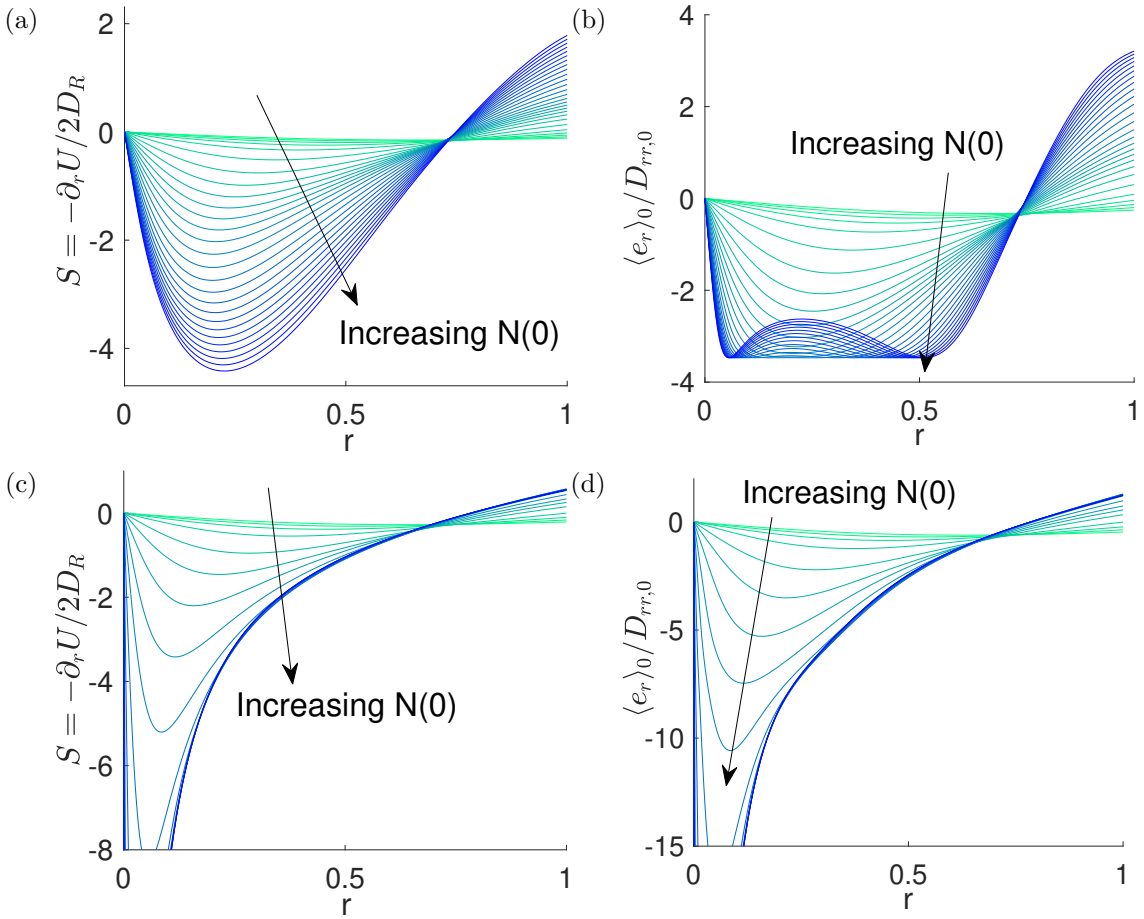

Figure 2.9: (a,c) Rotary Péclet number $S(r)$ and (b,d) net-flux-diffusion ratio $\langle p_r \rangle_0 / D_{rr,0}$ against radial position r along the continuation at $Q = 2.1$ in (a-b) model F and (c-d) model G.

can also compare this simplified model with model F and G in terms of S (fig. 2.8a). Notably, the approximation remains close to model G even in large shear.

Coincidentally, the behaviour of $\langle p_r \rangle_0 / D_{rr,0}$ against S in this 'linearised model' is the same as that of Kessler (1986). In Kessler (1986), $\langle p_r \rangle_0$ is linear to shear rate S and $D_{rr,0}$ is constant. In contrast, in both model G and the subsequent 'linearised model', $D_{rr,0} \sim S^{-2}$ and $\langle p_r \rangle_0 \sim S^{-1}$ as the magnitude of S increases towards infinity. As a result, the 'linearised model' shares the same linear behaviour in $\langle p_r \rangle_0 / D_{rr,0}(S)$ with the simpler model of Kessler (1986), despite the different approximations for $\langle p_r \rangle_0$ and $D_{rr,0}$. In the following, we will exploit the similarity in $\langle p_r \rangle_0 / D_{rr,0}(S)$ between the 'linearised model' and Kessler (1986) to understand the bifurcation.

Bifurcation of the steady solutions of the linearised model is shown in fig. 2.10. The bifurcation diagram of the linearised model is qualitatively similar to that of model G: as the solution is continued from the lower to upper branch, the swimmer number density at the pipe axis gradually becomes singular at $Ri \simeq Ri_s (= 57.68)$ irrespective of Q (compare with fig. 2.6a). The only qualitative difference between fig. 2.6a and fig. 2.10 is the small extra bumpy behaviour in the bifurcation curves

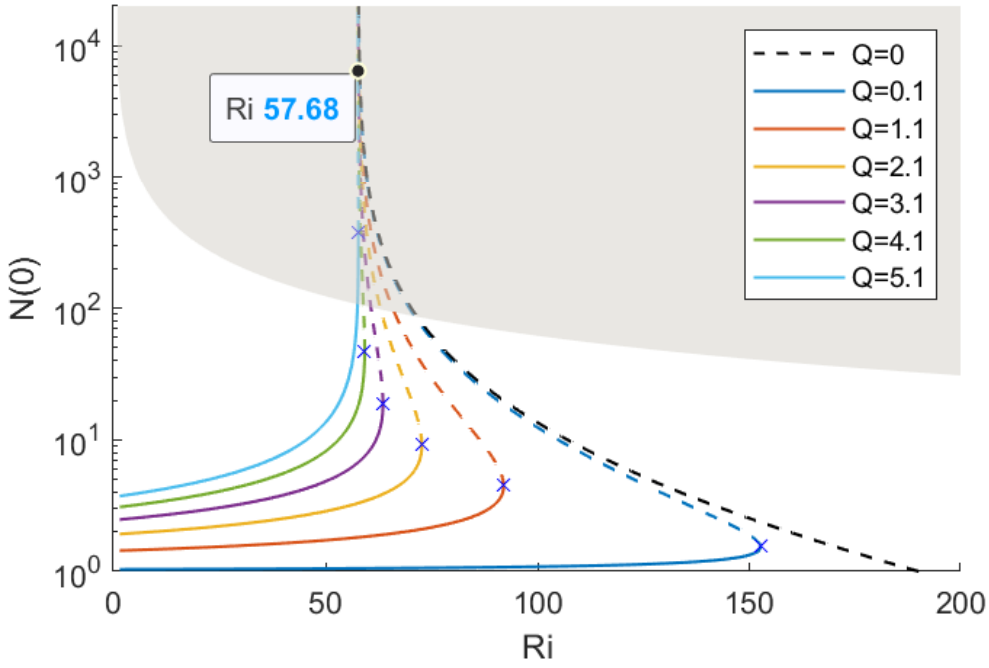

Figure 2.10: Bifurcation diagram of the linearised model with Ri for several Q. Here, the state of steady solution is represented by the swimmer number density at the pipe axis $N(0)$. As the solution is continued from the lower branch, $N(0) \to \infty$ at $Ri = Ri_s (\simeq 57.68)$. Also, ——, stable; - - - -, unstable, and the blue crosses (x) indicate the saddle-node point. The grey area indicates the cases where the volume fraction at the pipe axis is greater than 2.5% (see §1.3.2).

of model G, likely the consequence of the nonlinear behaviour of $\langle p_r \rangle_0 / D_{rr,0}(S)$ in model G. This suggests that the singularity at the centreline swimmer number density in model G indeed originates from the monotonically decreasing $\langle p_r \rangle_0 / D_{rr,0}$ with the decreasing (more negative) background shear rate S. In fact, as $S \to -\infty$, $\langle p_r \rangle_0$ scales with S^{-1} while $D_{rr,0}$ scales with S^{-2}, hence $\langle p_r \rangle_0 / D_{rr,0}$ scales with S (Bearon *et al.*, 2012). This implies that the origin of the singularity in $N(0)$ is essentially associated with the lack of translational diffusion flux relative to the advection flux caused by swimming in the radial direction in model G, as the magnitude of the local shear rate S increases with $N(0)$ towards infinity along the continuation.

The emergence of this singularity can be more precisely analysed. We now consider the following equation for $N(r)$, which can be obtained from (2.5) with $D_{rr,0}$ in (2.16) of the linearised model:

$$-\frac{1}{r}\frac{d}{dr}\left(r\frac{d}{dr}\ln N(r)\right) = 8\gamma(N(r)-1) + \eta \left.\frac{dU}{dr}\right|_{r=1}. \tag{2.17}$$

Here $\gamma = \eta Ri Re/16$ and $\eta(dU/dr)|_{r=1}$ represents the driving pressure gradient. Since $N(r)$ near the singular regime is highly concentrated near the pipe axis, we assume that the swimmers are highly focused in a small region around the axis: i.e. $r \in [0, \epsilon]$. Then, from the constraint of $N(r)$ given by (2.6), $N(r) \sim O(\epsilon^{-2})$ in $r \in [0, \epsilon]$. Therefore, in this region, we can introduce a relevant

rescaling of the radial coordinate $r = \epsilon R$, where R is of order unity, and define a normalised profile $N_0(R) = N(r/\epsilon)/N(0)$. Then, at $O(\epsilon^{-2})$, (2.17) is approximated as

$$\left(\frac{1}{N_0}\frac{dN_0}{dR}\right)^2 - \frac{1}{RN_0}\frac{dN_0}{dR} - \frac{1}{N_0}\frac{d^2N_0}{dR^2} = 8\gamma N_0(R). \tag{2.18}$$

Now, it is evident that (2.18) does not contain the driving pressure gradient anymore. This implies that, in the regime where the singular solution nearly develops, the form of the steady basics-state solution should approximately be independent of the pressure gradient and the flow rate for $r \in [0, \epsilon]$, confirming the numerical result for $N(0) > O(10^3)$ shown in fig. 2.10.

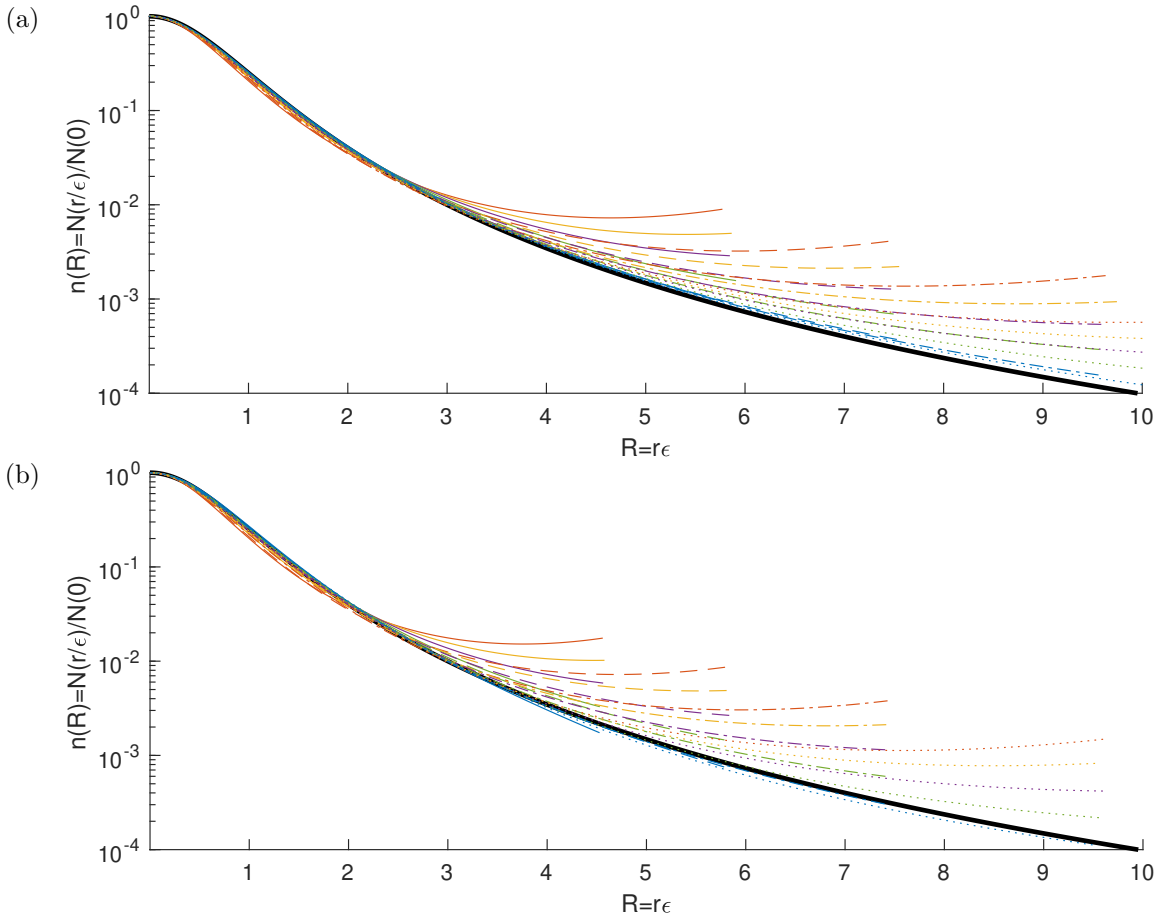

Figure 2.11: The swimmer distribution of the steady solutions normalised by the pipe axis value for several flow rates ($Q = 1, 2, 3, 4, 5$): (a) the linearised model; (b) model G. Here, $N(0) = 20$, ——; $N(0) = 33$, - - - - -; $N(0) = 55$, -·-·-·-; $N(0) = 90$, ····· for the coloured lines. The thick black solid line indicates the solution of Kessler (1986) given in (2.19).

The solution to (2.18) was previously obtained by Kessler (1986) with the far field boundary condition $N_0(\infty) = 0$: i.e.

$$N_0(R) = \frac{1}{(1 + \gamma R^2)^2}. \tag{2.19}$$

We note that (2.18) is the leading-order approximation of (2.17) valid only for $R \in [0, 1]$ (or, equivalently, $r \in [0, \epsilon]$). Therefore, (2.19) would be a good approximation of the full numerical

solution of (2.17) for any Q in this region. The normalised swimmer number density of its numerical solutions for several Q and $N(0)$ is compared with (2.19) in §2.4.3. Indeed, (2.19) shows an excellent agreement with the numerical solutions for $R \in [0, 1]$. We note that (2.19) is also a good approximation of the swimmer-density profile of model G near the pipe axis, as demonstrated in §2.4.3.

Finally, if the solution (2.19) is substituted into (2.6), the resulting swimmer number density at the pipe axis is obtained as

$$N(0) = \frac{1}{1-\gamma}. \tag{2.20}$$

From the definition of γ, this implies that $N(0)$ would be singular if $\gamma \to 1$. At $\gamma = 1$, $Ri = 16/(\eta Re)$, which should be a good approximation of Ri_s. Indeed, for the given Re and η of the linearised model, the value of $16/(\eta Re)$ is 57.66, which is in excellent agreement with the numerical singularity $Ri_s \simeq 57.68$ (see fig. 2.10).

The physical mechanism for the singularity is as follow. As Ri increases, the acceleration from the negative buoyancy of swimmers would increase local downflow and the magnitude of shear rate S, attracting more swimmers towards the centre from more negative $\langle p_r \rangle_0 / D_{rr,0}$. The increased swimmer number density would increase the local downflow further, and the same process would be repeated until the resulting averaged swimming flux and the radial diffusion are balanced (i.e. formation of a steady solution). However, as the local shear rate near the central axis of the pipe further increases due to increasing Ri and $N(0)$, the effective radial diffusivity is also decreasing. At some Ri, the lack of diffusion flux to counteract the positive feedback mechanism of gyrotactic focusing results in singularity. The physical process described here is similar to that of linear gyrotactic instability, except that the positive feedback mechanism here is highly nonlinear and results in a singularity.

2.5 Linear stability

In this section, we will perform a linear stability analysis with the steady plume solutions computed in §2.4. We will focus on the axisymmetric mode and the first non-axisymmetric mode, which are similar to the varicose and sinuous modes in downward channel flow (Hwang & Pedley, 2014*b*). The typical spatial structures of these two modes are visualised in fig. 2.12, demonstrating the similarity to fig. 8 in Hwang & Pedley (2014*b*): the axisymmetric mode is composed of a plume, the thickness of which varies along the axial direction, whereas the non-axisymmetric mode is composed of an anaxially meandering plume. In the present study we will focus more on the axisymmetric mode

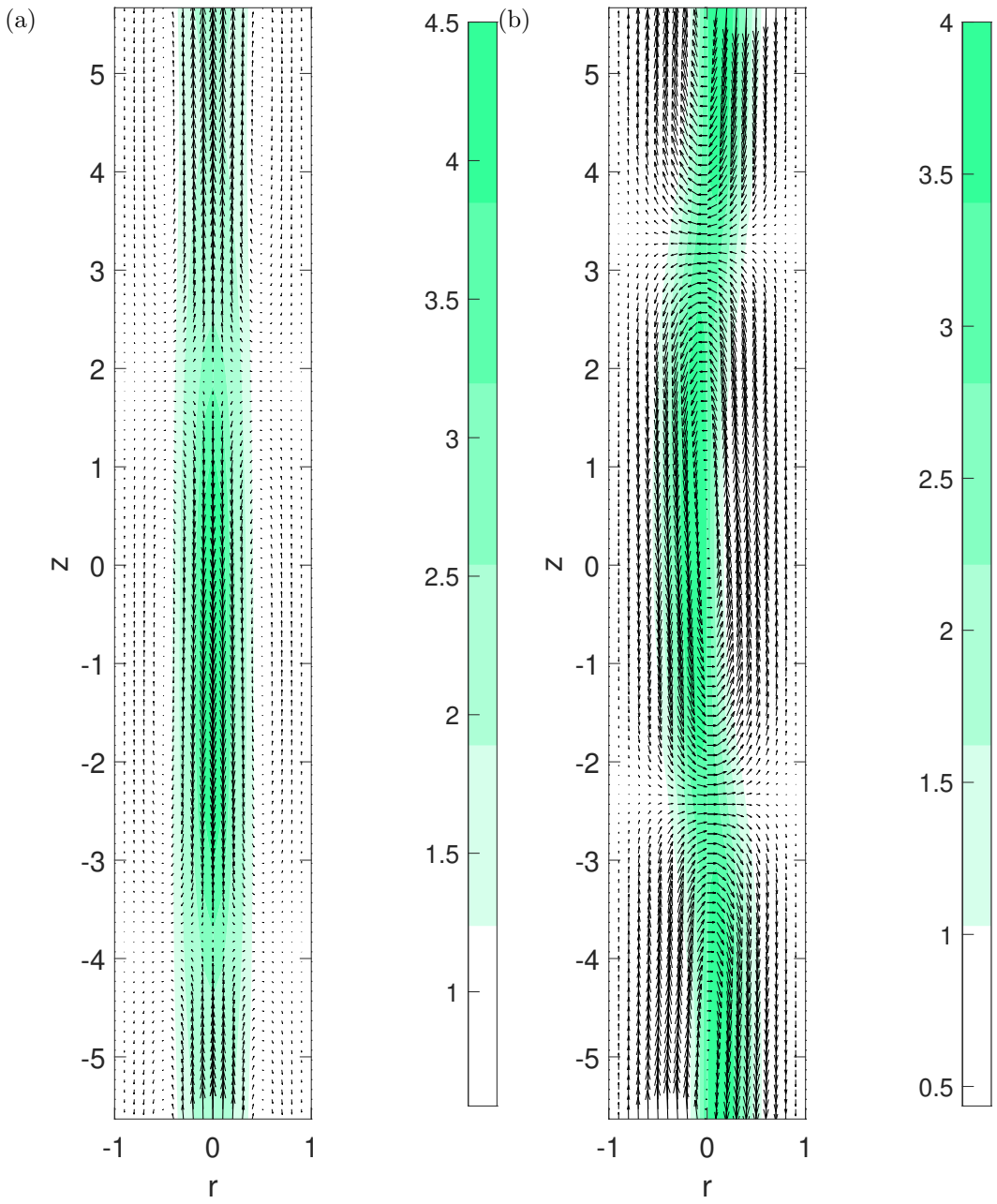

Figure 2.12: Spatial structure of the unstable (a) axisymmetric ($m = 0$) and (b) non-axisymmetric ($m = 1$) mode at $Ri = 92, Q = 1, \alpha = 0.56$, computed using a lower branch basic state. Here, the contours indicate $N(r) + an'(r, z)$ with an arbitrary value of a for visualisation, and the vectors represent the axial and radial perturbation velocity field.

($m = 0$) as it is more physically relevant and observable in experiments. The first non-axisymmetric mode (i.e. when $m = 1$) is also presented briefly.

Given the existence of multiple basic-state solutions for a given set of Ri and Q, it is not straightforward to present the conventional neutral stability diagram. Therefore, in this section we present the stability of the steady solutions along each of the continuation curves shown in §2.4. For each steady solution (basic state) and the corresponding set of parameters, the maximum growth rate $\omega_{i,max}$ is sought out for all real α. Here, the value of α used to search for $\omega_{i,max}$ ranges from 0.001 to 20, and the corresponding α_{max} is also computed.

2.5.1 Axisymmetric mode

Model F

Fig. 2.13 shows how the maximum growth rate $\omega_{i,max}$ and the corresponding streamwise wavenumber α_{max} change with Ri for each fixed Q along the continuation curves in fig. 2.4a. At low $Q(\lesssim 1)$, the basic state becomes unstable to axially varying perturbations near the first saddle-node point where $N(0)$ increases rapidly with Ri, as the solution continued from the lower to the middle branch. With a further continuation, the solution stabilises, in that the value of ω_i begins to reduce, before the second saddle-node point (fig. 2.13a). The streamwise wavenumber retaining the maximum growth rate also behaves similarly to $\omega_{i,max}$: α_{max} grows as the solution continued from the lower to the middle branch, and it decays again with a further continuation. Finally, as Q increases, $\omega_{i,max}$ obtained for all the steady solutions along the continuation decreases, implying that increasing the flow rate stabilises the streamwise perturbation.

Comparison of fig. 2.13a with fig. 2.4a also indicates that the destabilisation seems to correlate with the rapid increase in $N(0)$ of the basic state at least for the lower and middle branches. This suggests that the instability is presumably associated with the sharp gradient in the base flow and swimmer number density near the pipe axis, consistent with the previous observation in Hwang & Pedley (2014*b*) where the instability of this type (varicose mode Hwang & Pedley, 2014*b*) was shown to originate from the following simplified process:

$$\frac{\partial n'}{\partial t} \sim -n'\Big(\frac{\partial \langle p_r \rangle_0}{\partial r} + \frac{\langle p_r \rangle_0}{r}\Big). \tag{2.21}$$

This process also appears through the first to third terms in (2.10e) in the present pipe flow. We

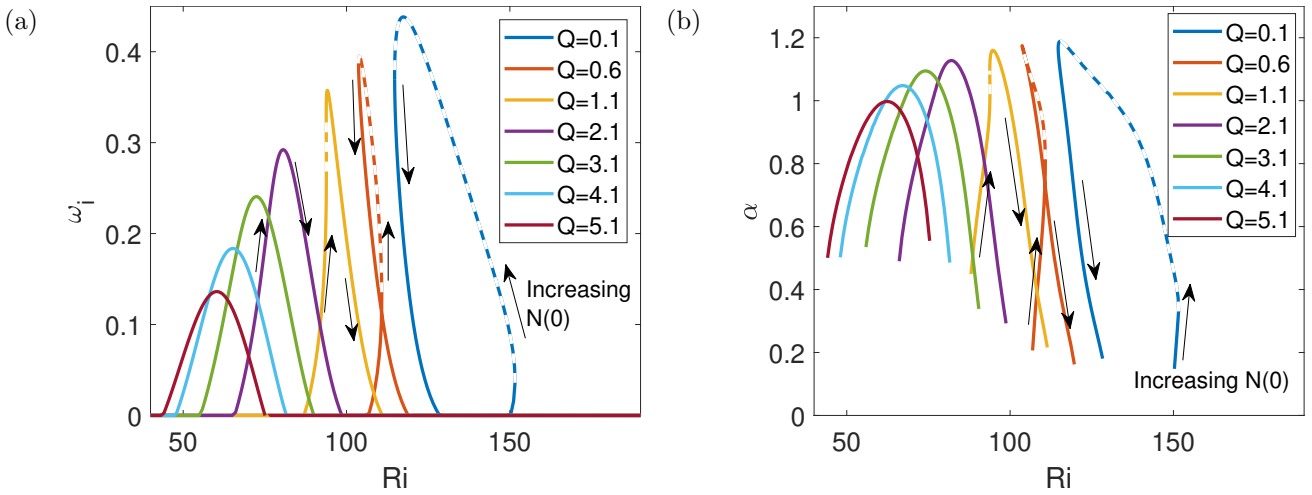

Figure 2.13: Stability of the axisymmetric mode (model F): (a) maximum growth rate $\omega_{i,max}$ and (b) the corresponding α_{max} of the steady solution at each Ri and Q. In (a), ——, stable; - - - -, unstable to streamwise-uniform perturbation.

note that $\partial\langle p_r\rangle_0/\partial r$ and $\langle p_r\rangle_0/r$ must be negative near the pipe axis, because the swimmers swim towards the centre ($\langle p_r\rangle_0 < 0$) near the pipe axis and $\langle p_r\rangle_0 = 0$ at the pipe axis, implying that the same mechanism of the instability is active in the vertical pipe case.

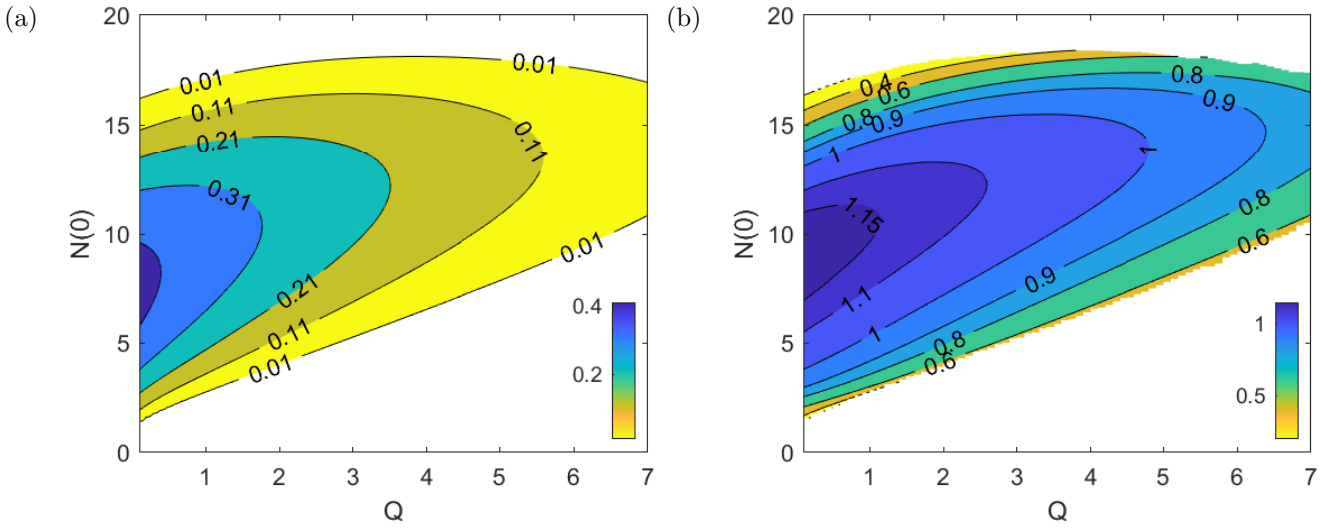

Figure 2.14: (a) The maximum growth rate $\omega_{i,max}$ and (b) the corresponding α_{max} in the $N(0) - Q$ plane (model F). Note that the contours do not contain any overlap because the basic state is stable before $N(0)$ decreases in the branch continuation.

To further explain the correlation between the growth rate and the nature of the steady solution near the pipe axis, the maximum growth rate $\omega_{i,max}$ in the $Q - N(0)$ plane is plotted in fig. 2.14. For $N(0) \lesssim 10$, the basic state is destabilised on increasing $N(0)$, consistent with the explanation given above. However, as $N(0)$ is further increased ($N(0) \gtrsim 10$), the solution is found to be stabilised again. Here, we note that there are no overlapping contour lines in fig. 2.14, which one might have expected from the existence of multiple $N(0)$ for a given flow rate (see fig. 2.4a). This is because the basic

state is stabilised ($\omega_i < 0$) well before $N(0)$ starts to decrease along the upper branch (see fig. 2.4a). In other words, the stabilisation takes place while $N(0)$ is still increasing along the continuation.

The stability analysis result here is qualitatively similar to that in Hwang & Pedley (2014*b*), although the stability diagram in the $Q - Ri$ space is not directly shown here due to the complexity emerging from the bifurcation of the basic state: the most unstable mode of the flow appears in the form of an axisymmetric blip instability like their varicose mode, and this instability is stabilised if the flow rate is sufficiently large. However, it should be mentioned that Hwang & Pedley (2014*b*) did not explore for $Ri > 90$. Therefore, it is unclear whether the stabilisation observed at higher $N(0)$ in the present pipe flow would also occur in their channel flow.

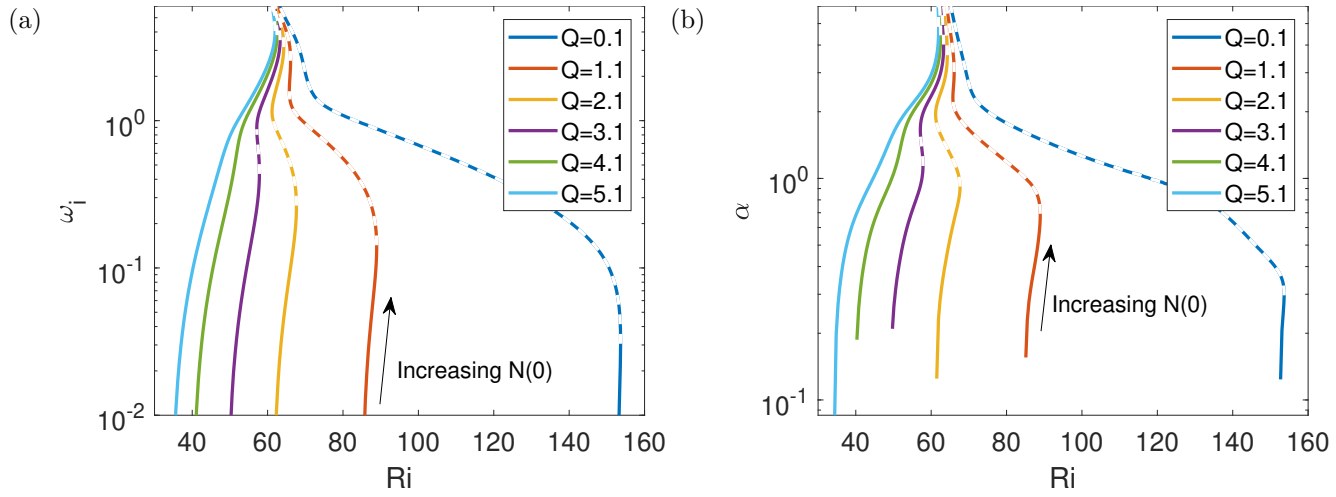

Figure 2.15: Stability of the axisymmetric mode (model G): (a) maximum growth rate $\omega_{i,max}$ and (b) the corresponding α_{max} of the steady solution at each Ri and Q. In (a), ——, stable; - - - -, unstable to streamwise-uniform perturbation.

Model G

Now, we perform a linear stability using model G. Fig. 2.15 shows how the maximum growth rate $\omega_{i,max}$ changes with Ri along the continuation curves in fig. 2.6a for each fixed Q. Due to the wider range of the values of $\omega_{i,max}$ emerging in model G, here we have chosen to plot $\omega_{i,max}$ in log scale in fig. 2.15. Similar to the result of model F, the basic state is destabilised near the first saddle-node point. However, in contrast with fig. 2.13, the basic state is no longer stabilised with the continuation to upper branches. Instead, it is found that the growth rate continues to increase, and the basic state always remains unstable along the continuation curve.

The maximum growth rate $\omega_{i,max}$ in the $Q - N(0)$ space is also plotted in fig. 2.16. It is interesting to note that the growth rate appears to be almost independent of Q at high enough $N(0)$. This is

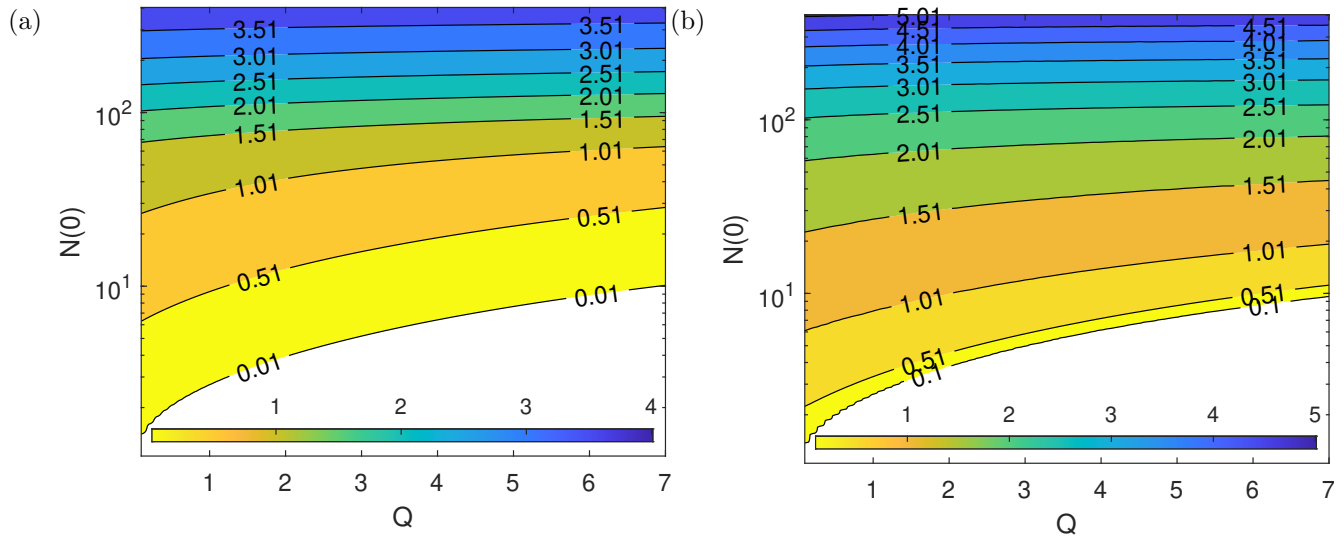

Figure 2.16: (a) The maximum growth rate $\omega_{i,max}$ and (b) the corresponding α_{max} in the $N(0) - Q$ plane (model G).

presumably because the profile of the basic-state solution is almost independent of Q for sufficiently high $N(0)$, as discussed in §2.4.3. This observation is also consistent with the notion that the instability is essentially driven by the local flow dynamics near the centreline of the pipe through (2.21).

The main difference in the stability of models F and G appears from the upper branch basic state. In a way, this would not be surprising because models F and G show significantly different upper branch states. Model F exhibits decreasing $N(0)$, as the steady basic-state solution is continued along the upper branch. By the contrary, model G shows increasing $N(0)$ with the continuation. This feature greatly impacts on the stability result, and we shall provide a further discussion on this issue in §2.6.1.

2.5.2 Non-axisymmetric mode

Finally, we have computed the stability of the non-axisymmetric mode (sinuous mode). It was found that, at $m = 1$, the non-axisymmetric mode is always the most unstable when $\alpha = 0$ in both model F and model G (i.e. when the perturbation is streamwise uniform). Fig. 2.17 shows how the maximum growth rate $\omega_{i,max}$ changes with Ri along the continuation curves shown in figs. 2.4a and 2.6a for models F and G, respectively. At low $Q(\sim 0.1)$, the base flow becomes unstable to azimuthally varying (and streamwise-uniform) perturbation at a lower Ri than the streamwise varying axisymmetric perturbation in both models, before the continuation reaches the first saddle-node point. For model F, the growth rate peaks at the middle branch, similar to the axisymmetric mode. However, as the solution continued to the upper branch, the non-axisymmetric mode is destabilising again, even

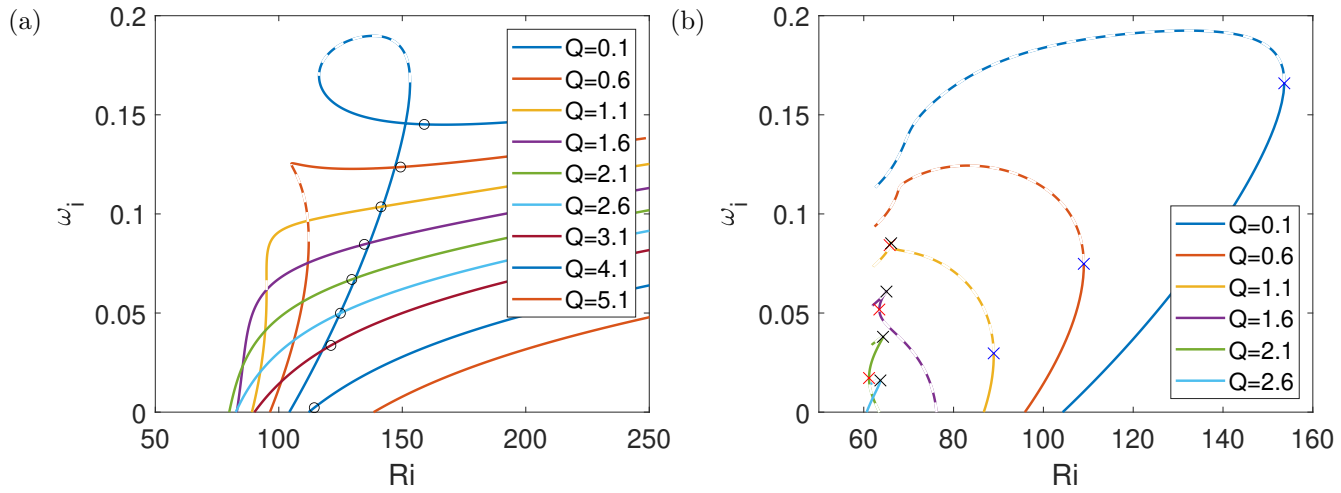

Figure 2.17: Stability of the non-axisymmetric mode: maximum growth rate $\omega_{i,max}$ at each Ri and Q, using (a) model F and (b) model G. In both figures, ——, stable; - - - -, unstable to streamwise-uniform perturbation. In (a) the point with maximum $N(0)$ is marked with a black circle in each curve. In (b) the blue, red and black crosses (x) indicate the first, second and third saddle-node points, respectively.

though $N(0)$ is decreasing at the upper branch. For model G, the non-axisymmetric mode stabilises after the first saddle-node point despite increasing $N(0)$.

As Q increases, $\omega_{i,max}$ obtained for all the steady solutions along the continuation decreases. At higher $Q(\gtrsim 1)$, for model F, $\omega_{i,max}$ remains increasing along the branch continuation even though $N(0)$ started decreasing (as shown by the point indicating maximum $N(0)$ along each continuation curve). For model G, because of the strong stabilising effect of the flow rate, the mode is only unstable when $Q \lesssim 3.0$. In fig. 2.17b, at higher $Q(\gtrsim 1)$, the mode is destabilising with increasing $N(0)$ before the third saddle-node point. The growth rate $\omega_{i,max}$ peaks at the third saddle-node point. Beyond the third saddle-node point where $N(0)$ tends toward infinity (i.e. approaching the singularity at Ri_s), $\omega_{i,max}$ decreases along the continuation curve. This is also the regime where there is a self-similar profile at the centre of the pipe, as discussed in §2.4.3, implying that the non-axisymmetric mode is stabilising when the self-similar plume structure becomes narrower.

The fact that the mode is most unstable when $\alpha = 0$ and that it is not as correlated to $N(0)$ as the axisymmetric mode strongly suggest that the non-axisymmetric mode is driven by a different mechanism. In fact, Hwang & Pedley (2014*b*) showed that the sinuous mode is driven by gyrotactic instability, even though Hwang & Pedley (2014*b*) did not take into account the spanwise variation. According to Hwang & Pedley (2014*b*), the gyrotactic instability is expected to originate from the following simplified process

$$\frac{\partial n'}{\partial t} \sim -\left(\langle p_r\rangle' \frac{\partial N}{\partial r} + N\frac{\partial \langle p_r\rangle'}{\partial r} + N\frac{\langle p_r\rangle'}{r} + N\frac{\partial \langle p_z\rangle'}{\partial z} + \frac{N}{r}\frac{\partial \langle p_\psi\rangle'}{\partial \psi}\right), \tag{2.22}$$

which also corresponds to the first term and the second line of (2.10e). We note that this gyrotactic instability mechanism is different from that of (2.21), which is driven by the gradient in the base flow average swimming. Although both mechanisms originate from gyrotaxis, the former is driven directly by gyrotaxis, while the latter is the result of the net flux of swimmers in the radial direction due to non-uniform shear rate. A more in-depth discussion on both mechanisms can be found in Hwang & Pedley (2014*b*).

To confirm this mechanism, we have performed the stability analysis with the second line of (2.10e) suppressed. The non-axisymmetric mode is found no longer unstable for all the parameter space for both model F and model G, which shows that the mode is indeed driven by the gyrotactic mechanism.

2.6 Summary and discussion

Thus far, we have explored the bifurcation and stability of a downflowing gyrotactic micro-organism suspension in a vertical pipe flow. This work provides a full picture of the bifurcation and stability of the gyrotactic plume in the original experiment of Kessler (1985*a*,*b*, 1986) with the more up-to-date continuum models (model G, in particular), while extending the stability analysis of Hwang & Pedley (2014*b*) for channels to pipes. In particular, both models F and G have been used in the present study, offering some useful physical insights into the benefits and drawbacks of the existing continuum descriptions.

2.6.1 Models F and G

The basic-state steady solutions from models F and G have been compared previously in a series of experimental and numerical studies (Bearon *et al.*, 2012; Croze *et al.*, 2013, 2017). In the present study a bifurcation analysis has been performed and revealed a complete description of the existence of multiple solutions, their mutual relations and the singularity threshold for the first time. In a stationary suspension, both models F and G exhibit a transcritical bifurcation with Ri (fig. 2.3). With the addition of a small flow rate Q, this transcritical bifurcation with Ri evolves into an imperfect bifurcation involving a saddle-node point (fig. 2.3). The further increase of the flow rate results in the disappearance of the saddle-node point, exhibiting a cusp bifurcation in terms of two parameters, Ri and Q (figs 2.4b, 2.6b).

Despite the qualitative similarity in the behaviour of the steady solutions of models F and G, especially

at low flow rates, they also exhibit several vital differences. These differences between models F and G stem fundamentally from how the translational diffusivity $\boldsymbol{D}_m$ changes with S, especially when $|S|$ is high (see fig. 2.8b). The difference in $D_{rr}(S)$ results in different bifurcation behaviour, as shown by the comparison between figs. 2.4a and 2.6a. The differences are particularly profound at high $N(0)$, where the magnitude of the background shear rate $|S|$ is large. In model F, the plume structure of the steady solution eventually smooths out as it is continued from the middle to the upper branch. This should be related to the recovery of D_{rr} in model F on increasing $|S|$. In contrast, the monotonically decreasing $D_{rr}(S)$ at large $|S|$ in model G causes the plume structure of the steady solution to be more focused as it is continued to the upper branch. This is also the essential reason why model G does not admit any steady solution, at some regime of Ri at a given finite Q. On the contrary, in model F, there always exists at least one steady solution, albeit not physically realistic.

As for the stability of the basic state, the main difference between the two models is that model F shows restabilisation of the axisymmetric mode on increasing $N(0)$, whereas model G exhibits a rapid increase in its growth rate (figs. 2.14, 2.16). Given that the only difference between models F and G is in the expression of the translational diffusivity, this difference should also originate from the diffusivity. It has been shown both numerically (Croze *et al.*, 2013) and experimentally (Croze *et al.*, 2017) that the diffusivity prediction of model F is not as accurate as model G in modelling gyrotactic focusing. This suggests that the restabilisation at high $N(0)$ is likely not physical but an artefact of model F. Furthermore, model F showed that the non-axisymmetric mode has a higher growth rate than the axisymmetric mode at high Ri, but this is not supported by any previous experiments, in which only the axisymmetric instability mode (i.e. blip) has been observed. On the contrary, under model G, the axisymmetric mode remained the dominant mode in most of the parameter space (except at very low flow rates), which is more consistent with the observation of blips in the experiment. These stability results suggest that model F shows little consistency with the experimental observations, and would not be as accurate as model G in predicting the blip occurrences.

2.6.2 Breakdown of the homogeneous shear assumption

Despite the encouraging result from model G, one should be aware of the limitation model G impose. In the application of the GTD theory outlined by Hill & Bees (2002) and Bearon *et al.* (2012), the shear rate of the flow was approximated to be locally homogeneous at each spatial point without taking into account the effect of inhomogeneity in the shear profile. However, the high swimmer density at the centre also gives rise to a rapidly changing shear rate in the solutions. This may also

break down the assumptions made in model G. In particular, model G cannot capture the shear trapping phenomena first demonstrated experimentally by Rusconi *et al.* (2014). However, Bearon & Hazel (2015) have utilised the Smoluchowski equation directly and shown that, even in the absence of gyrotaxis, non-spherical swimmers may still aggregate in the regions of high or low shear due to the inhomogeneity in the flow shear. In effect, such inhomogeneous shear can also generate an extra net advective swimmer-density flux towards or away from the centre, depending on the shear magnitude and the geometry of the swimmer (Vennamneni *et al.*, 2020), but model G cannot capture the shear trapping flux due to its quasi-homogeneous assumption. Given that the formation of the middle to upper branch solutions in the present study is strongly linked to the high shear rate near the centre, this shear trapping effect might also be significant were the swimmers not as spherical as we have assumed. The topic of shear trapping will be further investigated in chapter 4.

2.6.3 Effect of the bulk stress tensor

Despite the interesting bifurcation and the stability of the basic state, which may offer sound explanations to the previous experiments, care must also be taken in interpreting the present analysis with the assumptions made in modelling of the suspension. We have assumed in §2.2 that the contribution of swimming motions of individual micro-organisms to the flow field (i.e. the $(1/\rho^*)\boldsymbol{\nabla}^*\cdot\boldsymbol{\Sigma}_p^*$ term in (1.18)) would be negligible throughout the chapter. However, as the plume solution diverge near the critical Ri_s, we cannot rule out the possibility that the the stresslet tensor might be able to attenuate such singularity. To this end, we have recomputed the steady solutions using model G with the stresslet term included, assuming that it is the dominant stress from the swimmers besides the buoyancy force: see §1.4.5. The stresslet term considered is given by (1.16), where $\sigma_0^* = 10^{-10}\mathrm{gcm^2s^{-s}}$ for *C. augustae* (Pedley, 2010*b*).

Fig. 2.18 shows the effect of the stresslet term on the bifurcation of the steady solutions computed with model G. The stresslet term only slightly modifies how $N(0)$ changes with Ri, without significant impact on the result (fig. 2.18a). We have also arbitrarily increased σ_0 to further understand any potential role of the stresslet in the bifurcation (fig. 2.18b). As shown at the top of fig. 2.18b, the changes in the stresslet strength do not alter the singular behaviour of $N(0)$ (i.e. $N(0) \to \infty$). Moreover, the stresslet term seems to appear to introduce further bifurcation probably involving the emergence of unsteady solutions, as the Newton solver failed to converge within the prescribed residue ($> 10^{-4}$) in the parameter space where the middle branch solutions reside (dashed lines in fig. 2.18b). However, this issue has not been further pursued in the present study as the singular

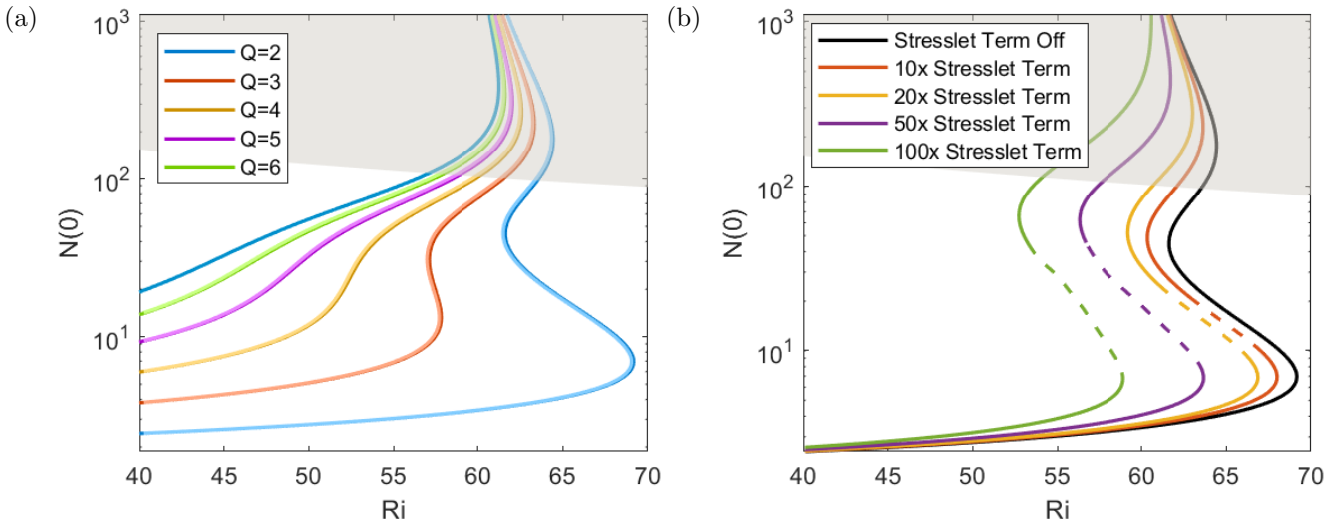

Figure 2.18: Bifurcation of steady plume solution (a) with (lighter lines) and without (darker lines) the stresslet for several Q and (b) for several arbitrarily scaled stresslet strengths σ_0 at $Q = 2$. The grey area indicates the cases where the volume fraction at the pipe axis is greater than 2.5%. In (a) the lighter and darker lines almost overlap. In (b) the dashed line (- - - -) represents the solutions obtained with large residue ($> 10^{-4}$) in the solver.

behaviour of $N(0)$ is still found to exist even with such an unphysically strong stresslet, implying that the removal of this singularity likely involve hydrodynamic interactions between swimmers in the semi-dilute regime (see §1.3.2 and §5.2.1).

2.6.4 Implications of the singularity and comparison with experiments

In §2.4.3 we have demonstrated that the solution blows up as $\gamma = \eta Ri Re/16 \to 1$, irrespective of the flow rate Q. We note that $\eta = \beta$ is strictly a parameter from the given swimmer properties and $ReRi$ is proportional to $N^*(h^*)^2$ if the swimmer properties and fluid viscosity are fixed. Here, we can define the cross-sectional area of the pipe as $A^* = (h^*)^2\pi$. Therefore, the physical interpretation of the singularity at $\gamma \to 1$ is that there exists a maximum number of swimmers per unit length of the pipe N^*A^* which the self-focused steady plume (upper branch) can hold.

Interestingly, the idea of having a limited capacity in the swimmer number per unit length of pipe of the steady plume has also been discussed in Kessler (1986). In the present study, we have extended the theory. We have demonstrated that if the flow rate is low enough with the centreline velocity at the order of the swimming speed, there exists a lower branch state which can surpass such a threshold. However, as shown in figs. 2.6a,10, the upper branch state still has the swimmer capacity threshold given by $\gamma = 1$, implying that there exist certain initial conditions which will never reach any steady state. Meanwhile, if the flow rate is high enough, the hysteresis disappear (figs. 2.6a,10) and a steady

solution given in this form is no longer possible beyond the capacity threshold.

In both the experiments of Kessler (1986) and Denissenko & Lukaschuk (2007) where plumes and blips are observed, the total number of swimmers (per unit length) N^*A^* is an order of magnitude higher than the capacity threshold. Therefore, no steady solution is obtained with model G in the regimes studied by Kessler (1986) and Denissenko & Lukaschuk (2007). Instead, in many cases, it was observed that the plume continued to self-focus until blips start to form. According to Kessler (1986), beyond the capacity threshold, the parallel assumption for calculating the plume structure broke down and led to the formation of blips, which is in contrast to Hwang & Pedley (2014*b*)'s theory of blips as an instability of the steady plume. However, given the strong correlation between $N(0)$ and the varicose instability (fig. 2.16), the physical mechanism of the varicose instability first suggested by Hwang & Pedley (2014*b*), i.e. the mechanism driven by the gradient in swimming flux in the radial direction, is still likely at play in the breakdown of the streamwise invariance while the plume is evolving towards the singularity. Therefore, Kessler (1986) was correct in suggesting the singularity, while Hwang & Pedley (2014*b*) provided the mechanism for the breakdown of the parallel symmetry.

In some cases, steady but very focussed plumes were observed in the experiments of Kessler (1986) and Denissenko & Lukaschuk (2007) even when the background swimmer density was higher than the capacity threshold. In those cases, it is likely that the hydrodynamic interactions between swimmers had helped keeping the number density from blowing up. More discussion of the semi-dilute effect on the plume will follow in §5.2.1.

Meanwhile, the experiment by Croze *et al.* (2017) is in the lower Ri regime where a steady solution can be found. In this regime, the dilute assumption and model G is accurate and blip formation is more likely to conform to the instability theory suggested by Hwang & Pedley (2014*b*). It is likely that the instability calculation can be repeated for *Dunaliella* and be directly comparable to the experimental set up of Croze *et al.* (2017).

Chapter 3

Bioconvection and the formation of multiple plumes

3.1 A brief introduction to bioconvection

In the previous chapter, we have demonstrated how gyrotactic microswimmers self-focus into a plume structure under the influence of a downflow. However, even without a downward flow, the coupling mechanism between gyrotaxis and negative buoyancy could still be linearly unstable in an initially quiescent and uniform suspension (Pedley *et al.*, 1988). The instability was believed to be responsible for initiating the convective pattern often observed in a shallow and well-mixed suspension of gyrotactic micro-organisms.

The convective pattern, coined as bioconvection by Platt (1961), was known much earlier than the discovery of gyrotaxis, partly because it is an easily observable and repeatable phenomenon. Documentations of bioconvective patterns can be traced back to as early as the 1860s (Bees, 2020), but the mathematical modelling of the phenomenon only gained traction in the 1970s. Prior to dicovering gyrotaxis, bioconvection was often understood as the result of an upper boundary and modelled as the coupling between negative buoyancy and gravitaxis, which is the tendency of micro-organisms to swim against gravity (e.g. Childress *et al.*, 1975). When enough negatively buoyant swimmers have accumulated at the upper surface due to gravitaxis, an overturning instability can arise, where some regions with enough accumulated swimmers sink with the fluid. The resulting upwelling and downwelling regions effectively form convective rolls, hence the name bioconvection. However, since the discovery of gyrotaxis, Pedley *et al.* (1988) have shown that a gyrotactic instability can arise in

an initially uniform and stationary suspension without an upper surface. Therefore, even for a well mixed and deep gyrotactic suspension, downwelling regions can still spontaneously form in the middle of the suspension (see fig. 3 of (Kessler, 1986)).

Pedley *et al.* (1988) has further compared the horizontal wavelength of the plume structures with observations in experiments but failed to obtain a good agreement. They proposed three potential origins for the discrepancy: 1) finite-depth effect; 2) poor estimation of diffusivity; 3) nonlinear evolution of the plumes. The first issue was tackled by Hill *et al.* (1989) and later by Bees *et al.* (1998), where the linear stability of shallow suspensions was examined. The second can be improved by using a better transport model than the constant and isotropic diffusivity in the primitive model. In the the previous chapter we have demonstrated that the generalised Taylor dispersion model (model G) is more accurate than model F. Therefore, in this chapter, we will mainly focus on the result from model G.

The main objective of this chapter is to address the third issue, i.e. the role of nonlinearity in the plume formation. Like in the previous chapter, an infinitely long pipe is considered, and the solution is assumed to be uniform in the axial and azimuthal directions. In other words, we will ignore the finite-depth effect for simplicity. Several previous studies have considered similar steady solutions for the nonlinear axially-uniform gyrotactic plume in a downflowing pipe. Kessler (1986) first derived an analytical solution (see eq. (2.19)), but it was limited to the case where the pressure gradient is zero. Bees & Croze (2010) obtained the solution asymptotically and found that there can be more than one solution for a given set of parameters. More recently, Bearon *et al.* (2012) and Croze *et al.* (2013, 2017) have computed the solution numerically using model G. Despite these advances made over the years, little attention has been paid to the existence of the solutions itself. Only in §2.4.3 have we discovered the existence of a steady solution is limited within a certain range of the parameters. Indeed, for a sufficiently large downflow, the solution obtained with model G does not exist when the Richardson number is greater than a critical value.

In this chapter, we will extend the findings of the previous chapter. We will consider both upward and downward flows, and exhaustively seek the nonlinear solutions, by extending the computation of the plume solutions in §2.4.1. In contrast to the previous chapter, here we seek solutions at a Richardson number much higher than the threshold Ri_s. Also, there can be more than one plume forming in the pipe. We will show that the number of plumes forming in the pipe is related to the transcritical bifurcation shown in §2.4.1. All these solutions emerge through a sequence of transcritical bifurcations as the Richardson number increases.

3.2 Problem formulation

The equations for the axisymmetric and axially uniform solution to the gyrotactic suspension in a cylindrical pipe is the same as the equations for the basic state in §2.2.2. However, to better show the stability of the solution in time, here we rewrite it as a set of unsteady equations

$$\frac{\partial U}{\partial t} = -G + \frac{1}{Re}\frac{1}{r}\frac{\partial}{\partial r}\left(r\frac{\partial U}{\partial r}\right) - Ri(N-1) \tag{3.1a}$$

and

$$\frac{\partial N}{\partial t} = -\frac{1}{r}\frac{\partial}{\partial r}(rN\langle p_r\rangle) + \frac{1}{d_r}\frac{1}{r}\frac{\partial}{\partial r}(rD_{rr}\frac{\partial N}{\partial r}), \tag{3.1b}$$

with the boundary conditions and compatibility conditions

$$U(1) = 0, \quad \left[\langle p_r\rangle N - \frac{D_{rr}}{d_r}\frac{\partial N}{\partial r}\right]\Big|_{r=1} = 0, \quad \frac{\partial U}{\partial r}\Big|_{r=0} = 0, \quad \frac{\partial N}{\partial r}\Big|_{r=0} = 0, \tag{3.1c}$$

and the normalisation conditions

$$\int_0^1 N(r;t)rdr = \frac{1}{2}. \tag{3.1d}$$

The downward flow rate Q is defined as

$$\int_0^1 U(r;t)rdr = -\frac{Q}{2\pi}. \tag{3.1e}$$

Some of the above equations are repeated for easier readership. Here, we define $G = \partial q/\partial z + Ri$ as the driving pressure gradient that excludes the hydrostatic pressure from the negative buoyant swimmers (i.e. $G = \partial q_0^d/\partial z$). If Q is steady and prescribed, then the pressure gradient is obtained as $G = (2/Re)\partial_r U|_{r=1}$. Note that the three parameters Q, Ri and G only share two degrees of freedom. If either two are prescribed, the reamining one shall be solved simultaneously with the solution.

Lastly, the steady version of (3.1) can be further simplified into (2.15) and

$$-\frac{1}{Re}\mathcal{D}^2 U = -Ri\left(N(0)\exp\left(d_r\int_0^r \frac{\langle p_r\rangle}{D_{rr}}dr\right) - 1\right) - G, \tag{3.2}$$

where $N(0)$ is determined by (2.6) and G is determined by (2.7). Here, we denote the radial Laplace operator by $\mathcal{D}^2 = (1/r)\partial_r(r\partial_r)$.

The above equations are solved using the pseudo-arclength and Newton-Raphson method provided in §2.3. However, in this chapter, we shall also implement two other pseudo-arclength continuation

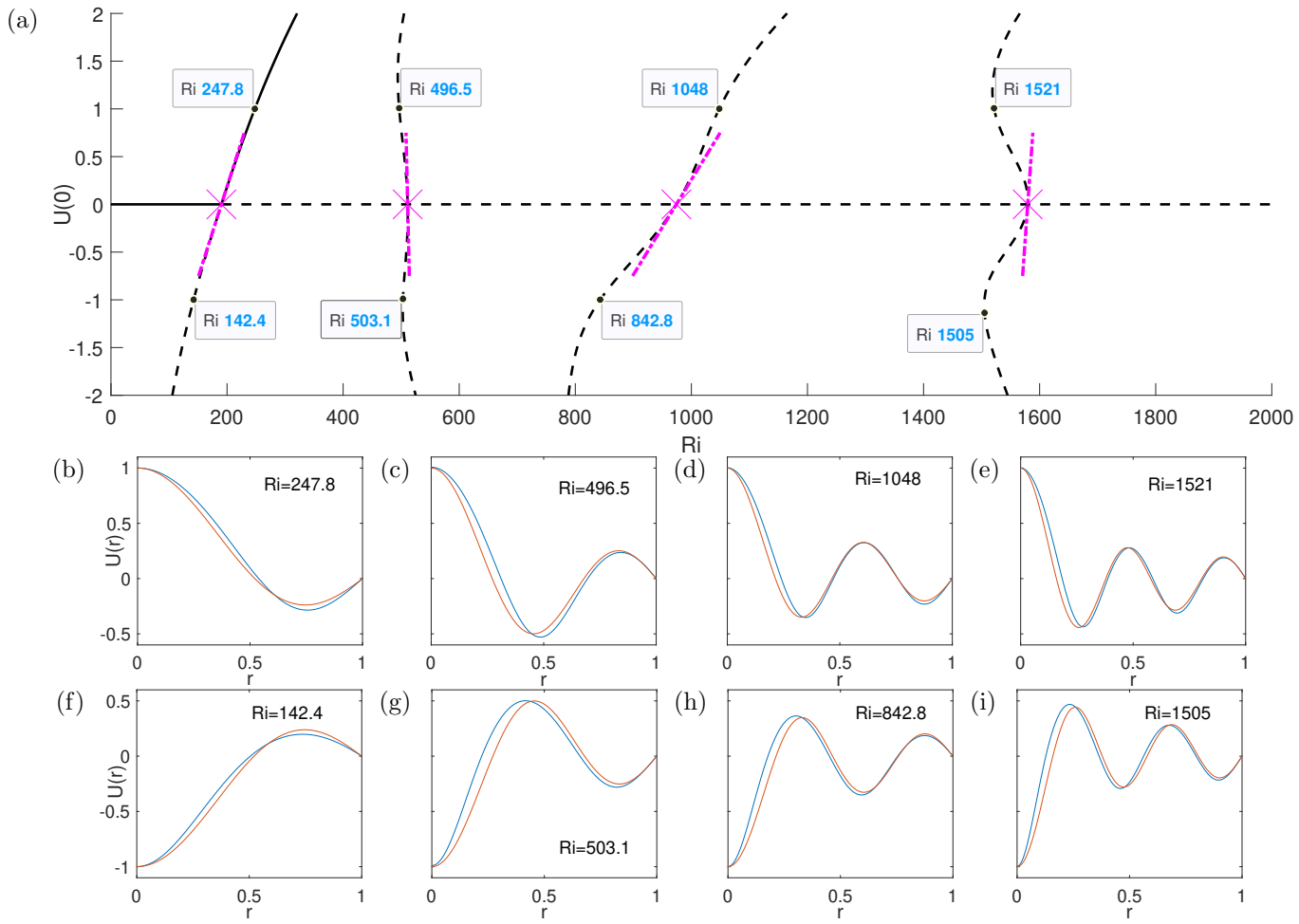

Figure 3.1: Comparison between numerical solutions of (3.2) and the linear and weakly non-linear analysis in §3.4. (a) Bifurcation diagram ($U(0)$ against Ri) of the $Q = 0$ solutions from (3.2). Here, the line type represents the stability of the solution: ——, stable; - - - -, unstable. The bifurcation point ($Ri_{c,n}$) from (3.7) is denoted by magenta crosses ($\times$), while the slope of the bifurcation curve calculated from (3.12) is indicated by the short magenta dot-dashed segment (–·–·–). The dotted blue lines (·····), representing $U(0) = \pm 1$, are added to locate the Ri values for (b-i). (b-i) Comparisons between the nonlinear steady solution (blue lines) and the corresponding (appropriately normalised) linear instability mode $\hat{u}(r)$ at $Q = 0$ and Ri as indicated in (a).

methods, one with a prescribed G and varying Ri or Q and one with a prescribed Ri and varying Q. The principle for the continuation algorithm is the same as that suggested in §2.3.5, which will not be repeated here for brevity.

3.3 Extending the low flow rate results

In §2.4.1 and fig. 2.3, we have briefly shown that there exist multiple branches of solutions at each Q as long as Q is near zero. Here, the same bifurcation diagram, but with a larger range of Ri and Q, is presented. In fig. 3.1a and fig. 3.2, the axial velocity $U(0)$ is used to represent the state of the steady solutions. Fig. 3.1a shows how the solution from (3.2) changes with Ri at $Q = 0$, while fig. 3.2 shows

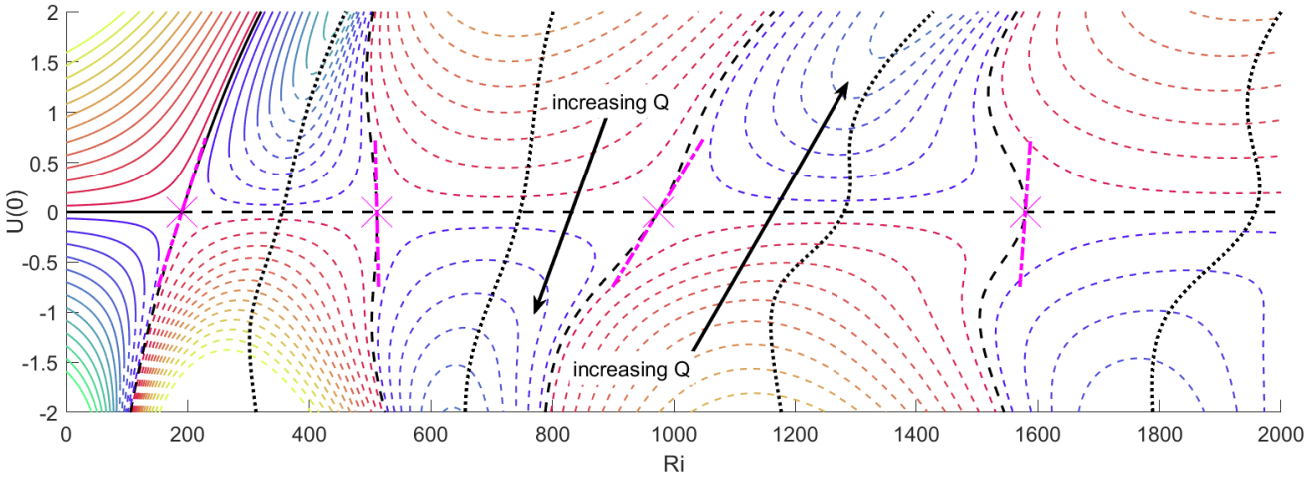

Figure 3.2: Contours of $U(0)$ against Ri at each given $Q \in [-2.5, 2.5]$. Here, each contour line in the $U(0) - Ri$ plane indicates the value of Q: black, $Q = 0$; blue to green, $Q \in [0.1, 2.5]$ with 0.2 increment; red to yellow, $Q \in [-2.5, -0.1]$ with -0.2 increment. The line type represents the stability of the solution: ——, stable; - - - -, unstable. The thick dotted black lines (·····) show the bifurcation by varying Q for given $G = 0$ (see §3.5).

the same at other Q in the range $[-2.5, 2.5]$. We have also plotted some of the steady solutions $U(r)$ when $|U(0)| = 1$ and $Q = 0$ in fig. 3.1b-i (blue lines), for reasons that will become apparent later in §3.4.1. The respective value of Ri for each $U(r)$ can be found in each panel of fig. 3.1b-i, as well as in fig. 3.1a.

Focusing on $Q = 0$, from fig. 3.1a, it is apparent that there exist multiple branches of steady solutions other than the uniform-suspension solution represented by $U(0) = 0$. In fact, as we increase Ri, there seems to be a countable but infinite number of branches emerging via a sequence of transcritical bifurcations. Each branch coincides with the uniform suspension at a certain Ri, which forms the bifurcation point. We shall define $Ri_{c,n}$ as the Richardson number of each bifurcation point from the left in fig. 3.1a, where n is the index. For convenience, we shall also index the $Q = 0$ branches accordingly too. For example, the first bifurcation at $Ri(= Ri_{c,1} \approx 190)$ is connected to the first $Q = 0$ branch (see the black line crossing the leftmost Ri_c in fig. 3.1a). At each bifurcation point, there is also an exchange of stability, as we examine the stability of the solution near each bifurcation (see §3.4.1). However, except for the first bifurcation, the stability exchange takes place not with the most unstable mode but with a less unstable one. When a small downflow or upflow is applied (i.e. $Q \neq 0$), each transcritical bifurcation point turns into a saddle-node point via an imperfect bifurcation. This is similar to the finding of §2.4.1 for the first branch solution, but the same happens to all the other branches.

3.4 The origin of an infinite number of solution branches

In this section, we will examine the linear stability of a uniform suspension in the vertical pipe. We will further restrict the perturbation to be axisymmetric, parallel and axially uniform, given the nature of the solutions of interest. To be consistent with our numerical results in §3.3 and fig. 3.1a, in this section we will fix the flow rate when adding the perturbation, i.e. $Q = 0$. We will demonstrate that the multiple transcritical bifurcations of the computed solutions are the result of the pipe geometry, which also confines the suspension in a domain with finite horizontal extent. We will then extend it to the weakly nonlinear regime, similarly to previous work by Bees & Hill (1999). The resulting amplitude equation demonstrates that all the bifurcations in fig. 3.1a are indeed transcritical.

3.4.1 Linear stability analysis

We first consider a perturbation to the stationary uniform suspension in a cylindrical pipe with infinite depth, i.e. $U = \epsilon u_1(r,t) + \epsilon^2 u_2(r,t) + O(\epsilon^3)$ and $N = 1 + \epsilon n_1(r,t) + \epsilon^2 n_2(r,t) + O(\epsilon^3)$. Given that $\langle p_r \rangle(S)$ is odd and $D_{rr}(S)$ is even with respect to the radial shear rate S, this yields

$$\langle p_r \rangle = \epsilon\zeta \frac{\partial u_1}{\partial r} + \epsilon^2 \zeta \frac{\partial u_2}{\partial r} + \mathcal{O}(\epsilon^3), \quad \text{and} \quad \frac{D_{rr}}{d_r} = D + \frac{\epsilon^2}{8 d_r^3} \frac{\partial^2 D_{rr}}{\partial S^2}\bigg|_{S=0} \left(\frac{\partial u_1}{\partial r}\right)^2 + \mathcal{O}(\epsilon^3), \tag{3.3}$$

where $\zeta = -(\partial_S \langle p_r \rangle|_{S=0})/(2d_r)$ (ζ is negative) and $D = D_{rr}|_{S=0}/d_r$ are constants that depend only on d_r and β. We also note that $-\zeta/D = \beta/2$ (see §2.4.3 and Bearon *et al.* 2012). At $\mathcal{O}(\epsilon)$, the perturbed equations for linear stability are then obtained as

$$\frac{\partial u_1}{\partial t} = \frac{1}{Re}\mathcal{D}^2 u_1 - Ri\ n_1 - G_1, \tag{3.4a}$$

and

$$\frac{\partial n_1}{\partial t} = -\zeta \mathcal{D}^2 u_1 + D\mathcal{D}^2 n_1, \tag{3.4b}$$

with boundary conditions

$$u_1(1) = 0, \quad \left[\zeta \frac{\partial u_1}{\partial r} - D\frac{\partial n_1}{\partial r}\right]\bigg|_{r=1} = 0. \tag{3.4c}$$

Because we have fixed $Q = 0$, the perturbed pressure gradient G_1 is found such that the flow rate is not altered by the perturbation, i.e.

$$\int_0^1 u_1 r dr = 0. \tag{3.4d}$$

While (3.4) can be solved numerically, we shall proceed to focus on the special case when one of the stability modes is neutrally stable. Introducing a neutrally stable and stationary normal mode (i.e. $u_1(r,t) = \hat{u}(r)$ and $n_1(r,t) = \hat{n}(r)$), (3.4) is then simplified into a single equation:

$$\mathcal{D}^2\hat{u} + \kappa^2\hat{u} = ReG_1, \tag{3.5}$$

where $\kappa^2 = -RiRe\zeta/D = RiRe\beta/2$. The left-hand side of (3.5) is the Bessel differential equation, which admits the Fourier–Bessel series as solutions. Substituting the boundary conditions, the mode shapes of $\hat{u}(r)$ should take the form

$$\hat{u}(r) = \frac{G_1 Re}{\kappa^2}\left(1 - \frac{J_0(\kappa r)}{J_0(\kappa)}\right), \tag{3.6}$$

where $J_m(r)$ is the m^{th} Bessel function of the first kind. Enforcement of (3.4d) into (3.6) subsequently leads to an infinite number of discrete values of $\kappa(=\kappa_{c,n})$ satisfying $J_2(\kappa_{c,n}) = 0$, at which (3.6) becomes a neutrally stable solution to (3.4). Here n indicates the n^{th} zeros of $J_2(r)$. In this case, G_1 in (3.6) becomes an arbitrary real constant, as (3.4d) is satisfied for any G_1. The values of $\kappa_{c,n}$ also yield the critical values of

$$Ri_{c,n} = \frac{2\kappa_{c,n}^2}{Re\beta} \tag{3.7}$$

for the neutral stability of each mode. These values of $Ri_{c,n}$ calculated from $\kappa_{c,n}$ match perfectly with the bifurcation points computed numerically in the previous section, as shown in fig. 3.1a. Finally, it should be mentioned that (3.7) is equivalent to (3.14) in Pedley *et al.* (1988) and (31) in Bees & Hill (1999), where a continuous set of the critical values of the parameters equivalent to Ri and κ are obtained from linear stability analysis. However, in the present study, the introduction of a finite domain in the radial direction results in discrete values of $\kappa_{c,n}$ and $Ri_{c,n}$ with the corresponding eigenmode in the form of a cylindrical harmonic (i.e. Bessel functions) that satisfies the given boundary conditions.

3.4.2 Weakly nonlinear analysis

We further proceed to perform a weakly nonlinear analysis close to $Ri_{c,n}$. In the previous study by Bees & Hill (1999), where a uniform suspension is considered in an unbounded domain, it was assumed that the leading nonlinear term would appear at the third order due to translational invariance of the suspension in the horizontal direction. However, in the present study, such invariance is broken due to the pipe's cylindrical geometry. Hence, there is no reason that the leading nonlinear term

would emerge at the third order. In this study, we start by assuming $Ri - Ri_{c,n} = \epsilon \Delta Ri$ (ΔRi is the normalised distance from the bifurcation point) with a slow time scale $T = \epsilon t$. Given the perturbation form introduced in §3.4.1, at $\mathcal{O}(\epsilon^2)$, we get

$$\partial_T u_1 + \Delta Ri \; n_1 = -\partial_t u_2 - G_2 + \frac{1}{Re}\mathcal{D}^2 u_2 - Ri_{c,n} \; n_2, \tag{3.8a}$$

where $G_2 = (2/Re)u_2'(1)$ and

$$\partial_T n_1 + \zeta \frac{1}{r}\partial_r \left(r(\partial_r u_1) n_1\right) = -\partial_t n_2 - \zeta \mathcal{D}^2 u_2 + D\mathcal{D}^2 n_2. \tag{3.8b}$$

We also introduce amplitude $A(T)$ for the linear perturbation

$$u_1(r,t,T) = A(T)\hat{u}(r) \quad \text{and} \quad n_1(r,t,T) = A(T)\hat{n}(r), \tag{3.9}$$

where the linear instability mode is normalised to be $\hat{u}(0) = 1$. Therefore, the normalised first-order velocity profile is

$$\hat{u}(r) = f_{c,n}(r) \equiv \left(1 - \frac{J_0(\kappa_{c,n} r)}{J_0(\kappa_{c,n})}\right) / \left(1 - \frac{1}{J_0(\kappa_{c,n})}\right). \tag{3.10}$$

Following the procedure of a weakly nonlinear analysis (e.g. Drazin, 2002), we apply the solvability condition to (3.8) using the adjoint of (3.4). Now, the adjoint of $\hat{u}$ is the same as $\hat{u} = f_{c,n}(r)$, and $\hat{n} = -\beta\hat{u}/2$. However, the adjoint of $\hat{n}$ is $(\zeta Re)^{-1} g_{c,n}(r)$, where $g_{c,n}(r)$ is

$$g_{c,n}(r) = \left(J_0(\kappa_{c,n}) - J_0(\kappa_{c,n} r) - \frac{r^2 - 1}{2}\kappa_{c,n} J_1(\kappa_{c,n})\right) / \left(J_0(\kappa_{c,n}) - 1\right). \tag{3.11}$$

From the solvability condition, we arrive at

$$\left(C + \frac{F}{DRe}\right)\partial_T A - \frac{\beta}{2} C \Delta Ri A - \frac{\beta E}{2Re} A^2 = 0, \tag{3.12}$$

where C, E and F are dependent on $\kappa_{c,n}$ and are defined by

$$C = \int_0^1 f_{c,n}(r)^2 r dr = \frac{\kappa_{c,n}^2}{8}\left(1 - \frac{1}{J_0(\kappa_{c,n})}\right)^{-2}, \tag{3.13}$$

$$E = \int_0^1 g_{c,n}(r)\partial_r \left[r f_{c,n}'(r) f_{c,n}(r)\right] dr, \tag{3.14}$$

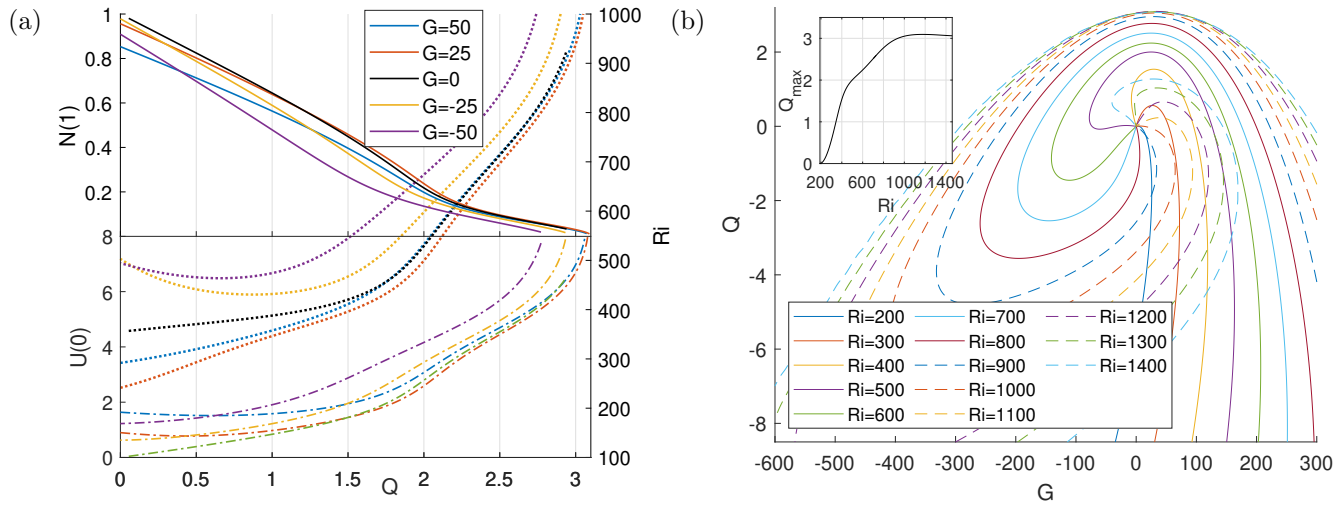

Figure 3.3: Continuations of the steady solution emerged from the first bifurcation point with $U(0) > 0$. (a) Plots of $U(0)(-\cdot-\cdot-)$, $Ri(\cdots\cdots)$ and $N(1)(——)$ for several G on increasing Q from 0. (b) The relation between G and Q for several fixed Ri. Inset: the maximum achievable flow rate $Q_{\max}$ plotted for each Ri.

$$F = \int_0^1 f_{c,n}(r) g_{c,n}(r) r dr = -\frac{3\kappa_{c,n}^2}{16}\left(1 - \frac{1}{J_0(\kappa_{c,n})}\right)^{-2}. \tag{3.15}$$

While C and F are found analytically, E is numerically integrated owing to the complexity of the Bessel function. The numerical values of $-CRe/E$ are plotted as the local slopes of the corresponding branch at each bifurcation point in fig. 3.1a.

Now, given the quadratic nonlinearity in (3.12), it is clear that all the bifurcations in fig. 3.1a are transcritical. We have also computed the slopes of the non-trivial branches in fig. 3.1a, which are given by $-CRe/E$, when they cross each bifurcation point. As shown by the dot-dashed lines in fig. 3.1a, the computed slopes match with those of the numerically computed nonlinear solutions perfectly at the bifurcation points.

Finally, the neutrally stable eigenmodes (3.6) used for the weakly nonlinear analysis (red line, with appropriate sign) are compared with the numerical solutions (blue line) around each bifurcation point (at $U(0) = \pm 1$) in fig. 3.1. As expected, there is an excellent agreement between them.

3.5 Existence of steady solution

As previously noted, there are three parameters Q, G and Ri that control the bifurcation of (3.1). Here, Q and G are dependent on each other, providing only two degrees of freedom in total. Now, without loss of generality, we shall vary the three parameters Q, G and Ri in a controlled manner to

explore the existence of the steady solutions reported in §3.3. We first prescribe G and continue the steady solutions to (3.1) by changing Q – the related bifurcation diagrams for $G = 0$ are also shown in fig. 3.2 (dotted lines). Here, we note that the change of Q for a given G requires a change of Ri, given the relation of the three parameters. Fig. 3.3a shows how $U(0)$, Ri and $N(1)$ change with Q for several prescribed G. It is found that all the solutions blow up at a certain respective threshold of Q (say $Q_{c,G}(G)$): as $Q \to Q_{c,G}(G)$, $U(0)$ and Ri blow up and $N(1)$ approaches zero (i.e. depletion of the swimmer number density at the wall).

To further explain the existence of a threshold value of Q, we also perform continuation by changing G for prescribed Ri. Fig. 3.3b shows the continuation of the first two steady solution branches reported in fig. 3.1a for fixed $Ri \in [200, 1400]$. Now, it becomes apparent that there exists a maximum achievable $Q(\equiv Q_{\max,Ri}(Ri))$ at each Ri. Plotting $Q_{\max,Ri}(Ri)$ against Ri (inset in fig. 3.3b) shows that $Q_{\max,Ri}$ reaches its maximum at $Q_{\max} \approx 3.1$ and $Ri \approx 1174$. The maximum downward flow rate $Q_{\max}(> 0)$ is typically achieved with a downward pressure gradient ($G > 0$) (i.e. $Q_{\max} = \max(Q_{c,G}(G))$ in fig. 3.3a). However, any further increase of G counter-intuitively decreases, rather than increases, the flow rate of the steady solution.

Lastly, we note that fig. 3.3 only shows the first and second solution branches that emerge from $Q = 0$ in fig. 3.1a. However, the same qualitative behaviours have been found from all the other solution branches: for example, the relation between $N(1)$ and Q, the blow-up of $U(0)$ and Ri as $Q \to Q_{c,G}$, and the existence of $Q_{\max}$.

3.6 Discussion

In this study, we have sought the nonlinear, steady and axisymmetric solutions for a suspension of gyrotactic swimmers in an infinitely long pipe. An infinite number of steady solutions have been found. Each of them stems from a transcritical bifurcation on the uniform solution. The exact values of the bifurcation points have also been found by solving the linearised equations for the neutral stabilities.

Comparing the present study with Bees & Hill (1999), who showed the existence of an uncountably infinite number of solutions to a similar set of equations in an unbounded domain, we can conclude that the countably infinite number of transcritical bifurcations originates from the finite horizontal domain and the flow geometry (i.e. pipe). Firstly, the finite horizontal domain yields discrete eigenvalues from the equations for the linear stability (3.4), making $(\kappa_{c,n}, Ri_{c,n})$ a discrete set rather than a continuous

curve. Hence we have a countably infinite number of bifurcation points. Secondly, the cylindrical geometry of the pipe breaks the translational invariance in the horizontal direction. In an unbounded domain, this invariance in the uniform suspension is broken by the primary bifurcation (i.e. pitchfork bifurcation (see Bees & Hill, 1999)). However, in the pipe, the primary bifurcation takes place in a circumstance where the translational invariance is already broken by the flow geometry, which leads to the primary bifurcation to be transcritical instead.

The existence of many steady solutions has also hinted at the possible dynamical route from a uniform suspension to the gyrotactic pattern. Except for the first branch, all the other steady solution branches found in fig. 3.1a are saddles in the state space. In other words, if a stationary and uniform suspension at $Ri > Ri_{c,n}$ is perturbed with the n^{th} most linearly unstable mode from (3.6), the system would first evolve towards the corresponding nonlinear steady solution. Therefore, the flow patterns related to the unstable solutions in the present study may well be observed at least transiently, before further development of the flow state or its breakdown in the axial and/or azimuthal directions. Indeed, early numerical simulations by Ghorai & Hill (1999, 2000) found such a transient dynamics, which strongly hinted at the dynamical importance of the initial perturbation. Furthermore, the increasing number of nonlinear steady solutions and linearly unstable mode as Ri increases strongly hinted at the increasing complexity of the system as Ri increases.

Finally, the emergence of multiple axisymmetric steady solutions with increasing Ri implies that similar solutions may well exist for the non-axisymmetric case. This implies that the route to the final flow pattern would be a highly complicated process, involving competition between the axisymmetric and non-axisymmetric states. Lastly, it should also be pointed out that these axially uniform steady solutions may also be unstable to axially varying perturbations (see §2.5).

Chapter 4

A new transport model for swimmers and biased Active Brownian Particles (ABPs)

4.1 The need for a new transport model for swimmers/biased ABPs

In chapter 2, we have explored in detail the consequences of model F and G and how the plume structure depends on the transport model. In particular, we have demonstrated that the singularity in the parameter space is highly sensitive to the effective diffusivity of swimmers in high shear. To this end, model G seems to provide a better accuracy (see §2.6.1). Despite the merit, model G also has an important limitation – it is only applicable to vorticity-dominant flows but not straining-dominant flows (see §1.5.2 and Bearon *et al.*, 2011). Indeed, in a recent review (Bees, 2020), this limitation of model G has been pointed out as a significant challenge for the modelling of bioconvection. Moreover, model G was derived for a homogenous shear flow. When applied to an inhomogeneous shear flow, the model would implicitly assume the flow is quasi-homogeneous locally. Therefore, it cannot describe the extra advection (or drift) caused by the inhomogeneity in the shear flow and cannot capture related phenomena such as the shear trapping of non-spherical swimmers with no taxis (Bearon & Hazel, 2015; Vennamneni *et al.*, 2020).

The uncertainty around the transport properties of swimmers, especially the effective diffusivity of swimmers, is an artefact of the coarse-grained transport model for swimmers. One way to remove such artefact is to solve the Smoluchowski equation directly. Still, as mentioned in §1.5, there remains a significant challenge in computational cost to solve the equation directly. One can reduce the

computational cost by using some symmetries to reduce the number of dimensions (e.g. Chen & Jiang, 1999; Saintillan & Shelley, 2008*a*; Saintillan, 2010; Jiang & Chen, 2020), but the symmetries are problem-specific. Another way to overcome the challenge is to come up with a better model.

As mentioned in §1.6, one of the key objectives of this thesis is to develop a new continuum model for the transport of swimmers. This chapter is going to propose a new transport model to overcome the inherent limitations of model G and the inaccuracy of model F. We will show that the Smoluchowski equation admits an exact transformation into a transport equation which shares many similarities to the platform used in model F and G. Combining this transformation with the method of multiple scales, this work proposes an approximated but novel transport equation for the swimmers, in which the orientation dynamics is determined only with the local flow information in the physical space like the previous models. We will show that this new model removes the limitations of model G and offers a more accurate prediction of the swimmer distribution in an inhomogeneous shear flow.

Lastly, one shall note a slight change of terminology in this chapter. In the previous chapters, microswimmers are mostly referred to as 'swimmers', which signifies their biological origin and their hydrodynamic contributions to the flow. However, in the following chapter, we will further simplify the problem by prescribing a flow field rather than solving the swimmer transport with the flow simultaneously. Still, the end goal is to solve the suspension dynamics with the flow simultaneously in future work. In other words, the swimmers' hydrodynamic contributions are neglected in this chapter for simplicity. To this end, the appropriate name for this class of particles is biased active Brownian particles (ABPs), or 'particles' for short. These particles can be artificial and self-propel in different ways, but they are assumed to have a negligible effect on the flow field. ABPs are governed by the same set of trajectories as in §1.4.1 and §1.4.3, but in addition to the rotational noise (§1.4.4), ABPs may also be subjected to translational noise. Therefore, D_T^* was also introduced in (1.11) alongside d_r^*. Also, as an extension of the conventional non-biased ABPs, in this section, we consider ABPs that can have a biased trajectory (e.g. gyrotaxis).

This chapter is organised as follows. In §4.2, the readers are reminded about the Smoluchowski equation that governs the configuration of the active Brownian particle suspension. Then, the non-dimensionalisation scheme of this chapter is introduced. After that, we will briefly summarise the discussion on model G thus far in §4.3. In §4.4, the exact transformation of the Smoluchowski equation into a transport equation is introduced. While the transformed equation cannot be directly used as a model, it sets up the mathematical platform for the local approximation. In §4.5, the local approximation is presented for the development of a novel transport equation model. Then,

the mathematical structure of this model is compared with that of model G. In §4.6, we will present examples of gyrotactic particle suspensions in one-dimensional vertical and horizontal shear flows and demonstrate the superiority of the newly-introduced model over model G. We will also compare these results with those obtained through the exact transformation of the Smoluchowski equation. In §4.8, we will further dissect the physical interpretation of the transformation compared to model G and discuss the physical origin of the dispersion of particles. Lastly, in §4.9, we will briefly outline the potential application of the local approximation and the remaining challenges in the proposed model.

4.2 Problem Formulation

We consider a dilute suspension of biased or non-biased active Brownian particles (ABPs), where there is randomness in both the physical $\mathbf{x}^*$- and orientational $\mathbf{p}$- spaces. The equations that govern the statistical configuration of the suspension were already introduced in §1.4.5, in which the probability density function $\Psi(\mathbf{x}^*, \mathbf{p}, t^*)$ is governed by the Smoluchowski equation (1.11). The deterministic part of the $\mathbf{x}^*$-space trajectory is governed by (1.10). As mentioned, we will neglect the sedimentation $\mathbf{u}_s^*$ for the time being. The self-propelling velocity is assumed to have a constant magnitude, but the direction $\mathbf{p}$ is changing according to (1.7), which accounts for the viscous rotation from the local flow and the gravitational torque. In this chapter, we will prescribe a flow field instead of solving it simultaneously.

4.2.1 Non-dimensionalisation

Equation (1.11) is subsequently non-dimensionalised with a suitable length and time scales. In this chapter, the characteristic length h^* is chosen from the given flow field, and the inverse of rotational diffusivity $1/d_r^*$ is selected as the time scale. Note that we have chosen the $\mathbf{p}$-space time scale rather than the swimming speed of the previous chapters. This is for the convenience of the later multi-scale approximation. However, we shall also use the characteristic speed U^* of the flow for the non-dimensionalisation of the flow field. Hence,

$$\mathbf{x} = \frac{\mathbf{x}^*}{h^*}, \quad t = t^* d_r^*, \quad \text{and} \quad \mathbf{u} = \frac{\mathbf{u}^*}{U^*}.$$

The dimensionless parameters for the motility V_s^*, the flow speed U^*, the translational diffusivity D_T^* and the gyrotactic timescale B^* are

$$Pe_s = \frac{V_s^*}{h^* d_r^*}, \quad Pe_f = \frac{U^*}{h^* d_r^*}, \quad D_T = \frac{D_T^*}{(h^*)^2 d_r^*}, \quad \text{and} \quad \beta = \frac{1}{2 d_r^* B^*}$$

respectively, in which Pe_f and Pe_s are the ambient flow and motility Péclet numbers. The dimensionless form of (1.11) is then given by

$$\frac{\partial \Psi}{\partial t} + \nabla_{\mathbf{x}} \cdot [(Pe_f \mathbf{u} + Pe_s \mathbf{p})\Psi] + \mathcal{L}_p(\mathbf{x}, t)\Psi = D_T \nabla_x^2 \Psi, \tag{4.1}$$

where we also introduce the $\mathbf{p}$-space linear operator

$$\mathcal{L}_p(\mathbf{x}, t)\Psi = \boldsymbol{\nabla}_{\mathbf{p}} \cdot \left[\left(\beta \left[\hat{\mathbf{k}} - (\hat{\mathbf{k}} \cdot \mathbf{p})\mathbf{p} \right] + \frac{Pe_f}{2} \boldsymbol{\Omega} \wedge \mathbf{p} + Pe_f \alpha_0 \mathbf{p} \cdot \boldsymbol{E} \cdot (\boldsymbol{I} - \mathbf{pp}) \right) \Psi \right] - \nabla_{\mathbf{p}}^2 \Psi. \tag{4.2}$$

By the divergence theorem, the integration over $\mathbf{p}$-space of the operator $\mathcal{L}_p(\mathbf{x}, t)$ acting on any arbitrary continuously differentiable function $a(\mathbf{p})$ satisfies

$$\int_{S_p} \mathcal{L}_p(\mathbf{x}, t)\, a(\mathbf{p})\, d^2\mathbf{p} = 0. \tag{4.3}$$

Physically, it is related to the conservation of probability distribution in $\mathbf{p}$-space. We also note that (4.2) may be modified to account for other taxes by including the relevant modelling terms, e.g. the run-and-tumble and chemotaxis process (see (1.12) and Subramanian & Koch 2009) or phototaxis (Williams & Bees, 2011). Therefore, we expect that many deterministic trajectories for the orientation dynamics would also be given as a linear operator $\mathcal{L}_p(\mathbf{x}, t)$ that satisfies (4.3). In the following sections, we will use the linear operator $\mathcal{L}_p(\mathbf{x}, t)$ to represent the orientation dynamics in $\mathbf{p}$-space to maintain this level of abstraction in the orientation dynamics.

4.3 Limitation of the GTD model

We have already introduced model G (§1.5.2) and discussed some of its limitations (§1.5.3 and §2.6.2). Here, we shall briefly summarise the discussion on model G so far.

Model G is based on two assumptions: 1) the timescale in $\mathbf{p}$-space is much faster than that of $\mathbf{x}$-space (a quasi-steady assumption in $\mathbf{p}$-space); 2) the size of the particle is much smaller than the length scale of the flow, allowing the approximation of a locally homogeneous velocity gradient tensor $\nabla \mathbf{u}$ (a

quasi-homogeneous shear assumption in $\mathbf{x}$-space). Under these assumptions, model G obtains the effective drift and diffusivity using the impulse response of (4.1). The effective drift and diffusivity are calculated from the impulse response using the Oldroyd time derivative of the first and second statistical moments in the limit of $t \to \infty$ (for further details, see Frankel & Brenner, 1991, 1993). The resulting advection-diffusion (or drift-diffusion) equation for the particle distribution $n(\mathbf{x}, t)$ is given by (1.20), or in the non-dimensionalisation scheme of this chapter,

$$\partial_t n + \boldsymbol{\nabla}_{\mathbf{x}} \cdot [(Pe_s \langle \mathbf{p} \rangle_g + Pe_f \mathbf{u}) n] = D_T \nabla_x^2 n + Pe_s^2 \boldsymbol{\nabla}_{\mathbf{x}} \cdot \boldsymbol{D}_G \boldsymbol{\nabla}_{\mathbf{x}} n. \tag{4.4}$$

The effective advection is given by the sum of $Pe_s \langle \mathbf{p} \rangle_g$ and $Pe_f \mathbf{u}$ and the effective diffusivity provided by $Pe_s^2 \boldsymbol{D}_G$, which is computed from eqs. (2.2i) and (2.2j). Here, note that the advective drift caused by the particles' motility is obtained from the ensemble-averaged velocity of individual particles, given that each of their orientational distribution is $g(\mathbf{x}, t; \mathbf{p})$. The term $Pe_s \langle \mathbf{p} \rangle_g$ can therefore be interpreted as the average motility of individual particles. Furthermore, symmetry is enforced in the tensor $\boldsymbol{D}_G$ as its definition is given by the second-order statistical moment's derivative in time.

Recent studies (Croze *et al.*, 2013, 2017) and our work in chapter 2 have shown that it offers a more accurate and physically relevant description for swimmer transport in both stationary and sheared suspensions than model F. However, as mentioned earlier, model G has some important limitations. Firstly, as discussed in §1.5.3, model G was developed for a pure shear flow. It would encounter singularities if the same formulae were applied to a straining-dominant flow (Bearon *et al.*, 2011). Secondly, as briefly discussed in §2.6.2, the homogeneous assumption in model G prevents it from accurately capturing the shear trapping phenomena observed in Rusconi *et al.* (2014), even though the direct solution of the Smoluchowski equation can capture the phenomena (Bearon & Hazel, 2015; Vennamneni *et al.*, 2020). This work aims to overcome these limitations by deriving a mathematically similar drift and dispersion coefficient but from a different perspective of the Smoluchowski equation.

4.4 Exact transformation into a transport equation

The purpose of this chapter is to obtain a transport equation that resembles (4.4). The key approach taken by Frankel & Brenner (1991, 1993) lies in the approximation of the Oldroyd time derivative of the first- and second-order statistical moments using Ψ in (4.1) for the 'phenomenological' effective drift $Pe_s \langle \mathbf{p} \rangle$ and diffusivity $\boldsymbol{D}_G$. Instead, in this chapter, we shall start by seeking an exact mathematical transformation of (4.1) into a transport equation that resembles (4.4). In particular, this transformation

will be utilised in §4.5 as the foundation for a new transport-equation-based model that can overcome the limitations of model G.

We define $n(\mathbf{x},t)$ and $f(\mathbf{x},\mathbf{p},t)$ as $\Psi(\mathbf{x},\mathbf{p},t) = n(\mathbf{x},t)f(\mathbf{x},\mathbf{p},t)$, so that $f(\mathbf{x},\mathbf{p},t)$ at each $\mathbf{x}$ becomes the probability density function in $\mathbf{p}$ space satisfying $\int_{S_p} f(\mathbf{p})d^2\mathbf{p} = 1$. Now, from (4.3), integration of (4.1) over $\mathbf{p}$-space gives the following equation in the $(\mathbf{x},t)$-space,

$$\partial_t n(\mathbf{x},t) + \boldsymbol{\nabla}_{\mathbf{x}} \cdot [(Pe_s\langle\mathbf{p}\rangle_f(\mathbf{x},t) + Pe_f\mathbf{u}(\mathbf{x},t))n(\mathbf{x},t)] = D_T\nabla_x^2 n(\mathbf{x},t), \tag{4.5}$$

where

$$\langle\mathbf{p}\rangle_f(\mathbf{x},t) \equiv \int_{S_p} \mathbf{p}f(\mathbf{x},\mathbf{p},t)d^2\mathbf{p}. \tag{4.6}$$

Here, we note that (4.5) appears as a standard advection-diffusion equation. However, in the absence of the full information of $\Psi(\mathbf{x},\mathbf{p},t)$, it is not solvable because $\langle\mathbf{p}\rangle_f(\mathbf{x},t)$ is still unknown. Furthermore, while some may interpret $\langle\mathbf{p}\rangle_f(\mathbf{x},t)$ as the normalised polar order (Saintillan & Shelley, 2015), it is not immediately apparent what is the precise physical implication of $Pe_s\langle\mathbf{p}\rangle_f(\mathbf{x},t)$ compared to $Pe_s\langle\mathbf{p}\rangle_g$ in (4.4) (c.f. Frankel & Brenner, 1991, 1993; Hill & Bees, 2002; Manela & Frankel, 2003). Therefore, it would be useful if there is an alternative form of (4.5), in which $\langle\mathbf{p}\rangle_f(\mathbf{x},t)$ can be replaced with $\langle\mathbf{p}\rangle_g(\mathbf{x},t)$ and the other related terms. More discussion on the comparison between $\langle\mathbf{p}\rangle_f$ and $\langle\mathbf{p}\rangle_g$ will follow in §4.8.1.

Multiplying (4.5) by $f(\mathbf{x},\mathbf{p},t)$ and subtracting it from (4.1) gives

$$\begin{aligned} n\,\partial_t f &+ (Pe_f\mathbf{u}\cdot\boldsymbol{\nabla}_{\mathbf{x}}f - D_T\nabla_x^2 f)n - 2D_T(\boldsymbol{\nabla}_{\mathbf{x}}f)\cdot(\boldsymbol{\nabla}_{\mathbf{x}}n) \\ &+ Pe_s(\mathbf{p}f - \langle\mathbf{p}\rangle_f f)\cdot\boldsymbol{\nabla}_{\mathbf{x}}n + Pe_s n(\mathbf{p}\cdot\boldsymbol{\nabla}_{\mathbf{x}}f - f\boldsymbol{\nabla}_{\mathbf{x}}\cdot\langle\mathbf{p}\rangle_f) \\ &+ n\mathcal{L}_p(\mathbf{x},t)f = 0, \end{aligned} \tag{4.7}$$

each term of which may be interpreted physically as described in table 4.1. Next, we introduce the following set of linear equations which use each term in (4.9) as the driving term:

$$\mathcal{L}_p(\mathbf{x},t)f_u(\mathbf{x},\mathbf{p},t) = Pe_f\mathbf{u}\cdot\boldsymbol{\nabla}_{\mathbf{x}}f, \tag{4.8a}$$

$$\mathcal{L}_p(\mathbf{x},t)f_{D_T}(\mathbf{x},\mathbf{p},t) = -D_T\nabla_x^2 f, \tag{4.8b}$$

$$\mathcal{L}_p(\mathbf{x},t)\mathbf{b}_{D_T}(\mathbf{x},\mathbf{p},t) = -2D_T\boldsymbol{\nabla}_{\mathbf{x}}f, \tag{4.8c}$$

$$\mathcal{L}_p(\mathbf{x},t)\mathbf{b}_c(\mathbf{x},\mathbf{p},t) = Pe_s(\mathbf{p} - \langle\mathbf{p}\rangle_f)f, \tag{4.8d}$$

$$\mathcal{L}_p(\mathbf{x},t)f_c(\mathbf{x},\mathbf{p},t) = Pe_s(\mathbf{p}\cdot\boldsymbol{\nabla}_{\mathbf{x}}f - f\boldsymbol{\nabla}_{\mathbf{x}}\cdot\langle\mathbf{p}\rangle_f), \tag{4.8e}$$

$$\mathcal{L}_p(\mathbf{x},t) f_{\partial t}(\mathbf{x},\mathbf{p},t) \;=\; \partial_t f. \tag{4.8f}$$

As a reminder, the $\mathbf{p}$-space operator $\mathcal{L}_p$ defined in (4.2) is the linear operator that defines the orientational flux due to taxes and viscous rotation by the locally linear flow field $\boldsymbol{\nabla}\mathbf{u}$. Here, the solutions $f_\star$ and $\mathbf{b}_\star$, with $(\cdot)_\star$ indicating any subscript above, are subjected to the integral condition $\int_{S_p} f_\star d^2\mathbf{p} = 0$ or $\int_{S_p} \mathbf{b}_\star d^2\mathbf{p} = \mathbf{0}$, so as not to contain the homogeneous solution. This enables us to define the solutions to (4.8) uniquely. Also, (4.8) is only integratable if the integration of the right-hand side of each equation in (4.8) over $\mathbf{p}$-space is zero due to the solvability condition in (4.3). The subtraction of (4.5) times f from (4.1) to get (4.7) ensures the solvability conditions are met in (4.8). Therefore, as long as the linear operator in $\mathbf{p}$-space $\mathcal{L}_p$ is continuous and fulfills the conditions in (4.3), the presented theorem will work.

Terms	Physical meaning
$n\,\partial_t f$	Unsteadiness of f in $\mathbf{p}$-space
$Pe_f n\mathbf{u}\cdot\boldsymbol{\nabla}_\mathbf{x} f$	Passive advection of f in $\mathbf{x}$ by the ambient flow $\mathbf{u}$
$-D_T(\nabla_x^2 f)n$	Translational diffusion of f in $\mathbf{x}$
$-2D_T(\boldsymbol{\nabla}_\mathbf{x} f)\cdot(\boldsymbol{\nabla}_\mathbf{x} n)$	Cross-translation diffusion in $\mathbf{x}$ between n and f
$Pe_s(\mathbf{p}f - \langle\mathbf{p}\rangle_f f)\cdot\boldsymbol{\nabla}_\mathbf{x} n$	Change in f induced by motility and gradient of particle distribution in $\mathbf{x}$
$Pe_s n(\mathbf{p}\cdot\boldsymbol{\nabla}_\mathbf{x} f - f\boldsymbol{\nabla}_\mathbf{x}\cdot\langle\mathbf{p}\rangle_f)$	Change in f induced by motility and inhomogeneity of f in $\mathbf{x}$

Table 4.1: Physical meaning of each term in equation (4.7)

Lastly, we note that the introduced variables are still functions of both $\mathbf{x}$ and t because $\mathcal{L}_p$ can have coefficients varying in $\mathbf{x}$ while f depends on both $\mathbf{x}$ and t. With the introduced variables, (4.7) can be rewritten as

$$[\mathcal{L}_p(\mathbf{b}_{D_T} + \mathbf{b}_c)]\cdot\boldsymbol{\nabla}_\mathbf{x} n + [\mathcal{L}_p(f_u + f_{D_T} + f_c + f_{\partial t} + f)]\, n = 0. \tag{4.9}$$

This leads to

$$[\mathbf{b}_{D_T} + \mathbf{b}_c]\cdot\boldsymbol{\nabla}_\mathbf{x} n + [f_u + f_{D_T} + f_c + f_{\partial t} + f]\, n = n\, g, \tag{4.10}$$

where the homogeneous solution $g(\mathbf{x},t;\mathbf{p})$, defined by

$$\mathcal{L}_p(\mathbf{x},t) g(\mathbf{x},t;\mathbf{p}) \;=\; 0 \quad \text{subject to} \tag{4.11a}$$

$$\int_{S_p} g(\mathbf{x},t;\mathbf{p}) d^2\mathbf{p} \;=\; 1, \tag{4.11b}$$

is added after multiplying $n(\mathbf{x},t)$, which can be obtained by integrating (4.10) over $\mathbf{p}$-space. Here, (4.11a) share the same formula for g as the orientional space Fokker-Planck equation (1.21) used in model F and model G. Despite the same formula and value, the g in model F and in this transformation

Terms	Physical meaning
$\langle \mathbf{p} \rangle_g$	Averaged motility of individual particle from the homogeneous solution of $\mathcal{L}_p$
$\mathbf{V}_{\partial t}$	Drift due to interaction between particles' orientational dynamics and the unsteadiness of f in $\mathbf{p}$-space
$\mathbf{V}_u$	Drift due to interaction between particles' orientational dynamics and passive advection of f in $\mathbf{x}$ by the flow field $\mathbf{u}$
$\mathbf{V}_c$	Drift due to interaction between particles' motility and the inhomogeneity of particles' orientational dynamics in $\mathbf{x}$
$\mathbf{V}_{D_T}$	Drift due to interaction between particles' orientational dynamics and translational diffusion of f in $\mathbf{x}$
$\boldsymbol{D}_{D_T}$	Dispersion from interaction between particles' orientational dynamics and the dispersion of n and f due to translational diffusion of f and n
$\boldsymbol{D}_c$	Dispersion due to interaction between particles' motility and orientational dynamics

Table 4.2: Physical meaning of each derived term in equation (4.15)

has a slightly different physical interpretation. In the context of model F, it represents the quasi-steady orientational p.d.f. at each local position in $\mathbf{x}$. Here, $g(\mathbf{x}, t; \mathbf{p})$ should be interpretted as the homogeneous solution of the operator $\mathcal{L}_p$, which is an artefact of the integration step (4.10). The exactness of g in this step contrasts the model F's interpretation of g as a quasi-steady approximation. Alternatively, g can also be interpretted the same way as model G, in which g is the Langrangian orientational p.d.f. of each particle in a homogeneous flow with the same velocity gradient as the local flow.

Note that (4.10) is merely a different form of (4.7). Still, it is a significant transformation for the next step. Multiplying $\mathbf{p}$ by (4.10) and integrating in $\mathbf{p}$-space then yields

$$(\boldsymbol{D}_{D_T} + \boldsymbol{D}_c) \cdot \boldsymbol{\nabla}_{\mathbf{x}} n + [\mathbf{V}_u + \mathbf{V}_{D_T} + \mathbf{V}_c + \mathbf{V}_{\partial t} + \langle \mathbf{p} \rangle_f] \, n = n \langle \mathbf{p} \rangle_g, \tag{4.12}$$

where

$$\mathbf{V}_\star(\mathbf{x}, t) = \int_{S_p} \mathbf{p} f_\star(\mathbf{x}, \mathbf{p}, t) d^2\mathbf{p}, \tag{4.13}$$

$$\boldsymbol{D}_\star(\mathbf{x}, t) = \int_{S_p} \mathbf{p}\mathbf{b}_\star(\mathbf{x}, \mathbf{p}, t) d^2\mathbf{p} \tag{4.14}$$

with $(\cdot)_\star$ indicating any of the subscripts used in (4.8). Now, it is important to note that this step is the equivalent of taking the first-order orientational moment of (4.10). Some may interpret it as just another way of taking the orientational moment of eq. (4.1) to get the evolution equation of the polar order $\langle p \rangle_f$ (c.f. Saintillan & Shelley, 2015, eq. 9.9). However, the key contribution of this work is that we have first taken the step from (4.9) to (4.10) before taking the orientational moment. As we

shall show in the next step, the resulting equation does not involve the higher moments, such as the nematic order. In this way, we have avoided the closure problem inherent in the evolution equations of the polar and nematic orders.

Lastly, replacing $n\langle\mathbf{p}\rangle_f$ in (4.5) with that of (4.12) leads to the following transport equation:

$$\begin{aligned} & \partial_t n + \boldsymbol{\nabla}_{\mathbf{x}} \cdot [(Pe_f \mathbf{u} + Pe_s(\langle\mathbf{p}\rangle_g - \mathbf{V}_u - \mathbf{V}_{D_T} - \mathbf{V}_c - \mathbf{V}_{\partial t}))n] \\ = \;& D_T \nabla_x^2 n + Pe_s \boldsymbol{\nabla}_{\mathbf{x}} \cdot (\boldsymbol{D}_{D_T} + \boldsymbol{D}_c) \cdot \boldsymbol{\nabla}_{\mathbf{x}} n. \end{aligned} \tag{4.15}$$

The important benefit of (4.15) is that it has a mathematical structure comparable to (4.4) of model G, as they share $Pe_s\langle\mathbf{p}\rangle_g$, which represents the average motility of individual particles. Furthermore, this is an exact transport equation directly obtained from (4.1) without making any assumptions. However, it should be mentioned that (4.15) is not the only transport equation one can obtain from (4.1) – indeed, we have already retrieved a different form of transport equation from (4.1) that is (4.5). This is essentially the consequence of taking the orientational moment from (4.10) to (4.12), which reduces the dimensionality of the derived equation. Similar to how the evolution equations of the polar and nematic orders were derived from the tensor harmonic expansion of (4.1) (c.f. Saintillan & Shelley, 2015, eqs 9.6-9.10), one can take any higher-order tensor harmonic expansion of (4.10) to get an equivalent of (4.12) for a higher-order moment. (The infinite expansion form a complete basis.) Alternatively, instead of the higher-order moments, one can also use some truncated basis of the $\mathbf{p}$-space (e.g. spherical harmonics) in place of $\mathbf{p}$ to form another set of equations. These equations can then be summed with (4.5) to arrive at some transport equations too. However, the particular choice $\mathbf{p}$ as the multiplication factor for this step is probably the most physically relevant because the resulting expression in (4.12) decomposes $\langle\mathbf{p}\rangle_f$ in (4.5) into the averaged motility of individual particle $Pe_s\langle\mathbf{p}\rangle_g$ and the other terms from (4.1). Hence, each term in (4.15) would also admit a physical implication, as listed in table 4.2. More importantly, later in §4.5.2, we will further show how $\langle\mathbf{p}\rangle_g$ and $\boldsymbol{D}_c$ in (4.15) can be related to the effective drift and diffusivity of model G. Lastly, it is also important to note that $\boldsymbol{D}_{D_T}$ and $\boldsymbol{D}_c$ in (4.15) do not necessarily describe a diffusion process, as they are not guaranteed to be either symmetric or positive definite. Therefore, one should be careful in understanding their actual roles, and, in this sense, (4.15) cannot precisely be referred to as an advection-diffusion equation. More discussions on this issue will follow in §4.5.2 and §4.8.2.

4.5 A new transport equation model using local flow information

While the transport equation in (4.15) is obtained without applying any approximation to (4.1), the formulae for $\mathbf{V}_\star$ and $\boldsymbol{D}_\star$ given in (4.8) are based on $f = \Psi/n$, requiring the full knowledge of Ψ (i.e. the solution to (4.1)). Therefore, the transformation discussed in §4.4 does not alleviate the difficulty related to the computational cost of the full Smouchowski equation (4.1). To resolve this issue, in this section, we will combine the transformation technique leading to (4.12) with a multiple time-scale asymptotic analysis. This results in an approximated form of (4.15) utilising only the local flow information (i.e. a local approximation).

4.5.1 Local approximation of the transformed transport equation

First, we assume $Pe_s(\equiv \epsilon) \ll 1$, $Pe_f \lesssim O(\epsilon)$ and $D_T \lesssim O(\epsilon)$, and define $\tilde{Pe}_f = Pe_f/\epsilon$ and $\tilde{D}_T = D_T/\epsilon$. Physically, these assumptions imply that the timescale in the orientational $\mathbf{p}$-space is much faster than that in $\mathbf{x}$-space (i.e. a quasi-steady assumption). Hence, the orientational component of Ψ (i.e. $f(\mathbf{x}, \mathbf{p}, t)$) will first relax to a quasi-equilibrium in $\mathbf{p}$-space while the $\mathbf{x}$-dependency of Ψ is still evolving slowly. This then enables us to introduce a slowly-varying time scale $T = \epsilon t$ for the dynamics of Ψ in $\mathbf{x}$-space.

The assumptions of this local approximation are most valid in phenomena such as gyrotactic focusing and bioconvection, where h^*/V_c^*, the time it takes for swimmers to swim across the container width or characteristic length, is longer than the orientation timescale $1/d_r^*$, and the flow speed is comparable to the swimming speed. For example, the parameters used to model the gyrotactic plume formation in chapter 2 give $h^*/V_c^* = 30.15$ and $1/d_r^* = 14.93$, while the flow rate was chosen such that the flow speed is comparable to the swimming speed. The approximation would be more accurate if the characteristic length is wider (e.g. bioconvection in chapter 3).

The standard multiple-scale asymptotic analysis is subsequently applied by expanding $\Psi = \Psi^{(0)} + \epsilon\Psi^{(1)} + \epsilon^2\Psi^{(2)} + O(\epsilon^3)$. We substitute the expansion into the Smoluchowski equation (4.1) and yield the following set of equations at successive orders of ϵ:

$$\mathcal{O}(1) \quad : \quad \partial_t \Psi^{(0)} + \mathcal{L}_p \Psi^{(0)} = 0; \tag{4.16a}$$

$$\mathcal{O}(\epsilon) \quad : \quad \partial_T \Psi^{(0)} + \mathbf{p} \cdot \boldsymbol{\nabla}_\mathbf{x} \Psi^{(0)} + \tilde{Pe}_f \mathbf{u} \cdot \boldsymbol{\nabla}_\mathbf{x} \Psi^{(0)} + \partial_t \Psi^{(1)} + \mathcal{L}_p \Psi^{(1)} = \tilde{D}_T \nabla_x^2 \Psi^{(0)}; \tag{4.16b}$$

$$\mathcal{O}(\epsilon^2) \quad : \quad \partial_T \Psi^{(1)} + \mathbf{p}\cdot\boldsymbol{\nabla}_{\mathbf{x}}\Psi^{(1)} + \tilde{Pe}_f \mathbf{u}\cdot\boldsymbol{\nabla}_{\mathbf{x}}\Psi^{(1)} + \partial_t \Psi^{(2)} + \mathcal{L}_p \Psi^{(2)} = \tilde{D}_T \nabla_x^2 \Psi^{(1)}; \text{etc..} \quad (4.16c)$$

Integrating over $\mathbf{p}$-space, (4.16) becomes:

$$\mathcal{O}(1) \quad : \quad \partial_t n^{(0)} = 0; \quad (4.17a)$$

$$\mathcal{O}(\epsilon) \quad : \quad \partial_T n^{(0)} + \partial_t n^{(1)} + \boldsymbol{\nabla}_{\mathbf{x}}\cdot\left[(\tilde{Pe}_f \mathbf{u} + \langle\mathbf{p}\rangle^{(0)})n^{(0)}\right] = \tilde{D}_T \nabla_x^2 n^{(0)}; \quad (4.17b)$$

$$\mathcal{O}(\epsilon^2) \quad : \quad \partial_T n^{(1)} + \partial_t n^{(2)} + \boldsymbol{\nabla}_{\mathbf{x}}\cdot\left[(\tilde{Pe}_f \mathbf{u} + \langle\mathbf{p}\rangle^{(1)})n^{(1)}\right] = \tilde{D}_T \nabla_x^2 n^{(1)}; \text{etc..} \quad (4.17c)$$

At the transient time $t \gtrsim \mathcal{O}(1)$ and each order of ϵ, we assume the time dependency of $\Psi^{(i)}$ in $\mathbf{p}$-space has reached quasi-equilibrium, while the time dependency of $\Psi^{(i)}$ in $\mathbf{x}$-space is slow. In other words, we assume that, at each order, $f^{(i)}$ is independent of t as it has reached quasi-equilibrium and $n^{(i)}$ independent of t because it only varies at the slow time scale T. Therefore, equation (4.16a) now becomes

$$\mathcal{L}_p f^{(0)} = 0, \quad (4.18)$$

which implies that the leading order orientational distribution $f^{(0)}$ takes the homogeneous solution of $\mathcal{L}_p(\mathbf{x}, t)$ as the solution, i.e. $f^{(0)} = g(\mathbf{x}, T; \mathbf{p})$.

Following a similar transformation to that in §4.4, we multiply (4.17b) by $f^{(0)}$ and subtract it from (4.16b). The subtraction is particularly important for biased ABPs compared to their non-biased counterpart, as it guarantees the solvability condition in (4.3). This operation is equivalent to the steps towards (4.7) in §4.4. The operation yields

$$\begin{aligned} & n^{(0)}\partial_T f^{(0)} \\ + \; & (\tilde{Pe}_f \mathbf{u}\cdot\boldsymbol{\nabla}_{\mathbf{x}} f^{(0)} - \tilde{D}_T \nabla_x^2 f^{(0)})n^{(0)} - 2D_T(\boldsymbol{\nabla}_{\mathbf{x}} f^{(0)})\cdot(\boldsymbol{\nabla}_{\mathbf{x}} n^{(0)}) \\ + \; & (\mathbf{p} - \langle\mathbf{p}\rangle^{(0)})f^{(0)}\cdot\boldsymbol{\nabla}_{\mathbf{x}} n^{(0)} + n^{(0)}(\mathbf{p}\cdot\boldsymbol{\nabla}_{\mathbf{x}} f^{(0)} - f^{(0)}\boldsymbol{\nabla}_{\mathbf{x}}\cdot\langle\mathbf{p}\rangle^{(0)}) \\ + \; & n^{(1)}\mathcal{L}_p f^{(1)} = 0. \end{aligned} \quad (4.19)$$

Now, (4.19) can be rewritten as

$$[\mathcal{L}_p(\mathbf{b}_{g,D_T} + \mathbf{b}_{g,c})]\cdot\boldsymbol{\nabla}_{\mathbf{x}} n^{(0)} + n^{(0)}\mathcal{L}_p\left[f_{g,u} + f_{g,D_T} + f_{g,c} + f_{g,\partial T}\right] + n^{(1)}\mathcal{L}_p f^{(1)} = 0, \quad (4.20)$$

where $f_{g,\star}$ and $\mathbf{b}_{g,\star}$ are defined by

$$\begin{aligned}
\mathcal{L}_p(\mathbf{x},T)f_{g,u}(\mathbf{x},T;\mathbf{p}) &= \tilde{P}e_f\mathbf{u}\cdot\boldsymbol{\nabla}_{\mathbf{x}}f^{(0)}, && (4.21a)\\
\mathcal{L}_p(\mathbf{x},T)f_{g,D_T}(\mathbf{x},T;\mathbf{p}) &= -\tilde{D}_T\nabla_x^2 f^{(0)}, && (4.21b)\\
\mathcal{L}_p(\mathbf{x},T)\mathbf{b}_{g,D_T}(\mathbf{x},T;\mathbf{p}) &= -2\tilde{D}_T\boldsymbol{\nabla}_{\mathbf{x}}f^{(0)}, && (4.21c)\\
\mathcal{L}_p(\mathbf{x},T)\mathbf{b}_{g,c}(\mathbf{x},T;\mathbf{p}) &= (\mathbf{p}-\langle\mathbf{p}\rangle_g)f^{(0)}, && (4.21d)\\
\mathcal{L}_p(\mathbf{x},T)f_{g,c}(\mathbf{x},T;\mathbf{p}) &= (\mathbf{p}\cdot\boldsymbol{\nabla}_{\mathbf{x}}f^{(0)} - f^{(0)}\boldsymbol{\nabla}_{\mathbf{x}}\cdot\langle\mathbf{p}\rangle_g). && (4.21e)\\
\mathcal{L}_p(\mathbf{x},T)f_{g,\partial T}(\mathbf{x},T;\mathbf{p}) &= \partial_T f^{(0)}, && (4.21f)
\end{aligned}$$

where all $f_{g,\star}$ and $\mathbf{b}_{g,\star}$ are subjected to the integral condition $\int_{S_p} d^2\mathbf{p} = 0$.

Equations (4.21) and (4.20) and are the equivalent of (4.8) and (4.9) respectively. We can then follow the same derivation as §4.4, which would lead to

$$\begin{aligned}
&\partial_T n^{(1)} + \boldsymbol{\nabla}_{\mathbf{x}}\cdot\left[(\langle\mathbf{p}\rangle_g + \tilde{P}e_f\mathbf{u})n^{(1)}\right]\\
&= \tilde{D}_T\nabla_x^2 n^{(1)} + \boldsymbol{\nabla}_{\mathbf{x}}\cdot\left[(\boldsymbol{D}_{g,c}+\boldsymbol{D}_{g,D_T})\boldsymbol{\nabla}_{\mathbf{x}}n^{(0)} + (\mathbf{V}_{g,u}+\mathbf{V}_{g,D_T}+\mathbf{V}_{g,c}+\mathbf{V}_{g,\partial T})n^{(0)}\right], \qquad (4.22)
\end{aligned}$$

where $\mathbf{V}_{g,\star}$ and $\boldsymbol{D}_{g,\star}$ are defined according to (4.13-4.14).

The subscript g signifies that they are approximated using $f^{(0)} = g$ in (4.21). However, in (4.21), we have used $f^{(0)}$ instead of g on the right-hand side to highlight their different physical interpretation. Although they share the same value, in the context of (4.18) and this asymptotic, $f^{(0)}$ is the quasi-steady orientational p.d.f. at each location $\mathbf{x}$, which has the same physical interpretation as the g of (1.21) in model F. In (4.21), the p.d.f. $f^{(0)}$, as an approximation of f, is used to formulate $\mathbf{V}_{g,\star}$ and $\boldsymbol{D}_{g,\star}$. However, as mentioned in the previous section, g and $\langle\mathbf{p}\rangle_g$ arise from the homogeneous solution of $\mathcal{L}_p$. The term arises from an exact integration of $\mathcal{L}_p$, not as an approximation of f. With the swimming speed Pe_s, the term $Pe_s\langle\mathbf{p}\rangle_g$ can also be interpreted as the average motility of individual particles. Model G obtained the same $Pe_s\langle\mathbf{p}\rangle_g$ in the Langrangian framework and gave $Pe_s\langle\mathbf{p}\rangle_g$ a similar interpretation as the current model. More discussion on this matter will follow in §4.8.1. To conclude, $\mathbf{V}_{g,\star}$ and $\boldsymbol{D}_{g,\star}$ arise from the quasi-steady approximation $f^{(0)}$, whereas $\langle\mathbf{p}\rangle_g$ arises from the exact homogeneous solution of $\mathcal{L}_p$.

Now, equation (4.22) is at $\mathcal{O}(\epsilon^2)$. If we are to recover how n evolve over the long time T, we can recompose $\partial_T n = \partial_T n^{(0)} + \epsilon\partial_T n^{(1)} + ...$, by summing up (4.17a-4.17c) with the corresponding ϵ scaling

while substituting (4.17c) with (4.22). Hence,

$$\begin{aligned} &Pe_s\partial_T n + \boldsymbol{\nabla}_{\mathbf{x}} \cdot [(Pe_s\langle \mathbf{p}\rangle_g + Pe_f\mathbf{u})n] \\ &\approx D_T\nabla_x^2 n + Pe_s^2\boldsymbol{\nabla}_{\mathbf{x}} \cdot \left[(\boldsymbol{D}_{g,c} + \boldsymbol{D}_{g,D_T})\boldsymbol{\nabla}_{\mathbf{x}} n^{(0)} + (\mathbf{V}_{g,u} + \mathbf{V}_{g,D_T} + \mathbf{V}_{g,c} + \mathbf{V}_{g,\partial T})n^{(0)}\right]. \end{aligned} \tag{4.23}$$

Note that we have only included $n^{(0)}$ and $n^{(1)}$ when recomposing n in this example as we are closing the problem at $\mathcal{O}(\epsilon^2)$. Therefore, (4.23) is accurate up to $\mathcal{O}(\epsilon^2)$. However, if we close the problem at a higher order, we can repeat a similar process from (4.19) to (4.22) at a higher order.

Here, we would argue that at the transient time $t \to \infty$, $\partial_t \approx Pe_s\partial_T$ and $n \approx n^{(0)}$. Because (4.23) is accurate up to $\mathcal{O}(\epsilon^2)$ while replacing $Pe_s^2 n^{(0)}$ with $Pe_s^2 n$ would only introduce an error at $\mathcal{O}(\epsilon^3)$, the substitution of $n^{(0)}$ by n shall not impact the accuracy of (4.23) tremendously. Under these approximations, we derive the approximated equation

$$\begin{aligned} \partial_t n \quad &+\boldsymbol{\nabla}_{\mathbf{x}} \cdot \left[Pe_s\left(\langle \mathbf{p}\rangle_g + \tilde{Pe}_f\mathbf{u}\right)n - Pe_s^2\left(\mathbf{V}_{g,u} + \mathbf{V}_{g,D_T} + \mathbf{V}_{g,c} + \mathbf{V}_{g,\partial T}\right)n\right] \\ &\approx Pe_s\tilde{D}_T\nabla_x^2 n + Pe_s^2\boldsymbol{\nabla}_{\mathbf{x}} \cdot [(\boldsymbol{D}_{g,c} + \boldsymbol{D}_{g,D_T})\boldsymbol{\nabla}_{\mathbf{x}} n] \end{aligned} \tag{4.24}$$

for the transport of $n(\mathbf{x}, t)$, where the drifts and dispersion coefficients are defined by (4.13-4.14) and (4.21).

The approximated transport equation (4.24) is identical to (4.15), except that their coefficients in (4.21) are now obtained by replacing f in (4.8) with g in (4.11a). This is a crucial advantage of (4.24) over (4.15) because g in (4.11a) can be solved pointwise at each $\mathbf{x}$ if the local flow information (i.e. $\boldsymbol{\Omega}$ and $\boldsymbol{E}$) is known. Therefore, (4.24) no longer requires the full solution to (4.1).

Here, the derivation above is similar to that of Bearon & Hazel (2015) and Vennamneni *et al.* (2020). However, in deriving (4.24), we have assumed $T = \epsilon t$. This time-scale separation is different from $T = \epsilon^2 t$ of Bearon & Hazel (2015) and Vennamneni *et al.* (2020). We note that the $\mathbf{V}_{g,\star}$ and $\boldsymbol{D}_{g,\star}$ terms in (4.24) scale with Pe_s^2, while the rest of the equation scales with Pe_s. Therefore, the effect of these terms appears only at $O(\epsilon^2)$, while the rest of the terms are still non-zero at $O(\epsilon)$. This contrasts with the non-biased ABPs suspensions considered in Bearon & Hazel (2015) and Vennamneni *et al.* (2020). In their cases, the translational diffusion was negligible ($D_T = 0$), the averaged orientation of individual particles was not biased ($\langle \mathbf{p}\rangle_g = \mathbf{0}$), and the flow was parallel such that $\mathbf{u} \cdot \boldsymbol{\nabla}_{\mathbf{x}} = 0$. Hence, if $T = \epsilon t$ was assumed, the equation at $O(\epsilon)$ would simply be degenerate. However, as an

extension from the non-biased ABPs, the equation at $O(\epsilon)$ becomes non-degenerate when biased motility (i.e. taxes) is included. In general, there is no reason that the leading-order equation has to have such a trivial solution in the presence of taxes, translational diffusion, or a non-parallel flow field. Therefore, these leading order effects require us to retain the scaling $T = \epsilon t$.

4.5.2 Comparison with model G

Model G was derived semi-heuristically by evaluating an effective drift and diffusion coefficient using the Oldroyd time derivative of first and second statistical moments of particle displacement (Frankel & Brenner, 1991, 1993). In contrast, the local approximation model in (4.24) was directly derived from the Smoluchowski equation (4.1). Despite the fundamentally different derivation procedures, (4.4) of model G and (4.24) of the local approximation model in this study share a lot in common. Apart from the same flow advection ($Pe_f\mathbf{u}$) and diffusion (D_T) terms, they share the same individual particles' motility $Pe_s\langle\mathbf{p}\rangle_g$ and have a similar form of effective diffusivity $\boldsymbol{D}_G$ and dispersion $\boldsymbol{D}_{g,c}$. In particular, the two models become identical for stationary non-diffusive ($Pe_f = D_T = 0$) suspensions, as will be shown below. These similarities suggest that the transformed equation (4.15) and its local approximation (4.24) are not only mathematically useful but also physically meaningful. In this subsection, we will make a detailed comparison between model G and the local approximation model from a theoretical perspective. Further comparisons will follow in §4.6 with some flowing examples.

1. *Assumptions*: Both model G and the local approximation model assume that the time scale in $\mathbf{p}$-space is much faster than that of $\mathbf{x}$-space (i.e. quasi-steady assumption). As a result, the intrinsic orientational dynamics of the particles in $\mathbf{p}$-space is not captured by either model, and the unsteadiness in these models are driven by the unsteady flow dynamics typically at a much larger time scale. However, unlike model G, the local approximation model does not assume local homogeneity in the background velocity gradient. As such, we shall see that this model has an important advantage over model G (see point (ii) and discussion in §4.7.1).

2. *Drift*: Compared to the drift term $Pe_s\langle\mathbf{p}\rangle_g$ in model G, the local approximation model contains extra drift terms, $-\mathbf{V}_{g,c}$, $-\mathbf{V}_{g,u}$, $-\mathbf{V}_{g,D_T}$ and $-\mathbf{V}_{g,\partial T}$. They originate from the transformation in §4.4. As described in table 4.2, these terms arise from the complicated interactions between particles' orientational dynamics and the particles' motility, the advection by the surrounding shear flow, the diffusion of particles and the unsteadiness of the prescribed flow field. Since $Pe_s = \epsilon$ in the local approximation, (4.24) suggests that these terms would be relatively less

important than the drift term $Pe_s\langle\mathbf{p}\rangle_g$. In this case, the drift term used in model G remains a good approximation. However, if $\langle\mathbf{p}\rangle_g \lesssim O(Pe_s)$, the drifts caused by these extra terms will become important. In §4.7.1, we shall demonstrate that such a case does happen in a parallel shear flow, especially through $\mathbf{V}_{g,c}$.

3. *Diffusion and dispersion*: Further to the given translation diffusion term with the diffusivity $Pe_s\tilde{D}_T(=D_T)$, the local approximation model in (4.24) exhibits the extra terms with the coefficients $\boldsymbol{D}_{g,c}$ and $\boldsymbol{D}_{D_T}$, which originates from the particles' motility and translational diffusion respectively (see table 4.2). The dispersion $\boldsymbol{D}_{g,c}$ is obtained from (4.21d), which only differs from (1.25a) of model G by the extra $\mathbf{b}_{GTD}\cdot\boldsymbol{G}$ term, while (1.25b) from GTD differs from (4.14) by the extra $\mathbf{b}_{GTD}\mathbf{b}_{GTD}\cdot\boldsymbol{G}/g$ term and the enforcement of symmetry. These differences are a consequence of extending the original GTD theory in a quiescent flow (Frankel & Brenner, 1989) to a shear flow (Frankel & Brenner, 1991, 1993). Therefore, the local approximation model shares the same formulae as the original GTD model in a quiescent flow but differs from model G when extended to a homogeneous shear flow. Another important difference between model G and the local approximation model is that model G does not have an equivalent $\boldsymbol{D}_{D_T}$ term. In GTD, D_T was superposed, but the interaction between D_T and the particles' motility was not considered, unlike the local approximation. Lastly, it should be stressed that there is no reason to enforce symmetry in $\boldsymbol{D}_{g,c}$ and $\boldsymbol{D}_{D_T}$ in the local approximation model, as they are directly derived by approximating the Smoluchowski equation (4.1). As such, the related processes are not necessarily diffusion. A more detailed discussion on the matter will follow in §4.8.2.

4. *Stationary and uniformly sheared suspensions*: While we have contrasted the two models, there are special cases where they show strong similarities. Firstly, if the suspension is quiescent with negligibly small translational diffusivity D_T, model G and the local approximation model are identical. Indeed, in this case, $\mathbf{V}_{g,\star}=0$, $\boldsymbol{D}_{g,D_T}=0$ and $\boldsymbol{D}_{g,c}=\boldsymbol{D}_G$ in (4.24), confirming the physical relevance of the local approximation model proposed in this chapter. Secondly, if the suspension is immersed into a uniform parallel shear flow with negligible D_T, the only difference at the steady-state is between $\boldsymbol{D}_{g,c}$ and $\boldsymbol{D}_G$. More specifically, the difference arises from the extra $\mathbf{b}_{GTD}\cdot\boldsymbol{G}$ in (2.2j) and $\mathbf{b}_{GTD}\mathbf{b}_{GTD}\cdot\boldsymbol{G}/g$ in (2.2i). Therefore, by the zero components in $\boldsymbol{G}$, the cross-stream direction component in the tensors $\boldsymbol{D}_{g,c}$ and $\boldsymbol{D}_G$ would be equal in a uniform parallel shear flow. However, as discussed in §4.3, the $\mathbf{b}_{GTD}\cdot\boldsymbol{G}$ term in (2.2j) can cause a singularity in $\boldsymbol{D}_G$ if $\mathbb{R}(\mathrm{eig}(\boldsymbol{G}))>0$. (In a parallel shear flow, the singularity does not arise because $\mathbb{R}(\mathrm{eig}(\boldsymbol{G}))=0$.) If the flow is straining-dominant, like the flow near a stagnation point (Bearon *et al.*, 2011), then $\boldsymbol{D}_G$ might become singular. By contrast, the local approximation

does not have this term for $\boldsymbol{D}_{g,c}$ in (4.21d). Therefore, as long as the orientational dynamics operator $\mathcal{L}_p$ is mathematically well-posed, the local approximation model does not suffer from this issue, offering a significant practical advantage over model G. In the following section, we shall make a more detailed comparison considering a couple of parallel flow examples.

4.6 Flow examples

Now, we will test the accuracy of the local approximation model proposed in §4.5. To this end, we will numerically solve the transport equation for the particle distribution from the local approximation model and model G, and their predictions will then be compared with the full analytical and numerical solution to the Smoluchowski equation (4.1). In line with the subject of this thesis, we will consider the suspension of bottom-heavy motile (i.e. gyrotactic) micro-organisms in a one-dimensional parallel shear flow.

4.6.1 Numerical method

Our numerical method is loosely based on the `Spherefun` package (Townsend *et al.*, 2016), which utilises the double Fourier sphere (DFS) method to represent the spherical space $\mathbf{p}$. The method transforms the longitude and latitude coordinates $(\lambda, \theta) \in [-\pi, \pi] \times [0, \pi]$ into two independent Fourier space variables. Here, we follow the definition of Townsend *et al.* (2016, p. C405) and define λ and θ such that each component of $\mathbf{p} = [p_x, p_y, p_z]^T$ can be written as

$$p_x = \cos\lambda \sin\theta, \qquad p_y = \sin\lambda \sin\theta, \qquad p_z = \cos\theta. \tag{4.25}$$

Periodicity in the spherical space was maintained by enforcing the reflectional symmetry in its transformed coefficients (see Townsend *et al.*, 2016, p. C406). The $\boldsymbol{\nabla}_{\mathbf{p}} \cdot [\dot{\mathbf{p}}\Psi]$ operation and the $\mathbf{p}$-dependent part of the $\boldsymbol{\nabla}_{\mathbf{x}} \cdot [\dot{\mathbf{x}}\Psi]$ operation in (4.1) were completely implemented in the spectral space. Meanwhile, based on the parallel assumption in the physical space $\mathbf{x}$, we have discretised the cross-stream direction (x or z, depending on the prescribed flow field) by a 6th order central difference scheme with an equispaced grid. Time integration was conducted semi-implicitly, in which the $\nabla^2_{\mathbf{p}}$ term was advanced with a second-order Crank-Nicolson method while the rest are marched with a third-order Runge-Kutta method. The matrix inversion arising in the Crank-Nicolson method was solved using the algorithm for the Helmholtz equation in the `Spherefun` package. For simplicity,

we have implemented a periodic boundary condition in the cross-stream direction. The method was validated by comparing the **p**-space results with the solver developed in §2.3 and with the analytical solution of the following example.

Since the numerical solutions of the Smoluchowski equation are compared with the steady results from model G and the local approximation, we have also computed the drifts and effective dispersion from the local approximation (4.21) by directly inverting the linear $\mathcal{L}_{\mathbf{p}}$ operator in spectral space. Meanwhile, model G's drifts and effective diffusivities were taken from the numerical methods developed for the previous chapters. We have also implemented the DFS method for model G. The drifts and effective diffusivities from the DFS method show negligible differences from that of the finite difference method described in §2.3, which acts as a validation for the current method. The resulting drifts and effective diffusivities/dispersions are then used in the transport equation to solve the steady solution of n (see (4.30-4.32)) by direct inversion in the discretised **x**-space.

4.7 A suspension of gyrotactic active particles in a prescribed vertical flow

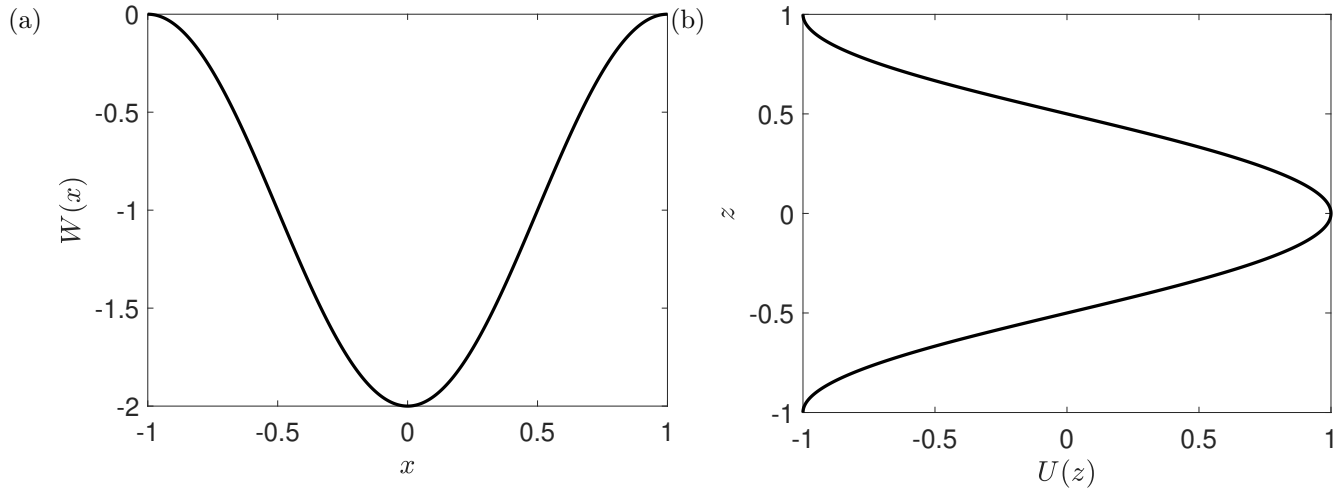

Figure 4.1: The prescribed flow profile for the examples in (a) §4.7 and (b) §4.7.4. In (a), the vertical flow is $W(x) = -\cos(\pi x) - 1$. In (b), the horizontal flow is $U(z) = \cos(\pi z)$.

In line with the theme of the thesis, we will revisit the formation of the gyrotactic plume in this example. However, we will not consider how the particles may alter the flow via buoyancy or hydrodynamic interactions for simplicity. Also, we will only consider the two-dimensional channel flow case instead of the cylindrical pipe considered in the previous chapters. We will apply a prescribed parallel shear flow $\mathbf{u}(\mathbf{x}) = [0, 0, W(x)]^T$ to the suspension.

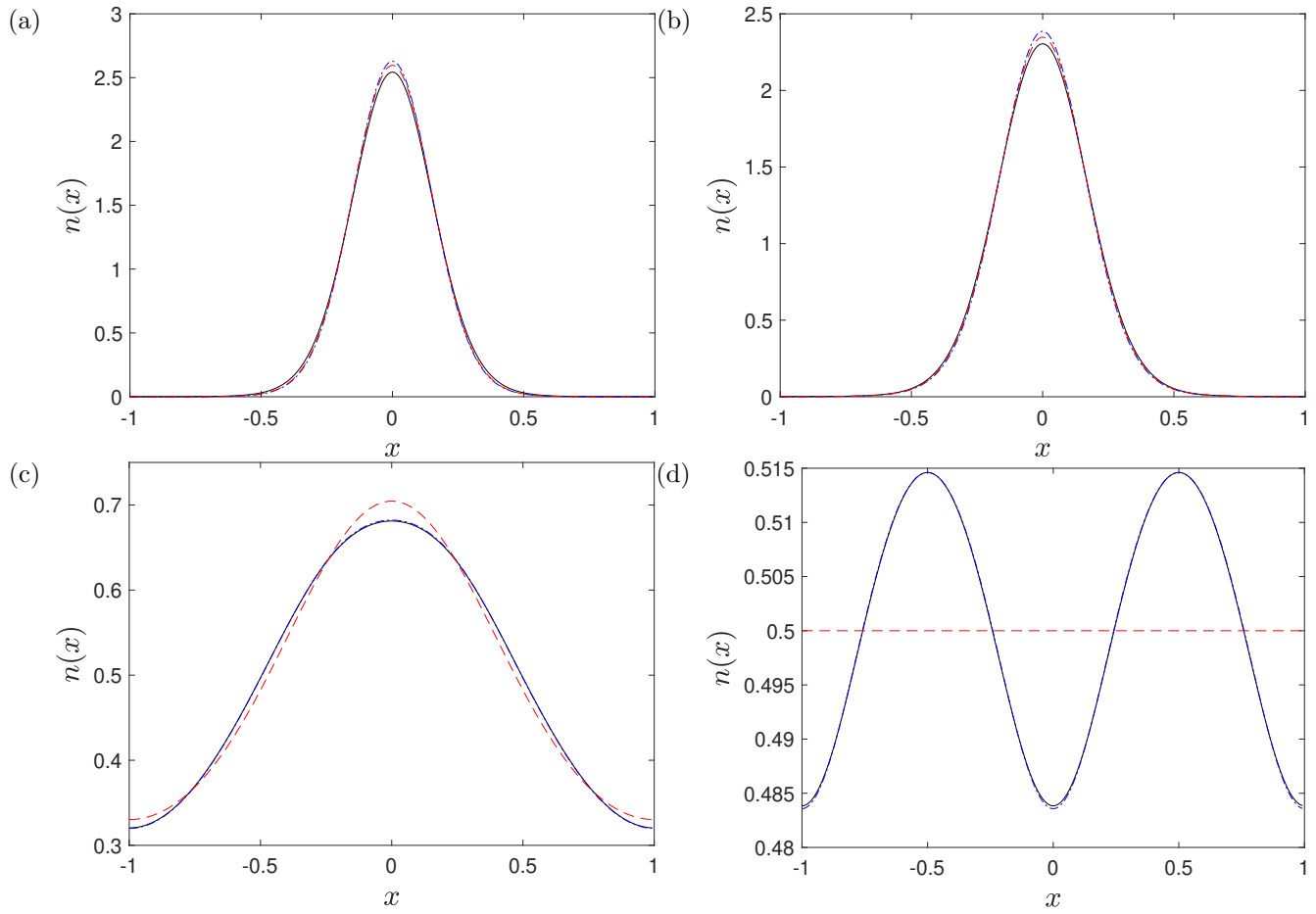

Figure 4.2: Comparison of the steady-state particle distributions given by the direct integration of (4.1) (black solid line, $n_{f,s}$), the local approximation model of §4.5 (blue dot-dashed line, $n_{g,s}$) and model G (red dashed line, n_{GTD}) of suspensions of (a) spherical and strongly gyrotactic ($\beta = 2.2$, $\alpha_0 = 0$), (b) non-spherical and strongly gyrotactic ($\beta = 2.2$, $\alpha_0 = 0.31$), (c) non-spherical and weakly gyrotactic ($\beta = 0.21$, $\alpha_0 = 0.31$) and (d) non-spherical and non-gyrotactic ($\beta = 0$, $\alpha_0 = 0.31$) particles. The suspensions are subjected to a vertical flow $W(x) = -\cos(\pi x) - 1$ with $Pe_s = 0.25$ and $Pe_f = 1$. Note that the vertical scale for $n(x)$ in (c, d) is much smaller than that in (a, b).

Four types of idealised motile micro-organisms are considered: a strongly gyrotactic and spherical particle ($\beta = 2.2$, $\alpha_0 = 0$), a strongly gyrotactic but non-spherical particle ($\beta = 2.2$, $\alpha_0 = 0.31$), a weakly gyrotactic non-spherical particle ($\beta = 0.21$, $\alpha_0 = 0.31$) and non-gyrotactic and non-spherical particle ($\beta = 0$, $\alpha_0 = 0.31$). The parameters $\beta = 2.2$ and $\alpha_0 = 0.31$ for the strongly gyrotactic particle is based on *Chlamydomonas augustae* (Pedley & Kessler, 1990; Croze *et al.*, 2010), while the gyrotactic parameter $\beta = 0.21$ for the weakly gyrotactic particle is based on *Dunaliella salina* (Croze *et al.*, 2017). Since we cannot find any experimental value of α_0 for *D. salina*, we will assume the weakly gyrotactic particle shares the same value of $\alpha_0 = 0.31$ for comparisons. Lastly, we have also considered a suspension of non-spherical and non-gyrotactic particles for completeness.

In the following subsections, we will first assume that the gyrotactic particle undergoes no translational diffusion and that the dilute suspension is well described by (4.1) with $D_T = 0$. Later, we will add

translational diffusion (i.e. finite D_T) to the particles to show the extra drift and dispersion that may arise from it. Also, to avoid the additional complication that may arise due to the boundary conditions in the physical space (e.g. wall accumulation of Ezhilan *et al.*, 2015), we will assume a periodicity of $2h^*$ in the x-direction. Therefore, the shear flow profile $W(x)$ is periodic in $x \in [-1, 1]$. For convenience, we shall also define the shear profile $S(x) = -(Pe_f/2)\partial_x W(x)$ with $W(x) = -\cos(\pi x) - 1$. The flow profile is plotted in fig. 4.1a. The initial condition of the suspension is given to be uniform in $(\mathbf{x}, \mathbf{p})$-space.

4.7.1 Steady solutions

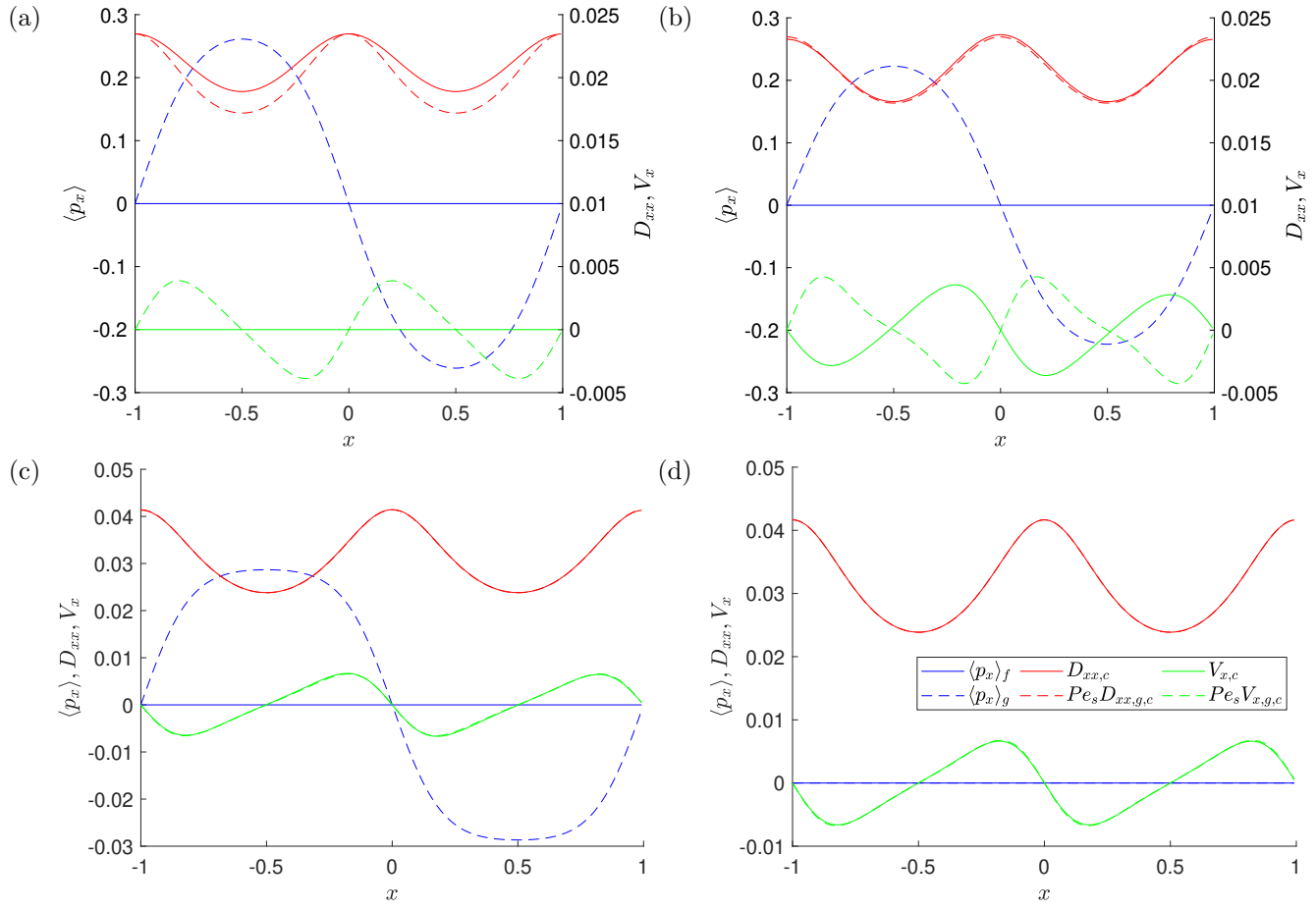

Figure 4.3: Comparison of the drifts and dispersion terms in (4.30-4.31,4.34) at the steady state. The plots show the values of $\langle p_x \rangle_f$ (blue, solid), $\langle p_x \rangle_g$ (blue, dashed), $D_{xx,c}$ (red, solid), $Pe_s D_{xx,g,c}$ (red, dashed), $V_{x,c}$, (green, dashed) and $Pe_s V_{x,g,c}$ (green, dashed) in a suspension of (a) spherical and strongly gyrotactic ($\beta = 2.2$, $\alpha_0 = 0$), (b) non-spherical and strongly gyrotactic ($\beta = 2.2$, $\alpha_0 = 0.31$), (c) non-spherical and weakly gyrotactic ($\beta = 0.21$, $\alpha_0 = 0.31$) and (d) non-spherical and non-gyrotactic ($\beta = 0$, $\alpha_0 = 0.31$) particles. The suspensions are subjected to a vertical flow $W(x) = -\cos(\pi x) - 1$ with $Pe_s = 0.25$ and $Pe_f = 1$.

In this subsection, we shall first compare the converged steady state with the prediction from the local approximation model and model G. Fig. 4.2 shows the particle distribution at converged steady

state $n_{f,s}$ after the numerical integration of the Smoluchowski equation for the suspensions of the idealised particles. Here, a non-negligibly large $Pe_s(\equiv 0.25)$ is deliberately chosen to highlight the deviation under the local approximation model from the exact solution to the Smoluchowski equation. In the case of spherical gyrotactic particle suspension (fig. 4.2a), an analytical solution (4.26) has been found for the steady state of spherical gyrotactic particle suspension in a vertical flow.

Analytical solution to a suspension of spherical gyrotactic swimmers in a vertical flow

If the gyrotactic active particles in a vertical flow is spherical, the steady solution of (4.1) can be written analytically as $\Psi(\mathbf{x}, \mathbf{p}, \infty) = n_s(x) f_s(\mathbf{p})$, where

$$f_s(\mathbf{p}) = \frac{\beta}{4\pi \sinh \beta} \exp\left(\beta \cos\theta\right), \tag{4.26a}$$

and

$$n_s(x) = A \exp\left(-\frac{\beta Pe_f W(x)}{2Pe_s}\right), \tag{4.26b}$$

where A is the normalisation factor determined by the integral condition $\int_{-1}^{1} n(x)dx = 1$. Equation (4.26) may also explain the results of Jiang & Chen (2020), who showed that the particle distribution is strongly dependent on β and the ratio between the two Péclet numbers (Pe_f/Pe_s).

If we substitute the corresponding parameters of this example into (4.12-4.15), we can recover

$$Pe_s D_{xx,c} \partial_x n_s = n_s \langle p_x \rangle_g, \tag{4.27}$$

which represents the equilibrium between a dispersion flux and the net-drift that is responsible for gyrotactic focusing. Note that $V_{x,c} = 0$ in this example because f_s is independent of $\mathbf{x}$. Here, to recover $D_{xx,c}$, we can substitute $f_s(\mathbf{p})$ into (4.8d) to get

$$b_{x,c}(\mathbf{x}; \mathbf{p}) = -\frac{Pe_s}{\beta S(x)} \left(f_s(\mathbf{p}) - g(\mathbf{p})\right), \tag{4.28}$$

and therefore

$$\begin{aligned} D_{xx,c} &= -\frac{Pe_s}{\beta S(x)} \left(\int_{S_p} f_s(\mathbf{p}) p_x d^2\mathbf{p} - \int_{S_p} g(\mathbf{p}) p_x d^2\mathbf{p} \right) \\ &= \frac{Pe_s}{\beta S(x)} \langle p_x \rangle_g. \end{aligned} \tag{4.29}$$

The numerical solution, in this case, agrees very well with the analytical solution (fig. 4.3a).

Comparison of the steady solutions

In fig. 4.2, we have also plotted the steady-state particle distribution given by the local approximation model in §4.5 ($n_{g,s}$) and model G (n_{GTD}) for other types of swimmers/particles. For strongly gyrotactic particles (figs. 4.2a,b), the two models give predictions very close to the exact results from the direct integration of the Smoluchowski equation, although model G is found to predict slightly better than the local approximation model. However, for weakly gyrotactic particles (fig. 4.2c), the small Pe_s local approximation outperforms model G. Lastly, if the particles are non-spherical and non-gyrotactic, the local approximation makes predictions almost identical to the exact result from the Smoluchowski equation. Inspite of the small variation in $n(x)$ in the non-gyrotactic case (note the small scale of $n(x)$ in fig. 4.3d), the shear trapping mechanism that causes such aggregation is the dominant effect in this case, and the aggregation can be observed in experiments (Rusconi *et al.*, 2014). Model G cannot predict the aggregation of particles due to shear trapping, giving a uniform distribution instead.

Now, we investigate the performance of the local approximation model and model G in terms of the coefficients of the transport equation given by each model. For a suspension of gyrotactic particles with $D_T = 0$ in a prescribed parallel shear flow, the exact steady solution for the particle distribution $n_{f,s} = n(x, \infty)$ is given from (4.15) by

$$\partial_x[(Pe_s\langle p_x\rangle_g - Pe_s V_{x,c})n_{f,s}] = Pe_s\partial_x[D_{xx,c}\partial_x n_{f,s}]. \tag{4.30}$$

Similarly, the steady solution to the local approximation model in (4.24), denoted by $n_{g,s}(x)$, is given by

$$\partial_x[(Pe_s\langle p_x\rangle_g - Pe_s^2 V_{x,g,c})n_{g,s}] = Pe_s^2\partial_x[D_{xx,g,c}\partial_x n_{g,s}]. \tag{4.31}$$

Finally, the steady solution to model G, $n_{GTD}(x)$, is given by

$$\partial_x[Pe_s\langle p_x\rangle_g n_{GTD}] = Pe_s^2\partial_x[D_{xx,GTD}\partial_x n_{GTD}]. \tag{4.32}$$

Fig. 4.3 shows the x-components of the drift and the phenomenological diffusion/dispersion coefficients. First, we compare the phenomenological diffusion/dispersion from the local approximation and model G with those from the exact transformation (see the right-hand side of (4.30-4.32)). We note from the discussion in §4.5.2 that $D_{xx,g,c} = D_{xx,GTD}$ for $\boldsymbol{G}$ considered in this case, as most of its components are zeros: compare $D_{xx,g,c}$ from (4.21d) and (4.14) with $D_{xx,GTD}$ from (2.2j) and (2.2i). Furthermore, when particles are spherical, $D_{xx,c}$ can be directly extracted as a function of the local vertical shear

rate S using the analytic solution of (4.1) given in §4.7.1. In fig. 4.4, $D_{xx,c}$, $D_{xx,g,c}$ and $D_{xx,GTD}$ are plotted as a function of the vertical shear rate S. It is found that $Pe_s D_{xx,g,c}$ (and $Pe_s D_{xx,GTD}$) approximates $D_{xx,c}$ quite well for all the range of S considered. In general, $D_{xx,c}$ remains a good approximation for $D_{xx,g,c}$ for all the four cases considered at all the horizontal location x (fig. 4.3). The good approximation of $D_{xx,c}$ by $Pe_s D_{xx,GTD}$ also explains why model G has consistently been found to outperform model F (Croze *et al.*, 2013, 2017).

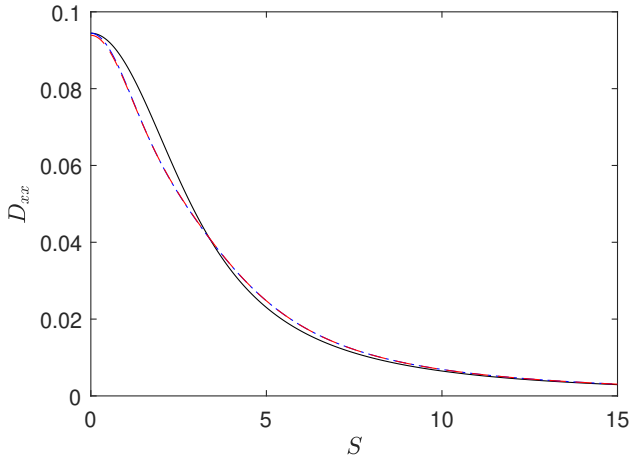

Figure 4.4: Comparison of the xx component of $\boldsymbol{D}_c/Pe_s$ (black line), $\boldsymbol{D}_{g,c}$ (blue dot-dash line) and $\boldsymbol{D}_G$ (red dashed line) as a function of the local vertical shear $S(x)$ for spherical gyrotactic particles ($\beta = 2.2$,$\alpha_0 = 0$), in which $\boldsymbol{D}_c/Pe_s$ is computed from $f_s(\mathbf{p})$ of §4.7.1. Note that $\boldsymbol{D}_{g,c}$ overlaps with $\boldsymbol{D}_G$ in the figure because they share the same formulae.

As for the left-hand side of (4.30-4.32), all methods share the same $\langle p_x \rangle_g$ term. However, the local approximation gives $V_{x,g,c}$ as an approximation of $V_{x,c}$, while model G does not have an equivalent term. Given that the local approximation model shares the same right-hand side as model G for the x component, the inclusion of $V_{x,g,c}$ becomes the differentiating factor for the performance of the two models in these examples. As shown in fig. 4.3, $V_{x,g,c}$ follows $V_{x,c}$ closely in the weakly gyrotactic cases (figs. 4.3c,d) but poorly in the strongly gyrotactic cases (figs. 4.3a,b). Hence, the local approximation model performs better than model G in fig. 4.2c but slightly worse in figs. 4.2a,b. However, in the strongly gyrotactic cases, the left-hand side of (4.30) and (4.31) are dominated by $\langle p_x \rangle_g$, so the poor estimation of $V_{x,c}$ does not strongly affect the overall performance of the local approximation model (figs. 4.2c,d).

Given the observation in the weakly gyrotactic cases (figs. 4.3c,d), the drift $\mathbf{V}_{g,c}$ seems to be an important term in (4.24). Here, we further discuss the importance of this term from a physical perspective. The term $\mathbf{V}_{g,c}$ arises from the inhomogeneity of the local flow field (i.e. shear $S(x)$ in this example). Given the GTD theory assumes a locally homogeneous shear flow (i.e. a quasi-homogeneous assumption), it cannot capture the effect of inhomogeneity in the shear $S(x)$ (see §4.5.2, point (i)), as

is evident from the lack of an equivalent term for $\mathbf{V}_{g,c}$ in (4.4). The form of (4.21e) for $\mathbf{V}_{g,c}$ suggests that there are two physical mechanisms at play that contribute to $\mathbf{V}_{g,c}$. One is the net flux caused by different levels of gyrotactic drift at different levels of shear at the adjacent location. The flux mainly manifests in the $-g\boldsymbol{\nabla}_{\mathbf{x}} \cdot \langle \mathbf{p} \rangle_g$ term in (4.21e), which diminishes in the absence of gyrotaxis. The other is the shear trapping mechanism of Bearon & Hazel (2015) and Vennamneni *et al.* (2020), which arises from the 'eccentric shape' of the particles. In the presence of inhomogeneous shear, the non-spherical shape leads to some inhomogeneity of g in the $\mathbf{x}$-space (for the detailed mechanism, see Vennamneni *et al.*, 2020). Therefore, having a non-uniform shear in $\mathbf{x}$-space can lead to non-zero $\boldsymbol{\nabla}_{\mathbf{x}} g$, even if the particle does not exhibit biased motility (i.e. $\langle \mathbf{p} \rangle_g = 0$). This behaviour would primarily manifest in the $\mathbf{p} \cdot \boldsymbol{\nabla}_{\mathbf{x}} g$ term in (4.21e).

The importance of the drift term with $\mathbf{V}_{g,c}$ can be further understood by examining the scaling of the four cases in fig. 4.2 and fig. 4.3. In the first case where the particles are spherical and strongly gyrotactic ($\alpha_0 = 0$, $\beta \sim O(1)$), the form of (4.24) implies $Pe_s^2 V_{x,g,c} \sim O(Pe_s^2)$, an order-of-magnitude smaller than $Pe_s \langle p_x \rangle_g$: i.e. $\langle \mathbf{p} \rangle_g \gg Pe_s V_{x,g,c}$. This behaviour remains the same in the second case, where the particles are non-spherical and strongly gyrotactic ($\alpha_0 \neq 0$, $\beta \sim O(1)$). However, in the third case where the particles are spheroidal and weakly gyrotactic ($\alpha_0 \sim \beta \sim O(Pe_s)$), $\langle p_x \rangle_g \sim Pe_s V_{x,g,c}$ due to $\langle p_x \rangle_g \sim O(Pe_s)$ from $\beta \sim O(Pe_s)$. Hence, if the particles are weakly gyrotactic, $V_{x,g,c}$ is of significance, and the local approximation model performs better than model G. Lastly, for the spheroidal and non-gyrotactic particles ($\alpha_0 \neq 0$, $\beta = 0$), $V_{x,g,c}$ becomes dominant while $\langle p_x \rangle_g = 0$. In this case, $V_{x,g,c}$ is purely from the shear trapping mechanism proposed by Bearon & Hazel (2015) and Vennamneni *et al.* (2020). Model G is no longer accurate due to the lack of a term equivalent to $V_{x,g,c}$ in (4.32): indeed, n_{GTD} from model G in fig. 4.2d gives a uniform distribution even though the exact solution $n_{f,s}$ shows a non-trivial wavy distribution. By the inclusion of the drift term $V_{x,g,c}$, $n_{g,s}$ from the local approximation model recovers the effect of inhomogeneity and gives an excellent prediction for $n_{f,s}$ obtained from the full Smoluchowski equation (fig. 4.2d).

4.7.2 Transient dynamics

In this subsection, we investigate the transient dynamics from the perspective of the exact transformed equation. Rewriting (4.5) for this example, we have

$$\partial_t n + Pe_s \partial_x \left[\langle p_x \rangle_f n \right] = 0, \tag{4.33}$$

in which $\langle p_x \rangle_f$ can be expanded through (4.12) into

$$\langle p_x \rangle_f = \langle p_x \rangle_g - V_{x,c} - V_{x,\partial t} - D_{xx,c} \frac{\partial_x n}{n}. \tag{4.34}$$

Substituting (4.34) into (4.33) yields the transport equation

$$\partial_t n + Pe_s \partial_x \left[(\langle p_x \rangle_g - V_{x,c} - V_{x,\partial t}) n \right] = \partial_x D_{xx,c} \partial_x n. \tag{4.35}$$

Figures B.1–4 in appendix B show how the balance in (4.34) evolves in time from a uniform suspension. In the beginning, all terms were zeros, except for $\langle p_x \rangle_g$ and the unsteadiness in f, which balance out each other. Note that the unsteadiness in f was transformed into a drift $V_{x,\partial t}$ in the transport equation (see (4.21f)). As the suspension starts to evolve, the **p**-space evolves first in the time scale of order unity (i.e. the fast time scale in §4.5) – note that the time scale in the **p**-space is $1/d_r^*$ (see §4.2). The fast-changing f drives the drift $V_{x,\partial t}$ away from $\langle p_x \rangle_g$ in the beginning, resulting in non-zero $\langle p_x \rangle_f$ in (4.34), which in turn generates the unsteadiness in n in (4.33). Therefore, $n(x,t)$ does not start evolving until $V_{x,\partial t}$ has become significantly different from $\langle p_x \rangle_g$. At $t \sim \mathcal{O}(1)$, $V_{x,\partial t}$ is close to zero, indicating that f has reached the quasi-steady regime, justifying the assumption of §4.5. It is also in this time interval where $V_{x,c} \approx V_{x,g,c}$ and $D_{xx,c} \approx D_{xx,g,c}$, implying that the local approximation in §4.5 would be valid after this short initial transient.

For $t \gtrsim \mathcal{O}(1)$, $n(x,t)$ evolves slowly, while $\langle p_x \rangle_f$ diminishes towards zero, mainly due to the increasing magnitude of $(\partial_x n/n)$ to balance $\langle p_x \rangle_g$ in (4.34). As $\langle p_x \rangle_f$ vanishes, $n(x,t)$ reaches a steady equilibrium. During this slow transient period, f also evolves slowly, but slow enough such that $V_{x,\partial t}$ remains insignificant. Note that, in this example, the prescribed flow field is steady, such that $V_{x,g,\partial T}$ vanishes. If the prescribed flow were unsteady in the long timescale T, we would also expect $V_{x,\partial t}$ to be significant and to be well approximated by $V_{x,g,\partial T}$. In all the examples considered, $D_{xx,c}$ remains close to the approximation $D_{xx,g,c}$. In a weakly and non-gyrotactic suspensions, $V_{x,c}$ does not evolve far from $V_{x,g,c}$ either, but in a strongly gyrotactic suspension, $V_{x,c}$ is found to change direction as $t \to \infty$. As mentioned in §4.7.1, $V_{x,c}$ is considerably small compared to $\langle p_x \rangle_g$ in this case. Therefore, regardless of the fact that $V_{x,g,c}$ differs from $V_{x,c}$, the local approximation model still performs well.

4.7.3 Effect of translational diffusion

Lastly, we will consider a non-zero translational diffusion for the previous examples. Micro-algae such as *Chlamydomos* and *Dunaliella* are often considered to have negligible thermal diffusion given their relatively large sizes (see reviews by Pedley & Kessler, 1992; Saintillan, 2018; Bees, 2020). Their random walk is often modelled only through the rotational diffusion by assuming that the intracellular biochemical noise only affects the rotational motion. However, in theory, there is no reason that the randomness can be modelled solely through the rotational diffusion without translational diffusion because the swimming mechanisms very often involve sophisticated noisy beating dynamics of cilia and flagella (e.g. Wan & Goldstein, 2014). Given the ambiguity in choosing a biologically relevant value for D_T, here we will simply consider some values of D_T to demonstrate the role of translational diffusion in the transport equation, i.e. $\mathbf{V}_{D_T}$ and $\boldsymbol{D}_{D_T}$.

We consider the steady-state particle distribution at an arbitrary value of $D_T = 0.01$, which is chosen to be of similar magnitude as $Pe_s\boldsymbol{D}_c$. This arbitrary choice was made to highlight the potential role of translational diffusion. Also, for biological microswimmers, any D_T value larger than $Pe_s\boldsymbol{D}_c$ would be physically unrealistic (c.f. experimental measurements of Croze *et al.* (2017)). We have also computed the steady-state at $D_T = 0.002$, but since the results are qualitatively the same, we shall only present the $D_T = 0.01$ case here.

The exact steady-state particle distribution $n_{f,s}(x)$ from the Smoluchowski equation (4.1) is given by

$$\partial_x[(Pe_s\langle p_x\rangle_g - Pe_s(V_{x,c} + V_{x,D_T}))n_{f,s}] = \partial_x[(D_T + Pe_s(D_{xx,c} + D_{xx,D_T}))\partial_x n_{f,s}], \tag{4.36}$$

and the distribution from the local approximation $n_{g,s}$ is given by

$$\partial_x[(Pe_s\langle p_x\rangle_g - Pe_s^2(V_{x,g,c} + V_{x,g,D_T}))n_{g,s}] = \partial_x[(D_T + Pe_s^2(D_{xx,g,c} + D_{xx,g,D_T}))\partial_x n_{g,s}]. \tag{4.37}$$

Note that $Pe_s^2 V_{x,g,D_T}$ and $Pe_s^2 D_{xx,g,D_T}$ scale with $Pe_s D_T$ from (4.21b) and (4.21c). Meanwhile, n_{GTD} is given by

$$\partial_x[Pe_s\langle \mathbf{p}\rangle_g n_{GTD}] = \partial_x[(D_T + Pe_s^2 D_{xx,GTD})\partial_x n_{GTD}]. \tag{4.38}$$

As shown before in §4.5.2, model G gives $D_{xx,GTD} = D_{xx,g,c}$. However, it does not offer any approximations for $V_{x,c}$, V_{x,D_T} and D_{xx,D_T}. Therefore, any difference between $n_{g,s}$ and n_{GTD} has to come from $V_{x,g,c}$, V_{x,g,D_T} and D_{x,g,D_T}.

Fig. 4.5 shows the steady-state particle distributions with $D_T = 0.01$ for the same parameters

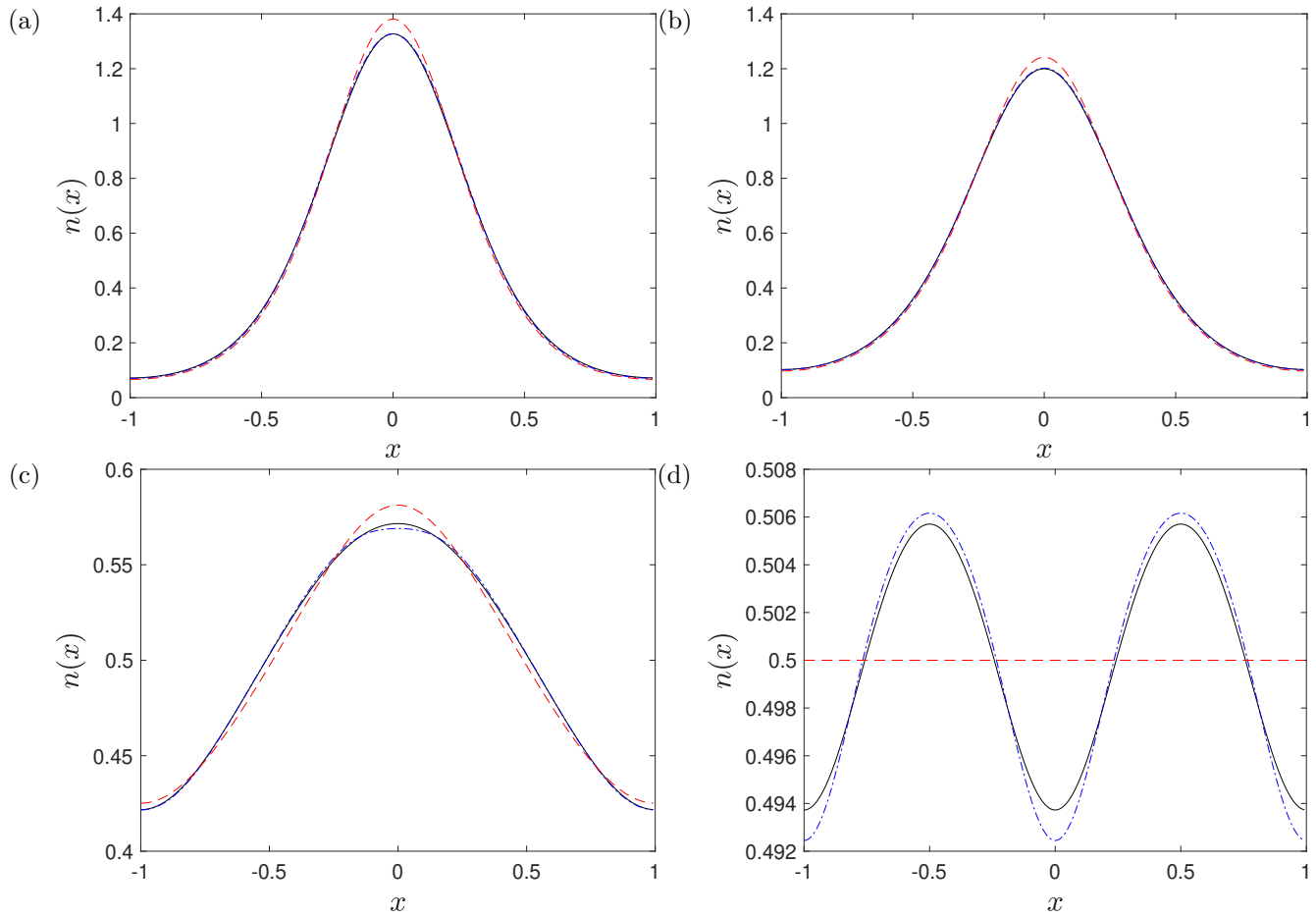

Figure 4.5: Comparison of the steady-state particle distributions given by the direct integration of (4.1) (black solid line, $n_{f,s}$), the local approximation of §4.5 (blue dot-dashed line, $n_{g,s}$) and model G (red dashed line, n_{GTD}) of suspensions of (a) spherical and strongly gyrotactic ($\beta = 2.2$, $\alpha_0 = 0$), (b) non-spherical and strongly gyrotactic ($\beta = 2.2$, $\alpha_0 = 0.31$), (c) non-spherical and weakly gyrotactic ($\beta = 0.21$, $\alpha_0 = 0.31$) and (d) non-spherical and non-gyrotactic ($\beta = 0$, $\alpha_0 = 0.31$) particles. The particles are diffusive such that $D_T = 0.01$. The suspensions are subjected to a vertical flow $W(x) = -\cos(\pi x) - 1$ with $Pe_s = 0.25$ and $Pe_f = 1$. Note that the vertical scale for $n(x)$ in (c, d) is much smaller than that in (a, b).

considered in fig. 4.2. One can see that the introduction of non-zero D_T has further smoothed out the particle distributions in all cases considered by comparing fig. 4.2 and fig. 4.5. However, D_T does not seem to have significantly altered most of the conclusions drawn in §4.7.1, except that the local approximation model now performs better than model G even in strongly gyrotactic suspensions. This improved performance can be attributed to several factors. Firstly, $V_{x,c}$ becomes closer to the approximation $V_{x,g,c}$ in strongly gyrotactic suspensions in the presence of D_T, as shown by figs. 4.6a,b in comparison with figs. 4.3a,b. Secondly, D_T gives rise to V_{x,D_T} (cyan solid lines in fig. 4.6), which can be as large in magnitude as $V_{x,c}$ in strongly gyrotactic cases (figs. 4.6a,b). Since model G does not contain either $\mathbf{V}_c$ or $\mathbf{V}_{D_T}$, the inclusion of $V_{x,g,c}$ and V_{x,g,D_T} approximating $V_{x,c}$ and V_{x,D_T} gives a better performance for the local approximation model. Thirdly, the introduction of D_T also gives rise to D_{xx,D_T} (magenta solid lines in fig. 4.6). Despite being not as large as $D_{xx,c}$ overall, D_{xx,D_T} has

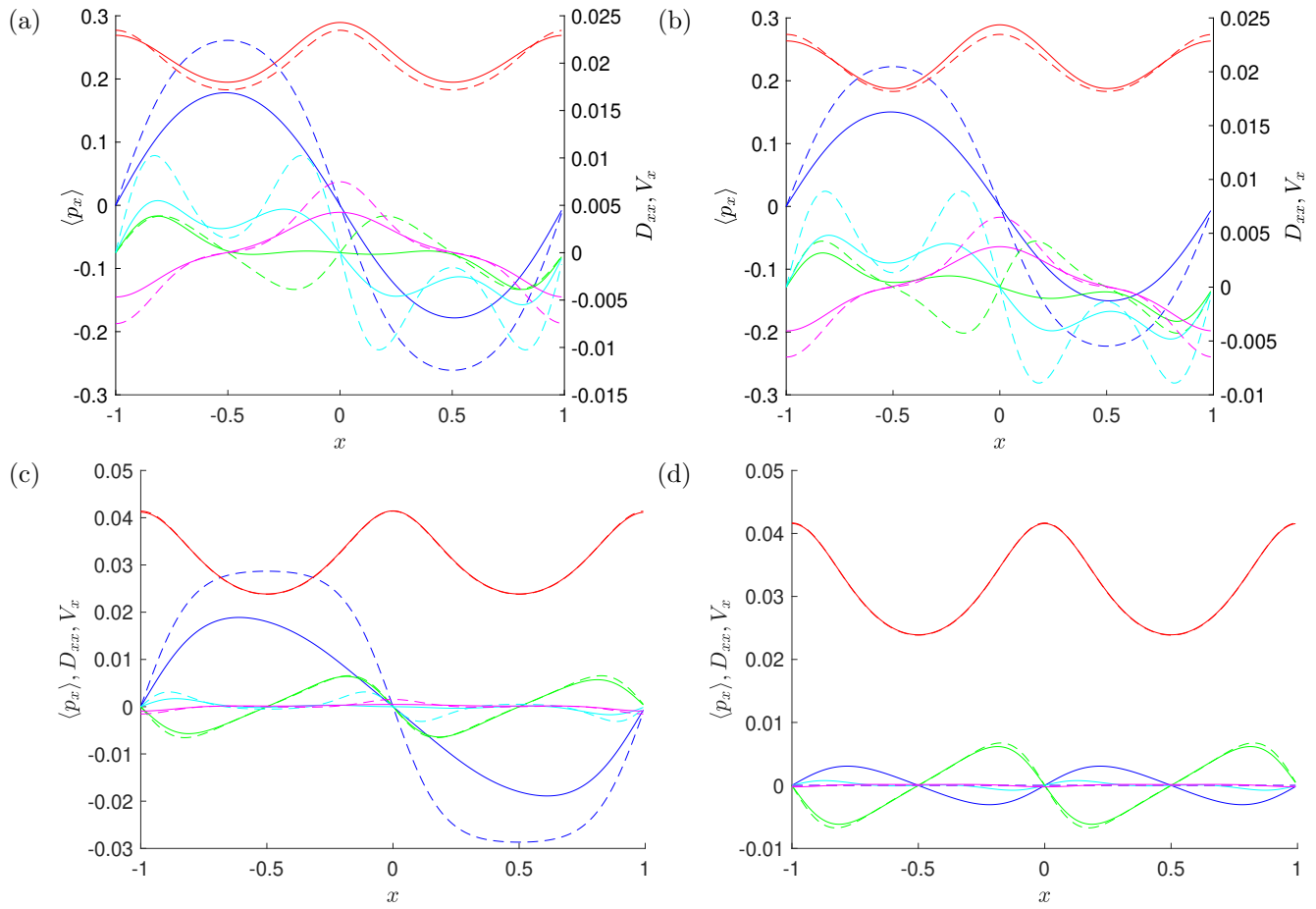

Figure 4.6: Comparison of the drifts and dispersion terms in (4.36-4.37) at the steady state. The plots show the values of $\langle p_x \rangle_f$ and $\langle p_x \rangle_g$ (blue), $D_{xx,c}$ and $Pe_s D_{xx,g,c}$ (red), $V_{x,c}$ and $Pe_s V_{x,g,c}$ (green), D_{xx,D_T} and $Pe_s D_{xx,g,D_T}$ (magneta), V_{x,D_T} and $Pe_s V_{x,g,D_T}$ (cyan) calculated using the steady-state $f(\mathbf{x}, \mathbf{p}, \infty)$ (solid lines) and $g(\mathbf{x}, \infty; \mathbf{p})$ (dashed lines) of a suspension of (a) spherical and strongly gyrotactic ($\beta = 2.2$, $\alpha_0 = 0$), (b) non-spherical and strongly gyrotactic ($\beta = 2.2$, $\alpha_0 = 0.31$), (c) non-spherical and weakly gyrotactic ($\beta = 0.21$, $\alpha_0 = 0.31$) and (d) non-spherical and non-gyrotactic ($\beta = 0$, $\alpha_0 = 0.31$) particles. The particles are diffusive such that $D_T = 0.01$. The suspensions are subjected to a vertical flow $W(x) = -\cos(\pi x) - 1$ with $Pe_s = 0.25$ and $Pe_f = 1$.

a variation over x comparable to that of $D_{xx,c}$ (magenta and red solid lines in fig. 4.6). Therefore, the local approximation model, which contains the terms with $V_{x,g,c}$, V_{x,g,D_T} and D_{x,g,D_T}, predicts particle distributions better than model G.

Comparing the strongly gyrotactic (fig. 4.6b) with the weakly gyrotactic case (fig. 4.6c), one can also conclude that the effect of V_{x,D_T} and D_{xx,D_T} are much stronger in strongly gyrotactic suspensions. Since V_{x,D_T} and D_{xx,D_T} are driven by $\boldsymbol{\nabla}_{\mathbf{x}} f$ and $\nabla^2_{\mathbf{x}} f$ according to (4.8b) and (4.8c), the large V_{x,D_T} and D_{xx,D_T} are likely driven by the larger variation of f in x induced by the stronger gyrotaxis.

Lastly, it is worth noting that D_{xx,D_T} and D_{xx,g,D_T} can be negative for some domain in x. As mentioned in §4.4, the terms with D_{xx,D_T} and D_{xx,g,D_T} do not necessarily represent diffusion – they depict the dispersive behaviour introduced by translational diffusion. Therefore, negative diagonal

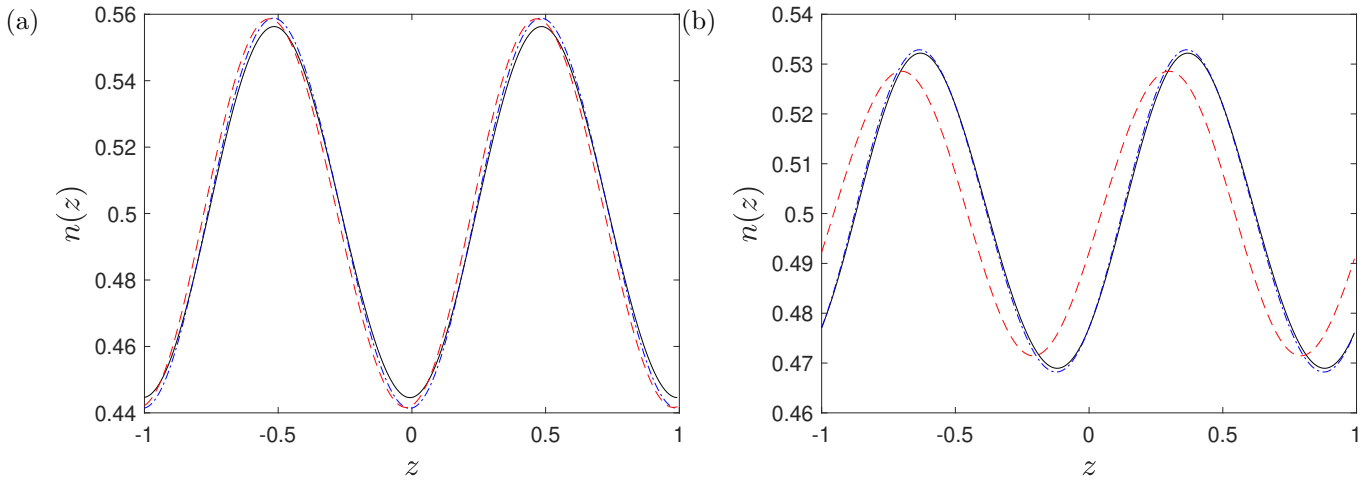

Figure 4.7: Comparison of the steady-state particle distributions given by the direct integration of (4.1) (black solid line, $n_{f,s}$), the local approximation of §4.5 (blue dot-dashed line, $n_{g,s}$) and model G (red dashed line, n_{GTD}) of suspensions of (a) strongly gyrotactic particles ($\beta = 2.2$, $\alpha_0 = 0.31$) and (b) weakly gyrotactic particles ($\beta = 0.21$, $\alpha_0 = 0.31$). The suspensions are subjected to horizontal shear flow $U(z) = \cos(\pi z)$ with $Pe_s = 0.25$ and $Pe_f = 1$.

values in $\boldsymbol{D}_{D_T}$ are allowed. They physically represent the reduction in the spreading of particles due to the interaction between the D_T-driven cross-dispersion between $n(\mathbf{x}, t)$ and f and the particles' orientational dynamics (see (4.8c) and table 4.2). The same interpretation can also be applied to the approximation $\boldsymbol{D}_{g,D_T}$. More discussion on the implication of these dispersion tensors will follow in §4.8.2.

4.7.4 A suspension of gyrotactic active particles in a prescribed horizontal flow

In this section, we consider a horizontal shear flow $\mathbf{u} = [U(z), 0, 0]^T$ in the gyrotactic suspension instead of a vertical shear flow. Similar to §4.7, we first assume an infinite $\mathbf{x}$-domain with a periodicity in z and no translational diffusion. The horizontal shear flow is prescribed as $U(z) = \cos(\pi z)$, as shown in fig. 4.1b. We also introduce the shear profile $S(z) = (Pe_f/2)\partial_z U(z)$. As noted in §4.5.2, the cross-stream dispersion $D_{zz,g,c}$ from the local approximation is the same as $D_{zz,GTD}$ from model G. It is similar to how $D_{xx,g,c} = D_{xx,GTD}$ in the vertical shear case. Fig. 4.7a shows that the steady-state particle distribution profiles $n(z)$ of the strongly gyrotactic suspension ($\beta = 2.2$,$\alpha_0 = 0.31$) computed from the local approximation model and model G is similar. Similar to the case in §4.7.1, the small differences come from the presence of $V_{z,g,c}$, which is relatively small when compared to $\langle \mathbf{p} \rangle_g$ (fig. 4.8a). However, in fig. 4.7b, the steady-state particle distribution profile $n(z)$ for weakly gyrotactic non-spherical particles ($\beta = 0.21$,$\alpha_0 = 0.31$) computed from the local approximation model is more

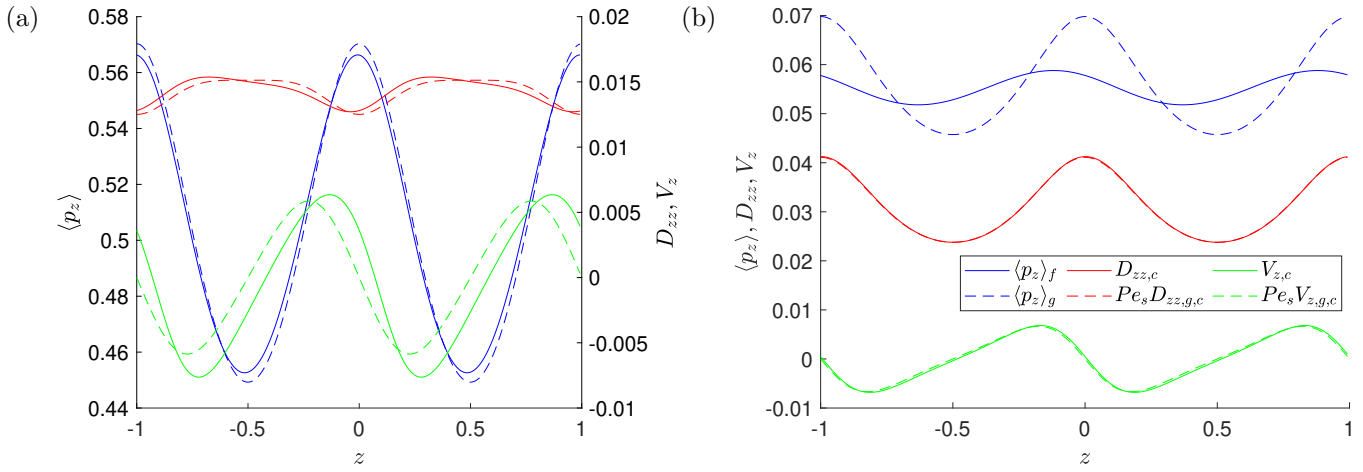

Figure 4.8: Comparison of the vertical drifts and dispersion terms at the steady state. The plots show the values of $\langle p_z \rangle_f$ (blue, solid), $\langle p_z \rangle_g$ (blue, dashed), $D_{zz,c}$ (red, solid), $Pe_s D_{zz,g,c}$ (red, dashed), $V_{z,c}$, (green, dashed) and $Pe_s V_{z,g,c}$ (green, dashed) at the steady state of a suspension of (a) strongly gyrotactic particles ($\beta = 2.2$, $\alpha_0 = 0.31$) and (b) weakly gyrotactic particles ($\beta = 0.21$, $\alpha_0 = 0.31$). The suspensions are subjected to a horizontal shear flow $U(z) = \cos(\pi z)$ with $Pe_s = 0.25$ and $Pe_f = 1$.

accurate than that of model G due to the presence of $V_{z,g,c}$, which is consistent with the prediction of §4.5.2. The explanation for the better performance of the local approximation method is the same as that in §4.7.1, in which the inclusion of $V_{z,g,c}$ is improving the prediction from the local approximation (fig. 4.8b).

The transient dynamics is also investigated for the horizontal flow. As shown in figs. B.5,6, the simulation initially shows the dominant balance between $V_{z,\partial t}$ and $\langle p_z \rangle_g$. At the time scale of order unity, $V_{z,\partial t}$ diminishes quickly, driven by the fast-changing f. At $t \gtrsim \mathcal{O}(1)$, $V_{z,\partial t}$ becomes insignificant, indicating that f has reached the quasi-steady regime. Meanwhile, the local approximation accurately predicts $V_{z,c} \approx V_{z,g,c}$ and $D_{zz,c} \approx D_{zz,g,c}$, similar to how $V_{x,c} \approx V_{x,g,c}$ and $D_{xx,c} \approx D_{xx,g,c}$ in §4.7.2. However, unlike the vertical flow cases, figs. B.5,6 show that $\langle p_z \rangle_f$ does not tend to zero as $t \to \infty$ in these horizontal flow cases. Instead, fig. 4.8 shows that they stay in roughly the same order as $\langle p_z \rangle_g$ at steady equilibrium. Moreover, both $V_{z,g,c}$ and $D_{zz,g,c}$ remain good approximations to $V_{z,c}$ and $D_{zz,c}$ respectively for a long time, even when particles are strongly gyrotactic. Therefore, when the flow is horizontal, the local approximation model outperforms model G even in strongly gyrotactic suspensions.

4.8 Discussion

4.8.1 Physical implication of the transformation

In this chapter, we set out to seek a model transport equation that can predict the particle distribution given by the Smoluchowski equation without solving the equation directly. To achieve the goal, in §4.4, we have shown how the Smoluchowski equation (4.1) can be transformed into a transport equation by expanding $\langle \mathbf{p} \rangle_f n$ in the integrated equation (4.5) into $\langle \mathbf{p} \rangle_g n$ and other drifts $\mathbf{V}_\star n$ and dispersions/diffusions $\boldsymbol{D}_\star \boldsymbol{\nabla}_\mathbf{x} n$. This expansion of $\langle \mathbf{p} \rangle_f$ shows a key difference from model G, which takes the averaged orientation $\langle \mathbf{p} \rangle_g$ of individual particle directly as the drift.

To better show the implication of this transformation, here we rewrite the procedures in §4.4 under the assumption of a parallel flow and $D_T = 0$. We can rewrite (4.5) as

$$\partial_t n(\mathbf{x}, t) + \boldsymbol{\nabla}_\mathbf{x} \cdot [(Pe_s \langle \mathbf{p} \rangle_f (\mathbf{x}, t)\, n(\mathbf{x}, t)] = 0, \tag{4.39}$$

in which $\langle \mathbf{p} \rangle_f n$ can be expanded through (4.12) or

$$\langle \mathbf{p} \rangle_f = \langle \mathbf{p} \rangle_g - \mathbf{V}_c - \mathbf{V}_{\partial t} - \boldsymbol{D}_c \frac{\boldsymbol{\nabla}_\mathbf{x} n}{n} \tag{4.40}$$

into the transport equation

$$\partial_t n + Pe_s \boldsymbol{\nabla}_\mathbf{x} \cdot [(\langle \mathbf{p} \rangle_g - \mathbf{V}_c - \mathbf{V}_{\partial t}) n] = Pe_s \boldsymbol{\nabla}_\mathbf{x} \cdot \boldsymbol{D}_c \boldsymbol{\nabla}_\mathbf{x} n. \tag{4.41}$$

Note that equations (4.39-4.41) are the equivalent of (4.33-4.35) in general coordinates. Now, eq. (4.39) and the rewritten eq. (4.41) yield two different interpretations of ABPs transport. In (4.39), particles are purely advected by the Eulerian motility flux $Pe_s \langle \mathbf{p} \rangle_f n$, which is the ensemble-averaged flux of particles coming in and out of a certain control volume at position $\mathbf{x}$ due to the motility of the particle. The flux depends on the orientational and spatial distribution of particles inside and at the vicinity of the control volume. However, in (4.41), the average Eulerian motility flux $Pe_s \langle \mathbf{p} \rangle_f n$ is decomposed into the flux from the average motility of individual particles $Pe_s \langle \mathbf{p} \rangle_g n$, the advective flux due to unsteadiness in particles' orientational dynamics $-Pe_s \mathbf{V}_{\partial t} n$, the shear trapping flux $-Pe_s \mathbf{V}_c n$ and the dispersion flux $-Pe_s \boldsymbol{D}_c \boldsymbol{\nabla}_\mathbf{x} n$.

It is evident from (4.40) that the average Eulerian motility flux $Pe_s \langle \mathbf{p} \rangle_f n$ is different from the flux of the average motility of individual particles $Pe_s \langle \mathbf{p} \rangle_g n$. However, it might also be counterintuitive at

first glance to decipher their differences. Here, the average motility of individual particles $Pe_s\langle\mathbf{p}\rangle_g$ is defined as the ensemble average of the self-propelling velocity of individual particles when subjected to the local velocity gradient or other local factors that may influence their orientation (e.g. taxes). The average motility of individual particles $Pe_s\langle\mathbf{p}\rangle_g$ is based on the average orientation of individual particles $\langle\mathbf{p}\rangle_g$, which is calculated from the homogeneous solution (g) to the operator $\mathcal{L}_\mathbf{p}$, representing the orientational dynamics of individual particles. It is a function of the local velocity gradient and the particles' property only and is independent of any $(\mathbf{x}, t)$-space configuration. In other words, $\langle\mathbf{p}\rangle_g$ is calculated when the orientational dynamics ($\mathcal{L}_\mathbf{p}$) is decoupled from the rest of the Smoluchowski equation. The resulting average motility $Pe_s\langle\mathbf{p}\rangle_g$ provides a Langrangian view of each individual's motility after being averaged in the local $\mathbf{p}$-space. Therefore, the average motility flux $Pe_s\langle\mathbf{p}\rangle_g n$ at each $(\mathbf{x}, t)$ depends only on the local velocity gradient at the specified location.

By contrast, the average Eulerian motility flux $Pe_s\langle\mathbf{p}\rangle_f n$ does consider the spatial and orientational distribution of particles at the nearby location in the $(\mathbf{x}, t)$-space. It is the result of averaging the particles' motility $Pe_s\mathbf{p}\Psi$ in the Smoluchowski equation (4.1). It includes the flux from the average motility of individuals $Pe_s\langle\mathbf{p}\rangle_g n$ and other fluxes from drifts and dispersions arising from the interaction between the orientational dynamics ($\mathcal{L}_\mathbf{p}$) and the rest of the Smoluchowski equation. For example, it includes the effect of the different orientation distribution at the nearby location, which gives rise to the extra shear trapping flux $-Pe_s\mathbf{V}_c n$, even when the average motility $Pe_s\langle\mathbf{p}\rangle_g$ is zero (as demonstrated in §4.7.1, fig. 4.3d). It also includes the effect of the changing orientation over time, which interacts with the orientational dynamics and manifests as the extra flux $-Pe_s\mathbf{V}_{\partial t} n$ through the particles' motility. Lastly, it includes the dispersion flux $Pe_s\boldsymbol{D}_c\boldsymbol{\nabla}_\mathbf{x} n$, which arises from the distribution of how the particles' instantaneous motilities are different from the averaged motility of the particles in the control volume. All of the above extra drifts and dispersions are dependent on the configuration of the suspension in $(\mathbf{x}, t)$-space (c.f. §4.7.2), in contrast to $Pe_s\langle\mathbf{p}\rangle_g$. Therefore, one may interpret $Pe_s\langle\mathbf{p}\rangle_g$ as the Langrangian view of each individual's motility and $Pe_s\langle\mathbf{p}\rangle_f$ as the Eulerian view of the overall drift of all the particles in the suspension at the given location due to the particles' motility.

The fact that $\langle\mathbf{p}\rangle_g$ is part of $\langle\mathbf{p}\rangle_f$ in (4.40) physically implies that the averaged motility of individuals only contributes to part of the overall Eulerian drift caused by particles' motility. It also indicates that particles dispersion physically comes from the same Eulerian motility flux $Pe_s\langle\mathbf{p}\rangle_f n$ that includes the effect of other drifting terms. This physical perspective is in stark contrast to that of model G. Model G takes $Pe_s\langle\mathbf{p}\rangle_g n$ directly as the overall motility flux from its approximation of the temporal growth rate of the first statistical moment (mean), which is effectively using $Pe_s\langle\mathbf{p}\rangle_g n$ as a first-order

approximation to $Pe_s\langle\mathbf{p}\rangle_f n$. Because of this, it does not capture the drifts like $\mathbf{V}_c$ and $\mathbf{V}_{\partial t}$. Meanwhile, the effective diffusivity $Pe_s^2\boldsymbol{D}_G$ is found by asymptotically matching it with the temporal growth rate of the second statistical moment (variance). Therefore, in the GTD derivation, it is hard to follow how $Pe_s^2\boldsymbol{D}_G$ arises from the particles' motility. On the contrary, the transformation introduced in this study has directly shown how the dispersion arises from the motility of the particle.

Extending the decomposition to a more general ABP suspension, the passive advection and translation diffusion of particles shall also interact with the orientational dynamics and give rise to extra drifts and dispersion through the particles' motility. Indeed, the interactions give rise to $\mathbf{V}_u$, $\mathbf{V}_{D_T}$ and $\boldsymbol{D}_{D_T}$, which has already been introduced in §4.4. Their physical meanings are summarised in table 4.2.

4.8.2 Non-trivial phenomenological dispersion

In §4.4 and §4.5.2, we have briefly highlighted that $\boldsymbol{D}_c$ and $\boldsymbol{D}_{D_T}$, and their respective approximation $\boldsymbol{D}_{g,c}$ and $\boldsymbol{D}_{g,D_T}$, are not necessarily positive definite and symmetric, as they are directly obtained through the Smoluchowski equation (4.1). In fact, there is no reason that the dispersive behaviour of suspensions originating from the orientational dynamics of each ABP would need to solely be described by a 'diffusion' process. This is in contrast to the effective diffusivity $\boldsymbol{D}_G$ of model G, which was positive definite and symmetric by definition (Frankel & Brenner, 1991, 1993). In this subsection, we shall further demonstrate that $\boldsymbol{D}_{g,c}$ is indeed asymmetric, in contrast to the positive definite $\boldsymbol{D}_G$. Focusing on spherical particles, here we shall show that $\boldsymbol{D}_{g,c}$ caused by dispersion is not necessarily symmetric.

Fig. 4.9 shows a component-wise comparison between $\boldsymbol{D}_c$, $\boldsymbol{D}_{g,c}$ and $\boldsymbol{D}_G$ as a function of the local shear rate $S(x)$ for a suspension of idealised spherical ($\alpha_0 = 0$) gyrotactic particles (with $\beta = 2.2$) in a vertical shear flow. In general, $\boldsymbol{D}_c$ obtained through the transformation is not a function of the local shear S alone as $\boldsymbol{D}_c$ is computed from $f(\mathbf{x}, \mathbf{p}, t)$. However, as shown in §4.7.1, for the particular case of a spherical gyrotactic particle suspension in vertical shear and at steady equilibrium, $\boldsymbol{D}_c/Pe_s$ can be written as a function of $S(x)$.

The comparison shows that $\boldsymbol{D}_c$ and the approximation $\boldsymbol{D}_{g,c}$ are highly asymmetric compared to the symmetric diffusivity tensor from model G when the shear rate is not zero. These non-symmetric dispersion tensors indicate that the diffusion process alone might not be the best physical description of the random walk of biased ABPs. Instead, we consider them as dispersions in the $(\mathbf{x}, \mathbf{p})$-space, analogous to the original Taylor-Aris dispersion (Taylor, 1953; Aris & Taylor, 1956). In the Taylor-Aris

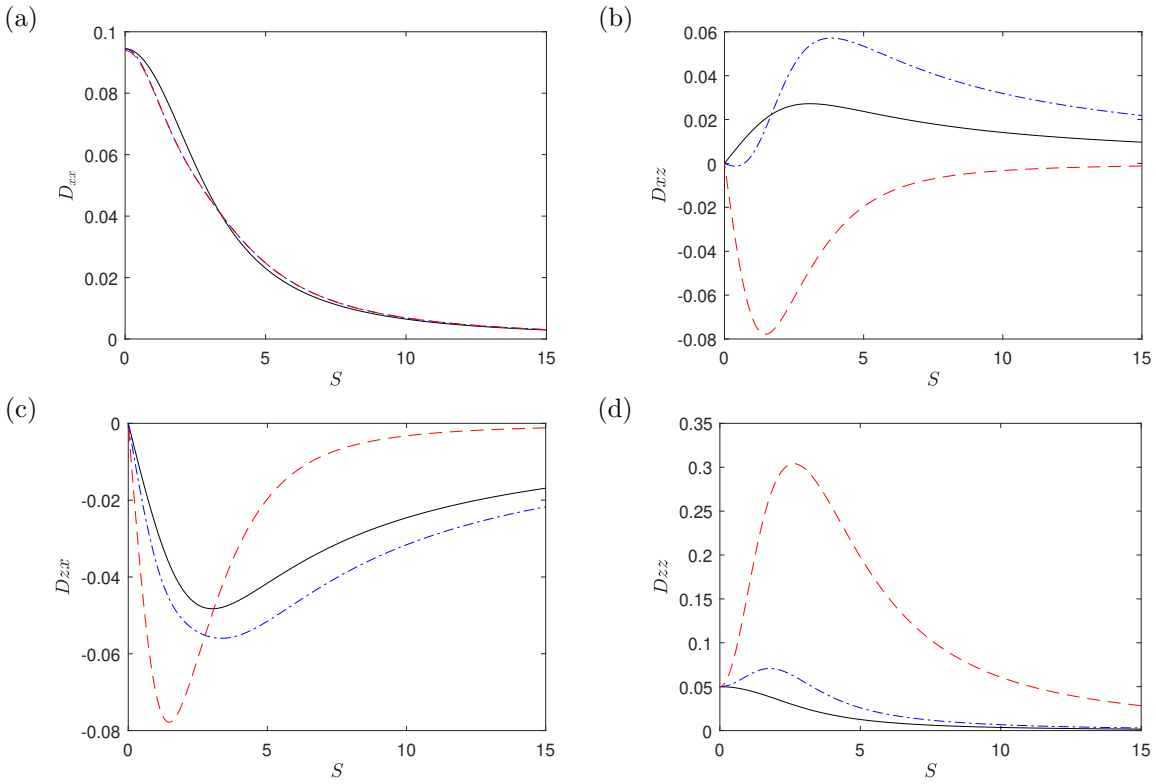

Figure 4.9: Comparisons of the components of $\boldsymbol{D}_c/Pe_s$ (black line), $\boldsymbol{D}_{g,c}$ (blue dot-dash line) and $\boldsymbol{D}_G$ (red dashed line) as a function of the local vertical shear $S(x)$ for a suspension of spherical gyrotactic particles ($\beta = 2.2$,$\alpha_0 = 0$), in which $\boldsymbol{D}_c/Pe_s$ is computed from $f_s(\mathbf{p})$ of §4.7.1.

dispersion, the cross-stream diffusion gives rise to additional streamwise dispersion through the shear flow. Similarly, in ABP suspensions, the rotational diffusion (in $\mathbf{p}$-space) gives rise to translational dispersion (in $\mathbf{x}$-space) through the particles' motility. While the extra streamwise dispersion in Taylor-Aris dispersion is sometimes referred to as 'effective diffusivity' (see Cussler, 2009, §4.5), it is not a physical diffusion caused by a translational random walk but the result of the combination of cross-stream diffusion and a shear flow. Similarly, the 'effective diffusivity' $\boldsymbol{D}_c$ here is not a diffusion from the translational random walk but the result of the interplay between particles' orientational dynamics and motility. Therefore, $\boldsymbol{D}_c$ and the approximation $\boldsymbol{D}_{g,c}$ do not necessarily have to conform to the symmetric and positive definite requirement of a physical diffusivity. This interpretation of $\boldsymbol{D}_c$ and $\boldsymbol{D}_{g,c}$ contrasts with the approach of the generalised Taylor dispersion model, in which the effective diffusivity $\boldsymbol{D}_G$ was obtained by the temporal asymptotic growth rate of the statistical variance of particle distribution using the classical definition of diffusion. By definition, $\boldsymbol{D}_G$ must be positive definite and symmetric.

A similar argument can be applied to $\boldsymbol{D}_{D_T}$ and $\boldsymbol{D}_{g,D_T}$. Because they are not obtained by the growth rate of the statistical variance but by the transformation of the Smoluchowski equation, they can have a negative xx component in §4.7.3. However, one should be careful not to isolate the tensor

and interpret it alone. The dispersion tensors $\boldsymbol{D}_{D_T}$ and $\boldsymbol{D}_{g,D_T}$, which have a $\mathcal{O}(Pe_s^2)$ impact on the transport equation, cannot exist without a positive D_T, which has a $\mathcal{O}(1)$ impact. Therefore, we are not claiming that swimmers will exhibit negative diffusion. Instead, a negative $\boldsymbol{D}_{D_T}$ or $\boldsymbol{D}_{g,D_T}$ implies that the coupling between the swimmer's orientation dynamics and translation diffusion can result in a small reduction in its 'effective diffusivity' compared to the translation diffusion alone.

4.8.3 Shear trapping in the presence of weak gyrotaxis

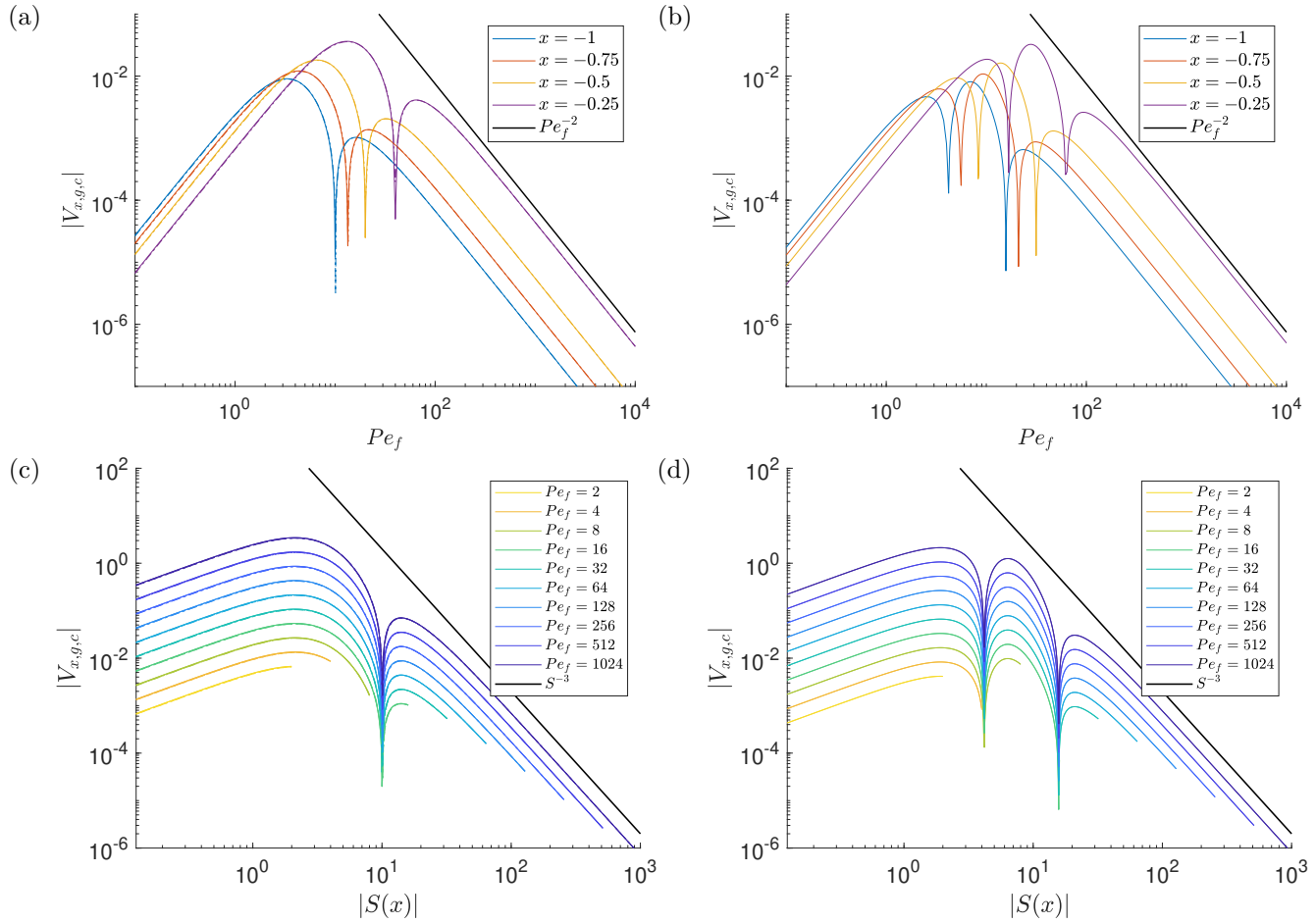

Figure 4.10: The absolute shear trapping advection in the x-direction ($|V_{x,g,c}|$) of non-spherical swimmers ($\alpha_0 = 0.31$), with (a, c) $\beta = 0$ (solid lines), $\beta = 0.21$ (dot-dash lines) and (b, d) $\beta = 2.2$, under prescibed Poiseulli flows at various flow rates. In (a, b), $|V_{x,g,c}|$ is plotted as a function of the ambient flow Pèclet number Pe_f at each location across different flow rate (c.f. fig. 9b of Vennamneni *et al.* (2020)). In (c, d), $|V_{x,g,c}|$ is plotted as a function of the local shear rate $S(x) = (-Pe_f/2)\partial_x W(x)$ at each prescribe flow. (c.f. fig. 9d of Vennamneni *et al.* (2020)). Note that in (a, c), the $\beta = 0$ (solid lines) and $\beta = 0.21$ (dot-dash lines) plots are virtually indistinguishable.

Since the discovery of shear trapping by Rusconi *et al.* (2014), there have been several works explaining the experimental observation. Ezhilan *et al.* (2015) demonstrated high-shear trapping with the Smoluchowski equation, although they focused mostly on the effect of translational diffusivity and the development of the boundary-layer-like wall accumulation due to the no-flux boundary

condition. Bearon & Hazel (2015) computed both high- and low-shear trapping from an individual-based simulation. They first demonstrated how to derive the effective drift, equivalent to $\mathbf{V}_{g,c}$ in this work, based on a low Pe_s asymptotics from the Smoluchowski equation. Recent work by Vennamneni *et al.* (2020) further investigated shear trapping based on the same asymptotic approach as Bearon & Hazel (2015). They explained the mechanism of both high- and low-shear trapping as the result of the same $\mathbf{V}_{g,c}$ term changing direction in different regimes of Pe_f.

However, none of the above work considered the effect of the presence of taxes on the shear trapping flux. Because of the non-vanishing gyrotactic drift $\langle \mathbf{p} \rangle_g$ in §4.5, the asymptotics by both Bearon & Hazel (2015) and Vennamneni *et al.* (2020) would break down if $\langle \mathbf{p} \rangle_g$ were non-zero. In §4.5, we have extended the methodology by Bearon & Hazel (2015) to include the effect of non-zero gyrotactic drift $\langle \mathbf{p} \rangle_g$ and demonstrated how the drift from taxis is more significant than the shear trapping drift (i.e. $Pe_s \langle \mathbf{p} \rangle_g \ll Pe_s^2 \mathbf{V}_{g,c}$). However, if the strength of the taxis is small (e.g. in the case of a weakly gyrotactic swimmer such as *Dunaliella*), the effect of shear trapping can also be as significant as that from the taxis.

To show the effect of gyrotaxis on shear trapping, we will compare the shear trapping flux $\mathbf{V}_{g,c}$ from the local approximation (§4.5) with that of Vennamneni *et al.* (2020). Following the flow configuration of Vennamneni *et al.* (2020), in this section, we consider a downward flowing ($-z$ direction) two-dimensional Poiseulle flow with the flow profile $W(x) = -(1 - x^2)$, where $x \in [-1, 1]$. We also define the shear profile $S(x) = -Pe_f x$.

However, before accounting for the effect of gyrotaxis, we must clarify the scaling of $\mathbf{V}_{g,c}$ with $S(x)$ and $S'(x)$. In (4.21e), we have shown that $\mathbf{V}_{g,c}$ depends on $\boldsymbol{\nabla}_{\mathbf{x}} g$. As g depends on the local velocity gradient, $\mathbf{V}_{g,c}$ depends on both the second-order derivative (gradient of gradient, which is a third-order tensor) and the gradient of the local velocity field, not just the gradient alone. Appendix C shows how $\mathbf{V}_{g,c}$ can be written explicitly as functions of the gradient and the second-order derivative of the local velocity field. In the context of a parallel flow, $\mathbf{V}_{g,c}$ would depend on both the local shear rate $S(x)$ and its gradient $S'(x)$. Vennamneni *et al.* (2020) showed that $\mathbf{V}_{g,c}$ scales with Pe_f^{-2} at high shear across different prescribed flows (c.f. fig. 4.10a) but did not distinguish the effect of $S(x)$ from that of $S'(x)$. In fig. 4.10c, we find that $\mathbf{V}_{g,c}$ scales with $S(x)^{-3}$ at high shear within the same flow. Note that in fig. 9d of Vennamneni *et al.* (2020), the $S(x)^{-3}$ scaling of $\mathbf{V}_{g,c}$ was also shown but was not apparent because they did not compute solutions at high enough Pe_f for the scaling to show. The reason behind the seemingly contradictory scaling (Pe_f^{-2} verses S^{-3}) of $\mathbf{V}_{g,c}$ was due to the contribution of $S'(x)$. Within the same parabolic flow (constant Pe_f), $S'(x)$ was kept constant

across x. Therefore, only $S(x)$ was varying across x and $\mathbf{V}_{g,c}(x)$ scales with $S(x)$ to the power -3. However, when compared across different parabolic flow profile with varying magnitude (changing Pe_f), both $S'(x)$ and $S(x)$ scale with Pe_f. In such a case, $\mathbf{V}_{g,c}$ scales with Pe_f^{-2}. Therefore, one can infer that $\mathbf{V}_{g,c} \propto S^{-3}S'(x)$, i.e. $\mathbf{V}_{g,c}$ also scales with $S'(x)$. This scaling is consistent with the formula derived in appendix C.

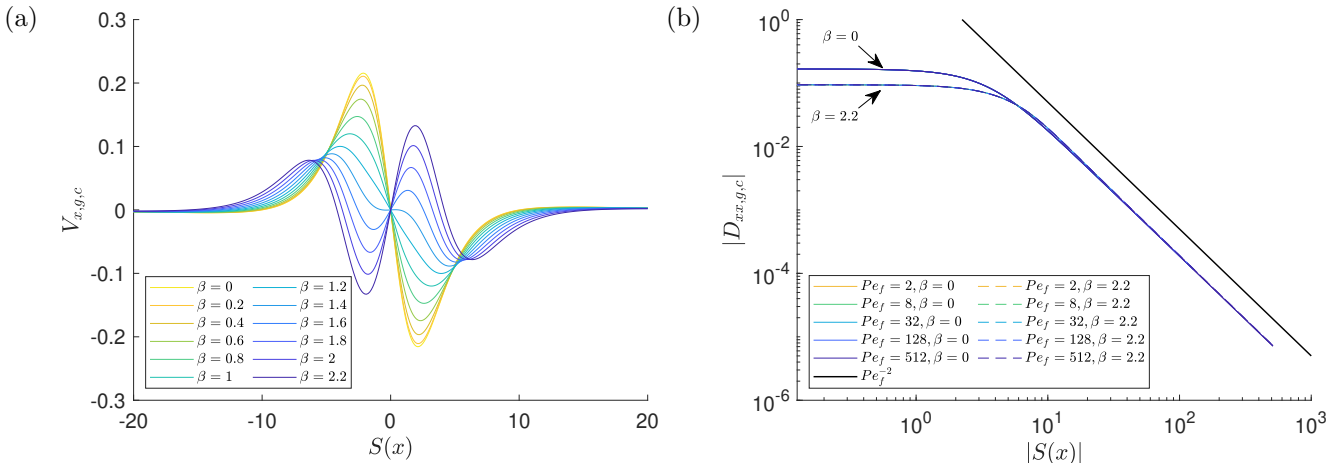

Figure 4.11: (a) The shear trapping advection in the x-direction ($V_{x,g,c}$) of non-spherical swimmers ($\alpha_0 = 0.31$) with various gyrotactic strength β against local shear $S(x)$ under a prescibed Poiseulli flow ($Pe_f = 64$).
(b) The absolute dispersion in the x-direction ($|D_{xx,g,c}|$) of non-spherical swimmers ($\alpha_0 = 0.31$) against local shear $S(x)$ in each prescibed Poiseulli flow. Results from swimmers with strong gyrotaxis ($\beta = 2.2$) are plotted in dashed lines, whereas those without gyrotaxis ($\beta = 0$) are plotted with solid lines. Note that results from the same β overlaps, implying that $|D_{xx,g,c}|$ is independent of the overall flow rate (Pe_f), but only depends on β and the local shear $S(x)$

Now, we can demonstrate the effect of gyrotaxis on shear trapping. In a Poiseulle flow profile, figs. 4.10a,c show that weak gyrotaxis has almost no impact on $\mathbf{V}_{g,c}$, but figs. 4.10b,d show that strong gyrotaxis, through the term $\boldsymbol{\nabla}_\mathbf{x} \cdot \langle \mathbf{p} \rangle_g$ in (4.21e), can reverse the direction of $\mathbf{V}_{g,c}$ at very low shear. Fig. 4.11a shows how increasing gyrotactic strength β can reverse the direction of $\mathbf{V}_{g,c}$ at low shear. However, as the shear rate S increases, $\boldsymbol{\nabla}_\mathbf{x} g$ becomes significant, such that it can reverse the $\mathbf{V}_{g,c}$ direction back into high-shear trapping we usually see in non-gyrotactic swimmers. Irrespective of β, the direction of $\mathbf{V}_{g,c}$ will reverse again from high-shear trapping (at a low shear) to low-shear trapping (at a high shear) as the shear rate S continue to increase. The reversal of $\mathbf{V}_{g,c}$ at low shear due to the term $\boldsymbol{\nabla}_\mathbf{x} \cdot \langle \mathbf{p} \rangle_g$ may explain why the direction of $\mathbf{V}_{g,c}$ in strongly gyrotactic swimmers is opposite to that of weakly gyrotactic or non-gyrotactic swimmers in fig. 4.3.

On the other hand, $D_{xx,g,c}$ only depends on the local shear and swimmers' property. Therefore, fig. 4.11b demonstrates a Pe_f^{-2} scaling irrespective of $S'(x)$, consistent with the observation by Vennamneni *et al.* (2020). Furthermore, the scaling does not seem to be strongly affected by β, as shown in fig. 4.11b.

4.9 Concluding remarks on the local approximation model

We have presented a method to transform the Smoluchowski equation into a transport equation exactly for a given flow field. The method involves decomposing the average Eulerian motility flux $Pe_s\langle\mathbf{p}\rangle_f n$ at a fixed location into the flux from the average Langrangian motility flux of individual particles $Pe_s\langle\mathbf{p}\rangle_g n$ and other contributions. The transformation has shown that $Pe_s\langle\mathbf{p}\rangle_g$ is different from $Pe_s\langle\mathbf{p}\rangle_f$ and only constitutes part of $Pe_s\langle\mathbf{p}\rangle_f$. The transformation also unveils the explicit form of the other drift and dispersion terms contributing to the overall average Eulerian motility. These terms include the shear trapping drift $\mathbf{V}_c$ and the particle dispersion $\boldsymbol{D}_c$ due to rotational diffusion. In addition, we have also discovered the drift $\mathbf{V}_{\partial t}$ due to the interaction between unsteadiness in orientation and orientational dynamics itself, the drift $\mathbf{V}_{D_T}$ and dispersion $\boldsymbol{D}_{D_T}$ arise from the interaction between translational diffusion and orientational dynamics, and the drift $\mathbf{V}_u$ from the interaction between passive advection of orientational distribution and orientational dynamics.

Although the transformation has revealed these new physical drifts and dispersions, which are physically interpretable in a transport equation, they cannot be directly used as a model due to the prerequisite to first obtain $\Psi(\mathbf{x},\mathbf{p},t)$ by solving the Smoluchowski equation directly. In this regard, this work has presented a new model based on the local approximation of the transformation, which only relies on the local flow information instead of the global flow configuration. By assuming that the time scale of the orientational dynamics is much faster than that of the spatial dynamics, we have approximated the orientational space probability density function $f(\mathbf{x},\mathbf{p},t) = \Psi/n$ by the homogeneous solution $g(\mathbf{x},t;\mathbf{p})$ of the orientational space operator $\mathcal{L}_p$, thereby circumventing the need to solve for Ψ. The approximation gives the same shear trapping drift $\mathbf{V}_{g,c}$ and the particle dispersion $\boldsymbol{D}_{g,c}$ as that of Bearon & Hazel (2015) and Vennamneni *et al.* (2020) when the particles have no taxes or diffusion, but it is also extendible to particles with taxes or translational diffusion. We have also made connections between $\boldsymbol{D}_{g,c}$ and the effective diffusivity $\boldsymbol{D}_G$ from model G. In a quiescent flow, the two tensors are equal. When the prescribed flow is parallel, $\boldsymbol{D}_{g,c}$ and $\boldsymbol{D}_G$ share the same cross-stream component (the xx component in verticle shear flows $\mathbf{u} = [0,0,W(x)]^T$ and zz component in horizontal shear flows $\mathbf{u} = [U(z),0,0]^T$). The comparison between the two models also highlighted the missing shear trapping drift $\mathbf{V}_{g,c}$ and the drift $\mathbf{V}_{D_T}$ and dispersion $\boldsymbol{D}_{D_T}$ from translational diffusion in model G. In particular, when the first-order drift $Pe_s\langle\mathbf{p}\rangle_g$ is small, the second-order drift from $Pe_s^2\mathbf{V}_{g,c}$ can become significant.

The numerical examples of suspensions in horizontal and vertical shear flows have further illustrated the importance of including $\mathbf{V}_{g,c}$. When $\langle\mathbf{p}\rangle_g$ from gyrotaxis is small, the local approximation method

better predicts the particle distribution than model G. In the extreme case where $\langle \mathbf{p} \rangle_g = 0$, model G would give an unphysical uniform distribution while the local approximation can accurately capture the shear trapping phenomena. Meanwhile, when $D_T \neq 0$, the local approximation method has also shown better prediction than model G because of the inclusion of $\mathbf{V}_{g,D_T}$ and $\boldsymbol{D}_{g,D_T}$ in addition to $\mathbf{V}_c$. Overall, this work has shown that the local approximation method is either on-par with or better than model G in approximating the transport of biased ABPs.

Chapter 5

Discussion

5.1 Using the Smoluchowski equation to directly model the formation of gyrotactic plumes

In chapters 2 and 3, we have focused on the formation of gyrotactic plume using model G. Then, chapter 4 has introduced the direct use of the Smoluchowski equation and the local approximation model in a prescribed flow field. In other words, we have ignored the effect of buoyancy in chapter 4. This section shall combine the knowledge of the previous chapters and re-model the gyrotactic plume using the full set of equations (1.11,1.18,1.19). Note that we will still consider the hydrodynamic contribution from the stresslet tensor negligible as the contribution from the buoyancy of swimmers remain dominant in this case.

While it is feasible to discretise the Smoluchowski equation directly under the parallel assumption, it is still significantly costly to compute all the solutions in the parameter space with the continuation algorithm introduced in §2.3.5. However, in the special case where swimmers are spherical and the flow is vertical, the analytical solution found in §4.7.1 might offer a shortcut. It was found that in this special case, the ratio between $\langle p_r \rangle$ and $D_{rr,c}$ from the exact transformation can be written out analytically, in the non-dimensionalisation of chapter 4, as

$$\frac{\langle p_r \rangle}{D_{rr,c}} = \frac{\beta S(x)}{Pe_s} = -\frac{\beta Pe_f}{2Pe_s}\frac{\partial W}{\partial x}. \tag{5.1}$$

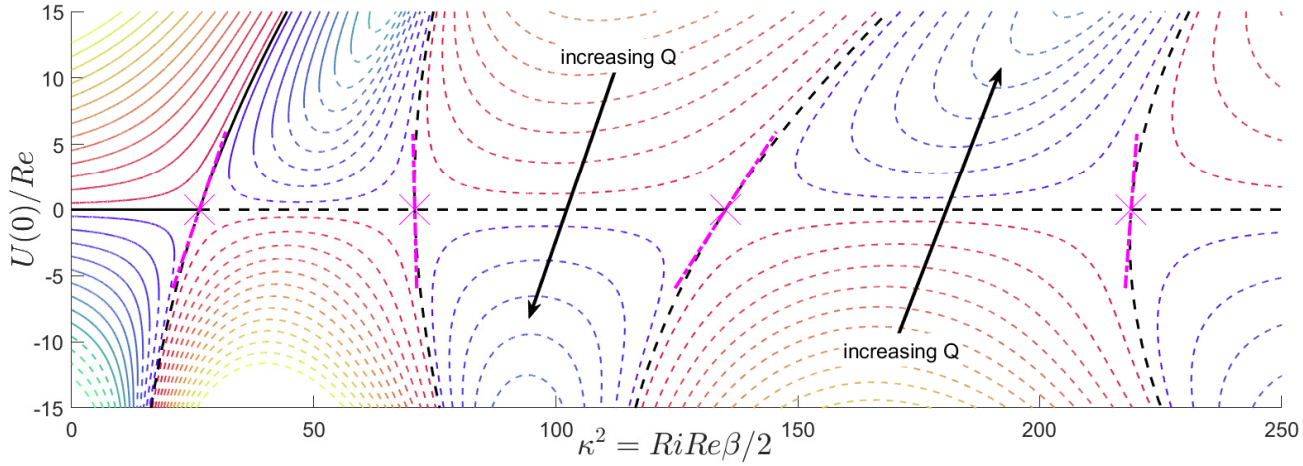

Figure 5.1: Contours of $U(0)/Re$ against κ^2 of the plume solutions at each given $Q \in [-2.5, 2.5]$, calculated using (5.2). The contour is valid for any dilute suspension of spherical gyrotactic swimmers subjected to a vertical flow. Here, each contour line in the $(U(0)/Re) - \kappa^2$ plane indicates the value of Q: black, $Q = 0$; blue to green, $Q \in [0.1, 2.5]$ with 0.2 increment; red to yellow, $Q \in [-2.5, -0.1]$ with -0.2 increment. The line type represents the stability of the solution: ——, stable; - - - -, unstable.

In the notation of chapters 2 and 3, (5.1) becomes

$$\frac{\langle p_r \rangle}{D_{rr,c}} = \beta S(x) = -\frac{\beta}{2d_r}\frac{\partial U}{\partial r}. \tag{5.2}$$

This relationship coincides exactly with the linearised model in §2.4.3 (c.f. eq. (2.16)). In other words, the linear line in fig. 2.8a representing the linearised model is coincidentally 'exact' if non-interacting swimmers are only contributing hydrodynamically via buoyancy. Meanwhile, fig. 2.10 shows the singularity in the 'exact' solution.

Therefore, the cusp bifurcation found in fig. 2.6a before the solution become singular is an artefact of the approximation of model G, which can be removed if the full the Smoluchowski equation is used to calculate the swimmer distribution instead of the approximation offered by model G.

In fig. 5.1, we have used (5.2) to recalculate the bifurcation diagram in fig. 3.2. The bifurcation point and the weakly nonlinear analysis remains the same because the analysis depends only on the linearised behaviour of $-\langle p_r \rangle / D_{rr}(S)$ at $S = 0$, which equals $(\beta/2)S$ regardless of the model used. However, the extended $Q = 0$ solution curves are smoothed out by the simpler linear relationship between $\langle p_r \rangle / D_{rr}$ and S. The linear relationship between $\langle p_r \rangle / D_{rr}$ and S also implies that, unlike fig. 3.2, the $Q = 0$ lines in fig. 5.1 are no longer specific to a certain β value but universal to all spherical gyrotactic swimmer suspensions in a vertical pipe.

However, it is important to reiterate that only in this special case, where swimmers are spherical and the flow is vertical, can $D_{rr,c}$ be written as a function of S. For other non-spherical swimmers,

$D_{rr,c}$ depends on the global solution, not just the local velocity field (e.g. §4.7.4). Nevertheless, its approximation $D_{rr,g,c}$ can be calculated at a function of S, and share same value as model G in a vertical shear flow.

5.2 Experimental implication

Given the bifurcations and singularities shown in chapters 2 and 3 and reiterated in the previous section, one can see that the gyrotactic plume formation in a dilute suspension is a complex dynamical system that exhibits multiple hystereses. Here we try to summarise the expected experimental observation based on the knowledge discovered in the thesis.

At a low enough $Ri < Ri_s$, a single plume is expected when a downflow is imposed. If the plume is focussed enough (high $N(0)$), the plume might become unstable to streamwise perturbation, and blips may form along the plume (fig. 2.16). This route to the formation of blips follows the blip instability mechanism suggested by Hwang & Pedley (2014*b*). If the flow rate is low enough, a sinuous instability mode might also arise (fig. 2.17b). On the other hand, if an upflow is imposed, gyrotactic swimmers will swim towards the wall. The stability of the upflowing solution has yet been analysed, partly due to the complication arising from the wall (see §5.3).

As Ri increases towards and beyond Ri_s, hysteresis occurs. At a low enough flow rate, where the crtical Richardson number Ri_c of the first saddle node of the respective flow rate Q is larger than Ri_s ($Q \lesssim 4$, c.f. fig. 2.10) and Ri is between Ri_s and Ri_c, the plume can either become steady (lower branch) or evolve towards a singularity ($N(0) \to \infty$) depending on the initial condition. If the initial condition is between the manifold of the lower branch and the unstable middle branch, the plume will likely evolve into the lower branch solution. However, if initially the plume is already beyond the manifold of the middle branch (e.g. high $N(0)$ or $-U(0)$), the system might evolve towards the singularity. Beyond the saddle node or if the flow rate is high ($Q \gtrsim 4$), there is no steady solution for a finite positive Q until after the first transcritical point. If a downflow is imposed in this regime, either the system will evolve toward the singularity, or the flow rate will not be achievable with a steady solution.

This saddle-node bifurcation might be demonstratable in an experiment. If a steady plume is formed at low Q and Ri smaller than that of the saddle node, one can perhaps 'kick' the system from the lower branch across the middle branch manifold and towards the singularity by increasing the velocity at the centre locally. Perhaps this can be achieved by the drop of a small but heavy sphere (e.g. a

ball bearing) at the centre of the pipe. Alternatively, one can gradually increase Ri from a lower branch solution by slowly adding more swimmers to the system while maintaining the same flow rate. Given the saddle-node bifurcation, a sudden loss of the steady solution is expected as Ri is gradually increased past the saddle node. Depending on how the pressure gradient or the flow rate is configured, the system may either suddenly evolve from the mild lower branch solution to a very sharp profile given by the singularity or struggle to achieve a steady solution with the targetted flow rate regardless of the pressure gradient.

As Ri further increases beyond the first transcritical point, multiple plumes are expected because κ^2 is increasing with Ri. As shown in fig. 5.1, the parameter $\kappa^2 = RiRe\beta/2$ determines the bifurcations. Although the solution profiles in fig. 3.1a remain axisymmetric, the increasing number of peak and trough in the steady profiles after each bifurcation strongly indicates the system's tendency to form multiple plumes. As $\kappa^2 = RiRe\beta/2$ scales with the average swimmer number density N^* and the pipe's cross-sectional area $(h^*)^2$, it matches the experimental observations where more plumes are formed in a wider container. However, the exact dynamical route towards multiple plumes remains to be solved. In chapter 3, the axisymmetric steady solutions at finite Q are nonlinear extensions of the Bessel functions from the linear and weakly nonlinear analysis of the $Q = 0$ solutions. So perhaps by the same technique, one can seek the solutions to multiple plumes by adding azimuthal variation to the Bessel functions and extending them nonlinearly at finite Q. We shall expect some of the unstable solutions (as represented by the dashed lines) in fig. 5.1 stabilises as we extend them to the azimuthally-varying variants, which may correspond to the multiple plumes observed in experiments.

Lastly, we shall discuss the singularity in the context of experimental observations. In §2.6.4, we have interpreted the threshold Ri_s at which singularity occurs as the maximum number of swimmers per unit length a plume can contain. It is a useful interpretation of the system behaviour within the physical presumption of the work. However, as the mathematical model evolves toward the singularity, physically, a singular solution is not possible. Rather, it signifies the breakdown of either the parallel assumption or the dilute assumption. The breakdown of the streamwise invariance, which results in blips, have already been discussed in §2.6.4. As for the dilute assumption, it may well be invalid near the centre of the pipe where the volume fraction becomes significant.

5.2.1 Semi-dilute effect

To address the issue of the far-field hydrodynamic interaction between swimmers, as discussed in §1.3.2, we have highlighted the parameter space where the dilute assumption would start breaking

down in grey in figs. 2.6a,2.10,2.18. The greyed-out areas represent the parameter regime in which the volume fraction at the pipe axis is higher than a threshold value of 2.5×10^{-2}.

As shown by the shaded area, the semi-dilute effect shall also play a role in preventing the singularity as $N(0)$ becomes very large. As the plume becomes very localised at the central axis where hydrodynamic interactions between swimmers start to dominate, Denissenko & Lukaschuk (2007) observed that the thickness of the plume stays roughly the same irrespective of flow rate and swimmer concentration. However, our scaling analysis in (2.18) suggested that the thickness shall scale with $N(0)^{-2}$ under the dilute assumption, which is tending towards zero as $N(0) \to \infty$. Therefore, it is likely that a semi-dilute effect has prevented $N(0)$ from tending toward infinity and the plume thickness from further shrinking. If the hypothesis of a universal plume thickness is true, then there exists a universal local profile $N_0(R)$ that can be calculated locally from the semi-dilute effect.

In the previous study by Ishikawa & Pedley (2007*a*) for a suspension of squirmers, it was shown that when the ambient flow is stationary, the rotational noise due to hydrodynamic interactions between randomly positioned swimmers scales with the volume fraction ϕ of the swimmers while the translational diffusivity decreases. We should note that in Ishikawa & Pedley (2007*a*), the rotational noise is purely due to higher-order hydrodynamic interactions in the semi-dilute regime, and not the swimmer's inherent rotational randomness. However, as an approximation, we can superpose an additional rotational diffusion due to swimmer-swimmer interactions. Therefore, although $N(0) \to \infty$ was found at $Ri \to Ri_s$ due to decreasing D_{rr} at high shear, in reality, the higher-order hydrodynamic interactions at such a high $N(0)$ might increase the effective rotational diffusivity d_r at the pipe axis. An increase in d_r will decrease $|S|$ and the magnitude of the ratio $\langle p_r \rangle_0 / D_{rr,0}$ locally (c.f. fig. 2.9), which might help attenuate the singularity. However, previous work such as Ishikawa & Pedley (2007*a*) was only performed in a quiescent ambient flow. The issue of how the effective d_r, and thereby $\langle p_r \rangle_0$ and $D_{rr,0}$, would change with the volume fraction in the presence of ambient shear has not been very well understood. In this respect, it would be interesting to see how additional modelling incorporating the semi-dilute effect would modify the plume in the future. Perhaps it can also shed light on the universal plume hypothesis.

5.3 Wall effect

It is well known that many biological swimmers tend to aggregate at the boundary in a confined suspension. The subject of how biological swimmers interact with an impenetrable surface has been

under intense investigation recently. Individually, swimmers' interaction with the surface depends on a range of factors, including but not limited to their geometry (e.g. Chen & Thiffeault, 2021), interactions with neighbouring swimmers (e.g. Drescher *et al.*, 2009), ciliary contact (Kantsler *et al.*, 2013) and their swimming mechanism (Spagnolie & Lauga, 2012). Some of these are the results of hydrodynamic interactions or nematic alignment with the boundary, but biological responses from the swimmers may also play a part in their aggregation at a surface (e.g. biofouling). Therefore, capturing the physical reality of swimmers at the boundary is a matter of understanding the microscopic dynamic of individual swimmers and their biology.

This work considers the swimmer suspension at the macroscopic level, in which swimmers are considered as a continuum via statistics. In this framework, we are not as concerned about how individual swimmer interacts with the boundary hydrodynamically or align with the boundary as how they swim towards the boundary in the first place. In other words, the current framework can capture wall-ward transport phenomena such as the high-shear trapping mechanism (Bearon & Hazel, 2015; Vennamneni *et al.*, 2020) or the wall accumulation due to a no-flux boundary condition (Ezhilan *et al.*, 2015) at the system's lengthscale, but not the microscopic interactions with the boundary that arise at the swimmers' lengthscale. Nevertheless, if one can represent these interactions as an extra term in the Smoluchowski equation or a suitable boundary condition in the $(\mathbf{x}, \mathbf{p})$-space, it might offer a way account for the microscopic wall-effect in the macroscopic framework. For example, the recent work by Chen & Thiffeault (2021) might offer some insight into how the geometry of a swimmer can be turned into a boundary condition in the Smoluchowski equation. After obtaining a suitable boundary condition for the Smoluchowski equation, it would be interesting to investigate how the transformation in §4.4 can be applied at the boundary in future work.

Lastly, it is worth noting that a no-flux boundary condition in the Smoluchowski equation is different from a no-flux boundary in the approximated transport equation in §4.5. Although both conditions only concern the $\mathbf{x}$-space flux, the swimming term $Pe_s\mathbf{p}\Psi$ implies that the $\mathbf{x}$-space flux is $\mathbf{p}$-dependent in the Smoluchowski equation. For example, in the absence of translation diffusion ($D_T = 0$), the Smoluchowski equation would become ill-posed unless the wall-normal component of $\langle \mathbf{p} \rangle_f$ is vanishing (c.f. Ezhilan *et al.*, 2015), while the transport equation would remain well-posed with the inclusion of an approximated dispersion tensor. The wall accumulation and the boundary-layer-like swimmer density profile near a no-flux wall have already been thoroughly discussed by Ezhilan *et al.* (2015), but it would be interesting to investigate further the physics of wall accumulation in the light of the transformed equation in future work.

Chapter 6

Conclusion

6.1 Summary of Thesis Achievements

In this thesis, we have modelled a suspension of gyrotactic microswimmers in a continuum framework. Much of the work focused on the formation of plumes and the subsequent blips in a dilute suspension using different transport models for the swimmers. We have compared their consequences in terms of the bifurcation and stability of the steady solution. Using the prediction of blips, we have concluded that the earlier Fokker-Planck model suggested by Pedley & Kessler (1990) is not as accurate as the later application of the generalised Taylor dispersion theory on gyrotactic swimmers (Manela & Frankel, 2003; Hill & Bees, 2002). The superiority of the GTD model is consistent with the recent experimental comparison of the two models in Croze *et al.* (2017).

The investigation into the formation of plumes and blips also led to the discovery of the complex bifurcation of the suspension in a verticle cylindrical pipe. At a low Richardson number, which represents the number of swimmers in the system or the pipe size, we have shown a threshold Ri_s at which the system tends towards a singular solution at the central axis of the pipe. The singularity is shown to be an extension of Kessler (1986), in which the concept of a limited capacity of swimmers in a single axisymmetric and steady plume was proposed. Our extension suggested that while it may be locally true, another lower branch of steady solutions can also exist beyond the Ri_s threshold, as long as the flow rate is low enough.

Furthermore, at an even higher Richardson number, we have shown a sequence of imperfect transcritical bifurcations of the uniform solution. Although the computed solutions remain axisymmetric, the bifurcating solutions strongly indicate the possibility of multiple plumes. Effectively, the analysis

has established how the increase in Richardson number promotes the formation of a bioconvective pattern with multiple plumes from a single plume.

While it is evident that the GTD model is more accurate than the *ad hoc* Fokker-Planck model, the GTD model is also limiting in applications. As we have demonstrated in chapter 4, it cannot capture the shear-trapping flux due to an inhomogeneous shear. It also cannot be used in a straining-dominant flow. To this end, we have proposed a new transport model for active Brownian particles (which are swimmers with negligible hydrodynamic contribution) based on the local approximation of an exact transformation of the Smoluchowski equation. The new model can capture the shear trapping phenomenon while being as accurate as the GTD model, especially in a weakly or non-gyrotactic swimmer suspension. It can also potentially overcome the limitation of the GTD model in a straining-dominant flow.

Along with the new model, we have also discovered many other drifts and dispersions that can arise from the interactions between the particles' orientational dynamics and other terms in the Smoluchowski equation, such as the unsteadiness in the orientational space due to an unsteady local flow field, the passive advection by the flow and the translational diffusion. These extra terms are highly non-trivial and may contribute to unexpected drifts or dispersions not foreseen by previous models. Further investigation into these terms may unveil more novel physics of swimmer/ABP suspensions.

6.2 Future Work and Outlook

6.2.1 Outstanding issues in the modelling of gyrotactic plumes and blips

Despite the progress made by this work in the theory describing gyrotactic plumes and blips, there is much work to be done to fully and accurately model the phenomenon. In the light of the transformation introduced in chapter 4, we have briefly shown how it might impact the conclusion drawn in chapters 2 and 3. Still, we have not recomputed the streamwise stability of the plume using the new model. Perhaps a better way to predict the blips is to directly linearise the Smoluchowski equation and compute the stability of the solution in §5.1. Although it will be more computationally expensive, it is feasible and can provide a more accurate result. As mentioned in §5.2, one of the challenges in predicting the blips is that theym can arise from an unsteady plume evolving towards the singularity. This challenge can be overcome by invoking a quasi-steady assumption and using the temporary

plume structure as the basic state for the streamwise stability analysis.

Another important aspect that has been neglected in the current work is the shape of the swimmers. In chapters 2 and 3 and §5.1, the swimmers are assumed spherical to simplify the work. However, as shown in chapter 4, the inhomogeneous shear may also contribute an extra shear trapping flux when the swimmers are elongated. In reality, neither *Chlamydomonas* nor *Dunaliella* species are spherical (although there is a lack of data on the shape of *Dunaliella* species). Therefore, it is important to include and study the effect of swimmers' shape in future work.

6.2.2 Future development of the local approximation model

As pointed out by a recent review (Bees, 2020), there is a gap between discrete modelling of individual swimmers/particles and their equivalent modelling at the continuum level. In particular, the restriction on the type of flow field imposed by the generalised Taylor dispersion model needs to be overcome to improve our understanding of the transport of swimmer/ABP suspension. The model presented in chapter 4, which is applicable to any flow field, is perhaps the most important contribution of this thesis. However, throughout the thesis, the analysis we have performed are predominantly in pure shear flows. We have yet to implement the new model in a straining-dominant flow. Therefore, the natural next step in developing the new model is to implement it in a general flow field that includes straining flow. The convective cell of Bearon *et al.* (2011) might be a good example to put the model to the test.

While the examples of chapter 4 focused mainly on gyrotactic ABPs, the framework presented can also be extended to other types of taxes, such as phototaxis, as well as other types of particle motions, such as the orientation-dependent sedimentation of elongated particles (e.g. Ardekani *et al.*, 2017; Clifton *et al.*, 2018; Lovecchio *et al.*, 2019). As mentioned in §1.4.2, as long as the taxis is an effective torque, it can be included in the operator $\mathcal{L}_p$. Then, the framework presented in chapter 4 to transform and locally approximate the orientational distribution will also be valid. Hence, the potential applications of the framework are vast.

6.2.3 Extending beyond the dilute assumption

The formation of the singular plume solution shows that there is always a possibility where swimmers self-aggregate and break the dilute assumption. Therefore, the current dilute framework needs to

be extended to the semi-dilute regime. To this end, pioneering work by Ishikawa *et al.* (2006, 2007) and Ishikawa & Pedley (2007*a*,*b*) based on discrete Stokesian simulation might offer a way to correct for the hydrodynamic interactions at the continuum level, as discussed in §5.2.1. Another important challenge to overcome is the interaction with the wall, which has already been thoroughly discussed in §5.3. Much work is still needed to incorporate these far- and near-field hydrodynamic interactions into the new model.

6.2.4 Applying the work to bioconvection and beyond

One of the objectives of the thesis is to better model and analyse the bioconvection of gyrotactic microswimmers. While we have not directly modelled the phenomenon, the work on gyrotactic plume, especially chapter 3, has provided some important foundational knowledge on gyrotactic bioconvection. To better connect this work on gyrotactic plumes with bioconvection, the work in chapter 3 shall be extended azimuthally, either with the new model or with the Smoluchowski equation. As mentioned in §5.2, one shall seek a stable solution with multiple plumes using the same continuation technique. The suggested analysis might provide crucial hints on the route toward a fully developed bioconvection from a dynamical system perspective. Also, previous predictions on the wavelength are based on outdated transport models, such as the primitive model (Ghorai & Hill, 2000, 2007; Ghorai *et al.*, 2015) or the Fokker-Planck model (Bees & Hill, 1999). The suggested analysis will likely give a more accurate prediction of the horizontal wavelength of gyrotactic plumes in a deep suspension. One may also further extend the analysis to include the finite-depth effect, similar to how Bees & Hill (1998) extended the previous analysis.

As shown by this work, gyrotactic bioconvection is a perplexing phenomenon and embodies many aspects of biophysics, ranging from the suspension dynamics, the high and low Reynolds number fluid mechanics to the microscopic biomechanics of the individual swimmers. Studying bioconvection helps us further the knowledge on these topics, which can then be applied to many applications, such as the gyrotactic trapping and patchiness of phytoplankton in the ocean and the modelling of biofuel production. This work has advanced the physics of bioconvection from the dynamical system perspective and has overcome the challenge of developing a transport model applicable in a general flow field. However, our work has also exposed many more challenges ahead, such as the tendency for a gyrotactic suspension to run into the semi-dilute regime due to the singularity. The accurate modelling of bioconvection remains an important milestone in the field of active suspension.

Bibliography

Alt, W. 1980 Biased random walk models for chemotaxis and related diffusion approximations. *J. Math. Biol.* **9** (2), 147–177.

Ardekani, M. N., Sardina, G., Brandt, L., Karp-Boss, L., Bearon, R. N. & Variano, E. A. 2017 Sedimentation of inertia-less prolate spheroids in homogenous isotropic turbulence with application to non-motile phytoplankton. *J. Fluid Mech.* **831**, 655–674.

Aris, R. & Taylor, G. I. 1956 On the dispersion of a solute in a fluid flowing through a tube. *Proc. R. Soc. A Math. Phys. Sci.* **235** (1200), 67–77.

Batchelor, G. K. 1970 The stress system in a suspension of free-force particles. *J. Fluid Mech.* **41**, 545–570.

Batchelor, G. K. 1972 Sedimentation in a dilute dispersion of spheres. *J. Fluid Mech.* **52** (2), 245–268.

Bearon, R. N., Bees, M. A. & Croze, O. A. 2012 Biased swimming cells do not disperse in pipes as tracers: A population model based on microscale behaviour. *Phys. Fluids* **24** (12), 121902.

Bearon, R. N. & Hazel, A. L. 2015 The trapping in high-shear regions of slender bacteria undergoing chemotaxis in a channel. *J. Fluid Mech.* **771**, R3.

Bearon, R. N., Hazel, A. L. & Thorn, G. J. 2011 The spatial distribution of gyrotactic swimming micro-organisms in laminar flow fields. *J. Fluid Mech.* **680**, 602–635.

Bees, M. A. 2020 Advances in Bioconvection. *Annu. Rev. Fluid Mech.* **52** (1), 449–476.

Bees, M. A. & Croze, O. A. 2010 Dispersion of biased swimming micro-organisms in a fluid flowing through a tube. *Proc. R. Soc. A Math. Phys. Eng. Sci.* **466**, 2057–2077.

Bees, M. A. & Croze, O. A. 2014 Mathematics for streamlined biofuel production from unicellular algae. *Biofuels* **5** (1), 53–65.

Bees, M. A. & Hill, N. A. 1998 Linear bioconvection in a suspension of randomly swimming, gyrotactic micro-organisms. *Phys. Fluids* **10** (8), 1864–1881.

Bees, M. A. & Hill, N. A. 1999 Non-linear bioconvection in a deep suspension of gyrotactic swimming micro-organisms. *J. Math. Biol.* **38** (2), 135–168.

Bees, M. A., Hill, N. A. & Pedley, T. J. 1998 Analytical approximations for the orientation distribution of small dipolar particles in steady shear flows. *J. Math. Biol.* **36**, 269–298.

Berg, H. C. 1993 *Random Walks in Biology*, expanded edn. Princeton, N.J.: Princeton University Press.

Berg, H. C. 2004 *E. Coli in Motion*. New York: Springer-Verlag.

Brady, J. F. & Bossis, G. 1988 Stokesian Dynamics. *Annu. Rev. Fluid Mech.* **20** (1), 111–157.

Brenner, H. 1980 General Theory of Taylor Dispersion Phenomena. *PCH Physicochem. Hydrodyn.* **1** (2-3), 91–123.

Bretherton, F. P. 1962 The motion of rigid particles in a shear flow at low Reynolds number. *J. Fluid Mech.* **14** (2), 284–304.

Chen, H. & Thiffeault, J.-L. 2021 Shape matters: A Brownian microswimmer in a channel. *J. Fluid Mech.* **916**, A15.

Chen, S. B. & Jiang, L. 1999 Orientation distribution in a dilute suspension of fibers subject to simple shear flow. *Physics of Fluids* **11** (10), 2878–2890.

Childress, S., Levandowsky, M. & Spiegel, E. A. 1975 Pattern formation in a suspension of swimming micro-organisms: Equations and stability theory. *J. Fluid Mech.* **69** (3), 591–613.

Clifton, W., Bearon, R. N. & Bees, M. A. 2018 Enhanced sedimentation of elongated plankton in simple flows. *IMA J. Appl. Math.* **83** (4), 743–766.

Cortez, R. 2001 The Method of Regularized Stokeslets. *SIAM J. Sci. Comput.* **23** (4), 1204–1225.

Croze, O. A., Ashraf, E. E. & Bees, M. A. 2010 Sheared bioconvection in a horizontal tube. *Phys. Biol.* **7** (4).

Croze, O. A., Bearon, R. N. & Bees, M. A. 2017 Gyrotactic swimmer dispersion in pipe flow: Testing the theory. *J. Fluid Mech.* **816**, 481–506.

Croze, O. A., Sardina, G., Ahmed, M., Bees, M. A. & Brandt, L. 2013 Dispersion of swimming algae in laminar and turbulent channel flows: Consequences for photobioreactors. *J. R. Soc. Interface* **10** (81), 20121041.

Cussler, E. L. 2009 Dispersion. In *Diffusion: Mass Transfer in Fluid Systems*, 3rd edn., pp. 95–110. Cambridge University Press.

Denissenko, P. & Lukaschuk, S. 2007 Velocity profiles and discontinuities propagation in a pipe flow of suspension of motile microorganisms. *Phys. Lett. A* **362** (4), 298–304.

Doi, M. & Edwards, S. 1988 Brownian Motion. In *The Theory of Polymer Dynamics*, *The International Series of Monographs on Physics* 73, pp. 46–90. Oxford: Oxford University Press.

Dombrowski, C., Cisneros, L., Chatkaew, S., Goldstein, R. E. & Kessler, J. O. 2004 Self-Concentration and Large-Scale Coherence in Bacterial Dynamics. *Phys. Rev. Lett.* **93** (9), 098103.

Drazin, P. G. 2002 Weakly Nonlinear Theory. In *Introduction to Hydrodynamic Stability*, chap. 5.2, pp. 74–82. Cambridge: Cambridge University Press.

Drescher, K., Dunkel, J., Cisneros, L. H., Ganguly, S. & Goldstein, R. E. 2011 Fluid dynamics and noise in bacterial cell-cell and cell-surface scattering. *Proc. Natl. Acad. Sci. U.S.A.* **108** (27), 10940–5.

Drescher, K., Goldstein, R. E., Michel, N., Polin, M., & Tuval, I. 2010*a* Direct measurement of the flow field around swimming microorganisms. *Phys. Rev. Lett.* **105** (16), 1–4.

Drescher, K., Goldstein, R. E. & Tuval, I. 2010*b* Fidelity of adaptive phototaxis. *Proc. Natl. Acad. Sci. U.S.A.* **107** (25), 11171–11176.

Drescher, K., Leptos, K. C., Tuval, I., Ishikawa, T., Pedley, T. J. & Goldstein, R. E. 2009 Dancing Volvox: Hydrodynamic Bound States of Swimming Algae. *Phys. Rev. Lett.* **102** (16), 168101.

Dunkel, J., Heidenreich, S., Drescher, K., Wensink, H. H., Bär, M. & Goldstein, R. E. 2013 Fluid Dynamics of Bacterial Turbulence. *Phys. Rev. Lett.* **110** (22), 228102.

Durham, W. M., Climent, E., Barry, M., De Lillo, F., Boffetta, G., Cencini, M. & Stocker, R. 2013 Turbulence drives microscale patches of motile phytoplankton. *Nat. Commun.* **4**, 1–7.

Durham, W. M., Kessler, J. O. & Stocker, R. 2009 Disruption of vertical motility by shear triggers formation of thin phytoplankton layers. *Science* **323** (5917), 1067–1070.

Durham, W. M. & Stocker, R. 2012 Thin Phytoplankton Layers: Characteristics, Mechanisms, and Consequences. *Annu. Rev. Mar. Sci.* **4** (1), 177–207.

Ezhilan, B., Alonso-Matilla, R. & Saintillan, D. 2015 On the distribution and swim pressure of run-and-tumble particles in confinement. *J. Fluid Mech.* **781**, R4.

Frankel, I. & Brenner, H. 1989 On the foundations of generalized Taylor dispersion theory. *J. Fluid Mech.* **204**, 97–119.

Frankel, I. & Brenner, H. 1991 Generalized Taylor dispersion phenomena in unbounded homogeneous shear flows. *J. Fluid Mech.* **230**, 147–181.

Frankel, I. & Brenner, H. 1993 Taylor dispersion of orientable brownian particles in unbounded homogeneous shear flows. *J. Fluid Mech.* **255**, 129–156.

Ghorai, S. & Hill, N. A. 1999 Development and stability of gyrotactic plumes in bioconvection. *J. Fluid Mech.* **400**, 1–31.

Ghorai, S. & Hill, N. A. 2000 Wavelengths of gyrotactic plumes in bioconvection. *Bull. Math. Biol.* **62** (3), 429–450.

Ghorai, S. & Hill, N. A. 2007 Gyrotactic bioconvection in three dimensions. *Phys. Fluids* **19** (5), 054107.

Ghorai, S., Singh, R. & Hill, N. A. 2015 Wavelength Selection in Gyrotactic Bioconvection. *Bull. Math. Biol.* **77** (6), 1166–1184.

Guasto, J. S., Johnson, K. A. & Gollub, J. P. 2010 Oscillatory Flows Induced by Microorganisms Swimming in Two Dimensions. *Phys. Rev. Lett.* **105** (16), 168102.

Guazzelli, É. & Hinch, J. 2011 Fluctuations and Instability in Sedimentation. *Annu. Rev. Fluid Mech.* **43** (1), 97–116.

Hill, N. A. & Bees, M. A. 2002 Taylor dispersion of gyrotactic swimming micro-organisms in a linear flow. *Phys. Fluids* **14** (8), 2598–2605.

Hill, N. A. & Häder, D.-P. 1997 A Biased Random Walk Model for the Trajectories of Swimming Micro-organisms. *J. Theor. Biol.* **186** (4), 503–526.

Hill, N. A., Pedley, T. J. & Kessler, J. O. 1989 Growth of bioconvection patterns in a suspension of gyrotactic micro-organisms in a layer of finite depth. *J. Fluid Mech.* **208**, 509–543.

Hinch, E. J. 1977 An averaged-equation approach to particle interactions in a fluid suspension. *J. Fluid Mech.* **83** (4), 695–720.

Hinch, E. J. & Leal, L. G. 1972*a* The effect of Brownian motion on the rheological properties of a suspensions of non-spherical particles. *J. Fluid Mech.* **52** (4), 683–712.

Hinch, E. J. & Leal, L. G. 1972*b* Note on the rheology of a dilute suspension of dipolar spheres with weak Brownian couples. *J. Fluid Mech.* **56** (4), 803–813.

Hinch, J. 2010 A perspective of Batchelor's research in micro-hydrodynamics. *J. Fluid Mech.* **663**, 8–17.

Hwang, Y. & Pedley, T. J. 2014*a* Bioconvection under uniform shear: Linear stability analysis. *J. Fluid Mech.* **738**, 522–562.

Hwang, Y. & Pedley, T. J. 2014*b* Stability of downflowing gyrotactic microorganism suspensions in a two-dimensional vertical channel. *J. Fluid Mech.* **749**, 750–777.

Ishikawa, T. & Pedley, T. J. 2007*a* Diffusion of swimming model micro-organisms in a semi-dilute suspension. *J. Fluid Mech.* **588**, 437–462.

Ishikawa, T. & Pedley, T. J. 2007*b* The rheology of a semi-dilute suspension of swimming model micro-organisms. *J. Fluid Mech.* **588**, 399–435.

Ishikawa, T., Pedley, T. J. & Yamaguchi, T. 2007 Orientational relaxation time of bottom-heavy squirmers in a semi-dilute suspension. *J. Theor. Biol.* **249** (2), 296–306.

Ishikawa, T., Simmonds, M. P. & Pedley, T. J. 2006 Hydrodynamic interaction of two swimming model micro-organisms. *J. Fluid Mech.* **568**, 119–160.

Jeffery, G. B. 1922 The motion of ellipsoidal particles immersed in a viscous fluid. *Proc. R. Soc. A Math. Phys. Eng. Sci.* **102**, 161–179.

Jiang, W. & Chen, G. 2019 Dispersion of active particles in confined unidirectional flows. *J. Fluid Mech.* **877**, 1–34.

Jiang, W. & Chen, G. 2020 Dispersion of gyrotactic micro-organisms in pipe flows. *J. Fluid Mech.* **889**, A18.

Kantsler, V., Dunkel, J., Polin, M. & Goldstein, R. E. 2013 Ciliary contact interactions dominate surface scattering of swimming eukaryotes. *Proc. Natl. Acad. Sci. U.S.A.* **110** (4), 1187–1192.

Kessler, J. O. 1984 Gyrotactic Buoyant Convection and Spontaneous Pattern Formation in Algal Cell Cultures. In *Nonequilibrium Cooperative Phenomena in Physics and Related Fields* (ed. Manuel G Velarde), pp. 241–248. Boston, MA: Springer US.

Kessler, J. O. 1985*a* Co-operative and concentrative phenomena of swimming micro-organisms. *Contemp. Phys.* **26**, 147–166.

Kessler, J. O. 1985*b* Hydrodynamic focusing of motile algal cells. *Nature* **313**, 218–220.

Kessler, J. O. 1986 Individual and collective fluid dynamics of swimming cells. *J. Fluid Mech.* **173**, 191–205.

Kessler, J. O., Hill, N. A. & Hader, D.-P. 1992 Orientation of swimming flagellates by simultaneously acting external factors. *J. Phycol.* **28** (6), 816–822.

Kim, S. & Karrila, S. J. 1991 *Microhydrodynamics: Principles and Selected Applications*. Boston: Butterworth-Heinemann.

Koch, D. L. & Subramanian, G. 2011 Collective Hydrodynamics of Swimming Microorganisms: Living Fluids. *Annu. Rev. Fluid Mech.* **43** (1), 637–659.

Lauga, E. 2020 *The fluid dynamics of cell motility*. *Cambridge texts in applied mathematics* 62. Cambridge, United Kingdom: Cambridge University Press.

Lauga, E. & Powers, T. R. 2009 The hydrodynamics of swimming microorganisms. *Reports Prog. Phys.* **72** (9), 096601.

Linkmann, M., Boffetta, G., Marchetti, M. C. & Eckhardt, B. 2019 Phase transition to large scale coherent structures in two-dimensional active matter turbulence. *Phys. Rev. Lett.* **122** (21), 214503.

Lovecchio, S., Climent, E., Stocker, R. & Durham, W. M. 2019 Chain formation can enhance the vertical migration of phytoplankton through turbulence. *Sci. Adv.* **5** (10), eaaw7879.

Lushi, E., Wioland, H. & Goldstein, R. E. 2014 Fluid flows created by swimming bacteria drive self-organization in confined suspensions. *Proc. Natl. Acad. Sci. U.S.A.* **111** (27), 9733–9738.

Manela, A. & Frankel, I. 2003 Generalized Taylor dispersion in suspensions of gyrotactic swimming micro-organisms. *J. Fluid Mech.* **490**, 99–127.

Marchetti, M. C., Joanny, J. F., Ramaswamy, S., Liverpool, T. B., Prost, J., Rao, M. & Simha, R. A. 2013 Hydrodynamics of soft active matter. *Rev. Mod. Phys.* **85** (3), 1143–1189.

Maretvadakethope, S., Keaveny, E. E. & Hwang, Y. 2019 The instability of gyrotactically trapped cell layers. *J. Fluid Mech.* **868**, R5.

Meseguer, A. & Trefethen, L. N. 2003 Linearized pipe flow to Reynolds number 10^7. *J. Comput. Phys.* **186** (1), 178–197.

O'Malley, S. & Bees, M. A. 2012 The Orientation of Swimming Biflagellates in Shear Flows. *Bull. Math. Biol.* **74** (1), 232–255.

Pedley, T. J. 2010*a* Collective Behaviour of Swimming Micro-organisms. *Exp. Mech.* **50** (9), 1293–1301.

Pedley, T. J. 2010*b* Instability of uniform micro-organism suspensions revisited. *J. Fluid Mech.* **647**, 335–359.

Pedley, T. J., Hill, N. A. & Kessler, J. O. 1988 The growth of bioconvection patterns in a uniform suspension of gyrotactic micro-organisms. *J. Fluid Mech.* **195**, 223–237.

Pedley, T. J. & Kessler, J. O. 1990 A new continuum model for suspensions of gyrotactic micro-organisms. *J. Fluid Mech.* **212**, 155–182.

Pedley, T. J. & Kessler, J. O. 1992 Hydrodynamic Phenomena In Suspensions Of Swimming Microorganisms. *Annu. Rev. Fluid Mech.* **24** (1), 313–358.

Platt, J. R. 1961 "Bioconvection Patterns" in Cultures of Free-Swimming Organisms. *Science* **133** (3466), 1766–1767.

Purcell, E. M. 1977 Life at low reynolds number. *J. Biol. Chem.* **45**, 3.

Rusconi, R., Guasto, J. S. & Stocker, R. 2014 Bacterial transport suppressed by fluid shear. *Nat. Phys.* **10** (3), 212–217.

Saintillan, D. 2010 The Dilute Rheology of Swimming Suspensions: A Simple Kinetic Model. *Exp Mech* **50** (9), 1275–1281.

Saintillan, D. 2018 Rheology of Active Fluids. *Annu. Rev. Fluid Mech.* **50** (1), 563–592.

Saintillan, D. & Shelley, M. J. 2007 Orientational order and instabilities in suspensions of self-locomoting rods. *Phys. Rev. Lett.* **99** (5), 1–4.

Saintillan, D. & Shelley, M. J. 2008*a* Instabilities and pattern formation in active particle suspensions: Kinetic theory and continuum simulations. *Phys. Rev. Lett.* **100** (17), 178103.

Saintillan, D. & Shelley, M. J. 2008*b* Instabilities, pattern formation, and mixing in active suspensions. *Phys. Fluids* **20** (12), 123304.

Saintillan, D. & Shelley, M. J. 2015 Theory of Active Suspensions. In *Complex Fluids in Biological Systems*, pp. 319–355. New York: Springer.

Schmid, P. J. & Henningson, D. S. 1994 Optimal energy density growth in Hagen–Poiseuille flow. *J. Fluid Mech.* **277**, 197–225.

Schmid, P. J. & Henningson, D. S. 2001 *Stability and Transition in Shear Flows*, *Applied Mathematical Sciences*, vol. 142. New York: Springer.

Schoeller, S. F. & Keaveny, E. E. 2018 From flagellar undulations to collective motion: Predicting the dynamics of sperm suspensions. *J. R. Soc. Interface* **15** (140), 20170834.

Schoeller, S. F., Townsend, A. K., Westwood, T. A. & Keaveny, E. E. 2021 Methods for suspensions of passive and active filaments. *J. Comput. Phys.* **424** (1), 109846.

Simha, R. A. & Ramaswamy, S. 2002 Hydrodynamic Fluctuations and Instabilities in Ordered Suspensions of Self-Propelled Particles. *Phys. Rev. Lett.* **89** (5), 058101.

Smith, D. J. 2009 A boundary element regularized Stokeslet method applied to cilia- and flagella-driven flow. *Proc. R. Soc. A Math. Phys. Eng. Sci.* **465** (2112), 3605–3626.

Smoluchowski, M. 1906 Zur kinetischen Theorie der Brownschen Molekularbewegung und der Suspensionen. *Annalen der Physik* **326** (14), 756–780.

Son, K., Menolascina, F. & Stocker, R. 2016 Speed-dependent chemotactic precision in marine bacteria. *Proc. Natl. Acad. Sci. U.S.A.* **113** (31), 8624–8629.

Spagnolie, S. E. & Lauga, E. 2012 Hydrodynamics of self-propulsion near a boundary: Predictions and accuracy of far-field approximations. *J. Fluid Mech.* **700**, 105–147.

Subramanian, G. & Koch, D. L. 2009 Critical bacterial concentration for the onset of collective swimming. *J. Fluid Mech.* **632**, 359–400.

Taylor, G. I. 1953 Dispersion of soluble matter in solvent flowing slowly through a tube. *Proc. R. Soc. A Math. Phys. Sci.* **219** (1137), 186–203.

Thom, R. 1989 *Structural Stability And Morphogenesis*. CRC Press.

Toner, J. & Tu, Y. 1998 Flocks, herds, and schools: A quantitative theory of flocking. *Phys. Rev. E* **58** (1), 4828.

Townsend, A., Wilber, H. & Wright, G. B. 2016 Computing with Functions in Spherical and Polar Geometries I. The Sphere. *SIAM J. Sci. Comput.* **38** (4), C403–C425.

Tătulea-Codrean, M. & Lauga, E. 2018 Artificial chemotaxis of phoretic swimmers: Instantaneous and long-time behaviour. *J. Fluid Mech.* **856**, 921–957.

Vennamneni, L., Nambiar, S. & Subramanian, G. 2020 Shear-induced migration of microswimmers in pressure-driven channel flow. *J. Fluid Mech.* **890**, A15.

Vladimirov, V. A., Denissenko, P. V., Pedley, T. J., Wu, M. & Moskalev, I. S. 2000 Algal motility measured by a laser-based tracking method. *Mar. Freshw. Res.* **51** (6), 589–600.

Wan, K. Y. & Goldstein, R. E. 2014 Rhythmicity, Recurrence, and Recovery of Flagellar Beating. *Phys. Rev. Lett.* **113** (23), 238103.

Weideman, J. A. C. & Reddy, S. C. 2000 A MATLAB Differentiation Matrix Suite. *ACM Trans. Math. Softw.* **26** (4), 465–519.

Wensink, H. H., Dunkel, J., Heidenreich, S., Drescher, K., Goldstein, R. E., Löwen, H. & Yeomans, J. M. 2012 Meso-scale turbulence in living fluids. *Proc. Natl. Acad. Sci. U.S.A.* **109** (36), 14308.

Williams, C. R. & Bees, M. A. 2011 Photo-gyrotactic bioconvection. *J. Fluid Mech.* **678**, 41–86.

Wioland, H., Woodhouse, F. G., Dunkel, J., Kessler, J. O. & Goldstein, R. E. 2013 Confinement Stabilizes a Bacterial Suspension into a Spiral Vortex. *Phys. Rev. Lett.* **110** (26), 268102.

Zeeman, E. C. 1976 Catastrophe Theory. *Sci. Am.* **234** (4), 65–83.

Appendix A

Detailed formulae for the stability analysis of the gyrotactic plume

A.1 Linearised equations for perturbed average orientation and diffusivity

In (2.10e) the values of $\boldsymbol{D}'_m$ and $\langle \mathbf{p} \rangle'$ are required. To obtain these values, we first need to compute $g(\mathbf{p})'$ with a perturbation of $\boldsymbol{\Omega}'$:

$$\boldsymbol{\nabla}_{\mathbf{p}} \cdot \left[\lambda[\hat{\mathbf{k}} - (\hat{\mathbf{k}} \cdot \mathbf{p})\mathbf{p}]g' + \frac{1}{2}\boldsymbol{\Omega} \wedge \mathbf{p}g' \right] - \nabla_p^2 g' = -\boldsymbol{\nabla}_{\mathbf{p}} \cdot \left[\frac{1}{2}\boldsymbol{\Omega}' \wedge \mathbf{p}g \right]. \tag{A.1}$$

Then, $\langle \mathbf{p} \rangle'$ can be computed with $g(\mathbf{p})'$ by

$$\langle \mathbf{p} \rangle' = \int_{S_p} \mathbf{p}g'(\mathbf{p}) \, d^2\mathbf{p}. \tag{A.2}$$

For model F, $\boldsymbol{D}'_F$ is obtained easily by (Hwang & Pedley, 2014*b*)

$$\boldsymbol{D}'_F = \tau(\langle \mathbf{pp} \rangle' - \langle \mathbf{p} \rangle \langle \mathbf{p} \rangle' - \langle \mathbf{p} \rangle \langle \mathbf{p} \rangle'). \tag{A.3}$$

However, for model G, the process is more involved, as $\boldsymbol{D}'_G$ not only depends on $\boldsymbol{\Omega}'$, but also $\boldsymbol{G}' = \boldsymbol{\nabla}\mathbf{u}'$. Hence,

$$\boldsymbol{D}'_G = \int_{S_p} \left[\mathbf{b}'_{GTD}\mathbf{p} + \frac{\mathbf{b}'_{GTD}\mathbf{b}_{GTD}}{g} \cdot \boldsymbol{G} + \frac{\mathbf{b}_{GTD}\mathbf{b}'_{GTD}}{g} \cdot \boldsymbol{G} \right.$$

$$-\frac{\mathbf{b}_{GTD}\mathbf{b}_{GTD}f'}{g^2}\cdot\boldsymbol{G}+\frac{\mathbf{b}_{GTD}\mathbf{b}_{GTD}}{g}\cdot\boldsymbol{G'}\Bigg]^{sym}d^2\mathbf{p}, \tag{A.4}$$

where the perturbed $\mathbf{b}'_{GTD}$ due to $\boldsymbol{G'}$ (and $\boldsymbol{\Omega}'$) is needed. We can compute $\mathbf{b}'_{GTD}$ by solving

$$\begin{aligned}\boldsymbol{\nabla}_{\mathbf{p}}\cdot[\dot{\mathbf{p}}\mathbf{b}'_{GTD}]-\nabla_p^2\mathbf{b}'_{GTD}-\mathbf{b}'_{GTD}\cdot\boldsymbol{G} &= -\langle\mathbf{p}\rangle' g+(\mathbf{p}-\langle\mathbf{p}\rangle)g'+\mathbf{b}_{GTD}\cdot\boldsymbol{G'}\\ &\quad -\boldsymbol{\nabla}_{\mathbf{p}}\cdot\left[\frac{1}{2}(\boldsymbol{\Omega}'\wedge\mathbf{p})\mathbf{b}_{GTD}\right].\end{aligned} \tag{A.5}$$

In practice, the left-hand side of (A.1) and (A.5) is the same linear operator used in (2.2d) and (1.25a), while their right-hand side can be viewed as different forcing terms. Therefore, g' and $\mathbf{b}'_{GTD}$ can be obtained by imposing the different forcing term on the right-hand side of (A.1) and (A.5), similarly to the framework of Hwang & Pedley (2014*a*,*b*).

A.2 Equations for linear stability

Using the framework in Appendix A.1, $\langle\mathbf{p}\rangle'$ and $\boldsymbol{D}'_m$ can be written as linear combinations of the components of $\boldsymbol{\Omega}'$ (models F and G) and $\boldsymbol{G'}$ (model G), hence also as a linear combination of $\mathbf{u}'$. This allows us to write $\langle\mathbf{p}\rangle'$ and $\boldsymbol{D}'_m$ as follows:

$$\langle p_r\rangle' = \frac{\xi_1}{d_r}\left(\frac{\partial u'_r}{\partial z}-\frac{\partial u'_z}{\partial r}\right); \tag{A.6a}$$

$$\langle p_\psi\rangle' = \frac{\xi_2}{d_r}\left(\frac{\partial u'_r}{\partial z}-\frac{\partial u'_z}{\partial r}\right); \tag{A.6b}$$

$$\langle p_z\rangle' = \frac{\xi_3}{d_r}\left(\frac{1}{r}\frac{\partial u'_z}{\partial\psi}-\frac{\partial u'_\psi}{\partial z}\right)+\frac{\xi_4}{rd_r}\left(\frac{\partial(ru'_\psi)}{\partial r}-\frac{\partial u'_r}{\partial\psi}\right); \tag{A.6c}$$

$$\begin{aligned}D'_{rr} &= \frac{1}{d_r}\left(\xi_5\frac{\partial u'_z}{\partial r}+\xi_6\frac{\partial u'_r}{\partial r}+\xi_7\frac{\partial u'_\psi}{\partial r}+\xi_8\frac{\partial u'_z}{\partial z}+\xi_9\frac{\partial u'_r}{\partial z}+\xi_{10}\frac{\partial u'_\psi}{\partial z}\right.\\ &+ \left.\frac{1}{r}\left(\xi_{11}\frac{\partial u'_z}{\partial\psi}+\xi_{12}\left(\frac{\partial u'_r}{\partial\psi}-u'_\psi\right)+\xi_{13}\left(\frac{\partial u'_\psi}{\partial\psi}+u'_r\right)\right)\right);\end{aligned} \tag{A.6d}$$

$$\begin{aligned}D'_{rz} &= \frac{1}{d_r}\left(\xi_{14}\frac{\partial u'_z}{\partial r}+\xi_{15}\frac{\partial u'_r}{\partial r}+\xi_{16}\frac{\partial u'_\psi}{\partial r}+\xi_{17}\frac{\partial u'_z}{\partial z}+\xi_{18}\frac{\partial u'_r}{\partial z}+\xi_{19}\frac{\partial u'_\psi}{\partial z}\right.\\ &+ \left.\frac{1}{r}\left(\xi_{20}\frac{\partial u'_z}{\partial\psi}+\xi_{21}\left(\frac{\partial u'_r}{\partial\psi}-u'_\psi\right)+\xi_{22}\left(\frac{\partial u'_\psi}{\partial\psi}+u'_r\right)\right)\right);\end{aligned} \tag{A.6e}$$

$$\begin{aligned}D'_{r\psi} &= \frac{1}{d_r}\left(\xi_{23}\frac{\partial u'_z}{\partial r}+\xi_{24}\frac{\partial u'_r}{\partial r}+\xi_{25}\frac{\partial u'_\psi}{\partial r}+\xi_{26}\frac{\partial u'_z}{\partial z}+\xi_{27}\frac{\partial u'_r}{\partial z}+\xi_{28}\frac{\partial u'_\psi}{\partial z}\right.\\ &+ \left.\frac{1}{r}\left(\xi_{29}\frac{\partial u'_z}{\partial\psi}+\xi_{30}\left(\frac{\partial u'_r}{\partial\psi}-u'_\psi\right)+\xi_{31}\left(\frac{\partial u'_\psi}{\partial\psi}+u'_r\right)\right)\right),\end{aligned} \tag{A.6f}$$

where ξ_{1-4} are the same for models F and G, but ξ_{5-31} are different for models F and G.

Application of the normal-mode assumption of (2.11) to (2.10), we get

$$i\alpha\hat{u_z} + \frac{1}{r}\frac{\partial r\hat{u_r}}{\partial r} + \frac{1}{r}im\hat{u_\psi} = 0, \tag{A.7a}$$

$$i\omega\hat{u_z} + L_{OS}\hat{u_z} + \frac{\partial U}{\partial r}\hat{u_r} = -i\alpha\hat{p} - Ri\ \hat{n}, \tag{A.7b}$$

$$i\omega\hat{u_r} + L_{OS}\hat{u_r} = -\frac{\partial\hat{p}}{\partial r} + \frac{1}{Re}(-\frac{\hat{u_r}}{r^2} - \frac{2im}{r^2}\hat{u_\psi}), \tag{A.7c}$$

$$i\omega\hat{u_\psi} + L_{OS}\hat{u_\psi} = -\frac{1}{r}im\hat{p} + \frac{1}{Re}(-\frac{\hat{u_\psi}}{r^2} + \frac{2im}{r^2}\hat{u_r}), \tag{A.7d}$$

$$\begin{aligned}
i\omega\hat{n} \;&+\; L_n\hat{n} \\
&+\; \frac{\partial N}{\partial r}\hat{u_r} + (\frac{\partial N}{\partial r} + N\frac{\partial}{\partial r} + \frac{N}{r})(\frac{i\alpha\xi_1}{d_r}\hat{u_r} - \frac{\xi_1}{d_r}\frac{\partial\hat{u_z}}{\partial r}) \\
&+\; i\alpha N\frac{\xi_2}{d_r}(i\alpha\hat{u_r} - \frac{\partial\hat{u_z}}{\partial r}) + \frac{imN}{r}(\frac{\xi_3}{d_r}(\frac{im}{r}\hat{u_z} - i\alpha\hat{u_\psi}) + \frac{\xi_4}{rd_r}(\frac{\partial r\hat{u_\psi}}{\partial r} - im\hat{u_r})) \\
&=\; \frac{1}{d_r^2}\left[(\frac{1}{r}\frac{\partial N}{\partial r} + \frac{\partial N}{\partial r}\frac{\partial}{\partial r} + \frac{\partial^2 N}{\partial r^2})\left(\xi_5\frac{\partial\hat{u_z}}{\partial r} + \xi_6\frac{\partial\hat{u_r}}{\partial r} + \xi_7\frac{\partial\hat{u_\psi}}{\partial r}\right.\right. \\
&+\; \left.i\alpha(\xi_8\hat{u_z} + \xi_9\hat{u_r} + \xi_{10}\hat{u_\psi}) + \frac{im}{r}(\xi_{11}\hat{u_z} + \xi_{12}\hat{u_r} + \xi_{13}\hat{u_\psi}) + \frac{1}{r}(-\xi_{12}\hat{u_\psi} + \xi_{13}\hat{u_r})\right) \\
&+\; i\alpha\frac{\partial N}{\partial r}\left(\xi_{14}\frac{\partial\hat{u_z}}{\partial r} + \xi_{15}\frac{\partial\hat{u_r}}{\partial r} + \xi_{16}\frac{\partial\hat{u_\psi}}{\partial r} + i\alpha(\xi_{17}\hat{u_z} + \xi_{18}\hat{u_r} + \xi_{19}\hat{u_\psi})\right. \\
&+\; \left.\frac{im}{r}(\xi_{20}\hat{u_z} + \xi_{21}\hat{u_r} + \xi_{22}\hat{u_\psi}) + \frac{1}{r}(-\xi_{21}\hat{u_\psi} + \xi_{22}\hat{u_r})\right) \\
&+\; \frac{im}{r}\frac{\partial N}{\partial r}\left(\xi_{23}\frac{\partial\hat{u_z}}{\partial r} + \xi_{24}\frac{\partial\hat{u_r}}{\partial r} + \xi_{25}\frac{\partial\hat{u_\psi}}{\partial r} + i\alpha(\xi_{26}\hat{u_z} + \xi_{27}\hat{u_r} + \xi_{28}\hat{u_\psi})\right. \\
&+\; \left.\left.\frac{im}{r}(\xi_{29}\hat{u_z} + \xi_{30}\hat{u_r} + \xi_{31}\hat{u_\psi}) + \frac{1}{r}(-\xi_{30}\hat{u_\psi} + \xi_{31}\hat{u_r})\right)\right],
\end{aligned} \tag{A.7e}$$

where

$$L_{OS} = i\alpha U - \frac{1}{Re}\left(\frac{1}{r}\frac{\partial}{\partial r}(r\frac{\partial}{\partial r}) - \alpha^2 - \frac{m^2}{r^2}\right), \tag{A.7f}$$

and

$$\begin{aligned}
L_n \;&=\; (\frac{\langle p_r\rangle_0}{r} + \frac{\partial\langle p_r\rangle_0}{\partial r}) + \langle p_r\rangle_0\frac{\partial}{\partial r} + i\alpha U + i\alpha\langle p_z\rangle_0 + \frac{im\langle p_z\rangle_0}{r} \\
&-\; \frac{1}{d_r}\left[\frac{1}{r}\left(D_{rr,0}\frac{\partial}{\partial r} + i\alpha D_{rz,0} + 2imD_{r\psi,0}\frac{\partial}{\partial r} + im\frac{\partial D_{r\psi,0}}{\partial r} - 2\alpha mD_{\psi z,0}\right)\right. \\
&+\; \frac{\partial D_{rr,0}}{\partial r}\frac{\partial}{\partial r} + 2i\alpha\frac{\partial D_{rz,0}}{\partial r} + i\alpha D_{rz,0}\frac{\partial}{\partial r} \\
&+\; \left.D_{rr,0}\frac{\partial^2}{\partial r^2} - \alpha^2 D_{zz,0} - \frac{m^2}{r^2}D_{\psi\psi,0}\right].
\end{aligned} \tag{A.7g}$$

The boundary conditions at the wall are

$$\hat{u_z}|_{r=1} = \hat{u_r}|_{r=1} = \hat{u_\psi}|_{r=1} = 0 \tag{A.7h}$$

and

$$N\hat{u_r} + N\langle p_r\rangle' + \langle p_r\rangle_0\hat{n} = \frac{1}{d_r}\left(D'_{rr}\frac{\partial N}{\partial r} + D_{rr,0}\frac{\partial \hat{n}}{\partial r} + i\alpha D_{rz,0}\hat{n} + im\frac{D_{r\psi,0}}{r}\hat{n}\right). \tag{A.7i}$$

The compatibility conditions at the centre of the pipe are

$$\hat{u_z} = \hat{u_r} = \hat{u_\psi} = \hat{p} = \frac{\partial \hat{n}}{\partial r} = 0 \quad \text{when} \quad m \geqslant 2; \tag{A.7j}$$

$$\hat{u_r} + i\hat{u_\psi} = 0, \hat{u_z} = \frac{\partial \hat{n}}{\partial r} = \hat{p} = 0 \quad \text{when} \quad m = 1; \tag{A.7k}$$

$$\hat{u_r} = \hat{u_\psi} = 0, \frac{\partial \hat{u_z}}{\partial r} = \frac{\partial \hat{n}}{\partial r} = 0 \quad \text{when} \quad m = 0. \tag{A.7l}$$

These equations can now be discretised in the radial direction and solved as an eigenvalue problem, as mentioned in §2.3.

Appendix B

Transient dynamics of sheared ABP suspension under transformation

This appendix shows the transient dynamics of the ABP suspensions in §4.6. The original intent of the author was to show the evolution of the drifts and dispersions from the exact transformation and the local approximation as movies. However, given the constraint of the format of this thesis, the snapshots at some choosen time are shown instead in this appendix.

The figures of these snapshots are shown in the next few pages.

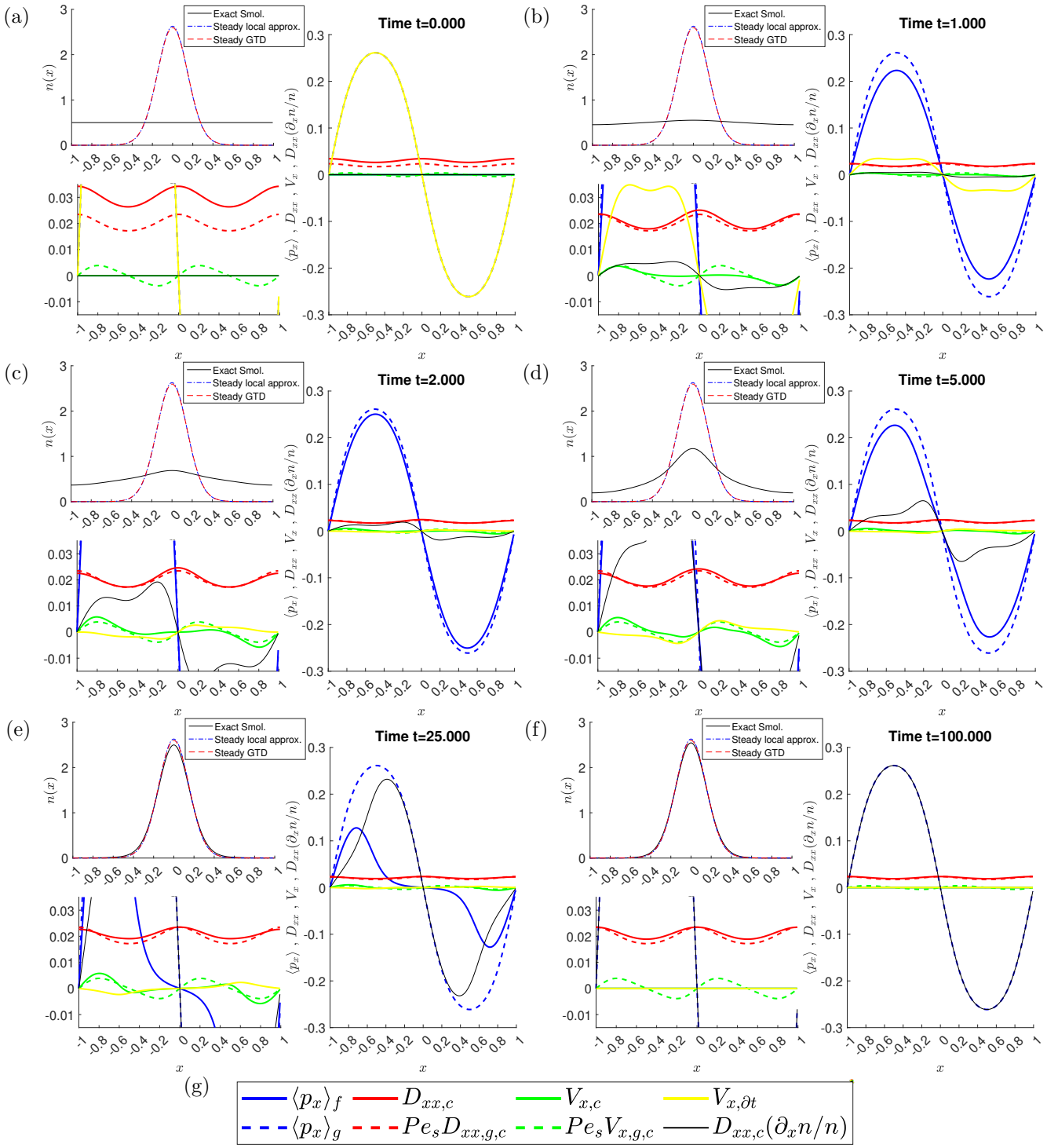

Figure B.1: The transient evolution of the particle distribution $n(x,t)$ (c.f. fig. 4.2a) and balancing of terms in (4.34) in comparison to their respective local approximation (c.f. fig. 4.3a) in a suspension of spherical and gyrotactic particles ($\beta = 2.2, \alpha_0 = 0$) subjected to a vertical shear flow $W(x) = -\cos(\pi x) - 1$ with $Pe_s = 0.25$ and $Pe_f = 1$. The bottom-left panel in each subfigure is the zoomed version of the panel on the right.

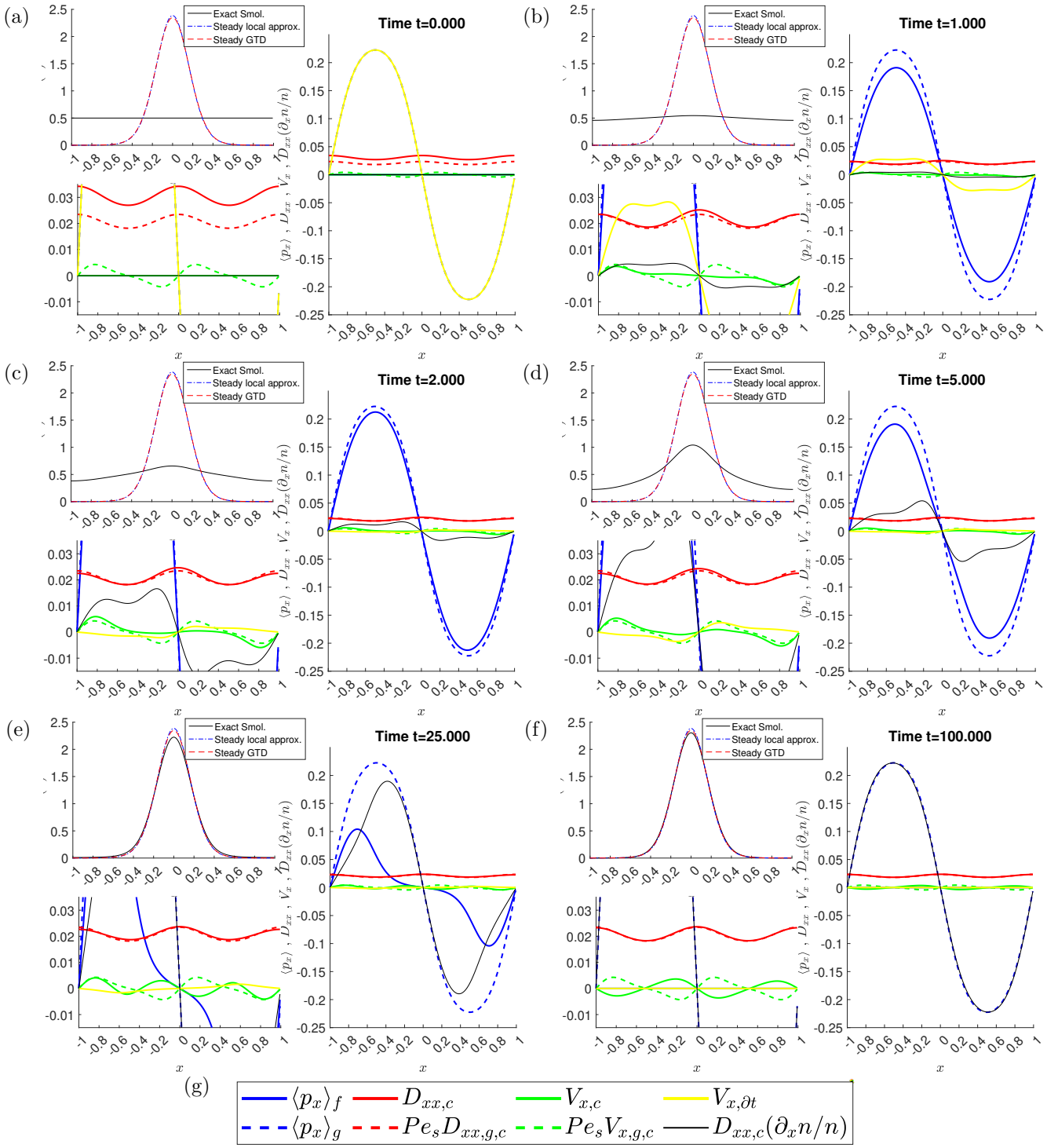

Figure B.2: The transient evolution of the particle distribution $n(x,t)$ (c.f. fig. 4.2b) and balancing of terms in (4.34) in comparison to their respective local approximation (c.f. fig. 4.3b) in a suspension of non-spherical and gyrotactic particles ($\beta = 2.2, \alpha_0 = 0.31$) subjected to a vertical shear flow $W(x) = -\cos(\pi x) - 1$ with $Pe_s = 0.25$ and $Pe_f = 1$. The bottom-left panel in each subfigure is the zoomed version of the panel on the right.

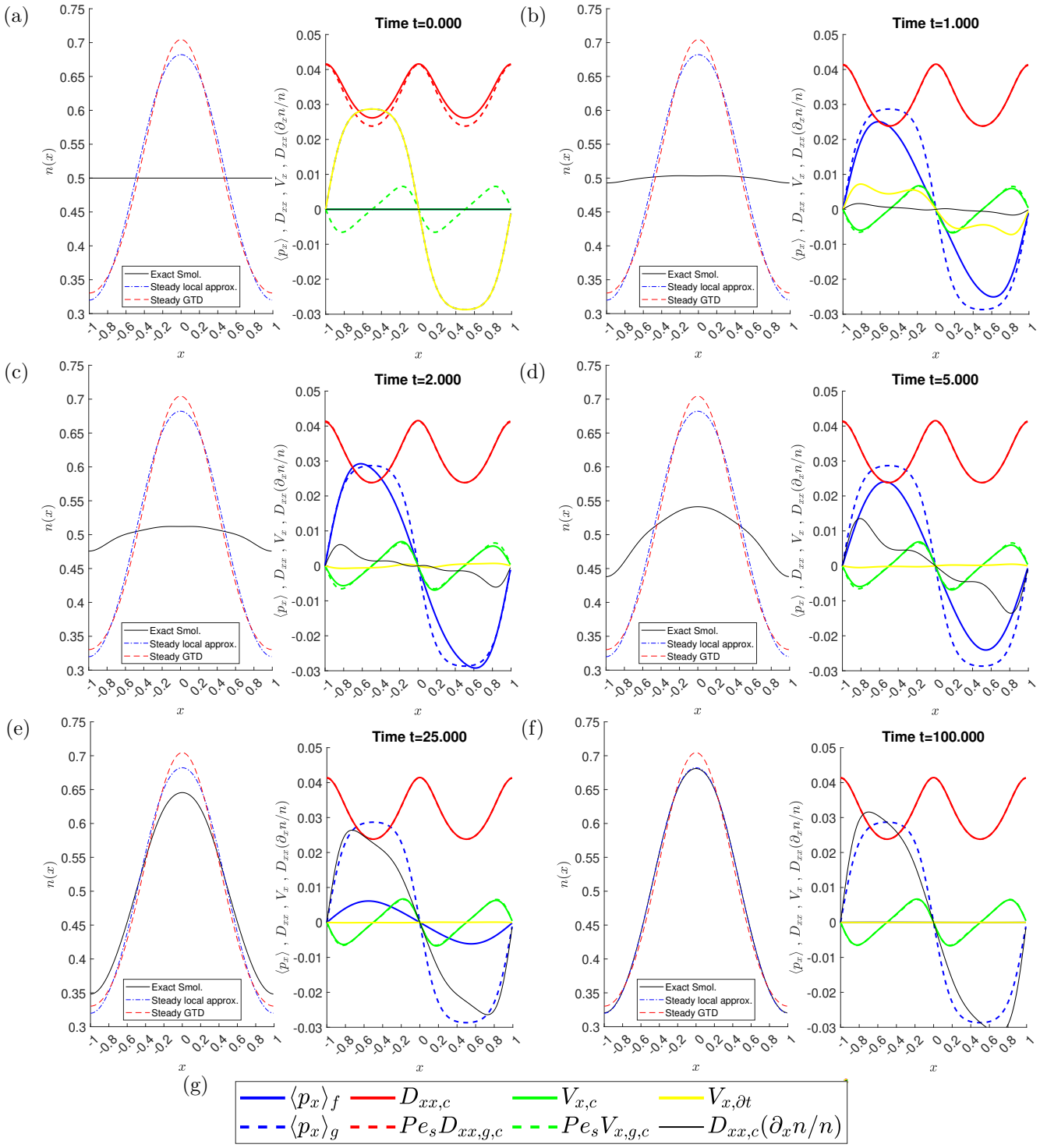

Figure B.3: The transient evolution of the particle distribution $n(x,t)$ (c.f. fig. 4.2c) and balancing of terms in (4.34) in comparison to their respective local approximation (c.f. fig. 4.3c) in a suspension of non-spherical and weakly gyrotactic particles ($\beta = 0.21, \alpha_0 = 0.31$) subjected to a vertical shear flow $W(x) = -\cos(\pi x) - 1$ with $Pe_s = 0.25$ and $Pe_f = 1$.

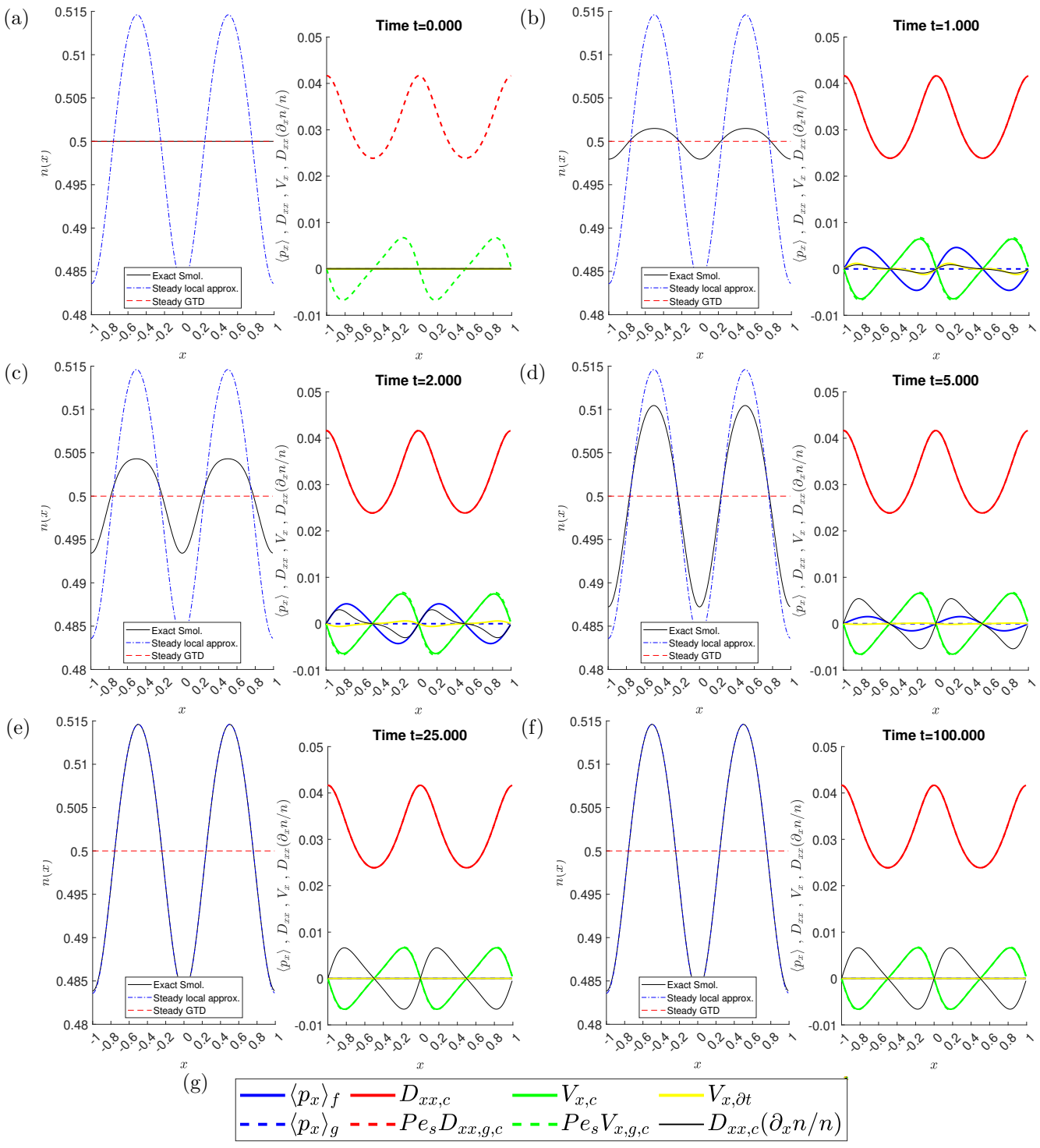

Figure B.4: The transient evolution of the particle distribution $n(x,t)$ (c.f. fig. 4.2d) and balancing of terms in (4.34) in comparison to their respective local approximation (c.f. fig. 4.3d) in a suspension of non-spherical and non-gyrotactic particles ($\beta = 0, \alpha_0 = 0.31$) subjected to a vertical shear flow $W(x) = -\cos(\pi x) - 1$ with $Pe_s = 0.25$ and $Pe_f = 1$.

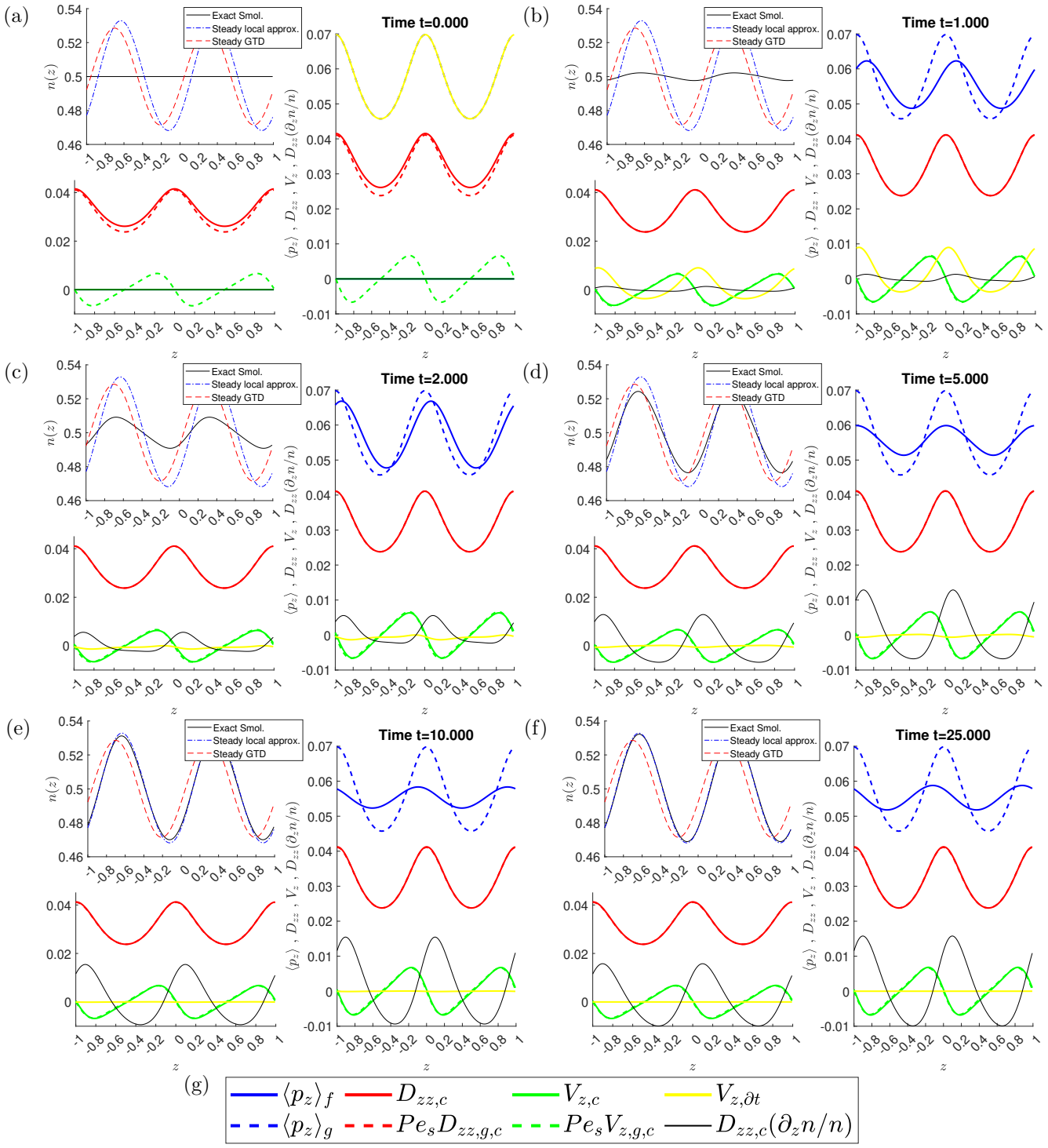

Figure B.5: The transient evolution of the particle distribution $n(x,t)$ (c.f. fig. 4.7a) and balancing of terms in (4.40) in comparison to their respective local approximation (c.f. fig. 4.8a) in a suspension of non-spherical and weakly gyrotactic particles ($\beta = 2.2, \alpha_0 = 0.31$) subjected to a horizontal shear flow $U(x) = \cos(\pi z)$ with $Pe_s = 0.25$ and $Pe_f = 1$. The bottom-left panel in each subfigure is the zoomed version of the panel on the right.

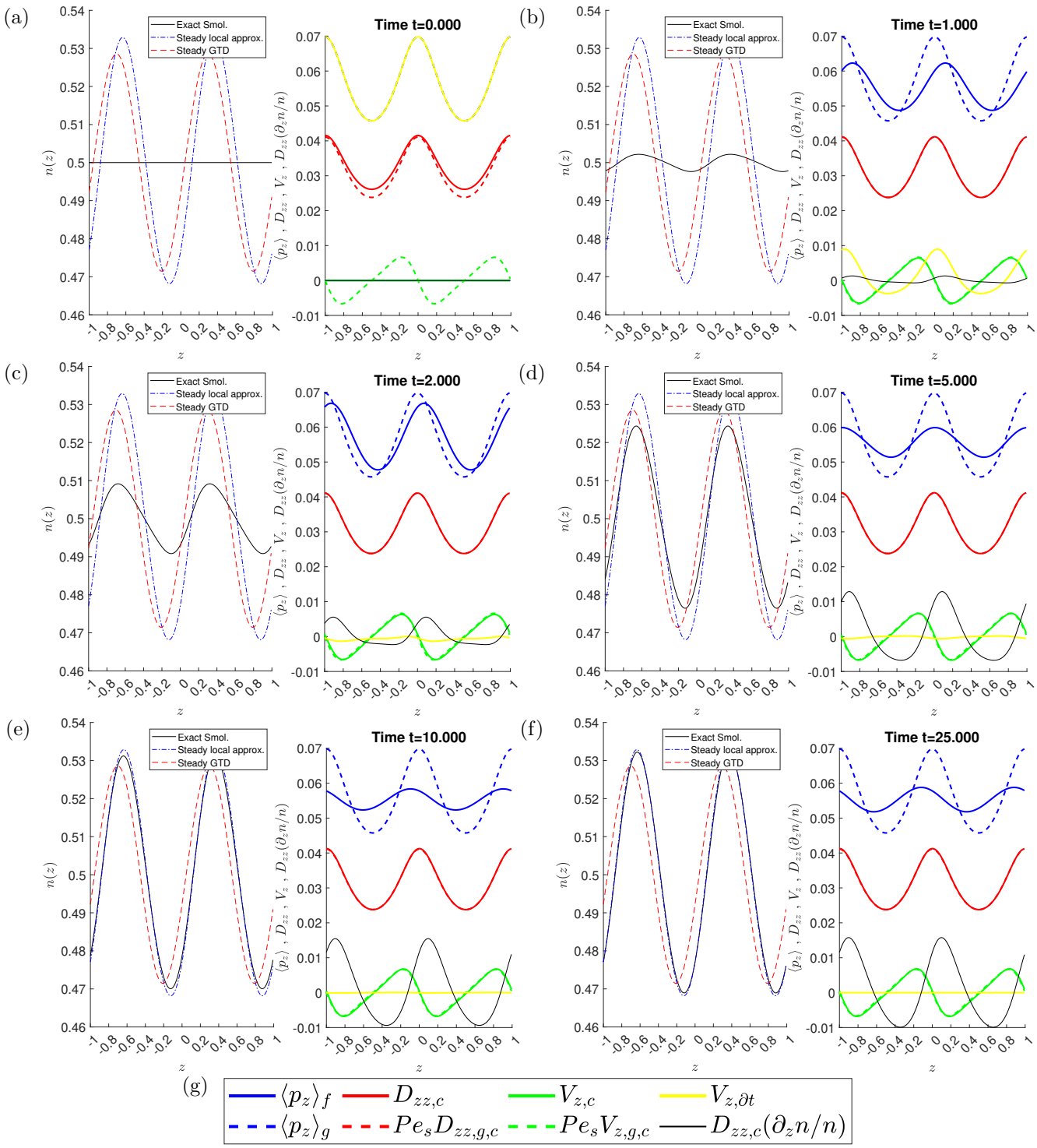

Figure B.6: The transient evolution of the particle distribution $n(x,t)$ (c.f. fig. 4.7b) and balancing of terms in (4.40) in comparison to their respective local approximation (c.f. fig. 4.8b) in a suspension of non-spherical and weakly gyrotactic particles ($\beta = 0.21, \alpha_0 = 0.31$) subjected to a horizontal shear flow $U(x) = \cos(\pi z)$ with $Pe_s = 0.25$ and $Pe_f = 1$.

Appendix C

The dependency of shear trapping flux on the second derivative of the velocity field

For gyrotactic swimmers, the corresponding orientational dynamics, as represented by $\mathcal{L}_p$ in (4.2), can be rewritten into two parts,

$$\mathcal{L}_p(\mathbf{x},t)a(\mathbf{p}) = Pe_f G_{ij}(\mathbf{x},t)\mathcal{L}^G_{\mathbf{p},ij}a(\mathbf{x},,t;\mathbf{p}) + \mathcal{L}^h_{\mathbf{p}}a(\mathbf{x},t;\mathbf{p}), \tag{C.1}$$

in which $G_{ij}(\mathbf{x},t)\mathcal{L}^G_{\mathbf{p},ij} = (\mathbf{\Omega}(\mathbf{x})\wedge\mathbf{p})/2 + \alpha_0\mathbf{p}\cdot\boldsymbol{E}\cdot(\boldsymbol{I}-\mathbf{pp})$ is the flow field dependent part (i.e. Jeffrey Orbit), while $\mathcal{L}^h_{\mathbf{p}} = \beta[\mathbf{k}-(\mathbf{k}\cdot\mathbf{p})\mathbf{p}] - \nabla^2_{\mathbf{p}}$ is the spatially homogeneous part of the operator. Here, $a(\mathbf{x},t;\mathbf{p})$ can be any arbitrary but continuous function in $\mathbf{p}$, $G_{ij} = \partial_{x_i}u_j$ and the Einstien summation of subscripts i, j and k are implicitly implied. If one take the $\mathbf{x}$-space gradient of $\mathcal{L}_p g(\mathbf{x},t;\mathbf{p}) = 0$, in which $g(\mathbf{x},t;\mathbf{p})$ is the homogeneous solution at each $(\mathbf{x},t)$, then

$$Pe_f\frac{\partial G_{i,j}}{\partial x_k}\mathcal{L}^G_{p,ij}g + \mathcal{L}_p\frac{\partial g}{\partial x_k} = 0. \tag{C.2}$$

Here, we define the second derivative of the velocity field , a third order tensor, as $H_{kij}(\mathbf{x},t) = \partial_{x_k}\partial_{x_i}u_k(\mathbf{x})$ such that the above can be rewritten as

$$Pe_f H_{kij}(\mathbf{x})\mathcal{L}^G_{p,ij}g + \mathcal{L}_p\partial_{x_k}g = 0. \tag{C.3}$$

Now, we define a new function $h_{ij}(\mathbf{x},t;\mathbf{p})$ in $\mathbf{p}$-space, where

$$\mathcal{L}_{\mathbf{p}}h_{ij}(\mathbf{x},t;\mathbf{p}) = -\mathcal{L}^G_{p,ij}g(\mathbf{x},t;\mathbf{p}), \tag{C.4}$$

and

$$\int_{S_p} h_{ij}(\mathbf{x}, t; \mathbf{p}) d^2\mathbf{p} = 0. \tag{C.5}$$

Therefore, by substituting h_{ij} into (C.3) and inverting the differential operator $\mathcal{L}_p$, one can get

$$Pe_f H_{kij}(\mathbf{x}, t) h_{ij}(\mathbf{x}, t; \mathbf{p}) = \mathcal{L}_p \partial_{x_k} g. \tag{C.6}$$

Following a similar procedure as §4.4, we multiply the above equation by $\mathbf{p}$ and take the $\mathbf{p}$-space integral again to get

$$Pe_f H_{kij}(\mathbf{x}, t) \langle p \rangle_{h,kij} = \partial_{x_k} \langle p_{x_k} \rangle_g = \boldsymbol{\nabla} \cdot \langle \mathbf{p} \rangle_g, \tag{C.7}$$

where we define

$$\langle p \rangle_{h,kij}(\mathbf{x}, t) = \int_{S_p} p_k h_{ij} d^2\mathbf{p}. \tag{C.8}$$

Now, we can rewrite (4.21e) as

$$\mathcal{L}_p f_{g,c} = g \boldsymbol{\nabla} \cdot \langle \mathbf{p} \rangle_g - \mathbf{p} \cdot \boldsymbol{\nabla} g = Pe_f H_{kij} (\langle p \rangle_{h,kij} g - p_k h_{ij}) \tag{C.9}$$

which also imply that $V_{g,c}$ scales with the second derivative of velocity $Pe_f H_{kij}$. In cases where the flow is parallel, it implies that $V_{g,c}$ is proportional to the gradient of shear S'.

Appendix D

Proof of permission to reuse figures

Fig. 1.2e is reproduced from Drescher *et al.* (2011), in which the authors retains copyright to the article and the National Academy of Sciences of the United States of America holds copyright to the collective work and retains an exclusive License to Publish. Permission is not required to reuse original figure for noncommercial and educational use.

Fig. 1.2f is reproduced from Guasto *et al.* (2010). Permission was granted by the publisher, American Physical Society, and the lead author, Prof. Jeffery S. Guasto, to reuse the figure in this thesis. The proves of permission are enclosed in the next few pages.

American Physical Society
Reuse and Permissions License

05-Aug-2021

This license agreement between the American Physical Society ("APS") and Lloyd Fung ("You") consists of your license details and the terms and conditions provided by the American Physical Society and SciPris.

Licensed Content Information

License Number:	**RNP/21/AUG/043019**
License date:	05-Aug-2021
DOI:	10.1103/PhysRevLett.105.168102
Title:	Oscillatory Flows Induced by Microorganisms Swimming in Two Dimensions
Author:	Jeffrey S. Guasto, Karl A. Johnson, and J. P. Gollub
Publication:	Physical Review Letters
Publisher:	American Physical Society
Cost:	USD $ 0.00

Request Details

Does your reuse require significant modifications: No

Specify intended distribution locations:	UK & Commonwealth (excluding Canada)
Reuse Category:	Reuse in a thesis/dissertation
Requestor Type:	Student
Items for Reuse:	Figures/Tables
Number of Figure/Tables:	1
Figure/Tables Details:	Figure 2a
Format for Reuse:	Electronic

Information about New Publication:

University/Publisher:	Imperial College London
Title of dissertation/thesis:	Modelling the transport and pattern formation of gyrotactic microswimmer suspensions
Author(s):	Lloyd Fung
Expected completion date:	Sep. 2021

License Requestor Information

Name:	Lloyd Fung
Affiliation:	Individual
Email Id:	lloyd.fung@imperial.ac.uk
Country:	United Kingdom

American Physical Society
Reuse and Permissions License

TERMS AND CONDITIONS

The American Physical Society (APS) is pleased to grant the Requestor of this license a non-exclusive, non-transferable permission, limited to Electronic format, provided all criteria outlined below are followed.

1. You must also obtain permission from at least one of the lead authors for each separate work, if you haven't done so already. The author's name and affiliation can be found on the first page of the published Article.
2. For electronic format permissions, Requestor agrees to provide a hyperlink from the reprinted APS material using the source material's DOI on the web page where the work appears. The hyperlink should use the standard DOI resolution URL, http://dx.doi.org/{DOI}. The hyperlink may be embedded in the copyright credit line.
3. For print format permissions, Requestor agrees to print the required copyright credit line on the first page where the material appears: "Reprinted (abstract/excerpt/figure) with permission from [(FULL REFERENCE CITATION) as follows: Author's Names, APS Journal Title, Volume Number, Page Number and Year of Publication.] Copyright (YEAR) by the American Physical Society."
4. Permission granted in this license is for a one-time use and does not include permission for any future editions, updates, databases, formats or other matters. Permission must be sought for any additional use.
5. Use of the material does not and must not imply any endorsement by APS.
6. APS does not imply, purport or intend to grant permission to reuse materials to which it does not hold copyright. It is the requestor's sole responsibility to ensure the licensed material is original to APS and does not contain the copyright of another entity, and that the copyright notice of the figure, photograph, cover or table does not indicate it was reprinted by APS with permission from another source.
7. The permission granted herein is personal to the Requestor for the use specified and is not transferable or assignable without express written permission of APS. This license may not be amended except in writing by APS.
8. You may not alter, edit or modify the material in any manner.
9. You may translate the materials only when translation rights have been granted.
10. APS is not responsible for any errors or omissions due to translation.
11. You may not use the material for promotional, sales, advertising or marketing purposes.
12. The foregoing license shall not take effect unless and until APS or its agent, Aptara, receives payment in full in accordance with Aptara Billing and Payment Terms and Conditions, which are incorporated herein by reference.
13. Should the terms of this license be violated at any time, APS or Aptara may revoke the license with no refund to you and seek relief to the fullest extent of the laws of the USA. Official written notice will be made using the contact information provided with the permission request. Failure to receive such notice will not nullify revocation of the permission.
14. APS reserves all rights not specifically granted herein.
15. This document, including the Aptara Billing and Payment Terms and Conditions, shall be the entire agreement between the parties relating to the subject matter hereof.